5.

COLLIDER COMPONENTS

IN Chapter 4 we presented the physics design of PEP-II. The parameters we have adopted to achieve a luminosity of 3×10^{33} cm^{-2} s^{-1}, and the beam separation scheme we have arrived at (driven mainly by background considerations), impose many requirements on the various technical components of the project. In this chapter, we describe these technical components, paying particular attention to those aspects that are most crucial to reaching the high luminosity we have specified. In general, the challenges to be met are associated with the high beam currents that must be stored in the two rings, 0.99 A in the high-energy ring (HER) and 2.14 A in the low-energy ring (LER). In all cases, we have designed the hardware to have adequate operating margin to ensure reliability, and we have employed proven design concepts wherever possible.

In Section 5.1 we describe the magnets and supports. In the case of the HER, nearly all of these magnets are existing PEP magnets, but we describe them briefly for completeness. Though the LER magnets will be newly constructed, they are based (with the exception of the dipoles) on proven PEP designs and are therefore straightforward to design and build. Magnets in the interaction region (IR), however, are technically quite challenging and are the key to the successful implementation of the beam separation scheme; these are described in Section 5.1.3.

The vacuum systems for the two rings are described in Section 5.2. The design challenges here are to provide a low background gas pressure in the face of copious synchrotron-radiation-induced photodesorption and to manage the high thermal loads associated with many megawatts of synchrotron radiation power. We have adopted a copper chamber for our design, based on its desirable properties in both these regards. In this section, we also describe the design and cooling for the various IR hardware components, such as the synchrotron radiation masks, the beam dumps, and the vertex detector beam pipe.

The other technically challenging aspects of the PEP-II design include the RF cavities (Section 5.5) and the feedback system (Section 5.6). The RF cavities must be designed to dissipate approximately 150 kW of power and to permit the effective damping of dangerous higher-order modes (HOMs) to Q values of about 70. This damping is accomplished with an innovative design in which three waveguides are attached to the body of the room-temperature cavity to remove the HOM power. The feedback system utilizes a bunch-by-bunch approach that is designed to handle the full bunch repetition rate of 238 MHz; the system employs a novel digital processing scheme that is very flexible and can accommodate both injection and colliding-beam conditions. Detailed simulations of system performance and tests of a portion of the system at SPEAR have demonstrated the efficacy of the design.

The remaining design aspects covered in Chapter 5—survey and alignment (Section 5.3), power supplies (Section 5.4), instrumentation and electronics (Section 5.7), and control system (Section 5.8) are relatively straightforward. Here too we have paid attention to providing flexibility and reliability in all components to ensure that PEP-II will indeed function as a "factory."

5.1 MAGNETS AND SUPPORTS

The magnet system in PEP-II provides the guide fields that bend and focus the charged particles, electrons in the HER and positrons in the LER. In the case of the HER, the lattice is designed to make use of most of the existing PEP magnets. The LER is an entirely new ring for which all magnets must be newly constructed.

Because PEP was designed to operate at 18 GeV, whereas the PEP-II HER has a nominal energy of 9 GeV, the PEP magnets are very conservatively designed for their new function. As discussed in Section 7.2, it is prudent to inspect the magnets when they are removed from the tunnel; as needed, the magnet coils will be refurbished to ensure their reliability for long-term PEP-II service. In addition, some of the magnets will be measured after reassembly to ensure that their fields remain the same.

We plan to reuse all of the PEP dipoles and quadrupoles for the PEP-II HER. Because the HER lattice uses more quadrupoles than did PEP, additional magnets must be fabricated. In the case of the dipoles, we need 192 regular bending magnets and an additional 16 PEP low-field bending magnets, for a total of 208 PEP dipoles; four short LER-style dipoles will also be used, making a grand total of 212 dipoles for the HER. All 144 sextupoles are available from PEP. For completeness, however, we describe the existing PEP magnets briefly in Section 5.1.1.

The quadrupole and sextupole magnets for the LER are designed to have the same aperture as the present PEP magnets. This is justified because the required beam-stay-clear aperture in the LER is almost identical to that of the HER, as discussed in Section 5.2.2. Basing the LER designs on PEP magnets minimizes the engineering and design efforts required, because the already-optimized pole profiles of the PEP magnets can be used without modification. The LER dipoles are much shorter than the PEP dipoles (0.45 m compared with 5.4 m for PEP) and will not be based on that pole profile. Design details for the LER magnets are presented in Section 5.1.2.

5.1.1 HER Magnets

As mentioned above, most of the magnets for the HER are existing PEP magnets. The only exception is the quadrupoles. Additional quadrupoles are needed for the HER because the FODO focusing structure (see Section 4.1) will be maintained throughout the straight sections, except for the IR-2 straight that houses the detector.

bunch approach that is designed to handle the full bunch repetition rate of 238 MHz; the system employs a novel digital processing scheme that is very flexible and can accommodate both injection and colliding-beam conditions. Detailed simulations of system performance and tests of a portion of the system at SPEAR have demonstrated the efficacy of the design.

The remaining design aspects covered in Chapter 5—survey and alignment (Section 5.3), power supplies (Section 5.4), instrumentation and electronics (Section 5.7), and control system (Section 5.8) are relatively straightforward. Here too we have paid attention to providing flexibility and reliability in all components to ensure that PEP-II will indeed function as a "factory."

5.1 MAGNETS AND SUPPORTS

The magnet system in PEP-II provides the guide fields that bend and focus the charged particles, electrons in the HER and positrons in the LER. In the case of the HER, the lattice is designed to make use of most of the existing PEP magnets. The LER is an entirely new ring for which all magnets must be newly constructed.

Because PEP was designed to operate at 18 GeV, whereas the PEP-II HER has a nominal energy of 9 GeV, the PEP magnets are very conservatively designed for their new function. As discussed in Section 7.2, it is prudent to inspect the magnets when they are removed from the tunnel; as needed, the magnet coils will be refurbished to ensure their reliability for long-term PEP-II service. In addition, some of the magnets will be measured after reassembly to ensure that their fields remain the same.

We plan to reuse all of the PEP dipoles and quadrupoles for the PEP-II HER. Because the HER lattice uses more quadrupoles than did PEP, additional magnets must be fabricated. In the case of the dipoles, we need 192 regular bending magnets and an additional 16 PEP low-field bending magnets, for a total of 208 PEP dipoles; four short LER-style dipoles will also be used, making a grand total of 212 dipoles for the HER. All 144 sextupoles are available from PEP. For completeness, however, we describe the existing PEP magnets briefly in Section 5.1.1.

The quadrupole and sextupole magnets for the LER are designed to have the same aperture as the present PEP magnets. This is justified because the required beam-stay-clear aperture in the LER is almost identical to that of the HER, as discussed in Section 5.2.2. Basing the LER designs on PEP magnets minimizes the engineering and design efforts required, because the already-optimized pole profiles of the PEP magnets can be used without modification. The LER dipoles are much shorter than the PEP dipoles (0.45 m compared with 5.4 m for PEP) and will not be based on that pole profile. Design details for the LER magnets are presented in Section 5.1.2.

5.1.1 HER Magnets

As mentioned above, most of the magnets for the HER are existing PEP magnets. The only exception is the quadrupoles. Additional quadrupoles are needed for the HER because the FODO focusing structure (see Section 4.1) will be maintained throughout the straight sections, except for the IR-2 straight that houses the detector.

5.1.1.1 Dipoles. The main parameters of the laminated PEP dipoles are summarized in Table 5-1 for conditions corresponding to the nominal PEP-II operating energy of 9 GeV. Physical dimensions of the magnet are shown in Fig. 5-1. Each magnet has a magnetic length of 5.4 m (212.607 in.) and weighs 7.4 tons. The coils, located above and below the midplane, are constructed of water-cooled aluminum, insulated with Mylar and fiberglass tape and vacuum potted in a radiation-hardened alumina-based epoxy. All dipoles will be disassembled and will have their coil insulation inspected and refurbished to ensure reliable service in PEP-II. After reassembly, a sample of magnets will be remeasured to ensure the constancy of their magnetic properties. To provide horizontal orbit correction, backleg windings are employed. Windings from a pair of dipoles on either side of a focusing quadrupole will be ganged together to form a single corrector.

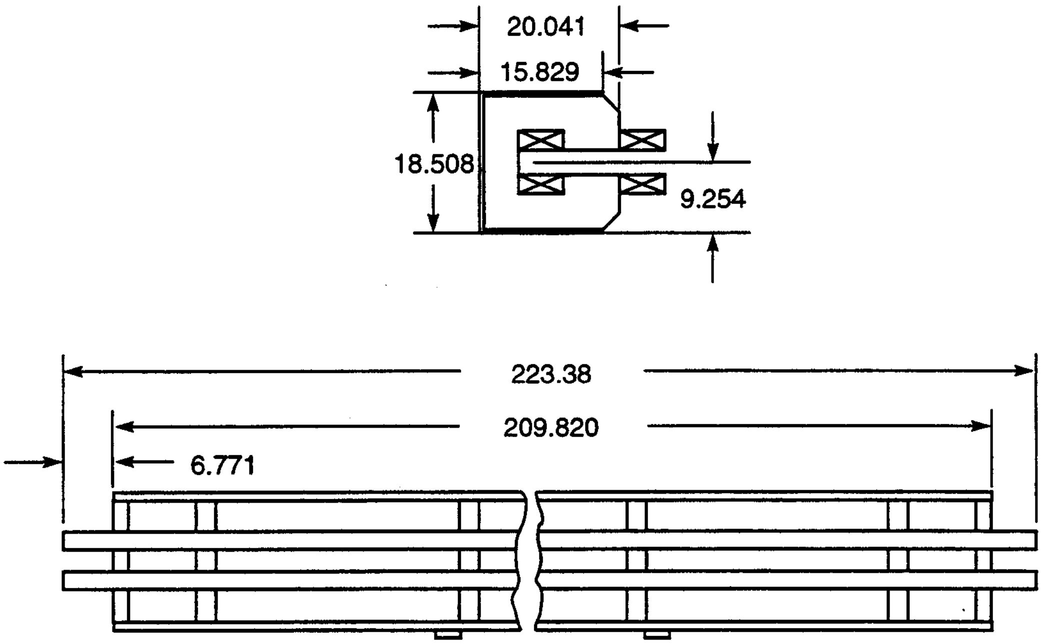

Fig. 5-1. End and side views of the HER bending magnet. Dimensions are given in inches.

Table 5-1. HER dipole parameters.

Magnet designation	2.8C212	2.8H17	5.8H85	5.8H80
Lattice designation	B	B4	B3	B2
Number of magnets	192	4	8	8
Field @ 9 GeV [T]	0.1819	0.0904	0.0216	0.0216
Integrated field @ 9 GeV [T·m]	0.9824	0.0407	0.0466	0.0431
Pole width [in.]	8.425	7.5	5.9	5.9
Gap height [in.]	2.787	2.787	5.875	5.875
Core length [in.]	209.820	14.930	79.085	72.685
Magnetic length [in.]	212.607	17.717	84.960	78.560
Width of useful field, 0.1% [in.]	4.725	4.00	3.15	3.15
Lamination height [in.]	15.433	16	13.38	13.38
Lamination width [in.]	18.19	17.8	10.47	10.47
Packing factor, minimum [%]	98	98	NA	NA
Core weight [lb]	14,168	2,000	1,500	1,500
Amp·turns @ 9 GeV	5,121	2,544	1,280	1,280
Turns	8	36	2	2
Pancakes per pole	1	1	1	1
Conductor dimensions [in.]	2.4 × 0.7	2.0 × 0.3125	2.4 × 0.7	2.4 × 0.7
Cooling hole diameter [in.]	0.25	0.1875	0.25	0.25
Conductor cross section [in.^{2}]	1.63	0.60	1.63	1.63
Current @ 9 GeV [A]	640.1	70.7	640.1	640.1
Resistance @ 40°C [mΩ]	5.1	7.2	0.4	0.4
Power @ 9 GeV [kW]	2.08	0.04	0.15	0.15
Voltage drop @ 9 GeV [V]	3.6	0.5	0.2	0.2
Coil weight [lb]	585	200	40	40
Number of water circuits	1	1	1	11
Water flow rate [gpm]	0.8	0.3	1.4	1.4
Water pressure drop [psi]	150	100	50	50
Temperature rise [°C]	5.3	0.4	0.4	0.4
Total power, magnets and bus [kW]	399.4	0.1	1.2	1.2
Total voltage, magnets and bus [V]	691.2	2.0	1.9	1.9
Total system water requirements [gpm]	144.4	1.4	11.0	11.4

5.1.1.2 Quadrupoles. As with the dipole magnets, all existing PEP quadrupoles will be reused for the HER. Altogether, 270 magnets are required for the PEP-II HER, of which 200 are available from PEP. The additional magnets will be fabricated using the same pole-tip profile developed for PEP, thus avoiding the need to develop a new design. Dimensions of a typical quadrupole magnet are shown in Fig. 5-2. The electrical characteristics of the existing quadrupoles, together with the new magnets, are summarized in Table 5-2. As is the case for the dipoles, the conductor for the quadrupoles is an aluminum extrusion. The insulating procedure used for the dipoles, employing Mylar, fiberglass tape, and alumina-loaded epoxy, will also be used for the quadrupole magnets.

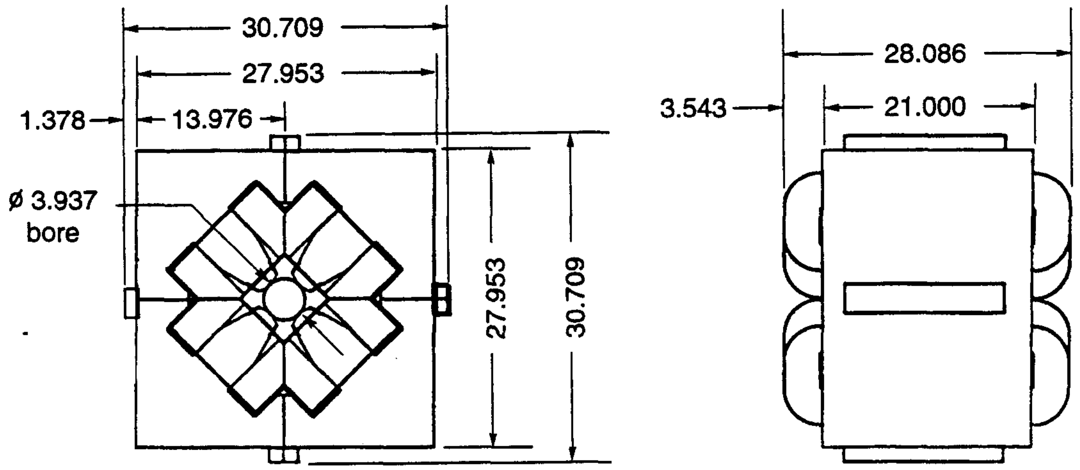

Fig. 5-2. End and side views of an HER quadrupole magnet. Dimensions are given in inches.

Table 5-2. HER quadrupole parameters. The column heads indicate whether the magnets are refurbished PEP quadrupoles or newly constructed magnets.

	PEP	PEP	PEP	New	PEP	PEP
Magnet designation	4Q22	4Q40	4Q40	4Q18	4Q40	4Q40
Lattice designation	QD	QD6	QDI	QDO	QDOI	QDP1
Number of magnets	54	2	2	14	2	2
Operating gradient [T/m]	7.33	7.89	1.95	8.83	2.98	4.06
Pole-tip field @ operating gradient [T]	0.366	0.394	0.097	0.441	0.149	0.203
Gradient-length product [T]	4.03	7.89	1.95	3.97	2.98	4.06
Inscribed radius [in.]	1.968	1.968	1.968	1.968	1.968	1.968
Minimum gap [in.]	1.457	1.457	1.457	1.457	1.457	1.457
Core length [in.]	19.69	37.40	37.40	15.75	37.40	37.40
Magnetic length [in.]	21.65	39.37	39.37	17.72	39.37	39.37
Lamination height [in.]	13.98	13.98	13.98	13.98	13.98	13.98
Lamination width [in.]	13.35	13.35	13.35	13.35	13.35	13.35
Packing factor, minimum [%]	98	98	98	98	98	98
Core weight [lb]	2898	5506	5506	2318	5506	5506
Amp-turns per pole @ 9 GeV	7280	7837	1935	8770	2965	4032
Turns per pole	57	57	57	57	57	57
Pancakes per pole	1	1	1	1	1	1
Conductor cross-sectional area [in.^{2}]	0.197	0.197	0.197	0.197	0.197	0.197
Conductor dimensions [in.]	0.5×0.5	0.5×0.5	0.5×0.5	0.5×0.5	0.5×0.5	0.5×0.5
Cooling hole diameter [in.]	0.25	0.25	0.25	0.25	0.25	0.25
Current @ 9 GeV [A]	128	137	34	154	52	71
Resistance @ 40°C [mΩ]	82	127	127	72	127	127
Power @ 9 GeV [kW]	1.3	2.4	0.2	1.7	0.3	0.6
Voltage drop @ 9 GeV [V]	10.5	17.5	4.3	11.1	6.6	9.0
Coil weight [lb]	282	438	438	248	438	438
Number of water circuits	1	2	1	1	1	1
Water flow rate [gpm]	0.5	1.2	0.4	0.6	0.4	0.4
Water pressure drop [psi]	150	150	150	150	150	150
Temperature rise [°C]	9.8	7.7	1.4	11.7	3.2	5.9
Total power (magnets and bus) [kW]	72.4	4.8	0.3	23.9	0.7	1.3
Total voltage [V]	567	35	9	156	13	18
Magnet system water requirements [gpm]	28	2	1	8	1	1

Table 5-2. HER quadrupole parameters. The column heads indicate whether the magnets are refurbished PEP quadrupoles or newly constructed magnets (continued).

	PEP	New	PEP	New	PEP	New
Magnet designation	4Q40	4Q18	4Q40	4Q18	4Q40	4Q18
Lattice designation	QDP3	QDP3	QDP5	QDP5	QDP7	QDP7
Number of magnets	2	2	2	2	2	2
Operating gradient [T/m]	4.02	8.94	4.00	8.89	3.99	8.88
Pole-tip field @ operating gradient [T]	0.201	0.447	0.200	0.444	0.199	0.444
Gradient-length product [T]	4.02	4.02	4.00	4.00	3.99	3.99
Inscribed radius [in.]	1.968	1.968	1.968	1.968	1.968	1.968
Minimum gap [in.]	1.457	1.457	1.457	1.457	1.457	1.457
Core length [in.]	37.40	15.75	37.40	15.75	37.40	15.75
Magnetic length [in.]	39.37	17.72	39.37	17.72	39.37	17.72
Lamination height [in.]	13.98	13.98	13.98	13.98	13.98	13.98
Lamination width [in.]	13.35	13.35	13.35	13.35	13.35	13.35
Packing factor, minimum [%]	98	98	98	98	98	98
Core weight [lb]	5506	2318	5506	2318	5506	2318
Amp-turns per pole @ 9 GeV	3999	8887	3974	8832	3964	8819
Turns per pole	57	57	57	57	57	57
Pancakes per pole	1	1	1	1	1	1
Conductor cross-sectional area [in.^{2}]	0.197	0.197	0.197	0.197	0.197	0.197
Conductor dimensions [in.]	0.5×0.5	0.5×0.5	0.5×0.5	0.5×0.5	0.5×0.5	0.5×0.5
Cooling hole diameter [in.]	0.25	0.25	0.25	0.25	0.25	0.25
Current @ 9 GeV [A]	70	156	70	155	70	155
Resistance @ 40°C [mΩ]	127	72	127	72	127	72
Power @ 9 GeV [kW]	0.6	1.8	0.6	1.7	0.6	1.7
Voltage drop @ 9 GeV [V]	8.9	11.3	8.9	11.2	8.9	11.2
Coil weight [lb]	438	248	438	248	438	248
Number of water circuits	1	1	1	1	1	1
Water flow rate [gpm]	0.4	0.6	0.4	0.6	0.4	0.6
Water pressure drop [psi]	150	150	150	150	150	150
Temperature rise [°C]	5.8	12.0	5.7	11.8	5.7	11.8
Total power (magnets and bus) [kW]	1.3	3.5	1.2	3.5	1.2	3.5
Total voltage [V]	18	23	18	22	18	22
Magnet system water requirements [gpm]	1	1	1	1	1	1

Table 5-2. HER quadrupole parameters. The column heads indicate whether the magnets are refurbished PEP quadrupoles or newly constructed magnets (continued).

	PEP	PEP	PEP	PEP	New	New
Magnet designation	4Q29	4Q29	4Q29	4Q29	4Q18	4Q18
Lattice designation	QDSO1	QDSO1E	QDSO2	QDSO2E	QDSOL	QDSOR
Number of magnets	1	4	1	4	1	1
Operating gradient [T/m]	5.33	5.62	5.35	5.66	8.61	8.61
Pole-tip field @ operating gradient [T]	0.266	0.281	0.267	0.283	0.430	0.430
Gradient-length product [T]	3.89	4.10	3.91	4.13	3.87	3.87
Inscribed radius [in.]	1.968	1.968	1.968	1.968	1.968	1.968
Minimum gap [in.]	1.457	1.457	1.457	1.457	1.457	1.457
Core length [in.]	26.77	26.77	26.77	26.77	15.75	15.75
Magnetic length [in.]	28.74	28.74	28.74	28.74	17.72	17.72
Lamination height [in.]	13.98	13.98	13.98	13.98	13.98	13.98
Lamination width [in.]	13.35	13.35	13.35	13.35	13.35	13.35
Packing factor, minimum [%]	98	98	98	98	98	98
Core weight [lb]	3941	3941	3941	3941	2318	2318
Amp-turns per pole @ 9 GeV	5297	5585	5317	5623	8550	8550
Turns per pole	57	57	57	57	57	57
Pancakes per pole	1	1	1	1	1	1
Conductor cross-sectional area [in.^{2}]	0.197	0.197	0.197	0.197	0.197	0.197
Conductor dimensions [in.]	0.5×0.5	0.5×0.5	0.5×0.5	0.5×0.5	0.5×0.5	0.5×0.5
Cooling hole diameter [in.]	0.25	0.25	0.25	0.25	0.25	0.25
Current @ 9 GeV [A]	93	98	93	99	150	150
Resistance @ 40°C [mΩ]	100	100	100	100	72	72
Power @ 9 GeV [kW]	0.9	1.0	0.9	1.0	1.6	1.6
Voltage drop @ 9 GeV [V]	9.3	9.8	9.4	9.9	10.8	10.8
Coil weight [lb]	345	345	345	345	248	248
Number of water circuits	1	1	1	1	1	1
Water flow rate [gpm]	0.5	0.5	0.5	0.5	0.6	0.6
Water pressure drop [psi]	150	150	150	150	150	150
Temperature rise [°C]	7.1	7.8	7.1	7.9	11.1	11.1
Total power (magnets and bus) [kW]	9	39	9	40	1.6	1.6
Total voltage [V]	1	39	9	40	11	11
Magnet system water requirements [gpm]	0	2	0	2	1	1

Table 5-2. HER quadrupole parameters. The column heads indicate whether the magnets are refurbished PEP quadrupoles or newly constructed magnets (continued).

	New	New	New	New	PEP	PEP
Magnet designation	4Q18	4Q18	4Q18	4Q18	4Q22	4Q22
Lattice designation	QDS11	QDS11E	QDS12	QDS12E	QDS1L	QDS1R
Number of magnets	1	4	1	4	1	1
Operating gradient [T/m]	8.61	9.37	9.79	9.41	7.98	8.01
Pole-tip field @ operating gradient [T]	0.430	0.468	0.489	0.470	0.399	0.400
Gradient-length product [T]	3.87	4.22	4.41	4.24	4.39	4.41
Inscribed radius [in.]	1.968	1.968	1.968	1.968	1.968	1.968
Minimum gap [in.]	1.457	1.457	1.457	1.457	1.457	1.457
Core length [in.]	15.75	15.75	15.75	15.75	19.69	19.69
Magnetic length [in.]	17.72	17.72	17.72	17.72	21.65	21.65
Lamination height [in.]	13.98	13.98	13.98	13.98	13.98	13.98
Lamination width [in.]	13.35	13.35	13.35	13.35	13.35	13.35
Packing factor, minimum [%]	98	98	98	98	98	98
Core weight [lb]	2318	2318	2318	2318	2898	2898
Amp-turns per pole @ 9 GeV	8550	9309	9728	9352	7925	7960
Turns per pole	57	57	57	57	57	57
Pancakes per pole	1	1	1	1	1	1
Conductor cross-sectional area [in.^{2}]	0.197	0.197	0.197	0.197	0.197	0.197
Conductor dimensions [in.]	0.5×0.5	0.5×0.5	0.5×0.5	0.5×0.5	0.5×0.5	0.5×0.5
Cooling hole diameter [in.]	0.25	0.25	0.25	0.25	0.25	0.25
Current @ 9 GeV [A]	150	163	171	164	139	140
Resistance @ 40°C [mΩ]	72	72	72	72	82	82
Power @ 9 GeV [kW]	1.6	1.9	2.1	1.9	1.6	1.6
Voltage drop @ 9 GeV [V]	10.8	11.8	12.3	11.9	11.4	11.5
Coil weight [lb]	248	248	248	248	282	282
Number of water circuits	1	1	1	1	1	1
Water flow rate [gpm]	0.6	0.6	0.6	0.6	0.5	0.5
Water pressure drop [psi]	150	150	150	150	150	150
Temperature rise [°C]	11.1	13.1	14.3	13.2	11.6	11.7
Total power (magnets and bus) [kW]	1.6	7.7	2.1	7.8	1.6	1.6
Total voltage [V]	11	47	12	47	11	11
Magnet system water requirements [gpm]	1	2	1	2	1	1

Table 5-2. HER quadrupole parameters. The column heads indicate whether the magnets are refurbished PEP quadrupoles or newly constructed magnets (continued).

	PEP	PEP	PEP	PEP	New	New
Magnet designation	4Q22	4Q22	4Q22	4Q22	4Q18	4Q18
Lattice designation	QDS21	QDS21E	QDS22	QDS22E	QDS2L	QDS2R
Number of magnets	1	4	1	4	1	1
Operating gradient [T/m]	7.19	7.72	7.17	7.71	8.68	8.76
Pole-tip field @ operating gradient [T]	0.359	0.386	0.358	0.385	0.434	0.438
Gradient-length product [T]	3.95	4.25	3.94	4.24	3.90	3.94
Inscribed radius [in.]	1.968	1.968	1.968	1.968	1.968	1.968
Minimum gap [in.]	1.457	1.457	1.457	1.457	1.457	1.457
Core length [in.]	19.69	19.69	19.69	19.69	15.75	15.75
Magnetic length [in.]	21.65	21.65	21.65	21.65	17.72	17.72
Lamination height [in.]	13.98	13.98	13.98	13.98	13.98	13.98
Lamination width [in.]	13.35	13.35	13.35	13.35	13.35	13.35
Packing factor, minimum [%]	98	98	98	98	98	98
Core weight [lb]	2898	2898	2898	2898	2318	2318
Amp-turns per pole @ 9 GeV	7140	7672	7119	7656	8621	8701
Turns per pole	57	57	57	57	57	57
Pancakes per pole	1	1	1	1	1	1
Conductor cross-sectional area [in.^{2}]	0.197	0.197	0.197	0.197	0.197	0.197
Conductor dimensions [in.]	0.5×0.5	0.5×0.5	0.5×0.5	0.5×0.5	0.5×0.5	0.5×0.5
Cooling hole diameter [in.]	0.25	0.25	0.25	0.25	0.25	0.25
Current @ 9 GeV [A]	125	135	125	134	151	153
Resistance @ 40°C [mΩ]	82	82	82	82	72	72
Power @ 9 GeV [kW]	1.3	1.5	1.3	1.5	1.7	1.7
Voltage drop @ 9 GeV [V]	10.3	11.1	10.3	11.1	10.9	11.0
Coil weight [lb]	282	282	282	282	248	248
Number of water circuits	1	1	1	1	1	1
Water flow rate [gpm]	0.5	0.5	0.5	0.5	0.6	0.6
Water pressure drop [psi]	150	150	150	150	150	150
Temperature rise [°C]	9.4	10.9	9.4	10.9	11.3	11.5
Total power (magnets and bus) [kW]	1.3	6.0	1.3	5.9	1.7	1.7
Total voltage [V]	10	44	10	44	11	11
Magnet system water requirements [gpm]	1	2	1	2	1	1

Table 5-2. HER quadrupole parameters. The column heads indicate whether the magnets are refurbished PEP quadrupoles or newly constructed magnets (continued).

	PEP	PEP	PEP	PEP	PEP	PEP
Magnet designation	4Q22	4Q22	4Q22	4Q22	4Q22	4Q22
Lattice designation	QDS31	QDS31E	QDS32	QDS32E	QDS3L	QDS3R
Number of magnets	1	4	1	4	1	1
Operating gradient [T/m]	7.33	7.33	7.33	7.33	7.33	7.33
Pole-tip field @ operating gradient [T]	0.366	0.366	0.366	0.366	0.366	0.366
Gradient-length product [T]	4.03	4.03	4.03	4.03	4.03	4.03
Inscribed radius [in.]	1.968	1.968	1.968	1.968	1.968	1.968
Minimum gap [in.]	1.457	1.457	1.457	1.457	1.457	1.457
Core length [in.]	19.69	19.69	19.69	19.69	19.69	19.69
Magnetic length [in.]	21.65	21.65	21.65	21.65	21.65	21.65
Lamination height [in.]	13.98	13.98	13.98	13.98	13.98	13.98
Lamination width [in.]	13.35	13.35	13.35	13.35	13.35	13.35
Packing factor, minimum [%]	98	98	98	98	98	98
Core weight [lb]	2898	2898	2898	2898	2898	2898
Amp-turns per pole @ 9 GeV	7280	7280	7280	7280	7280	7280
Turns per pole	57	57	57	57	57	57
Pancakes per pole	1	1	1	1	1	1
Conductor cross-sectional area [in.^{2}]	0.197	0.197	0.197	0.197	0.197	0.197
Conductor dimensions [in.]	0.5×0.5	0.5×0.5	0.5×0.5	0.5×0.5	0.5×0.5	0.5×0.5
Cooling hole diameter [in.]	0.25	0.25	0.25	0.25	0.25	0.25
Current @ 9 GeV [A]	128	128	128	128	128	128
Resistance @ 40°C [mΩ]	82	82	82	82	82	82
Power @ 9 GeV [kW]	1.3	1.3	1.3	1.3	1.3	1.3
Voltage drop @ 9 GeV [V]	10.5	10.5	10.5	10.5	10.5	10.5
Coil weight [lb]	282	282	282	282	282	282
Number of water circuits	1	1	1	1	1	1
Water flow rate [gpm]	0.5	0.5	0.5	0.5	0.5	0.5
Water pressure drop [psi]	150	150	150	150	150	150
Temperature rise [°C]	9.8	9.8	9.8	9.8	9.8	9.8
Total power (magnets and bus) [kW]	1.3	5.4	1.3	5.4	1.3	1.3
Total voltage [V]	11	42	11	42	11	11
Magnet system water requirements [gpm]	1	2	1	2	1	1

Table 5-2. HER quadrupole parameters. The column heads indicate whether the magnets are refurbished PEP quadrupoles or newly constructed magnets (continued).

	PEP	PEP	PEP	New	PEP
Magnet designation	4Q29	4Q40	4Q40	4Q18	4Q40
Lattice designation	QF	QF7	QFI	QFO	QFOI
Number of magnets	60	2	2	16	2
Operating gradient [T/m]	5.48	5.96	1.92	8.83	4.08
Pole-tip field @ operating gradient [T]	0.274	0.298	0.096	0.441	0.204
Gradient-length product [T]	4.00	5.96	1.92	3.97	4.08
Inscribed radius [in.]	1.968	1.968	1.968	1.968	1.968
Minimum gap [in.]	1.457	1.457	1.457	1.457	1.457
Core length [in.]	26.77	37.40	37.40	15.75	37.40
Magnetic length [in.]	28.74	39.37	39.37	17.72	39.37
Lamination height [in.]	13.98	13.98	13.98	13.98	13.98
Lamination width [in.]	13.35	13.35	13.35	13.35	13.35
Packing factor, minimum [%]	98	98	98	98	98
Core weight [lb]	3941	5506	5506	2318	5506
Amp-turns per pole @ 9 GeV	5450	5923	1905	8770	4054
Turns per pole	57	57	57	57	57
Pancakes per pole	1	1	1	1	1
Conductor cross-sectional area [in.^{2}]	0.197	0.197	0.197	0.197	0.197
Conductor dimensions [in.]	0.5×0.5	0.5×0.5	0.5×0.5	0.5×0.5	0.5×0.5
Cooling hole diameter [in.]	0.25	0.25	0.25	0.25	0.25
Current @ 9 GeV [A]	96	104	33	154	71
Resistance @ 40°C [mΩ]	100	127	127	72	127
Power @ 9 GeV [kW]	0.9	1.4	0.1	1.7	0.6
Voltage drop @ 9 GeV [V]	9.6	13.2	4.3	11.1	9.1
Coil weight [lb]	345	438	438	248	438
Number of water circuits	1	1	1	1	1
Water flow rate [gpm]	0.5	0.4	0.4	0.6	0.4
Water pressure drop [psi]	150	150	150	150	150
Temperature rise [°C]	7.5	12.7	1.3	11.7	6.0
Total power (magnets and bus) [kW]	55.0	2.8	0.3	27.3	1.3
Total voltage [V]	575	26	9	178	18
Magnet system water requirements [gpm]	28	1	1	9	1

Table 5-2. HER quadrupole parameters. The column heads indicate whether the magnets are refurbished PEP quadrupoles or newly constructed magnets (continued).

	PEP	New	PEP	New	PEP	PEP
Magnet designation	4Q40	4Q18	4Q22	4Q18	4Q22	4Q22
Lattice designation	QFP2	QFP4	QFP6	QFP8	QFS11	QFS11E
Number of magnets	4	4	4	4	1	4
Operating gradient [T/m]	4.29	9.46	7.61	9.22	9.48	8.06
Pole-tip field @ operating gradient [T]	0.214	0.473	0.380	0.461	0.474	0.403
Gradient-length product [T]	4.29	4.26	4.19	4.15	5.22	4.43
Inscribed radius [in.]	1.968	1.968	1.968	1.968	1.968	1.968
Minimum gap [in.]	1.457	1.457	1.457	1.457	1.457	1.457
Core length [in.]	37.40	15.75	19.69	15.75	19.69	19.69
Magnetic length [in.]	39.37	17.72	21.65	17.72	21.65	21.65
Lamination height [in.]	13.98	13.98	13.98	13.98	13.98	13.98
Lamination width [in.]	13.35	13.35	13.35	13.35	13.35	13.35
Packing factor, minimum [%]	98	98	98	98	98	98
Core weight [lb]	5506	2318	2898	2318	2898	2898
Amp-turns per pole @ 9 GeV	4259	9403	7561	9163	9423	8005
Turns per pole	57	57	57	57	57	57
Pancakes per pole	1	1	1	1	1	1
Conductor cross-sectional area [in.^{2}]	0.197	0.197	0.197	0.197	0.197	0.197
Conductor dimensions [in.]	0.5×0.5	0.5×0.5	0.5×0.5	0.5×0.5	0.5×0.5	0.5×0.5
Cooling hole diameter [in.]	0.25	0.25	0.25	0.25	0.25	0.25
Current @ 9 GeV [A]	75	165	133	161	165	140
Resistance @ 40°C [mΩ]	127	72	82	72	82	82
Power @ 9 GeV [kW]	0.7	2.0	1.5	1.9	2.3	1.6
Voltage drop @ 9 GeV [V]	9.5	11.9	10.9	11.6	13.6	11.6
Coil weight [lb]	438	248	282	248	282	282
Number of water circuits	1	1	1	1	1	1
Water flow rate [gpm]	0.4	0.6	0.5	0.6	0.5	0.5
Water pressure drop [psi]	150	150	150	150	150	150
Temperature rise [°C]	6.6	13.4	10.6	12.7	16.4	11.9
Total power (magnets and bus) [kW]	2.8	7.9	5.8	7.5	2.2	6.5
Total voltage [V]	38	48	44	46	14	46
Magnet system water requirements [gpm]	2	2	2	2	1	2

Table 5-2. HER quadrupole parameters. The column heads indicate whether the magnets are refurbished PEP quadrupoles or newly constructed magnets (continued).

	PEP	PEP	PEP	PEP	New	New
Magnet designation	4Q22	4Q22	4Q22	4Q22	4Q18	4Q18
Lattice designation	QFS12	QFS12E	QFS1L	QFS1R	QFS21	QFS21E
Number of magnets	1	4	1	1	1	4
Operating gradient [T/m]	9.48	8.08	9.76	9.80	11.77	10.55
Pole-tip field @ operating gradient [T]	0.474	0.404	0.488	0.490	0.588	0.527
Gradient-length product [T]	5.22	4.44	5.37	5.39	5.30	4.75
Inscribed radius [in.]	1.968	1.968	1.968	1.968	1.968	1.968
Minimum gap [in.]	1.457	1.457	1.457	1.457	1.457	1.457
Core length [in.]	19.69	19.69	19.69	19.69	15.75	15.75
Magnetic length [in.]	21.65	21.65	21.65	21.65	17.72	17.72
Lamination height [in.]	13.98	13.98	13.98	13.98	13.98	13.98
Lamination width [in.]	13.35	13.35	13.35	13.35	13.35	13.35
Packing factor, minimum [%]	98	98	98	98	98	98
Core weight [lb]	2898	2898	2898	2898	2318	2318
Amp-turns per pole @ 9 GeV	9423	8025	9696	9742	11695	10479
Turns per pole	57	57	57	57	57	57
Pancakes per pole	1	1	1	1	1	1
Conductor cross-sectional area [in.^{2}]	0.197	0.197	0.197	0.197	0.197	0.197
Conductor dimensions [in.]	0.5×0.5	0.5×0.5	0.5×0.5	0.5×0.5	0.5×0.5	0.5×0.5
Cooling hole diameter [in.]	0.25	0.25	0.25	0.25	0.25	0.25
Current @ 9 GeV [A]	165	141	170	171	205	184
Resistance @ 40°C [mΩ]	82	82	82	82	72	72
Power @ 9 GeV [kW]	2.3	1.6	2.4	2.4	3.0	2.4
Voltage drop @ 9 GeV [V]	13.6	11.6	14.0	14.1	14.8	13.3
Coil weight [lb]	282	282	282	282	248	248
Number of water circuits	1	1	1	1	1	1
Water flow rate [gpm]	0.5	0.5	0.5	0.5	0.6	0.6
Water pressure drop [psi]	150	150	150	150	150	150
Temperature rise [°C]	16.4	11.9	17.4	17.6	20.7	16.6
Total power (magnets and bus) [kW]	2.2	6.5	2.4	2.4	3.0	9.8
Total voltage [V]	14	46	14	14	15	53
Magnet system water requirements [gpm]	1	2	1	1	1	2

Table 5-2. HER quadrupole parameters. The column heads indicate whether the magnets are refurbished PEP quadrupoles or newly constructed magnets (continued).

	NEW	NEW	NEW	NEW	PEP	PEP
Magnet designation	4Q18	4Q18	4Q18	4Q18	4Q29	4Q29
Lattice designation	QFS22	QFS22E	QFS2L	QFS2R	QFS31	QFS31E
Number of magnets	1	4	1	1	1	4
Operating gradient [T/m]	11.75	10.53	11.68	11.74	5.61	6.16
Pole-tip field @ operating gradient [T]	0.588	0.526	0.584	0.587	0.280	0.308
Gradient-length product [T]	5.29	4.74	5.26	5.28	4.10	4.49
Inscribed radius [in.]	1.968	1.968	1.968	1.968	1.968	1.968
Minimum gap [in.]	1.457	1.457	1.457	1.457	1.457	1.457
Core length [in.]	15.75	15.75	15.75	15.75	26.77	26.77
Magnetic length [in.]	17.72	17.72	17.72	17.72	28.74	28.74
Lamination height [in.]	13.98	13.98	13.98	13.98	13.98	13.98
Lamination width [in.]	13.35	13.35	13.35	13.35	13.35	13.35
Packing factor, minimum [%]	98	98	98	98	98	98
Core weight [lb]	2318	2318	2318	2318	3941	3941
Amp-turns per pole @ 9 GeV	11678	10465	11605	11666	5575	6117
Turns per pole	57	57	57	57	57	57
Pancakes per pole	1	1	1	1	1	1
Conductor cross-sectional area [in.^{2}]	0.197	0.197	0.197	0.197	0.197	0.197
Conductor dimensions [in.]	0.5×0.5	0.5×0.5	0.5×0.5	0.5×0.5	0.5×0.5	0.5×0.5
Cooling hole diameter [in.]	0.25	0.25	0.25	0.25	0.25	0.25
Current @ 9 GeV [A]	205	184	204	205	98	107
Resistance @ 40°C [mΩ]	72	72	72	72	100	100
Power @ 9 GeV [kW]	3.0	2.4	3.0	3.0	1.0	1.2
Voltage drop @ 9 GeV [V]	14.8	13.3	14.7	14.8	9.8	10.8
Coil weight [lb]	248	248	248	248	345	345
Number of water circuits	1	1	1	1	1	1
Water flow rate [gpm]	0.6	0.6	0.6	0.6	0.5	0.5
Water pressure drop [psi]	150	150	150	150	150	150
Temperature rise [°C]	20.7	16.6	20.4	20.6	7.8	9.4
Total power (magnets and bus) [kW]	3.0	9.7	3.0	3.0	1.0	4.6
Total voltage [V]	15	53	15	15	10	43
Magnet system water requirements [gpm]	1	2	1	1	0	2

Table 5-2. HER quadrupole parameters. The column heads indicate whether the magnets are refurbished PEP quadrupoles or newly constructed magnets (continued).

	PEP	PEP	PEP	PEP	NEW	NEW
Magnet designation	4Q29	4Q29	4Q29	4Q29	4Q60	4Q60
Lattice designation	QFS32	QFS32E	QFS3L	QFS3R	QD4	QF5
Number of magnets	1	4	1	1	2	2
Operating gradient [T/m]	5.62	6.16	5.61	5.62	7.37	6.00
Pole-tip field @ operating gradient [T]	0.281	0.308	0.281	0.281	0.369	0.300
Gradient-length product [T]	4.10	4.50	4.10	4.10	11.556	9.403
Inscribed radius [in.]	1.968	1.968	1.968	1.968	1.968	1.968
Minimum gap [in.]	1.457	1.457	1.457	1.457	1.457	1.457
Core length [in.]	26.77	26.77	26.77	26.77	60.72	60.72
Magnetic length [in.]	28.74	28.74	28.74	28.74	61.70	61.70
Lamination height [in.]	13.98	13.98	13.98	13.98	10.5	10.5
Lamination width [in.]	13.35	13.35	13.35	13.35	10.5	10.5
Packing factor, minimum [%]	98	98	98	98	98	98
Core weight [lb]	3941	3941	3941	3941	5465	5465
Amp-turns per pole @ 9 GeV	5579	6123	5577	5579	7339	5961
Turns per pole	57	57	57	57	12	12
Pancakes per pole	1	1	1	1	1	1
Conductor cross-sectional area [in.^{2}]	0.197	0.197	0.197	0.197	0.197	0.197
Conductor dimensions [in.]	0.5×0.5	0.5×0.5	0.5×0.5	0.5×0.5	0.5×0.5	0.5×0.5
Cooling hole diameter [in.]	0.25	0.25	0.25	0.25	0.25	0.25
Current @ 9 GeV [A]	98	107	98	98	611.6	497
Resistance @ 40°C [mΩ]	100	100	100	100	43.8	43.8
Power @ 9 GeV [kW]	1.0	1.2	1.0	1.0	16.4	10.8
Voltage drop @ 9 GeV [V]	9.8	10.8	9.8	9.8	26.8	21.8
Coil weight [lb]	345	345	345	345	125	125
Number of water circuits	1	1	1	1	4	4
Water flow rate [gpm]	0.5	0.5	0.5	0.5	4.8	4.8
Water pressure drop [psi]	150	150	150	150	50	50
Temperature rise [°C]	7.8	9.4	7.8	7.8	13	8.6
Total power (magnets and bus) [kW]	1.0	4.6	1.0	1.0	32.8	21.6
Total voltage [V]	10	43	10	10	54	44
Magnet system water requirements [gpm]	0	2	0	0	9.6	9.6

5.1.1.3 Sextupoles. For chromaticity correction in the PEP-II HER, 144 sextupoles are required; all are from PEP. The nominal operating point of the HER is quite similar to that of PEP, and since the sextupoles were designed for 18-GeV operation, they have ample margin for any reasonable HER operating parameters. The dimensions of the sextupole are shown in Fig. 5-3, and the electrical characteristics for the various sextupole types at the nominal HER energy are summarized in Table 5-3. Coil design and insulation are the same as for the dipoles and quadrupoles, discussed above.

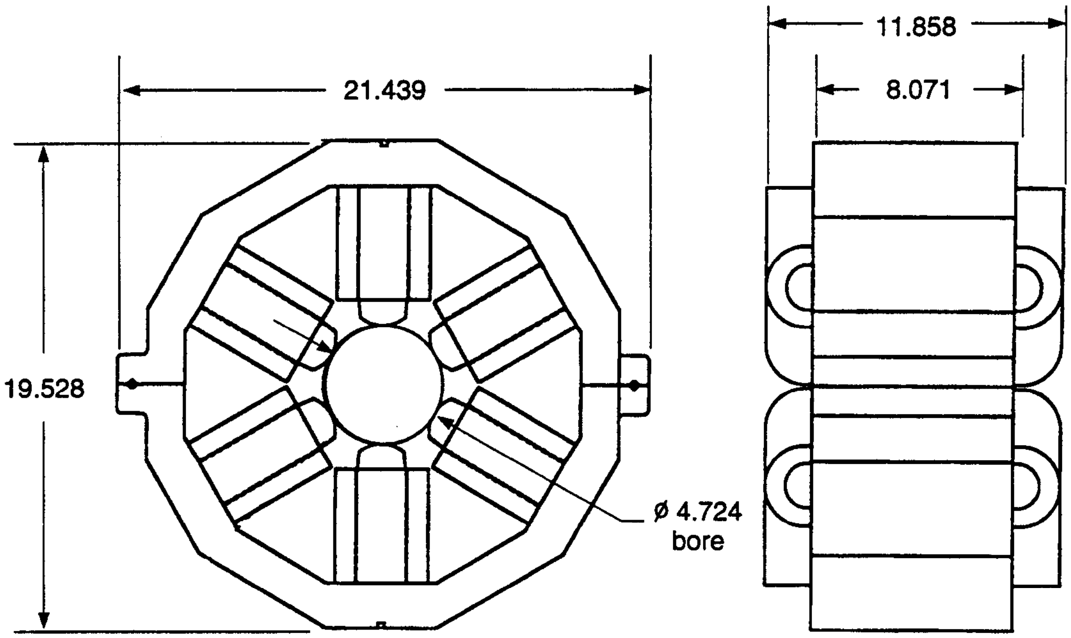

Fig. 5-3. End and side views of a PEP/HER sextupole magnet. Dimensions are given in inches.

Table 5-3. HER sextupole parameters.

Magnet designation	10 SD	10 SF	10 SD	10 SF	10 SD	10 SF
Lattice designation	SD	SF	SD6	SF6	SD5	SF5
Number of magnets	48	48	1	1	1	1
Operating gradient [T/m^2]	79.654	42.029	61.903	96.006	60.042	54.908
Pole-tip field @ operating gradient [T]	0.143	0.076	0.111	0.173	0.108	0.099
Integrated strength @ 9 GeV [T/m]	10.40	5.49	8.08	12.54	7.84	7.17
Aperture inscribed radius [in.]	2.362	2.362	2.362	2.362	2.362	2.362
Core length [in.]	8.071	8.071	8.071	8.071	8.071	8.071
Magnetic length [in.]	10.041	10.041	10.041	10.041	10.041	10.041
Core weight [lb]	170	170	170	170	170	170
Amp turns per pole	2269	1197	1763	2735	1710	1564
Turns per pole	24	24	24	24	24	24
Pancakes per pole	1	1	1	1	1	1
Square conductor dimensions [in.]	0.375	0.375	0.375	0.375	0.375	0.375
Cooling hole diameter [in.]	0.125	0.125	0.125	0.125	0.125	0.125
Conductor cross-sectional area [in.^{2}]	0.127	0.127	0.127	0.127	0.127	0.127
Current @ 9 GeV [A]	94.5	49.9	73.5	114.0	71.3	65.2
Coil length/pole [ft]	49.6	49.6	49.6	49.6	49.6	49.6
Resistance @ 40°C [mΩ]	31	31	31	31	31	31
Power @ 9 GeV [kW]	0.3	0.1	0.2	0.4	0.2	0.1
Voltage drop @ 9 GeV [V]	3.0	1.6	2.3	3.6	2.2	2.0
Coil weight [lb]	44	44	44	44	44	44
Number of water circuits	1	1	1	1	1	1
Water flow rate [gpm]	0.2	0.2	0.2	0.2	0.2	0.2
Water pressure drop [psi]	150	150	150	150	150	150
Temperature rise [°C]	5.9	1.6	3.6	8.6	3.3	2.8
Total magnet power [kW]	20.1	5.6	0.3	0.8	0.3	0.3
Total voltage [V]	145.0	74.8	2.3	3.6	2.2	2.0
Total system water requirements [gpm]	13.0	13.0	0.4	0.4	0.4	0.4

Table 5-3. HER sextupole parameters (continued).

Magnet designation	10 SD	10 SF	10 SD	10 SF	10 SD	10 SF
Lattice designation	SD4	SF4	SD6	SF6	SD5	SF5
Number of magnets	1	1	1	1	1	1
Operating gradient [T/m^2]	105.073	11.618	61.903	96.006	60.042	54.908
Pole-tip field @ operating gradient [T]	0.189	0.021	0.111	0.173	0.108	0.099
Integrated strength @ 9 GeV [T/m]	13.72	1.52	8.08	12.54	7.84	7.17
Aperture inscribed radius [in.]	2.362	2.362	2.362	2.362	2.362	2.362
Core length [in.]	8.071	8.071	8.071	8.071	8.071	8.071
Magnetic length [in.]	10.041	10.041	10.041	10.041	10.041	10.041
Core weight [lb]	170	170	170	170	170	170
Amp turns per pole	2993	331	1763	2735	1710	1564
Turns per pole	24	24	24	24	24	24
Pancakes per pole	1	1	1	1	1	1
Square conductor dimensions [in.]	0.375	0.375	0.375	0.375	0.375	0.375
Cooling hole diameter [in.]	0.125	0.125	0.125	0.125	0.125	0.125
Conductor cross-sectional area [in.^{2}]	0.127	0.127	0.127	0.127	0.127	0.127
Current @ 9 GeV [A]	124.7	13.8	73.5	114.0	71.3	65.2
Coil length/pole [ft]	49.6	49.6	49.6	49.6	49.6	49.6
Resistance @ 40°C [mΩ]	31.29	31.29	31.29	31.29	31.29	31.29
Power @ 9 GeV [kW]	0.49	0.01	0.17	0.41	0.16	0.13
Voltage drop @ 9 GeV [V]	3.9	0.4	2.3	3.6	2.2	2.0
Coil weight [lb]	44	44	44	44	44	44
Number of water circuits	1	1	1	1	1	1
Water flow rate [gpm]	0.18	0.18	0.18	0.18	0.18	0.18
Water pressure drop [psi]	150	150	150	150	150	150
Temperature rise [°C]	10.3	0.1	3.6	8.6	3.3	2.8
Total magnet power [kW]	1.0	0.0	0.3	0.8	0.3	0.3
Total voltage [V]	3.9	0.4	2.3	3.6	2.2	2.0
Total system water requirements [gpm]	0.4	0.4	0.4	0.4	0.4	0.4

Table 5-3. ***HER sextupole parameters (continued).***

Magnet designation	10 SD	10 SF	10 SD	10 SF	10 SD	10 SF
Lattice designation	SD4	SF4	SD6A	SF6A	SD5A	SF5A
Number of magnets	1	1	1	1	1	1
Operating gradient [T/m^2]	105.073	11.618	150.104	75.742	60.042	107.835
Pole-tip field @ operating gradient [T]	0.189	0.021	0.270	0.136	0.108	0.194
Integrated strength @ 9 GeV [T/m]	13.72	1.52	19.60	9.89	7.84	14.08
Aperture inscribed radius [in.]	2.362	2.362	2.362	2.362	2.362	2.362
Core length [in.]	8.071	8.071	8.071	8.071	8.071	8.071
Magnetic length [in.]	10.041	10.041	10.041	10.041	10.041	10.041
Core weight [lb]	170	170	170	170	170	170
Amp turns per pole	2993	331	4276	2158	1710	3072
Turns per pole	24	24	24	24	24	24
Pancakes per pole	1	1	1	1	1	1
Square conductor dimensions [in.]	0.375	0.375	0.375	0.375	0.375	0.375
Cooling hole diameter [in.]	0.125	0.125	0.125	0.125	0.125	0.125
Conductor cross-sectional area [in.^{2}]	0.127	0.127	0.127	0.127	0.127	0.127
Current @ 9 GeV [A]	124.7	13.8	178.2	89.9	71.3	128.0
Coil length/pole [ft]	49.6	49.6	49.6	49.6	49.6	49.6
Resistance @ 40°C [mΩ]	31.29	31.29	31.29	31.29	31.29	31.29
Power @ 9 GeV [kW]	0.49	0.01	0.99	0.25	0.16	0.51
Voltage drop @ 9 GeV [V]	3.9	0.4	5.6	2.8	2.2	4.0
Coil weight [lb]	44	44	44	44	44	44
Number of water circuits	1	1	1	1	1	1
Water flow rate [gpm]	0.18	0.18	0.18	0.18	0.18	0.18
Water pressure drop [psi]	150	150	150	150	150	150
Temperature rise [°C]	10.3	0.1	20.9	5.3	3.3	10.8
Total magnet power [kW]	1.0	0.0	2.0	0.5	0.3	1.0
Total voltage [V]	3.9	0.4	5.6	2.8	2.2	4.0
Total system water requirements [gpm]	0.4	0.4	0.4	0.4	0.4	0.4

Table 5-3. HER sextupole parameters (continued).

Magnet designation	10 SD	10 SF	10 SD	10 SF	10 SD	10 SF
Lattice designation	SD4A	SF4A	SD6A	SF6A	SD5A	SF5A
Number of magnets	1	1	1	1	1	1
Operating gradient [T/m^2]	150.104	13.659	150.104	75.742	60.042	107.835
Pole-tip field @ operating gradient [T]	0.270	0.025	0.270	0.136	0.108	0.194
Integrated strength @ 9 GeV [T/m]	19.60	1.78	19.60	9.89	7.84	14.08
Aperture inscribed radius [in.]	2.362	2.362	2.362	2.362	2.362	2.362
Core length [in.]	8.071	8.071	8.071	8.071	8.071	8.071
Magnetic length [in.]	10.041	10.041	10.041	10.041	10.041	10.041
Core weight [lb]	170	170	170	170	170	170
Amp turns per pole	4276	389	4276	2158	1710	3072
Turns per pole	24	24	24	24	24	24
Pancakes per pole	1	1	1	1	1	1
Square conductor dimensions [in.]	0.375	0.375	0.375	0.375	0.375	0.375
Cooling hole diameter [in.]	0.125	0.125	0.125	0.125	0.125	0.125
Conductor cross-sectional area [in.^{2}]	0.127	0.127	0.127	0.127	0.127	0.127
Current @ 9 GeV [A]	178.2	16.2	178.2	89.9	71.3	128.0
Coil length/pole [ft]	49.6	49.6	49.6	49.6	49.6	49.6
Resistance @ 40°C [mΩ]	31.29	31.29	31.29	31.29	31.29	31.29
Power @ 9 GeV [kW]	0.99	0.01	0.99	0.25	0.16	0.51
Voltage drop @ 9 GeV [V]	5.6	0.5	5.6	2.8	2.2	4.0
Coil weight [lb]	44	44	44	44	44	44
Number of water circuits	1	1	1	1	1	1
Water flow rate [gpm]	0.18	0.18	0.18	0.18	0.18	0.18
Water pressure drop [psi]	150	150	150	150	150	150
Temperature rise [°C]	20.9	0.2	20.9	5.3	3.3	10.8
Total magnet power [kW]	2.0	0.0	2.0	0.5	0.3	1.0
Total voltage [V]	5.6	0.5	5.6	2.8	2.2	4.0
Total system water requirements [gpm]	0.4	0.4	0.4	0.4	0.4	0.4

Table 5-3. HER sextupole parameters (continued).

Magnet designation	10 SD	10 SF	10 SD	10 SF	10 SD	10 SF
Lattice designation	SD4A	SF4A	SD1A	SF1A	SD2A	SF2A
Number of magnets	1	1	1	1	1	1
Operating gradient [T/m^2]	150.104	13.659	130.921	17.952	150.104	86.190
Pole-tip field @ operating gradient [T]	0.270	0.025	0.236	0.032	0.270	0.155
Integrated strength @ 9 GeV [T/m]	19.60	1.78	17.10	2.34	19.60	11.26
Aperture inscribed radius [in.]	2.362	2.362	2.362	2.362	2.362	2.362
Core length [in.]	8.071	8.071	8.071	8.071	8.071	8.071
Magnetic length [in.]	10.041	10.041	10.041	10.041	10.041	10.041
Core weight [lb]	170	170	170	170	170	170
Amp turns per pole	4276	389	3730	511	4276	2455
Turns per pole	24	24	24	24	24	24
Pancakes per pole	1	1	1	1	1	1
Square conductor dimensions [in.]	0.375	0.375	0.375	0.375	0.375	0.375
Cooling hole diameter [in.]	0.125	0.125	0.125	0.125	0.125	0.125
Conductor cross-sectional area [in.^{2}]	0.127	0.127	0.127	0.127	0.127	0.127
Current @ 9 GeV [A]	178.2	16.2	155.4	21.3	178.2	102.3
Coil length/pole [ft]	49.6	49.6	49.6	49.6	49.6	49.6
Resistance @ 40°C [mΩ]	31.29	31.29	31.29	31.29	31.29	31.29
Power @ 9 GeV [kW]	0.99	0.01	0.76	0.01	0.99	0.33
Voltage drop @ 9 GeV [V]	5.6	0.5	4.9	0.7	5.6	3.2
Coil weight [lb]	44	44	44	44	44	44
Number of water circuits	1	1	1	1	1	1
Water flow rate [gpm]	0.18	0.18	0.18	0.18	0.18	0.18
Water pressure drop [psi]	150	150	150	150	150	150
Temperature rise [°C]	20.9	0.2	15.9	0.3	20.9	6.9
Total magnet power [kW]	2.0	0.0	1.5	0.0	2.0	0.7
Total voltage [V]	5.6	0.5	4.9	0.7	5.6	3.2
Total system water requirements [gpm]	0.4	0.4	0.4	0.4	0.4	0.4

Table 5-3. HER sextupole parameters (continued).

Magnet designation	10 SD	10 SF	10 SD	10 SF	10 SD	10 SF
Lattice designation	SD3A	SF3A	SD1A	SF1A	SD2A	SF2A
Number of magnets	1	1	1	1	1	1
Operating gradient [T/m^2]	2.000	90.062	130.921	17.952	150.104	86.190
Pole-tip field @ operating gradient [T]	0.004	0.162	0.236	0.032	0.270	0.155
Integrated strength @ 9 GeV [T/m]	7.84	11.76	17.10	2.34	19.60	11.26
Aperture inscribed radius [in.]	2.362	2.362	2.362	2.362	2.362	2.362
Core length [in.]	8.071	8.071	8.071	8.071	8.071	8.071
Magnetic length [in.]	10.041	10.041	10.041	10.041	10.041	10.041
Core weight [lb]	170	170	170	170	170	170
Amp turns per pole	57	2566	3730	511	4276	2455
Turns per pole	24	24	24	24	24	24
Pancakes per pole	1	1	1	1	1	1
Square conductor dimensions [in.]	0.375	0.375	0.375	0.375	0.375	0.375
Cooling hole diameter [in.]	0.125	0.125	0.125	0.125	0.125	0.125
Conductor cross-sectional area [in.^{2}]	0.127	0.127	0.127	0.127	0.127	0.127
Current @ 9 GeV [A]	2.4	106.9	155.4	21.3	178.2	102.3
Coil length/pole [ft]	49.6	49.6	49.6	49.6	49.6	49.6
Resistance @ 40°C [mΩ]	31.29	31.29	31.29	31.29	31.29	31.29
Power @ 9 GeV [kW]	0.00	0.36	0.76	0.01	0.99	0.33
Voltage drop @ 9 GeV [V]	0.1	3.3	4.9	0.7	5.6	3.2
Coil weight [lb]	44	44	44	44	44	44
Number of water circuits	1	1	1	1	1	1
Water flow rate [gpm]	0.18	0.18	0.18	0.18	0.18	0.18
Water pressure drop [psi]	150	150	150	150	150	150
Temperature rise [°C]	0.0	7.5	15.9	0.3	20.9	6.9
Total magnet power [kW]	0.0	0.7	1.5	0.0	2.0	0.7
Total voltage [V]	0.1	3.3	4.9	0.7	5.6	3.2
Total system water requirements [gpm]	0.4	0.4	0.4	0.4	0.4	0.4

Table 5-3. HER sextupole parameters (continued).

Magnet designation	10 SD	10 SF	10 SD	10 SF	10 SD	10 SF
Lattice designation	SD3A	SF3A	SD1	SF1	SD2	SF2
Number of magnets	1	1	1	1	1	1
Operating gradient [T/m^2]	60.042	90.062	104.863	5.674	105.073	78.654
Pole-tip field @ operating gradient [T]	0.108	0.162	0.189	0.010	0.189	0.142
Integrated strength @ 9 GeV [T/m]	7.84	11.76	13.70	0.74	13.72	10.27
Aperture inscribed radius [in.]	2.362	2.362	2.362	2.362	2.362	2.362
Core length [in.]	8.071	8.071	8.071	8.071	8.071	8.071
Magnetic length [in.]	10.041	10.041	10.041	10.041	10.041	10.041
Core weight [lb]	170	170	170	170	170	170
Amp turns per pole	1710	2566	2987	162	2993	2241
Turns per pole	24	24	24	24	24	24
Pancakes per pole	1	1	1	1	1	1
Square conductor dimensions [in.]	0.375	0.375	0.375	0.375	0.375	0.375
Cooling hole diameter [in.]	0.125	0.125	0.125	0.125	0.125	0.125
Conductor cross-sectional area [in.^{2}]	0.127	0.127	0.127	0.127	0.127	0.127
Current @ 9 GeV [A]	71.3	106.9	124.5	6.7	124.7	93.4
Coil length/pole [ft]	49.6	49.6	49.6	49.6	49.6	49.6
Resistance @ 40°C [mΩ]	31.29	31.29	31.29	31.29	31.29	31.29
Power @ 9 GeV [kW]	0.16	0.36	0.48	0.00	0.49	0.27
Voltage drop @ 9 GeV [V]	2.2	3.3	3.9	0.2	3.9	2.9
Coil weight [lb]	44	44	44	44	44	44
Number of water circuits	1	1	1	1	1	1
Water flow rate [gpm]	0.18	0.18	0.18	0.18	0.18	0.18
Water pressure drop [psi]	150	150	150	150	150	150
Temperature rise [°C]	3.3	7.5	10.2	0.0	10.3	5.7
Total magnet power [kW]	0.3	0.7	1.0	0.0	1.0	0.5
Total voltage [V]	2.2	3.3	3.9	0.2	3.9	2.9
Total system water requirements [gpm]	0.4	0.4	0.4	0.4	0.4	0.4

Table 5-3. HER sextupole parameters (continued).

Magnet designation	10 SD	10 SF	10 SD	10 SF	10 SD	10 SF
Lattice designation	SD3	SF3	SD1	SF1	SD2	SF2
Number of magnets	1	1	1	1	1	1
Operating gradient [T/m^2]	60.042	90.272	104.863	5.674	105.073	78.654
Pole-tip field @ operating gradient [T]	0.108	0.162	0.189	0.010	0.189	0.142
Integrated strength @ 9 GeV [T/m]	7.84	11.79	13.70	0.74	13.72	10.27
Aperture inscribed radius [in.]	2.362	2.362	2.362	2.362	2.362	2.362
Core length [in.]	8.071	8.071	8.071	8.071	8.071	8.071
Magnetic length [in.]	10.041	10.041	10.041	10.041	10.041	10.041
Core weight [lb]	170	170	170	170	170	170
Amp turns per pole	1710	2572	2987	162	2993	2241
Turns per pole	24	24	24	24	24	24
Pancakes per pole	1	1	1	1	1	1
Square conductor dimensions [in.]	0.375	0.375	0.375	0.375	0.375	0.375
Cooling hole diameter [in.]	0.125	0.125	0.125	0.125	0.125	0.125
Conductor cross-sectional area [in.^{2}]	0.127	0.127	0.127	0.127	0.127	0.127
Current @ 9 GeV [A]	71.3	107.2	124.5	6.7	124.7	93.4
Coil length/pole [ft]	49.6	49.6	49.6	49.6	49.6	49.6
Resistance @ 40°C [mΩ]	9	31.29	31.29	31.29	31.29	31.29
Power @ 9 GeV [kW]	0.05	0.36	0.48	0.00	0.49	0.27
Voltage drop @ 9 GeV [V]	0.6	3.4	3.9	0.2	3.9	2.9
Coil weight [lb]	44	44	44	44	44	44
Number of water circuits	1	1	1	1	1	1
Water flow rate [gpm]	0.18	0.18	0.18	0.18	0.18	0.18
Water pressure drop [psi]	150	150	150	150	150	150
Temperature rise [°C]	1.0	7.6	10.2	0.0	10.3	5.7
Total magnet power [kW]	0.1	0.7	1.0	0.0	1.0	0.5
Total voltage [V]	0.6	3.4	3.9	0.2	3.9	2.9
Total system water requirements [gpm]	0.4	0.4	0.4	0.4	0.4	0.4

Table 5-3. HER sextupole parameters (continued).

Magnet designation	10 SD	10 SF
Lattice designation	SD3	SF3
Number of magnets	1	1
Operating gradient [T/m^2]	60.042	90.272
Pole-tip field @ operating gradient [T]	0.108	0.162
Integrated strength @ 9 GeV [T/m]	7.84	11.79
Aperture inscribed radius [in.]	2.362	2.362
Core length [in.]	8.071	8.071
Magnetic length [in.]	10.041	10.041
Core weight [lb]	170	170
Amp turns per pole	1710	2572
Turns per pole	24	24
Pancakes per pole	1	1
Square conductor dimensions [in.]	0.375	0.375
Cooling hole diameter [in.]	0.125	0.125
Conductor cross-sectional area [in.^{2}]	0.127	0.127
Current @ 9 GeV [A]	71.3	107.2
Coil length/pole [ft]	49.6	49.6
Resistance @ 40°C [mΩ]	31.29	31.29
Power @ 9 GeV [kW]	0.16	0.36
Voltage drop @ 9 GeV [V]	2.2	3.4
Coil weight [lb]	44	44
Number of water circuits	1	1
Water flow rate [gpm]	0.18	0.18
Water pressure drop [psi]	150	150
Temperature rise [°C]	3.3	7.6
Total magnet power [kW]	0.3	0.7
Total voltage [V]	2.2	3.4
Total system water requirements [gpm]	0.4	0.4

5.1.2 LER Magnets

All magnets for the LER will be newly constructed. However, the beam-stay-clear aperture requirements for the LER are sufficiently similar to those of the HER (and PEP) that it is justifiable to use the same magnet aperture dimensions. (It is worth noting here that a review of the anticipated gas loads in both the HER and the LER indicates very little difference between the two; this argues for the choice of a vacuum chamber of similar aperture in the two rings.)

The main benefit of keeping the same magnet aperture is that the new LER magnets can take advantage of the well-proven pole-tip profiles developed for PEP and PETRA (using the computer program POISSON); that is, the magnets can be very similar to PEP magnets, with only the external dimensions changed to reflect the lower field requirements at the nominal 3.1-GeV operating point. In this way, we substantially reduce our R&D and engineering costs.

The design of the new magnets will be optimized by minimizing the sum of the installed capital cost plus ten years of operating cost at the design energy. This means that prudent attention is paid to reducing power consumption. Despite this, the LER magnets use proportionately more power than the PEP/HER magnets. This comes about because the PEP magnets were optimized for 18-GeV operation, where the power consumption is higher than at 9 GeV.

5.1.2.1 Dipoles. The LER dipole design was dictated by several considerations. First, the LER magnets must be mounted above the HER. To minimize the weight that must be rigidly supported, it is important to reduce the size of the dipoles considerably, compared with the PEP design. Second, the problems with synchrotron-radiation-induced gas desorption are eased considerably if the dipole is kept short enough to permit its synchrotron radiation fan to exit the magnet completely (as discussed in detail in Section 5.2). Finally, the lattice parameters of the LER call for a relatively high emittance and short damping times compared with what would result from a low-field bending magnet lattice. Although we have chosen to provide wigglers to adjust these parameters, the choice of a short, higher-field dipole helps to reduce the demands on the wigglers and to spread the synchrotron radiation power around more of the ring.

The LER arc dipole magnet physical dimensions are shown in Fig. 5-4. The key

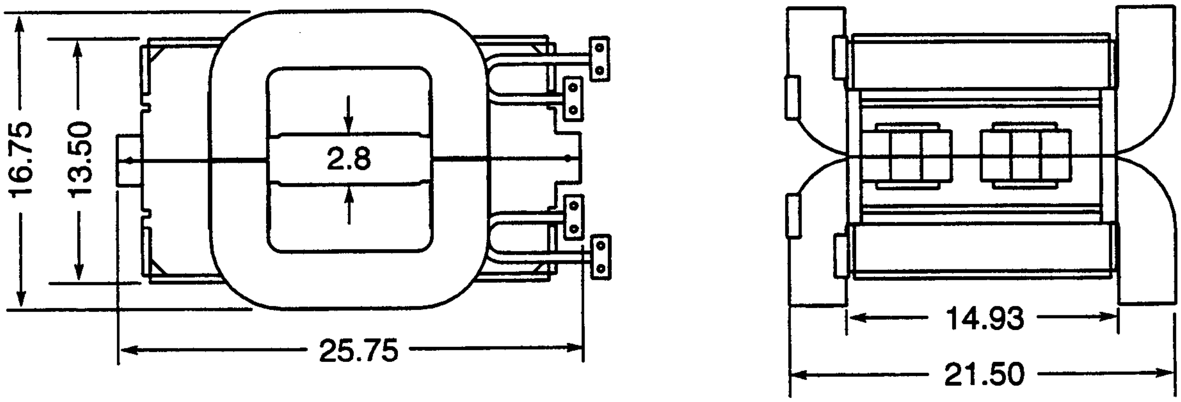

Fig. 5-4. End and side views of the LER bending magnet. Dimensions are given in inches.

dimensions are the core length of 14.92 in. and the gap of 2.8 in. The electrical properties of the LER dipole at its nominal operating energy of 3.1 GeV are summarized in Table 5-4.

To reduce production costs and to maximize magnet-to-magnet uniformity, the main ring magnets for the LER are of laminated construction. The dipole magnets will be constructed of one-piece laminations, 1/16-in. thick, punched from a decarburized, annealed, low-carbon steel sheet, such as Armco special magnet steel. This material—which has been used successfully for many accelerator applications, including those at PEP and Fermilab—exhibits high saturation induction, modest coercive force, and low remanent field. The estimated steel weight to manufacture the required 222 bending magnets is 250 tons.

Laminations will be punched with built-in fiducials to provide convenient external references for alignment, as discussed in Section 5.3. In addition, for reasons explained below, new witness marks will be introduced into the die at each heat-change to ensure magnet uniformity. Particular attention will be paid to the wear on the die. The vendor will be required to keep track of the number of laminations punched between die sharpenings and to provide SLAC with sample laminations on a regular basis, so that in-house inspections can be made to ensure that undue wear (>0.0005 in.) has not taken place on the critical surfaces (thereby producing out-of-tolerance laminations).

The vendor responsible for stacking the laminations will be required to deburr and then stack them, using laminations from consecutive heats. If this is done, the pattern generated by the witness marks will be obvious upon visual inspection. If the observed pattern is regular, the core will be acceptable, whereas an irregular pattern will indicate a lack of quality control on the part of the manufacturer and will be sufficient cause for rejecting the magnet core.

Laminations will be rotated after stacking each (approximately) 4-in. segment of the core. In this way, errors due to the slight variation in the thickness of the laminations will be eliminated. (This thickness error, referred to as "crowning," is well known to occur in flat rolled sheet due to curvature in the rollers caused by forces generated during the production of the sheet.) The precise number of laminations that are stacked before performing such a rotation, which can only be determined when the number of heats is known, will be sufficient to ensure that the regular periodicity of the witness marks is retained.

The magnets operate at low fields, well below saturation, and thus are more sensitive to core length than to the density of the lamination packing. Therefore, to maximize magnet-to-magnet reproducibility, particular attention will be paid to the length of the core (rather than its packing factor).

The magnet end-plates will be manufactured by numerically controlled mills and will contain the necessary holes for mounting coil retainers and other such devices. Angle plates welded to both the end-plates and the laminations will provide the torsional rigidity necessary to stabilize the cores and prevent twisting or bending.

Magnet coils will be of water-cooled aluminum, extruded from billets using porthole dies to provide continuous lengths up to several thousand feet. This technique obviates the need to make joints in the coil, thus eliminating the possibility of leaks. The length of a typical coil is about 150 ft, so there will be minimal waste at the end of each reel of conductor. The estimated weight of one dipole, including coils, is 2200 lb.

Table 5-4. LER dipole parameters.

Magnet designation	2.8H18	2.8H40	2.8H24	2.8H29	2.8H24	2.8H98
Bending angle [deg]	1.875	3.657	0.321	2	1.329	6.925
Lattice designation	B	B1	B2	B3	B4	B5
Number of magnets	192	8	2	4	2	2
Field [T]	0.752	0.660	0.097	0.481	0.400	0.500
Integrated field [T·m]	0.338	0.660	0.058	0.361	0.240	1.250
Pole width [in.]	8	8	8	8	8	8
Gap height [in.]	2.87	2.8	2.8	2.8	2.8	2.8
Core length [in.]	14.85	36.57	20.82	26.73	20.82	95.63
Magnetic length [in.]	17.72	39.37	23.62	29.53	23.62	98.43
Width of useful field, 0.1% [in.]	4.00	4.00	4.00	4.00	4.00	4.00
Lamination height [in.]	6.75	6.75	6.75	6.75	6.75	6.75
Lamination width [in.]	23	23	23	23	23	23
Packing factor, minimum [%]	98	98	98	98	98	98
Core weight [lb]	1,306	4,903	1,832	2,352	1,832	8,415
Amp·turns	21,804	18,665	2,731	13,614	11,308	14,142
Turns	36	36	36	36	36	36
Pancakes per pole	1	1	1	1	1	1
Conductor dimensions [in.]	0.5×0.5	0.5×0.5	0.5×0.5	0.5×0.5	0.5×0.5	0.5×0.5
Cooling hole diameter [in.]	0.1875	0.1875	0.1875	0.1875	0.1875	0.1875
Conductor cross section [in.^{2}]	0.22	0.22	0.22	0.22	0.22	0.22
Conductor length/pole [ft]	202	352	238	273	238	687
Current [A]	605.68	518.47	75.87	378.18	314.12	392.83
Resistance @ 40°C [mΩ]	24.4	42.5	28.7	33.0	28.7	82.9
Power [kW]	4.47	11.42	0.08	2.36	1.42	6.39
Voltage drop [V]	7.4	20	1.1	6.2	4.5	16.3
Coil weight [lb]	104	182	122	140	122	353
Number of water circuits	2	4	1	2	2	2
Water flow rate, total [gpm]	1.3	1.92	0.4	1.1	1.2	0.7
Water pressure drop [psi]	150	150	150	150	150	150
Temperature rise [°C]	13.2	22.6	0.8	8.2	4.6	36.4
Total power (magnets and bus) [kW]	858	91.2	0.2	9.4	2.8	18.2
Total voltage (magnets and bus) [V]	1420	160	2	25	9	33
Total system water requirements (gpm)	248	15	1	4	2	1

*Table 5-4. **LER dipole parameters** (continued).*

Magnet designation	2.8H49	2.8H28	2.8H12	2.8H59
Bending angle [deg]	4.973	1.5	0.166	10.048
Lattice designation	B6	B7	B8	B9
Number of magnets	4	2	2	2
Field [T]	0.718	0.451	0.100	1.209
Integrated field [T·m]	0.898	0.271	0.030	1.814
Pole width [in.]	8	8	8	8
Gap height [in.]	2.8	2.8	2.8	2.8
Core length [in.]	46.41	20.82	9.01	56.26
Magnetic length [in.]	49.21	23.62	11.81	59.06
Width of useful field, 0.1% [in.]	4.00	4.00	4.00	4.00
Lamination height [in.]	16	6.75	6.75	6.75
Lamination width [in.]	23	23	23	23
Packing factor, minimum [%]	96	98	98	98
Core weight [lb]	4,084	1,832	793	4,950
Amp·turns	20,313	3.1	2,825	34,199
Turns	36	36	36	96
Pancakes per pole	1	1	1	1
Conductor dimensions [in.]	0.5×0.5	0.5×0.5	0.5×0.5	0.5×0.5
Cooling hole diameter [in.]	0.1875	0.1875	0.1875	0.1875
Conductor cross section [in.^{2}]	0.22	0.22	0.22	0.22
Conductor length/pole [ft]	392	238	167	1202
Current [A]	564.24	0.09	78.47	356.24
Resistance @ 40°C [mΩ]	47.2	28.7	20.2	145.0
Power [kW]	7.52	0.00	0.06	9.20
Voltage drop [V]	13.3	0.0	0.8	25.8
Coil weight [lb]	201	122	86	617
Number of water circuits	2	2	2	4
Water flow rate, total [gpm]	0.9	1.2	1.4	2.1
Water pressure drop [psi]	150	150	150	150
Temperature rise [°C]	31.6	0.0	0.2	16.8
Total power (magnets and bus) [kW]	30	0.0	1.2	18.4
Total voltage (magnets and bus) [V]	53	0.0	2	52
Total system water requirements (gpm)	4	2	3	4

5.1.2.2 Quadrupoles. The standard LER quadrupole has a length of 17.0 in. and a bore diameter of 3.937 in.; its physical dimensions are shown in Fig. 5-5. The electrical properties of the quadrupoles corresponding to the nominal energy are summarized in Table 5-5.

The LER quadrupoles will be constructed, and the laminations handled, in the same manner described for the dipole magnets, except that they will use four-piece construction. The anticipated weight of steel is larger than that for the dipoles, about 550 tons, thus requiring more heats (about eight rather than five).

The design will include numerically machined end-plates with predrilled holes to mount the beam position monitors. These end-plates will be used to sandwich the laminations together. As with the dipoles, angles welded to the corners of the laminations will provide the required torsional rigidity and stiffness. Four cores, fitted with water-cooled aluminum coils approximately 180 ft long and extruded by the same technique as used for the bending magnets, will be bolted together to form one quadrupole weighing an estimated 2000 lb.

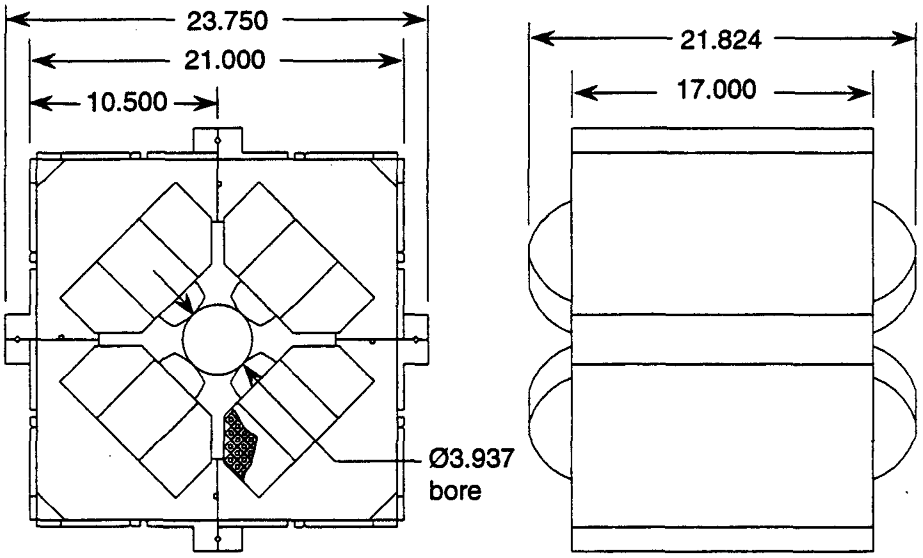

Fig. 5-5. End and side views of an LER quadrupole magnet. Dimensions are given in inches.

Table 5-5. LER quadrupole parameters.

Magnet designation	4Q17	4Q17	4Q17	4Q40	4Q40	4Q40
Location in ring	Arc	Arc	R2	R2	R2	R2
Lattice designation	QF	QD	IQF1	IQD2	IQF3	IQD4
Number of magnets	74	80	2	2	2	2
Operating gradient [T/m]	4.55	4.50	7.12	5.04	4.53	5.05
Pole-tip field @ operating gradient [T]	0.227	0.225	0.356	0.252	0.226	0.253
Gradient length product [T]	1.96	1.93	3.06	5.04	4.529	5.05
Inscribed radius [in.]	1.968	1.968	1.968	1.968	1.968	1.968
Minimum gap [in.]	1.457	1.457	1.457	1.457	1.457	1.457
Core length [in.]	15.95	15.95	15.95	38.39	38.39	38.39
Magnetic length [in.]	16.93	16.93	16.93	39.37	39.37	39.37
Lamination height [in.]	11.88	11.88	11.88	13.98	13.98	13.98
Lamination width [in.]	10.50	10.50	10.50	13.35	13.35	13.35
Packing factor, minimum [%]	98	98	98	98	98	98
Core weight [lb]	1786	1786	1786	6142	6142	6142
Amp-turns per pole	4521	4467	7075	5006	4500	5022
Turns per pole	37	37	37	56	56	56
Pancakes per pole	1	1	1	1	1	1
Conductor cross-sectional area [in.^{2}]	0.198	0.198	0.198	0.198	0.198	0.198
Cooling hole diameter [in.]	0.25	0.25	0.25	0.25	0.25	0.25
Conductor dimensions [in.]	0.5×0.5	0.5×0.5	0.5×0.5	0.5×0.5	0.5×0.5	0.5×0.5
Conductor length/pole [ft]	176	176	176	476	476	476
Current [A]	122	121	191	89	80	90
Resistance @ 40°C [mΩ]	47	47	47	127	127	127
Power [kW]	0.70	0.69	1.72	1.02	0.82	1.02
Voltage drop [V]	5.8	5.7	9.0	11.4	10.2	11.4
Coil weight [lb]	81.4	81.4	81.4	220.2	220.2	220.2
Number of water circuits	1	1	1	1	1	1
Water flow rate [gpm]	0.7	0.7	0.7	0.4	0.4	0.4
Water pressure drop [psi]	150	150	150	150	150	150
Temperature rise [°C]	3.80	3.71	9.32	9.43	7.62	9.49
Total magnet power [kW]	52.0	54.8	3.4	2.0	1.6	2.0
Total magnet water requirements [gpm]	51.9	56.1	1.4	0.8	0.8	0.8

Table 5-5. LER quadrupole parameters (continued).

Magnet designation	4Q17	4Q40	4Q40	4Q40	4Q40	4Q17
Location in ring	R2	R2	R2	R2	R2	R2
Lattice designation	IQF5	IQF6	IQD7	IQF8	IQD9	IQD10
Number of magnets	2	2	2	2	2	4
Operating gradient [T/m]	10.35	5.20	5.98	9.80	7.31	7.12
Pole-tip field @ operating gradient [T]	0.517	0.260	0.299	0.490	0.365	0.356
Gradient length product [T]	4.45	5.20	5.98	9.80	7.31	3.06
Inscribed radius [in.]	1.968	1.968	1.968	1.968	1.968	1.968
Minimum gap [in.]	1.457	1.457	1.457	1.457	1.457	1.457
Core length [in.]	15.95	38.39	38.39	38.39	38.39	15.95
Magnetic length [in.]	16.93	39.37	39.37	39.37	39.37	16.93
Lamination height [in.]	11.88	13.98	11.88	13.98	13.98	11.88
Lamination width [in.]	10.50	13.35	10.50	13.35	13.35	10.50
Packing factor, minimum [%]	98	98	98	98	98	98
Core weight [lb]	1786	6142	4299	6142	6142	1786
Amp·turns per pole	10285	5163	5942	9739	7261	7079
Turns per pole	37	56	56	56	56	37
Pancakes per pole	1	1	1	1	1	1
Conductor cross-sectional area [in.^{2}]	0.198	0.198	0.198	0.198	0.198	0.198
Cooling hole diameter [in.]	0.25	0.25	0.25	0.25	0.25	0.25
Conductor dimensions [in.]	0.5×0.5	0.5×0.5	0.5×0.5	0.5×0.5	0.5×0.5	0.5×0.5
Conductor length/pole [ft]	176	476	476	476	476	176
Current [A]	278	92	106	174	130	191
Resistance @ 40°C [mΩ]	47	127	127	127	127	47
Power [kW]	3.63	1.08	1.43	3.85	2.14	1.72
Voltage drop [V]	13.1	11.7	13.5	22.1	16.5	13.1
Coil weight [lb]	81.4	220.2	220.2	220.2	220.2	81.4
Number of water circuits	1	2	2	4	2	1
Water flow rate [gpm]	0.7	1.2	1.2	3.5	1.2	0.7
Water pressure drop [psi]	150	150	150	150	150	150
Temperature rise [°C]	19.69	3.45	4.57	4.22	6.82	9.33
Total magnet power [kW]	7.3	2.2	2.9	7.7	4.3	6.9
Total magnet water requirements [gpm]	1.4	2.4	2.4	6.9	2.4	2.8

Table 5-5. LER quadrupole parameters (continued).

Magnet designation	4Q17	4Q17	4Q17	4Q40	4Q17	4Q17
Location in ring	R2	R2	R2	R2	R2	R2
Lattice designation	IQF11	IQD12	IQD13	IQF14	IQD15	IQF16
Number of magnets	4	2	2	2	2	2
Operating gradient [T/m]	11.75	10.46	7.04	8.25	5.87	19.21
Pole-tip field @ operating gradient [T]	0.587	0.523	0.352	0.413	0.293	0.960
Gradient length product [T]	5.05	4.50	3.03	8.25	2.52	8.26
Inscribed radius [in.]	1.968	1.968	1.968	1.968	1.968	1.968
Minimum gap [in.]	1.457	1.457	1.457	1.457	1.457	1.457
Core length [in.]	15.95	15.95	15.95	38.39	15.95	15.95
Magnetic length [in.]	16.93	16.93	16.93	39.37	16.93	16.93
Lamination height [in.]	11.88	11.88	11.88	13.98	11.88	11.88
Lamination width [in.]	10.50	10.50	10.50	13.35	10.50	10.50
Packing factor, minimum [%]	98	98	98	98	98	98
Core weight [lb]	1786	1786	1786	6142	1786	1786
Amp·turns per pole	11670	10388	6991	8200	5834	19084
Turns per pole	37	37	37	56	37	37
Pancakes per pole	1	1	1	1	1	1
Conductor cross-sectional area [in.^{2}]	0.198	0.198	0.198	0.198	0.198	0.198
Cooling hole diameter [in.]	0.25	0.25	0.25	0.25	0.25	0.25
Conductor dimensions [in.]	0.5×0.5	0.5×0.5	0.5×0.5	0.5×0.5	0.5×0.5	0.5×0.5
Conductor length/pole [ft]	176	176	176	476	176	176
Current [A]	315	281	189	146	158	516
Resistance @ 40°C [mΩ]	47	47	47	127	47	47
Power [kW]	4.68	3.71	1.68	2.73	1.17	12.51
Voltage drop [V]	14.8	13.2	8.9	18.6	7.4	24.3
Coil weight [lb]	81.4	81.4	81.4	220.2	81.4	81.4
Number of water circuits	2	2	1	2	1	4
Water flow rate [gpm]	2.0	2.0	0.7	1.2	0.7	5.9
Water pressure drop [psi]	150	150	150	150	150	150
Temperature rise [°C]	8.72	6.91	9.10	8.70	6.33	8.02
Total magnet power [kW]	18.7	7.4	3.4	5.5	2.3	25.0
Total magnet water requirements [gpm]	8.2	4.1	1.4	2.4	1.4	11.9

Table 5-5. LER quadrupole parameters (continued).

Magnet designation	4Q17	4Q17	4Q17	4Q17	4Q17	4Q17
Location in ring	R2	R2	IR DS	IR DS	IR DS	IR DS
Lattice designation	IQD17	IQF18	QF1	QD2	QF3	QD4
Number of magnets	2	2	2	2	2	2
Operating gradient [T/m]	10.54	8.89	7.07	6.33	5.18	3.46
Pole-tip field @ operating gradient [T]	0.527	0.444	0.354	0.316	0.259	0.173
Gradient length product [T]	4.53	3.82	3.04	2.72	2.23	1.49
Inscribed radius [in.]	1.968	1.968	1.968	1.968	1.968	1.968
Minimum gap [in.]	1.457	1.457	1.457	1.457	1.457	1.457
Core length [in.]	15.95	15.95	15.95	15.95	15.95	15.95
Magnetic length [in.]	16.93	16.93	16.93	16.93	16.93	16.93
Lamination height [in.]	11.88	11.88	11.88	11.88	11.88	11.88
Lamination width [in.]	10.50	10.50	10.50	10.50	10.50	10.50
Packing factor, minimum [%]	98	98	98	98	98	98
Core weight [lb]	1786	1786	1786	1786	1786	1786
Amp·turns per pole	10469	8834	7027	6291	5147	3436
Turns per pole	37	37	37	37	37	37
Pancakes per pole	1	1	1	1	1	1
Conductor cross-sectional area [in.^{2}]	0.198	0.198	0.198	0.198	0.198	0.198
Cooling hole diameter [in.]	0.25	0.25	0.25	0.25	0.25	0.25
Conductor dimensions [in.]	0.5×0.5	0.5×0.5	0.5×0.5	0.5×0.5	0.5×0.5	0.5×0.5
Conductor length/pole [ft]	176	176	176	176	176	176
Current [A]	283	239	190	170	139	93
Resistance @ 40°C [mΩ]	47	47	47	47	47	47
Power [kW]	3.76	2.68	1.70	1.36	0.91	0.41
Voltage drop [V]	13.3	11.2	8.9	8.0	6.5	4.4
Coil weight [lb]	81.4	81.4	81.4	81.4	81.4	81.4
Number of water circuits	2	2	1	1	1	1
Water flow rate [gpm]	2.0	2.0	0.7	0.7	0.7	0.7
Water pressure drop [psi]	150	150	150	150	150	150
Temperature rise [°C]	7.02	5.00	9.19	7.37	4.93	2.20
Total magnet power [kW]	7.5	5.4	3.4	2.7	1.8	0.8
Total magnet water requirements [gpm]	4.1	4.1	1.4	1.4	1.4	1.4

Table 5-5. LER quadrupole parameters (continued).

Magnet designation	4Q17	4Q17	4Q17	4Q17	4Q17	4Q17
Location in ring	IR DS	R4	R4	R4	R4	R4
Lattice designation	QF5	QDT4	QFT4	QDT3	QFT3	QDT2
Number of magnets	2	1	2	2	2	2
Operating gradient [T/m]	4.55	1.88	3.29	3.57	4.14	3.48
Pole-tip field @ operating gradient [T]	0.227	0.094	0.165	0.178	0.207	0.174
Gradient length product [T]	1.96	0.81	1.42	1.53	1.78	1.50
Inscribed radius [in.]	1.968	1.968	1.968	1.968	1.968	1.968
Minimum gap [in.]	1.457	1.457	1.457	1.457	1.457	1.457
Core length [in.]	15.95	15.95	15.95	15.95	15.95	15.95
Magnetic length [in.]	16.93	16.93	16.93	16.93	16.93	16.93
Lamination height [in.]	11.88	11.88	11.88	11.88	11.88	11.88
Lamination width [in.]	10.50	10.50	10.50	10.50	10.50	10.50
Packing factor, minimum [%]	98	98	98	98	98	98
Core weight [lb]	1786	1786	1786	1786	1786	1786
Amp·turns per pole	4518	1870	3270	3542	4113	3460
Turns per pole	37	37	37	37	37	37
Pancakes per pole	1	1	1	1	1	1
Conductor cross-sectional area [in.^{2}]	0.198	0.198	0.198	0.198	0.198	0.198
Cooling hole diameter [in.]	0.25	0.25	0.25	0.25	0.25	0.25
Conductor dimensions [in.]	0.5×0.5	0.5×0.5	0.5×0.5	0.5×0.5	0.5×0.5	0.5×0.5
Conductor length/pole [ft]	176	176	176	176	176	176
Current [A]	122	51	88	96	111	94
Resistance @ 40°C [mΩ]	47	47	47	47	47	47
Power [kW]	0.70	0.12	0.37	0.43	0.58	0.41
Voltage drop [V]	5.7	2.4	4.2	4.5	5.2	4.4
Coil weight [lb]	81.4	81.4	81.4	81.4	81.4	81.4
Number of water circuits	1	1	1	1	1	1
Water flow rate [gpm]	0.7	0.7	0.7	0.7	0.7	0.7
Water pressure drop [psi]	150	150	150	150	150	150
Temperature rise [°C]	3.80	0.65	1.99	2.34	3.15	2.23
Total magnet power [kW]	1.4	0.1	0.7	0.9	1.2	0.8
Total magnet water requirements [gpm]	1.4	0.7	1.4	1.4	1.4	1.4

Table 5-5. LER quadrupole parameters (continued).

Magnet designation	4Q17	4Q17	4Q17	4Q17	4Q17	4Q17
Location in ring	R4	R4	R4	R3	R3	R3
Lattice designation	QFT2	QDT1	QFT1	QF1	QD1	QF2
Number of magnets	2	2	2	1	1	1
Operating gradient [T/m]	4.83	4.04	4.90	4.16	5.58	4.38
Pole-tip field @ operating gradient [T]	0.242	0.202	0.245	0.208	0.279	0.219
Gradient length product [T]	2.08	1.74	2.11	1.79	2.40	1.88
Inscribed radius [in.]	1.968	1.968	1.968	1.968	1.968	1.968
Minimum gap [in.]	1.457	1.457	1.457	1.457	1.457	1.457
Core length [in.]	15.95	15.95	15.95	15.95	15.95	15.95
Magnetic length [in.]	16.93	16.93	16.93	16.93	16.93	16.93
Lamination height [in.]	11.88	11.88	11.88	11.88	11.88	11.88
Lamination width [in.]	10.50	10.50	10.50	10.50	10.50	10.50
Packing factor, minimum [%]	98	98	98	98	98	98
Core weight [lb]	1786	1786	1786	1786	1786	1786
Amp·turns per pole	4801	4011	4871	4137	5544	4348
Turns per pole	37	37	37	37	37	37
Pancakes per pole	1	1	1	1	1	1
Conductor cross-sectional area [in.^{2}]	0.198	0.198	0.198	0.198	0.198	0.198
Cooling hole diameter [in.]	0.25	0.25	0.25	0.25	0.25	0.25
Conductor dimensions [in.]	0.5×0.5	0.5×0.5	0.5×0.5	0.5×0.5	0.5×0.5	0.5×0.5
Conductor length/pole [ft]	176	176	176	176	176	176
Current [A]	130	108	132	112	150	118
Resistance @ 40°C [mΩ]	47	47	47	47	47	47
Power [kW]	0.79	0.55	0.82	0.59	1.06	0.65
Voltage drop [V]	6.1	5.1	6.2	5.3	7.1	5.5
Coil weight [lb]	81.4	81.4	81.4	81.4	81.4	81.4
Number of water circuits	1	1	1	1	1	1
Water flow rate [gpm]	0.7	0.7	0.7	0.7	0.7	0.7
Water pressure drop [psi]	150	150	150	150	150	150
Temperature rise [°C]	4.29	3.00	4.42	3.19	5.72	3.52
Total magnet power [kW]	1.6	1.1	1.6	0.6	1.1	0.6
Total magnet water requirements [gpm]	1.4	1.4	1.4	0.7	0.7	0.7

Table 5-5. LER quadrupole parameters (continued).

Magnet designation	4Q17	4Q17	4Q17	4Q17	4Q17	4Q17
Location in ring	R3	R3	R3	R3	R3	R6
Lattice designation	QD2	QF3	QD3	QF4	QD4	QFW1
Number of magnets	1	1	1	1	1	2
Operating gradient [T/m]	4.95	4.84	4.12	4.77	4.55	2.52
Pole-tip field @ operating gradient [T]	0.247	0.242	0.206	0.239	0.227	0.126
Gradient length product [T]	2.13	2.08	1.77	2.05	1.96	1.08
Inscribed radius [in.]	1.968	1.968	1.968	1.968	1.968	1.968
Minimum gap [in.]	1.457	1.457	1.457	1.457	1.457	1.457
Core length [in.]	15.95	15.95	15.95	15.95	15.95	15.95
Magnetic length [in.]	16.93	16.93	16.93	16.93	16.93	16.93
Lamination height [in.]	11.88	11.88	11.88	11.88	11.88	11.88
Lamination width [in.]	10.50	10.50	10.50	10.50	10.50	10.50
Packing factor, minimum [%]	98	98	98	98	98	98
Core weight [lb]	1786	1786	1786	1786	1786	1786
Amp·turns per pole	4917	4810	4097	4744	4520	2505
Turns per pole	37	37	37	37	37	37
Pancakes per pole	1	1	1	1	1	1
Conductor cross-sectional area [in.^{2}]	0.198	0.198	0.198	0.198	0.198	0.198
Cooling hole diameter [in.]	0.25	0.25	0.25	0.25	0.25	0.25
Conductor dimensions [in.]	0.5×0.5	0.5×0.5	0.5×0.5	0.5×0.5	0.5×0.5	0.5×0.5
Conductor length/pole [ft]	176	176	176	176	176	176
Current [A]	133	130	111	128	122	68
Resistance @ 40°C [mΩ]	47	47	47	47	47	47
Power [kW]	0.83	0.79	0.58	0.77	0.70	0.22
Voltage drop [V]	6.3	6.1	5.2	6.0	5.7	3.2
Coil weight [lb]	81.4	81.4	81.4	81.4	81.4	81.4
Number of water circuits	1	1	1	1	1	1
Water flow rate [gpm]	0.7	0.7	0.7	0.7	0.7	0.7
Water pressure drop [psi]	150	150	150	150	150	150
Temperature rise [°C]	4.50	4.31	3.12	4.19	3.80	1.17
Total magnet power [kW]	0.8	0.8	0.6	0.8	0.7	0.4
Total magnet water requirements [gpm]	0.7	0.7	0.7	0.7	0.7	1.4

Table 5-5. LER quadrupole parameters (continued).

Magnet designation	4Q17	4Q17	4Q17	4Q17	4Q17	4Q17
Location in ring	R6	R6	R6	R6	R6	R8
Lattice designation	QDW2	QFW3	QFW4	QDW5	QFW6	QDI
Number of magnets	2	2	2	2	2	2
Operating gradient [T/m]	1.64	3.92	0.28	2.02	3.58	0.66
Pole-tip field @ operating gradient [T]	0.082	0.196	0.014	0.101	0.179	0.033
Gradient length product [T]	0.70	1.69	0.12	0.87	1.54	0.28
Inscribed radius [in.]	1.968	1.968	1.968	1.968	1.968	1.968
Minimum gap [in.]	1.457	1.457	1.457	1.457	1.457	1.457
Core length [in.]	15.95	15.95	15.95	15.95	15.95	15.95
Magnetic length [in.]	16.93	16.93	16.93	16.93	16.93	16.93
Lamination height [in.]	11.88	11.88	11.88	11.88	11.88	11.88
Lamination width [in.]	10.50	10.50	10.50	10.50	10.50	10.50
Packing factor, minimum [%]	98	98	98	98	98	98
Core weight [lb]	1786	1786	1786	1786	1786	1786
Amp·turns per pole	1628	3895	283	2009	3553	654
Turns per pole	37	37	37	37	37	37
Pancakes per pole	1	1	1	1	1	1
Conductor cross-sectional area [in.^{2}]	0.198	0.198	0.198	0.198	0.198	0.198
Cooling hole diameter [in.]	0.25	0.25	0.25	0.25	0.25	0.25
Conductor dimensions [in.]	0.5×0.5	0.5×0.5	0.5×0.5	0.5×0.5	0.5×0.5	0.5×0.5
Conductor length/pole [ft]	176	176	176	176	176	176
Current [A]	44	105	8	54	96	18
Resistance @ 40°C [mΩ]	47	47	47	47	47	47
Power [kW]	0.09	0.52	0.00	0.14	0.43	0.01
Voltage drop [V]	2.1	5.0	0.4	2.6	4.5	0.8
Coil weight [lb]	81.4	81.4	81.4	81.4	81.4	81.4
Number of water circuits	1	1	1	1	1	1
Water flow rate [gpm]	0.7	0.7	0.7	0.7	0.7	0.7
Water pressure drop [psi]	150	150	150	150	150	150
Temperature rise [°C]	0.49	2.82	0.01	0.75	2.35	0.08
Total magnet power [kW]	0.2	1.0	0.0	0.3	0.9	0.0
Total magnet water requirements [gpm]	1.4	1.4	1.4	1.4	1.4	1.4

Table 5-5. LER quadrupole parameters (continued).

Magnet designation	4Q17	4Q17	4Q17	4Q17	4Q17	4Q17
Location in ring	R8	R8	R8	R10	R10	R10
Lattice designation	QFI	QDOI	QFOI	QDT4A	QFT4A	QDT3A
Number of magnets	2	2	2	1	2	2
Operating gradient [T/m]	1.47	2.34	4.17	1.88	3.29	3.57
Pole-tip field @ operating gradient [T]	0.074	0.117	0.208	0.094	0.165	0.178
Gradient length product [T]	0.63	1.01	1.79	0.81	1.42	1.53
Inscribed radius [in.]	1.968	1.968	1.968	1.968	1.968	1.968
Minimum gap [in.]	1.457	1.457	1.457	1.457	1.457	1.457
Core length [in.]	15.95	15.95	15.95	15.95	15.95	15.95
Magnetic length [in.]	16.93	16.93	16.93	16.93	16.93	16.93
Lamination height [in.]	11.88	11.88	11.88	11.88	11.88	11.88
Lamination width [in.]	10.50	10.50	10.50	10.50	10.50	10.50
Packing factor, minimum [%]	98	98	98	98	98	98
Core weight [lb]	1786	1786	1786	1786	1786	1786
Amp-turns per pole	1464	2323	4138	1870	3270	3542
Turns per pole	37	37	37	37	37	37
Pancakes per pole	1	1	1	1	1	1
Conductor cross-sectional area [in.^{2}]	0.198	0.198	0.198	0.198	0.198	0.198
Cooling hole diameter [in.]	0.25	0.25	0.25	0.25	0.25	0.25
Conductor dimensions [in.]	0.5×0.5	0.5×0.5	0.5×0.5	0.5×0.5	0.5×0.5	0.5×0.5
Conductor length/pole [ft]	176	176	176	176	176	176
Current [A]	40	63	112	51	88	96
Resistance @ 40°C [mΩ]	47	47	47	47	47	47
Power [kW]	0.07	0.19	0.59	0.12	0.37	0.43
Voltage drop [V]	1.9	3.0	5.3	2.4	4.2	4.5
Coil weight [lb]	81.4	81.4	81.4	81.4	81.4	81.4
Number of water circuits	1	1	1	1	1	1
Water flow rate [gpm]	0.7	0.7	0.7	0.7	0.7	0.7
Water pressure drop [psi]	150	150	150	150	150	150
Temperature rise [°C]	0.40	1.00	3.19	0.65	1.99	2.34
Total magnet power [kW]	0.1	0.4	1.2	0.1	0.7	0.9
Total magnet water requirements [gpm]	1.4	1.4	1.4	0.7	1.4	1.4

Table 5-5. LER quadrupole parameters (continued).

Magnet designation	4Q17	4Q17	4Q17	4Q17	4Q17	4Q17
Location in ring	R10	R10	R10	R10	R10	R5
Lattice designation	QFT3A	QDT2A	QFT2A	QDT1A	QFT1A	QF1
Number of magnets	2	2	2	2	2	1
Operating gradient [T/m]	4.14	3.48	4.83	4.04	4.90	4.16
Pole-tip field @ operating gradient [T]	0.207	0.174	0.242	0.202	0.245	0.208
Gradient length product [T]	1.78	1.50	2.08	1.74	2.11	1.79
Inscribed radius [in.]	1.968	1.968	1.968	1.968	1.968	1.968
Minimum gap [in.]	1.457	1.457	1.457	1.457	1.457	1.457
Core length [in.]	15.95	15.95	15.95	15.95	15.95	15.95
Magnetic length [in.]	16.93	16.93	16.93	16.93	16.93	16.93
Lamination height [in.]	11.88	11.88	11.88	11.88	11.88	11.88
Lamination width [in.]	10.50	10.50	10.50	10.50	10.50	10.50
Packing factor, minimum [%]	98	98	98	98	98	98
Core weight [lb]	1786	1786	1786	1786	1786	1786
Amp·turns per pole	4113	3460	4801	4011	4871	4137
Turns per pole	37	37	37	37	37	37
Pancakes per pole	1	1	1	1	1	1
Conductor cross-sectional area [in.^{2}]	0.198	0.198	0.198	0.198	0.198	0.198
Cooling hole diameter [in.]	0.25	0.25	0.25	0.25	0.25	0.25
Conductor dimensions [in.]	0.5×0.5	0.5×0.5	0.5×0.5	0.5×0.5	0.5×0.5	0.5×0.5
Conductor length/pole [ft]	176	176	176	176	176	176
Current [A]	111	94	130	108	132	112
Resistance @ 40°C [mΩ]	47	47	47	47	47	47
Power [kW]	0.58	0.41	0.79	0.55	0.82	0.59
Voltage drop [V]	5.2	4.4	6.1	5.1	6.2	5.3
Coil weight [lb]	81.4	81.4	81.4	81.4	81.4	81.4
Number of water circuits	1	1	1	1	1	1
Water flow rate [gpm]	0.7	0.7	0.7	0.7	0.7	0.7
Water pressure drop [psi]	150	150	150	150	150	150
Temperature rise [°C]	3.15	2.23	4.29	3.00	4.42	3.19
Total magnet power [kW]	1.2	0.8	1.6	1.1	1.6	0.6
Total magnet water requirements [gpm]	1.4	1.4	1.4	1.4	1.4	0.7

Table 5-5. LER quadrupole parameters (continued).

Magnet designation	4Q17	4Q17	4Q17	4Q17	4Q17	4Q17
Location in ring	R5	R5	R5	R5	R5	R5
Lattice designation	QD1	QF2	QD2	QF3	QD3	QF4
Number of magnets	1	1	1	1	1	1
Operating gradient [T/m]	5.58	4.38	4.95	4.84	4.12	4.77
Pole-tip field @ operating gradient [T]	0.279	0.219	0.247	0.242	0.206	0.239
Gradient length product [T]	2.40	1.88	2.13	2.08	1.77	2.05
Inscribed radius [in.]	1.968	1.968	1.968	1.968	1.968	1.968
Minimum gap [in.]	1.457	1.457	1.457	1.457	1.457	1.457
Core length [in.]	15.95	15.95	15.95	15.95	15.95	15.95
Magnetic length [in.]	16.93	16.93	16.93	16.93	16.93	16.93
Lamination height [in.]	11.88	11.88	11.88	11.88	11.88	11.88
Lamination width [in.]	10.50	10.50	10.50	10.50	10.50	10.50
Packing factor, minimum [%]	98	98	98	98	98	98
Core weight [lb]	1786	1786	1786	1786	1786	1786
Amp·turns per pole	5544	4348	4917	4810	4097	4744
Turns per pole	37	37	37	37	37	37
Pancakes per pole	1	1	1	1	1	1
Conductor cross-sectional area [in.^{2}]	0.198	0.198	0.198	0.198	0.198	0.198
Cooling hole diameter [in.]	0.25	0.25	0.25	0.25	0.25	0.25
Conductor dimensions [in.]	0.5×0.5	0.5×0.5	0.5×0.5	0.5×0.5	0.5×0.5	0.5×0.5
Conductor length/pole [ft]	176	176	176	176	176	176
Current [A]	150	118	133	130	111	128
Resistance @ 40°C [mΩ]	47	47	47	47	47	47
Power [kW]	1.06	0.65	0.83	0.79	0.58	0.77
Voltage drop [V]	7.1	5.5	6.3	6.1	5.2	6.0
Coil weight [lb]	81.4	81.4	81.4	81.4	81.4	81.4
Number of water circuits	1	1	1	1	1	1
Water flow rate [gpm]	0.7	0.7	0.7	0.7	0.7	0.7
Water pressure drop [psi]	150	150	150	150	150	150
Temperature rise [°C]	5.72	3.52	4.50	4.31	3.12	4.19
Total magnet power [kW]	1.1	0.6	0.8	0.8	0.6	0.8
Total magnet water requirements [gpm]	0.7	0.7	0.7	0.7	0.7	0.7

Table 5-5. LER quadrupole parameters (continued).

Magnet designation	4Q17	4Q17	4Q17	4Q17	4Q17	4Q17
Location in ring	R5	R9	R9	R9	R9	R9
Lattice designation	QD4	QF1A	QD1A	QF2A	QD2A	QF3A
Number of magnets	1	1	1	1	1	1
Operating gradient [T/m]	4.55	4.16	5.58	4.38	4.95	4.84
Pole-tip field @ operating gradient [T]	0.227	0.208	0.279	0.219	0.247	0.242
Gradient length product [T]	1.96	1.79	2.40	1.88	2.13	2.08
Inscribed radius [in.]	1.968	1.968	1.968	1.968	1.968	1.968
Minimum gap [in.]	1.457	1.457	1.457	1.457	1.457	1.457
Core length [in.]	15.95	15.95	15.95	15.95	15.95	15.95
Magnetic length [in.]	16.93	16.93	16.93	16.93	16.93	16.93
Lamination height [in.]	11.88	11.88	11.88	11.88	11.88	11.88
Lamination width [in.]	10.50	10.50	10.50	10.50	10.50	10.50
Packing factor, minimum [%]	98	98	98	98	98	98
Core weight [lb]	1786	1786	1786	1786	1786	1786
Amp·turns per pole	4520	4137	5544	4348	4917	4810
Turns per pole	37	37	37	37	37	37
Pancakes per pole	1	1	1	1	1	1
Conductor cross-sectional area [in.^{2}]	0.198	0.198	0.198	0.198	0.198	0.198
Cooling hole diameter [in.]	0.25	0.25	0.25	0.25	0.25	0.25
Conductor dimensions [in.]	0.5×0.5	0.5×0.5	0.5×0.5	0.5×0.5	0.5×0.5	0.5×0.5
Conductor length/pole [ft]	176	176	176	176	176	176
Current [A]	122	112	150	118	133	130
Resistance @ 40°C [mΩ]	47	47	47	47	47	47
Power [kW]	0.70	0.59	1.06	0.65	0.83	0.79
Voltage drop [V]	5.7	5.3	7.1	5.5	6.3	6.1
Coil weight [lb]	81.4	81.4	81.4	81.4	81.4	81.4
Number of water circuits	1	1	1	1	1	1
Water flow rate [gpm]	0.7	0.7	0.7	0.7	0.7	0.7
Water pressure drop [psi]	150	150	150	150	150	150
Temperature rise [°C]	3.80	3.19	5.72	3.52	4.50	4.31
Total magnet power [kW]	0.7	0.6	1.1	0.6	0.8	0.8
Total magnet water requirements [gpm]	0.7	0.7	0.7	0.7	0.7	0.7

Table 5-5. LER quadrupole parameters (continued).

Magnet designation	4Q17	4Q17	4Q17	4Q17	4Q17	4Q17
Location in ring	R9	R9	R9	R11	R11	R11
Lattice designation	QD3A	QF4A	QD4A	QF1A	QD1A	QF2A
Number of magnets	1	1	1	1	1	1
Operating gradient [T/m]	4.12	4.77	4.55	4.16	5.58	4.38
Pole-tip field @ operating gradient [T]	0.206	0.239	0.227	0.208	0.279	0.219
Gradient length product [T]	1.77	2.05	1.96	1.79	2.40	1.88
Inscribed radius [in.]	1.968	1.968	1.968	1.968	1.968	1.968
Minimum gap [in.]	1.457	1.457	1.457	1.457	1.457	1.457
Core length [in.]	15.95	15.95	15.95	15.95	15.95	15.95
Magnetic length [in.]	16.93	16.93	16.93	16.93	16.93	16.93
Lamination height [in.]	11.88	11.88	11.88	11.88	11.88	11.88
Lamination width [in.]	10.50	10.50	10.50	10.50	10.50	10.50
Packing factor, minimum [%]	98	98	98	98	98	98
Core weight [lb]	1786	1786	1786	1786	1786	1786
Amp·turns per pole	4097	4744	4520	4137	5544	4348
Turns per pole	37	37	37	37	37	37
Pancakes per pole	1	1	1	1	1	1
Conductor cross-sectional area [in.^{2}]	0.198	0.198	0.198	0.198	0.198	0.198
Cooling hole diameter [in.]	0.25	0.25	0.25	0.25	0.25	0.25
Conductor dimensions [in.]	0.5×0.5	0.5×0.5	0.5×0.5	0.5×0.5	0.5×0.5	0.5×0.5
Conductor length/pole [ft]	176	176	176	176	176	176
Current [A]	111	128	122	112	150	118
Resistance @ 40°C [mΩ]	47	47	47	47	47	47
Power [kW]	0.58	0.77	0.70	0.59	1.06	0.65
Voltage drop [V]	5.2	6.0	5.7	5.3	7.1	5.5
Coil weight [lb]	81.4	81.4	81.4	81.4	81.4	81.4
Number of water circuits	1	1	1	1	1	1
Water flow rate [gpm]	0.7	0.7	0.7	0.7	0.7	0.7
Water pressure drop [psi]	150	150	150	150	150	150
Temperature rise [°C]	3.12	4.19	3.80	3.19	5.72	3.52
Total magnet power [kW]	0.6	0.8	0.7	0.6	1.1	0.6
Total magnet water requirements [gpm]	0.7	0.7	0.7	0.7	0.7	0.7

Table 5-5. LER quadrupole parameters (continued).

Magnet designation	4Q17	4Q17	4Q17	4Q17	4Q17	4Q17
Location in ring	R11	R11	R11	R11	R11	R12
Lattice designation	QD2A	QF3A	QD3A	QF4A	QD4A	QFW1A
Number of magnets	1	1	1	1	1	2
Operating gradient [T/m]	4.95	4.84	4.12	4.77	4.55	2.52
Pole-tip field @ operating gradient [T]	0.247	0.242	0.206	0.239	0.227	0.126
Gradient length product [T]	2.13	2.08	1.77	2.05	1.96	1.08
Inscribed radius [in.]	1.968	1.968	1.968	1.968	1.968	1.968
Minimum gap [in.]	1.457	1.457	1.457	1.457	1.457	1.457
Core length [in.]	15.95	15.95	15.95	15.95	15.95	15.95
Magnetic length [in.]	16.93	16.93	16.93	16.93	16.93	16.93
Lamination height [in.]	11.88	11.88	11.88	11.88	11.88	11.88
Lamination width [in.]	10.50	10.50	10.50	10.50	10.50	10.50
Packing factor, minimum [%]	98	98	98	98	98	98
Core weight [lb]	1786	1786	1786	1786	1786	1786
Amp·turns per pole	4917	4810	4097	4744	4520	2505
Turns per pole	37	37	37	37	37	37
Pancakes per pole	1	1	1	1	1	1
Conductor cross-sectional area [in.^{2}]	0.198	0.198	0.198	0.198	0.198	0.198
Cooling hole diameter [in.]	0.25	0.25	0.25	0.25	0.25	0.25
Conductor dimensions [in.]	0.5×0.5	0.5×0.5	0.5×0.5	0.5×0.5	0.5×0.5	0.5×0.5
Conductor length/pole [ft]	176	176	176	176	176	176
Current [A]	133	130	111	128	122	68
Resistance @ 40°C [mΩ]	47	47	47	47	47	47
Power [kW]	0.83	0.79	0.58	0.77	0.70	0.22
Voltage drop [V]	6.3	6.1	5.2	6.0	5.7	3.2
Coil weight [lb]	81.4	81.4	81.4	81.4	81.4	81.4
Number of water circuits	1	1	1	1	1	1
Water flow rate [gpm]	0.7	0.7	0.7	0.7	0.7	0.7
Water pressure drop [psi]	150	150	150	150	150	150
Temperature rise [°C]	4.50	4.31	3.12	4.19	3.80	1.17
Total magnet power [kW]	0.8	0.8	0.6	0.8	0.7	0.4
Total magnet water requirements [gpm]	0.7	0.7	0.7	0.7	0.7	1.4

Table 5-5. LER quadrupole parameters (continued).

Magnet designation	4Q17	4Q17	4Q17	4Q17	4Q17
Location in ring	R12	R12	R12	R12	R12
Lattice designation	QDW2A	QFW3A	QFW4A	QDW5A	QFW6A
Number of magnets	2	2	2	2	2
Operating gradient [T/m]	1.64	3.92	0.28	2.02	3.58
Pole-tip field @ operating gradient [T]	0.082	0.196	0.014	0.101	0.179
Gradient length product [T]	0.70	1.69	0.12	0.87	1.54
Inscribed radius [in.]	1.968	1.968	1.968	1.968	1.968
Minimum gap [in.]	1.457	1.457	1.457	1.457	1.457
Core length [in.]	15.95	15.95	15.95	15.95	15.95
Magnetic length [in.]	16.93	16.93	16.93	16.93	16.93
Lamination height [in.]	11.88	11.88	11.88	11.88	11.88
Lamination width [in.]	10.50	10.50	10.50	10.50	10.50
Packing factor, minimum [%]	98	98	98	98	98
Core weight [lb]	1786	1786	1786	1786	1786
Amp·turns per pole	1628	3895	283	2009	3553
Turns per pole	37	37	37	37	37
Pancakes per pole	1	1	1	1	1
Conductor cross-sectional area [in.^{2}]	0.198	0.198	0.198	0.198	0.198
Cooling hole diameter [in.]	0.25	0.25	0.25	0.25	0.25
Conductor dimensions [in.]	0.5×0.5	0.5×0.5	0.5×0.5	0.5×0.5	0.5×0.5
Conductor length/pole [ft]	176	176	176	176	176
Current [A]	44	105	8	54	96
Resistance @ 40°C [mΩ]	47	47	47	47	47
Power [kW]	0.09	0.52	0.00	0.14	0.43
Voltage drop [V]	2.1	5.0	0.4	2.6	4.5
Coil weight [lb]	81.4	81.4	81.4	81.4	81.4
Number of water circuits	1	1	1	1	1
Water flow rate [gpm]	0.7	0.7	0.7	0.7	0.7
Water pressure drop [psi]	150	150	150	150	150
Temperature rise [°C]	0.49	2.82	0.01	0.75	2.35
Total magnet power [kW]	0.2	1.0	0.0	0.3	0.9
Total magnet water requirements [gpm]	1.4	1.4	1.4	1.4	1.4

5.1.2.3 Sextupoles. The LER sextupole physical dimensions are shown in Fig. 5-6. These magnets have a length of 8.071 in. and a bore of 4.724 in. Their electrical properties, corresponding to the nominal energy, are summarized in Table 5-6.

The LER sextupoles will be identical to the present PEP short (8-in.) sextupoles. This will permit us to interchange magnets between the LER and HER, if necessary, and minimizes the required number of spares. Manufacturing techniques will be the same as those described above for the LER dipoles and quadrupoles, although the anticipated steel requirement of about 50 tons will come from only a single heat. For this reason, witness marks will not be needed for the sextupoles. Laminations will still be reversed periodically, however, to account for the crowning referred to above.

Table 5-6. LER sextupole parameters.

Magnet designation	4.5S	4.5S	4.5S	4.5S
Lattice designation	SF1	SD1	SX	SY
Number of magnets	72	72	4	4
Operating gradient [T/m^2]	25.62	45.60	113.75	186.13
Pole tip field @ operating gradient [T]	0.046	0.082	0.205	0.335
Integrated strength [T/m]	7.53	13.40	33.43	54.70
Aperture inscribed radius [in.]	2.362	2.362	2.362	2.362
Core length [in.]	8.071	8.071	8.071	8.071
Magnetic length [in.]	10.041	10.041	10.041	10.041
Core weight [lb]	170	170	170	170
Amp·turns per pole	730	1299	3240	5302
Turns per pole	24	24	24	24
Pancakes per pole	1	1	1	1
Conductor cross-sectional area [in.^{2}]	0.127	0.127	0.127	0.127
Cooling hole diameter [in.]	0.125	0.125	0.125	0.125
Conductor dimension [in.]	0.375	0.375	0.375	0.375
Current [A]	30.4	54.1	135.0	220.9
Resistance @ 40°C [mΩ]	31	31	31	31
Power [kW]	0.03	0.09	0.57	1.53
Voltage drop [V]	1.0	1.7	4.2	6.9
Coil weight [lb]	44	44	44	44
Number of water circuits	1	1	1	1
Water flow rate [gpm]	0.2	0.2	0.2	0.2
Water pressure drop [psi]	150	150	150	150
Temperature rise [°C]	0.6	1.9	12.0	32.2
Total magnet power [kW]	2.1	6.6	2.3	6.1
Total voltage [V]	68.5	121.9	16.9	27.6
Total system water requirements [gpm]	13.0	13.0	0.7	0.7

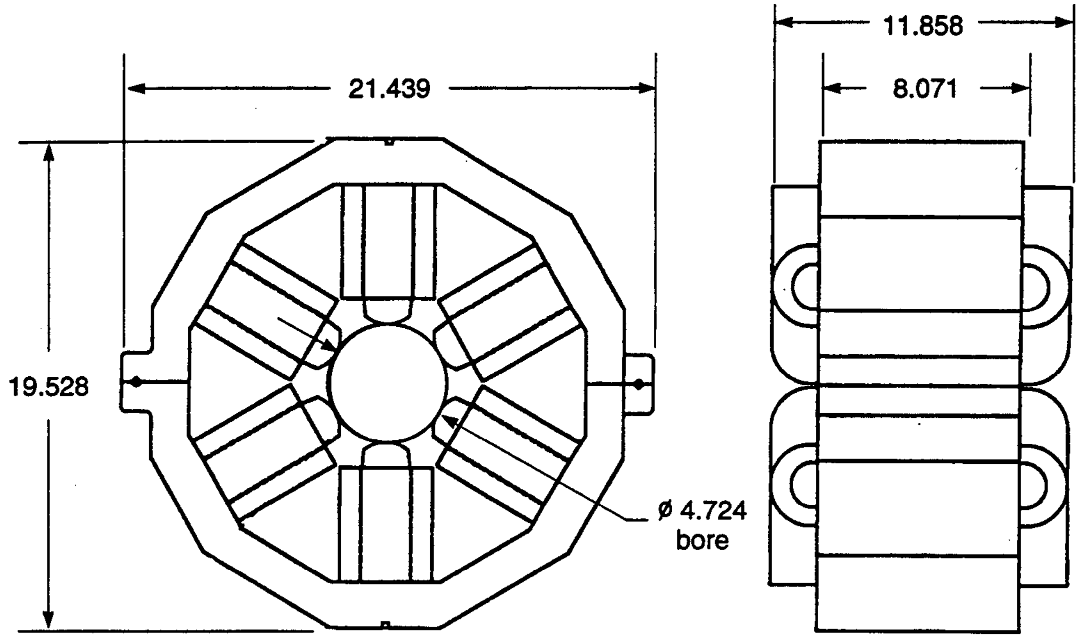

Fig. 5-6. End and side views of the LER sextupole magnet. Dimensions are given in inches.

5.1.3 Interaction Region Magnets and Supports

5.1.3.1 Permanent Magnets. Only the final focusing quadrupoles, Q1, and the magnetic separation dipoles, B1, are located within 2 m of the interaction point (IP). At these close distances, they will be inside the detector and immersed in its solenoidal magnetic field. The only viable magnet technologies for such an environment are superconducting or permanent magnets. A conventional electromagnet with iron pole tips would have its iron saturated and its field distorted by the detector field. For the IR magnets, required field strengths and apertures are within the reach of modern rare-earth–cobalt (REC) alloys, and superconducting technology is not demanded. For PEP-II, the choice of a permanent-magnet design was based on the following characteristics of such magnets:

- Their interaction with the external detector solenoid is minimal. Because magnetized REC is a magnetically hard material with little free magnetic moment left over to interact with external fields, it is magnetically transparent with a permeability μ near the μ_0 of free space. In the standard Halbach configuration [Halbach, 1981] these magnet assemblies project little external field to generate forces between the detector solenoid and the REC assembly.
- They avoid the complexity, cost, and reliability problems inherent in cryogenic operation.
- They are compact and avoid cryogenic plumbing and cryostats, both of which would significantly reduce the detector acceptance solid angle.

- They are nearly free of fringe fields that could otherwise complicate particle tracking in the detector.
- They avoid the safety aspects of superconducting systems; they will not quench—a possible advantage in a high-current storage ring.

There are also drawbacks to our choice of permanent magnet technology. Foremost among these is the fact that permanent magnets offer only a limited adjustment capability. In our design, we have added trim windings on all permanent magnets in the IR to alleviate this lack of flexibility. Other issues include the following:

- The field quality of a REC magnet depends on accurate magnetization of its constituent blocks; special techniques and equipment must be developed to measure block magnetization, and to assemble and adjust blocks.
- Strong demagnetizing external fields and high temperatures must be avoided if field quality is to be preserved. Quadrupole and dipole fields are assembled from sector-shaped REC blocks arrayed in a circle around the magnet aperture [Halbach, 1981]. Each block is magnetized in an appropriate direction so that the magnetic field varies approximately as $\cos(N\theta)$ around the bore, where $N = 1$ for dipoles, $N = 2$ for quadrupoles, etc. The optimal compromise between the number of blocks, M, and the field quality is to use $M = 16$ for a quadrupole and $M = 8$ for a dipole. These configurations are shown in Fig. 5-7.

The magnetic and mechanical properties of the PEP-II IR magnets are summarized in Table 5-7.

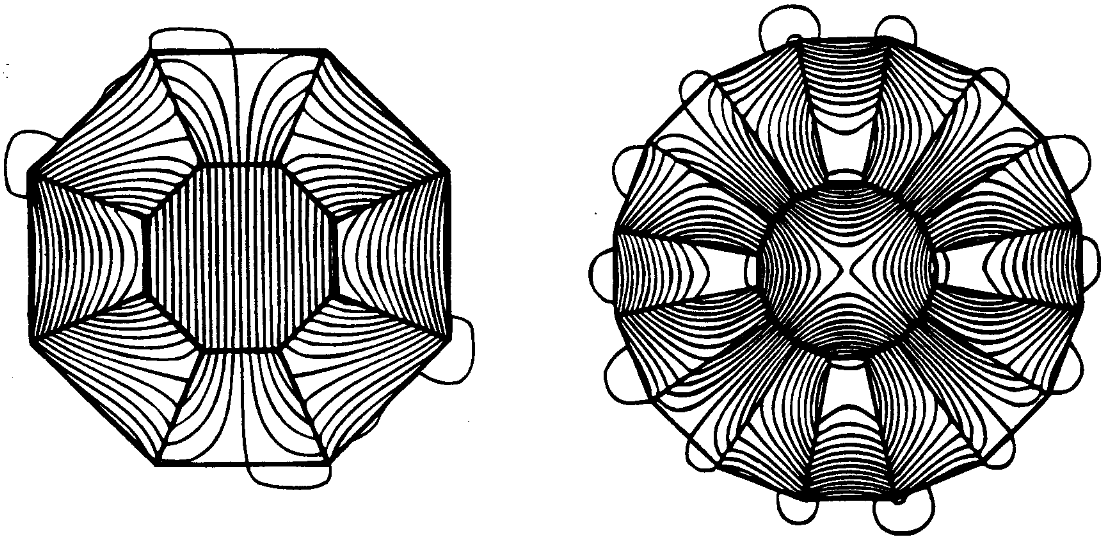

Fig. 5-7. Field lines for an 8-block permanent magnet dipole (left) and a 16-block quadrupole (right).

Table 5-7. Magnetic and mechanical dimensions for the IP permanent magnets.

	$B(r_1)$ [T]	Gradient [T/m]	r_1 [cm]	r_2 [cm]	L [cm]	Weight [kg]
B1	0.80	—	4.9[a]	9.7[a]	50.0	98
Q1	0.89	10.64	8.7	16.6	120.0	633

[a] B1 is tapered; r_1 and r_2 values are averages.

For quadrupoles ($N = 2$), the magnetic field at the aperture radius, $B(r_1)$, is related to the inner and outer radii, r_1 and r_2, by

$$B(r_1) = 2C_N B_r\left(1 - \frac{r_1}{r_2}\right) \tag{5-1}$$

where B_r is the remanent field of the permanent magnet material and

$$C_N = \frac{\cos^N\left(\frac{\pi}{M}\right)\sin\left(\frac{N\pi}{M}\right)}{\frac{N\pi}{M}} \tag{5-2}$$

Whereas Q1 is built up from 24 identical 5-cm-thick slices, B1 is a tapered magnet. The transverse field on axis for this magnet can be computed as the superposition of fields from each separate slice [Bowden, 1991]:

$$B_y(0,0,z) = \sum_{i=1}^{10} B_i(z - z_i) \tag{5-3}$$

For a slice $2l$ thick with remanent field B_r,

$$B_i(z - z_i) = B_r\left[\frac{1}{2}\ln\left(\frac{\sqrt{\bar{z}^2 + r_2^2} + \bar{z}}{\sqrt{\bar{z}^2 + r_1^2} + \bar{z}}\right) + \frac{1}{4}\left(\frac{\bar{z}}{\sqrt{\bar{z}^2 + r_2^2}} - \frac{\bar{z}}{\sqrt{\bar{z}^2 + r_1^2}}\right)\right]\Bigg|_{\bar{z} = z - z_i + l}^{\bar{z} = z - z_i - l} \tag{5-4}$$

Figure 5-8 shows the transverse field on axis for B1.

Choice of Material. The PEP-II magnets will be assembled from Sm_2Co_{17}, a material having a high remanent field ($B_r = 1.05$ T). Figure 5-9 shows the *B-H* curves of some of these materials. Commercial grades of Sm_2Co_{17} are available.

The *B-H* relation for a candidate material, R26HS (see Table 5-8), shows a linear $\mu_r \approx 1$ for the entire second quadrant. An external demagnetizing *H* field must actually

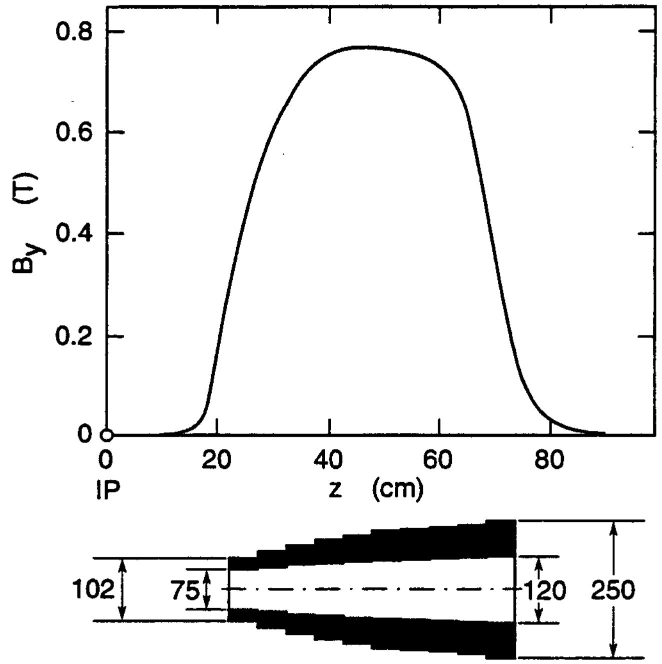

Fig. 5-8. Transverse field on axis for the tapered B1 dipole magnet. Dimensions are in mm.

exceed B_r/μ_0 of the material before nonlinearities and hysteresis develop, causing permanent demagnetization of the material. For lower external fields, simple linear superposition of fields holds. Since the detector axial solenoidal field is nearly orthogonal to the transverse field of the beamline magnets, the two fields are not expected to interact. The high Curie temperature of Sm_2Co_{17} allows this material to be used at temperatures up to 500°C, and its low temperature coefficient should preserve field quality. Lastly, the chosen material has good radiation-resistance properties [Luna, 1989], so its performance is not expected to degrade in the relatively harsh environment of the PEP-II IR.

Table 5-8. Properties of R26HS magnetic material.

Material	B_r [T]	Temperature coefficient [%/°C]	Curie temperature [°C]	Density [g/cm^3]
R26HS	1.05	−0.03	820	8.4

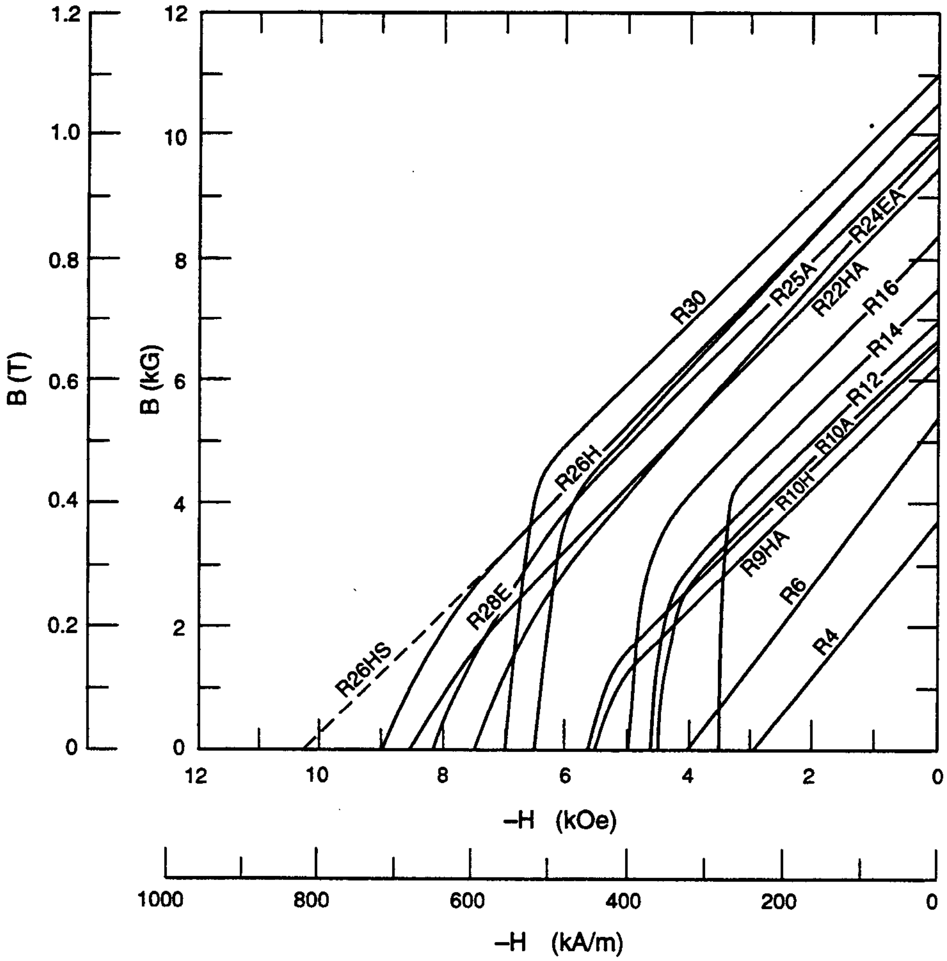

Fig. 5-9. B-H curves for various permanent-magnet materials.

Permanent Magnet Assembly. Both the B1 dipoles and the Q1 quadrupoles will be built up from "pineapple-ring" shaped slices of permanent magnet blocks held in alignment on a common beam pipe mandrel. Individual trapezoidal blocks of Sm_2Co_{17} are collared together between aluminum rings to restrain the magnetic hoop forces. For the 5-cm-thick slices of Q1, these hoop forces are approximately 200 lb.

Taken together, fabrication of the IR magnets will involve nearly one thousand precisely machined and magnetized blocks of Sm_2Co_{17}. The field quality of the resulting magnets depends critically on their precise magnetization. The magnitude, direction, and uniformity of the magnetization **M** will therefore be held to tight tolerances inside each block. In addition, variations can, to some degree, be accommodated by selective assembly and adjustment of final block positions. In any case, block magnetization will be measured before assembly. Even perfectly magnetized individual blocks do not produce simple, uniform **B** fields. Figure 5-10 shows the **B** field pattern for two typical uniform magnetizations of a block. The **B** field is related to block magnetization by

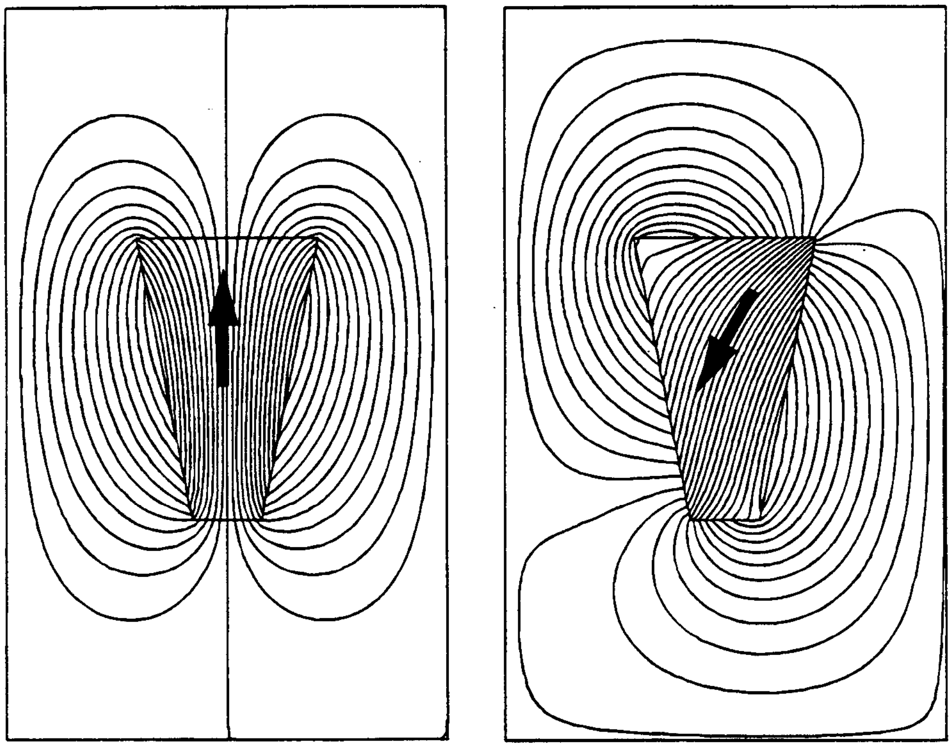

Fig. 5-10. Field patterns for two typical uniform magnetizations of permanent-magnet-material blocks.

$$\mathbf{B}(\mathbf{r}) = \mu_0 \mathbf{M}(\mathbf{r}) + \frac{\mu_0}{4\pi}\left[\int_S \mathbf{M}\cdot\mathbf{n}\,\frac{(\mathbf{r}-\mathbf{r}')}{|\mathbf{r}-\mathbf{r}'|^3}\,da' - \int_V \nabla\cdot\mathbf{M}\,\frac{(\mathbf{r}-\mathbf{r}')}{|\mathbf{r}-\mathbf{r}'|^3}\,dV\right] \qquad (5\text{-}5)$$

If the block has perfectly uniform magnetization ($\nabla\cdot\mathbf{M} = 0$), then **B** and **M** differ only by a surface integral over the shape of the block. Using the above relation, the internal magnetization field of a block can be inspected by making measurements of **B** over its surface. Figure 5-11 illustrates this inspection procedure.

A simple jig will be used to determine the coordinate frame and measurement points on the surface at which the normal component of **B** is measured. These data will then be used to calculate the magnitude and direction of **M** inside the block. Estimates of the uniformity of **M** can also be computed. If magnetic tolerances can be tightly held by this inspection procedure, it would greatly reduce the magnetic trimming involved in the final assembly of the magnet.

Rare-earth permanent-magnet blocks with strength and magnetic direction tolerances of ±2% and ±2°, respectively, were achieved in production 8 years ago [Herb, 1985]. The large number of blocks required for each Q1 (384) makes it practical to sort and selectively assemble blocks to optimize the field quality. Grouping blocks with similar magnetic errors in the same axial slice of the magnet reduces the unwanted field harmonics associated with random magnetic errors. By this means, random multipole strengths can be held at or below 1×10^{-3} of the quadrupole field at the magnet bore radius. Remaining field errors

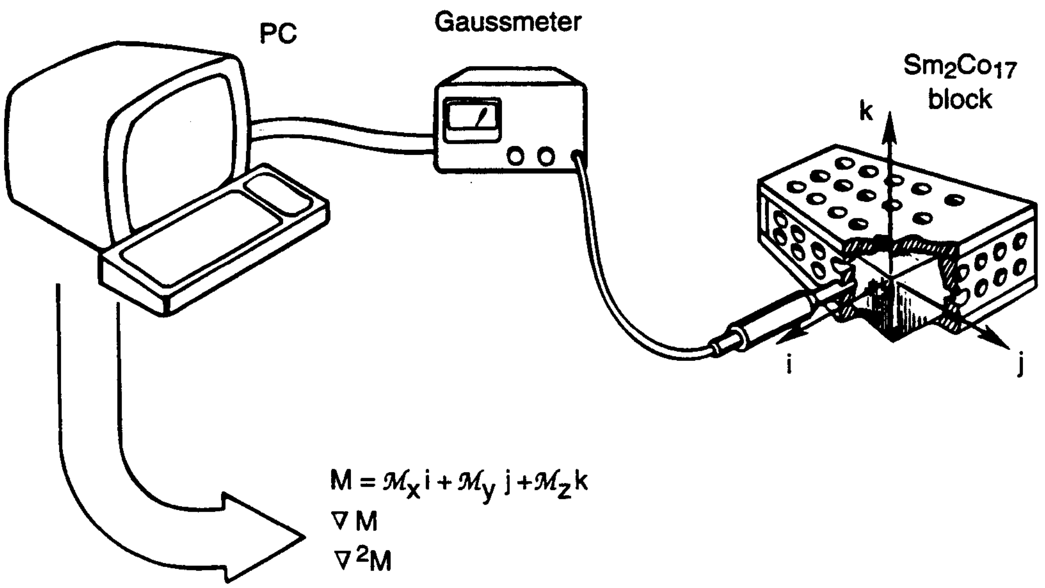

Fig. 5-11. Schematic representation of a procedure to inspect permanent-magnet blocks before assembly.

will be corrected by addition of small shim pieces of Sm_2Co_{17} at appropriate locations around the outer circumference of each slice [Bowden, 1993]. An algorithm for systematically calculating these correction shims has been developed, based on Halbach [1981b].

Each slice of either B1 or Q1 will have the same angular orientation as its neighbors. North poles will be adjacent to north poles and south poles adjacent to south poles. This slice-to-slice juxtaposition of like poles will generate internal axial repulsion forces of 3000 lb in the case of Q1. These forces are carried by the beam pipe mandrel and clamping flanges at each end of the magnet.

Permanent magnets have already been successfully applied to storage rings at SLAC [Spencer, 1985] and elsewhere [Herb, 1987]. We consider the technology to be a mature one, well suited to this application.

5.1.3.2 IP Support Barrel. PEP-II poses difficult support and alignment problems for the final magnetic elements near the IP. Bunch spacing is only 1.26 m and requires magnetic separation of the two beams to begin at ±20 cm from the collision point. The final quadrupoles are completely buried inside the detector. Previous storage rings have placed the equivalent magnets on separate individual supports, cantilevered in from the detector entrance. Unfortunately, such a support is difficult to make rigid, and the relative alignment of the magnets is not easily measurable once they are installed.

As shown in Fig. 5-12, for PEP-II we intend to avoid this limitation by using a single support "barrel" through the detector, from one end to the other, to carry all magnets. In addition to carrying the beam separation dipoles B1 and the final permanent-magnet quadrupoles, Q1, the support barrel carries the central vertex detector. Other equipment carried inside the barrel includes the water-cooled masks that shield the detector from the

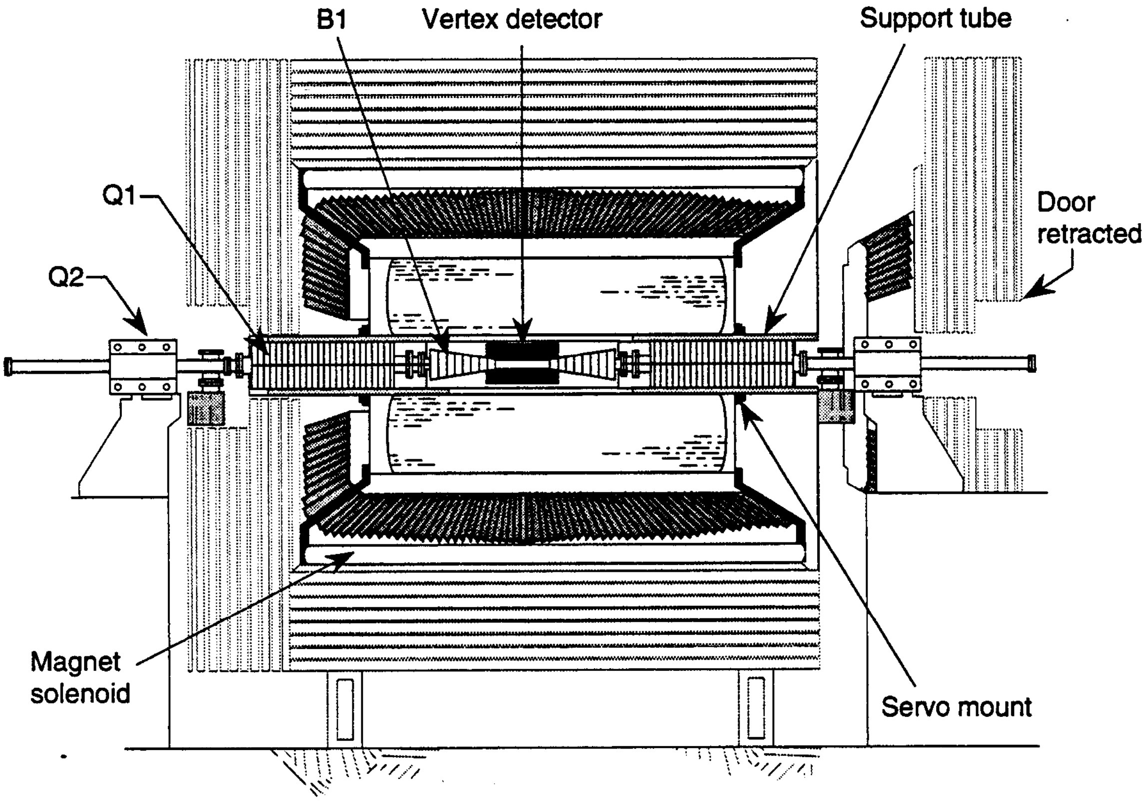

Fig. 5-12. Tube or barrel to support the permanent magnets, beam pipe, and vertex detector inside the drift chamber.

HEB and LEB synchrotron radiation fans (see Sections 4.2 and 5.2.7), radial ion pumps, and BPMs. Plumbing and cabling for this equipment passes through the barrel, while vertex detector cabling is carried on the outside.

Our choice of a single support barrel has two important advantages over previous designs:

- Magnetic elements on each side of the IP are directly connected by a rigid structure that maintains their relative alignment
- All components can be preassembled and aligned in the barrel outside the detector, where precise and effective survey techniques can be employed

Barrel Mounts. The barrel is supported from the detector drift chamber end-plates. These support locations are approximately at the quarter-points of the barrel, thus balancing end and midpoint deflections. This reduces deflection nearly 50-fold compared with a simple end support, and raises the natural frequency of the structure by a factor of 7. The barrel rests on roller cams (consisting of a spherical roller that bears on a shaft with 1.5-mm eccentric journals; see Fig. 5-13) at each end of the drift chamber. Two roller cams locate the barrel axis at one end, and three roller cams fix the axis and roll at the other

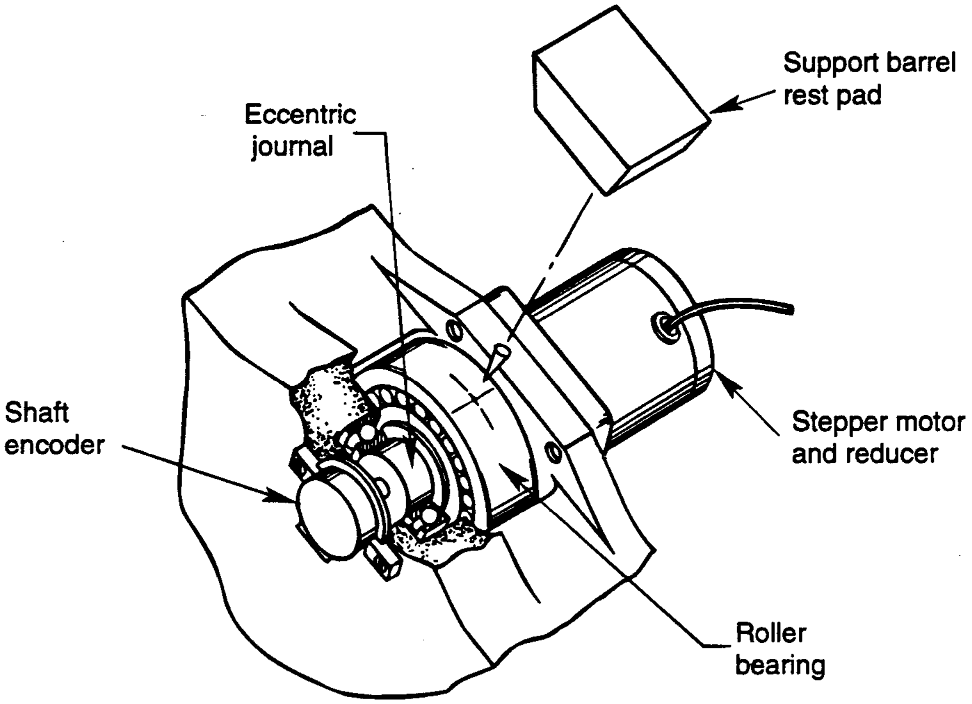

Fig. 5-13. Detail of roller cam for supporting and adjusting the support barrel.

end, as shown in Fig. 5-14. During operation, only the eccentric shaft rotates, displacing the outer bearing race. The race remains in fixed contact with its barrel support pad, so no sliding motions are involved; only rolling motion occurs. All five roller cams are driven by stepper motors through gear reducers, allowing five-axis remote positioning of the barrel; that is, the barrel position can be adjusted by ±1.5 mm in x and y, along with pitch, roll, and yaw, during beam operation.

With this technique, positioning of the support barrel to an accuracy of a few microns is practical. Because excursions are cyclic and naturally limited by cam lift, no limit switches are needed to protect against damage. Except for a fixed z restraint at one end, the barrel mount is fully kinematic and free of any over-constraints that might distort internal alignment. A similar remote-positioning mount design has been used successfully for the final triplets in the SLC interaction region [Bowden and Putallaz, 1985].

Barrel Construction. The support barrel consists of three separable sections. The two outboard ends, which carry the heavy quadrupoles, are made from 0.75-in.-wall nonmagnetic stainless-steel pipe. Access ports and magnet mounting points will be machined into the walls. The middle barrel section is of sandwich construction, with carbon-fiber facings and a foam core. This section must be nearly transparent to radiation and insensitive to thermal distortion. During installation, when the loaded barrel (3500 lb) must be temporarily supported from its end points, fiber stresses reach a maximum of 8000 psi at the midspan of the carbon tube. Figure 5-15 shows the barrel construction details.

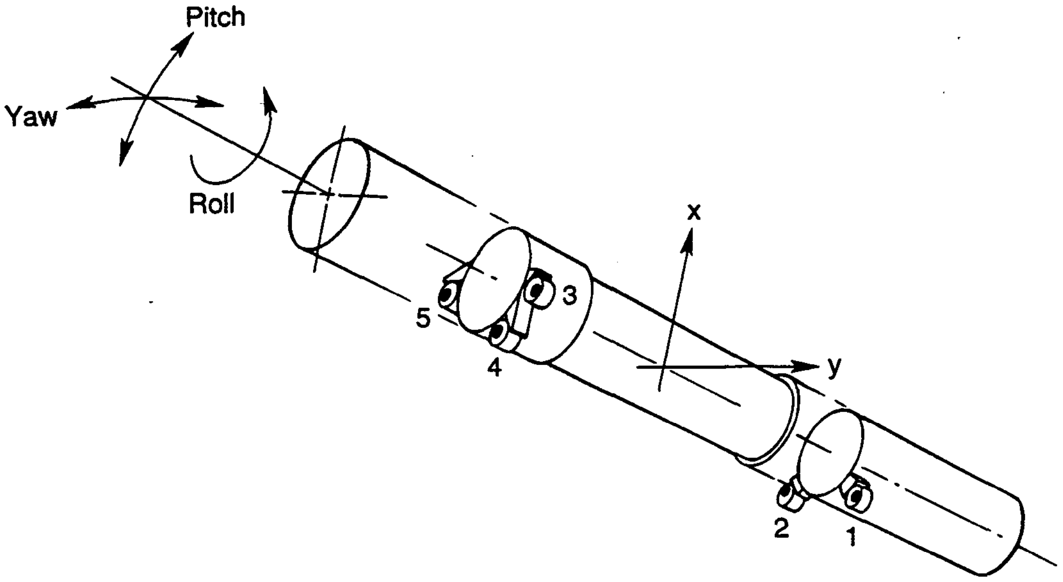

Fig. 5-14. View of the support barrel, showing its five remotely adjusted roller cams.

The most damaging thermal distortion is bending of the barrel due to transverse temperature gradients. Expansion of the warmer top of the barrel and contraction of the cooler bottom would cause the barrel to arch upward, as shown in Fig. 5-16. Because carbon fibers shorten slightly with increasing temperature (see Table 5-9), the center barrel section can be compensated to approximately zero expansion, either by balancing the fiber pitch helix angle against the high expansion coefficient of the resin matrix, or by cladding the fiber layers (which have a negative expansion coefficient) with a thin (say, 10-μm) layer of a material having a positive expansion coefficient, such as aluminum. Because the two outer stainless-steel ends of the barrel are only about one-third of the total length L, it should be possible to hold the total distortion δ (defined in Fig. 5-16), below 25 μm per °C. In addition to the protection afforded by our fabrication method and materials, the

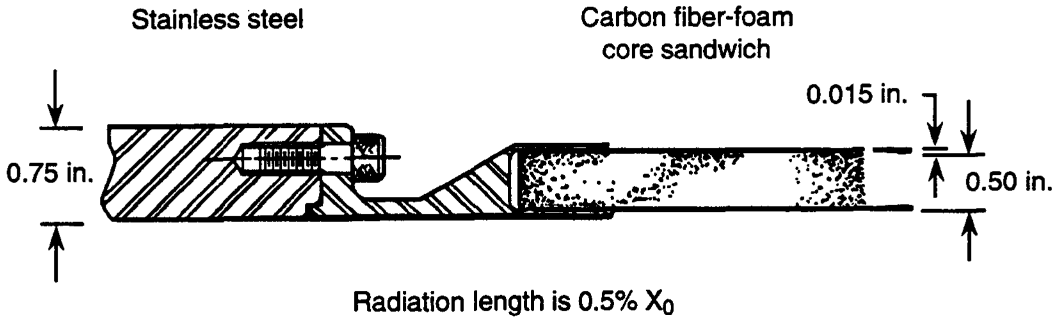

Fig. 5-15. Detail of joint between the thin inner section of the support barrel and the outer stainless-steel section.

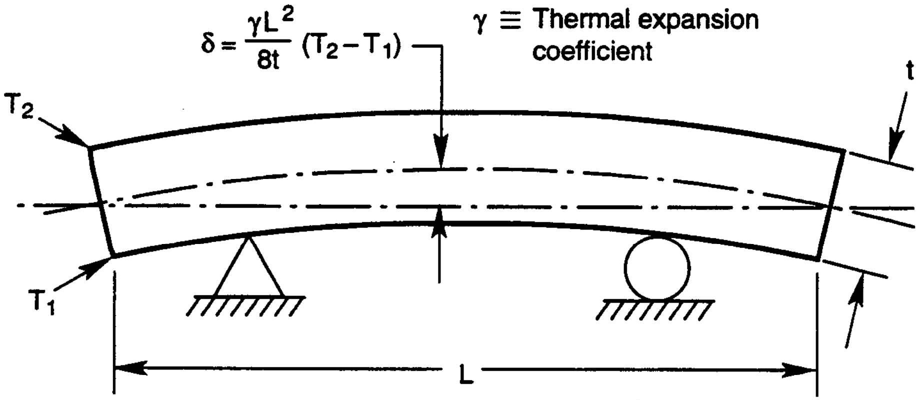

Fig. 5-16. Curvature of support barrel resulting from a temperature difference between its top and bottom.

barrel will be well sealed from natural convection by the detector, and water cooling of local heat sources will prevent asymmetric heating from causing temperature differences greater than 1°C.

Ground Motion. Because PEP-II consists of two independent storage rings, microseismic ground motion could possibly interfere with beam collisions. The spectrum of ground motion measured at SLAC [Bowden, 1985] is shown in Fig. 5-17, along with its amplitude distribution. Most ground motion is found in the 1- to 10-Hz band, whereas the barrel resonant frequency is about 30 Hz; therefore, no strong coupling will occur. The vertical beam-spot size is 6 μm in PEP-II, about 100 times the amplitude of the average microseismic noise. Quadrupole amplification will use up some, but not all, of the available margin. Further, because the barrel ensures a smooth fundamental-mode response to the vibration modes, the relative motions of the quadrupoles will be much smaller than the vibration amplitude of the barrel itself. Previous measurements at SLAC of mechanical noise from cooling-water flow have shown that this source usually does not make a significant contribution. Thus, we conclude that mechanical vibration will not be a serious problem for the barrel support.

Table 5-9. Thermal expansion coefficients and deflection of the materials that make up the 4.35-m barrel.

Material	γ [$\Delta L/L$ per °C]	δ [μm per °C]
Stainless steel	1.7×10^{-5}	113.0
Aluminum	2.3×10^{-5}	153.0
Carbon fiber 0°	-5.6×10^{-7}	-3.7
Carbon fiber 90°	3.6×10^{-5}	235.0

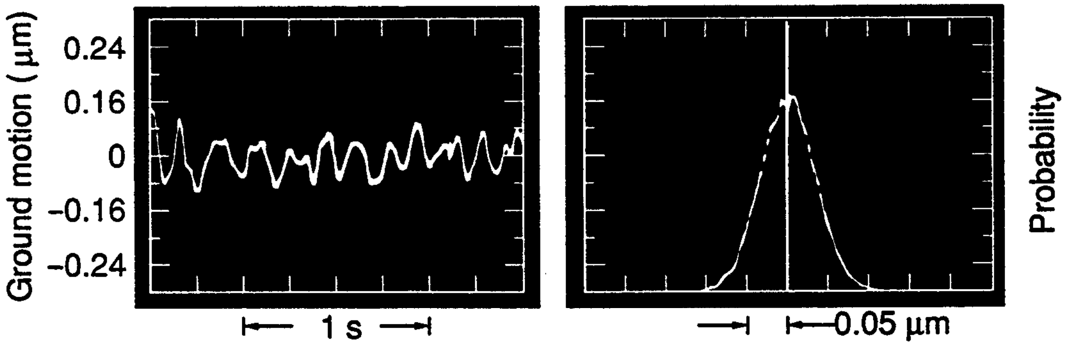

Fig. 5-17. Ground motion measured at SLAC.

Barrel Assembly and Component Alignment. The technical difficulties of assembling 4 m of heavy and delicate beamline equipment in a close-fitting support barrel has already been solved for the SLC final triplets, as demonstrated in Fig. 5-18.

Figure 5-19 is a cross section through half the support barrel length. The barrel assembly separates into three independent modules. The center section, made of carbon-fiber tube, houses the central vertex detector and the B1 deflection dipoles. This central section will be built up in the laboratory as part of the physics detector complex. For commissioning the storage rings in the absence of the detector, there is the option for a simple temporary substitute aluminum tube carrying only the B1 magnets and beam diagnostics instrumentation.

The two outboard stainless steel tubes carry the Q1 quadrupoles. Magnet mounts are installed and adjusted from the outside of the barrel. Magnets are clamped near their ends by shimmed bolts through the barrel wall, as shown in Fig. 5-19. Bolts work in four opposing pairs. The position of one bolt in each pair is fixed by a replaceable shim washer. The opposing bolt preloads the magnet mount through a spring-loaded pusher. The amount of preload is set by a second shim under this bolt. Adjustment of the alignment is made by changing shim thicknesses. Whenever a fixed bolt shim is changed, the corresponding preload shim is changed to maintain the nominal preload. In this way, forces and deflections are held constant during the alignment procedure. Adjustment of one magnet position does not affect another, and the tightening torque on the support bolts does not affect magnet position. When this technique was used on the SLC final triplets, alignment by shim changes converged in two iterations. This method is well-matched to modern survey procedures based on computer-linked theodolites and sophisticated survey software, of the type described in Section 5.3.

Final joining of the three sections into a complete barrel will be done on an assembly/alignment stand capable of supporting and aligning each barrel section independently. To bolt together the vacuum flange between Q1 and B1, the Q1 magnet will be temporarily supported through access windows in the support barrel. Then the support barrel can be pulled back on rollers, like a sleeve, opening access to the beam pipe vacuum flange. After leak checking, the stainless steel barrel is rolled forward and bolted to the flange of the central carbon tube.

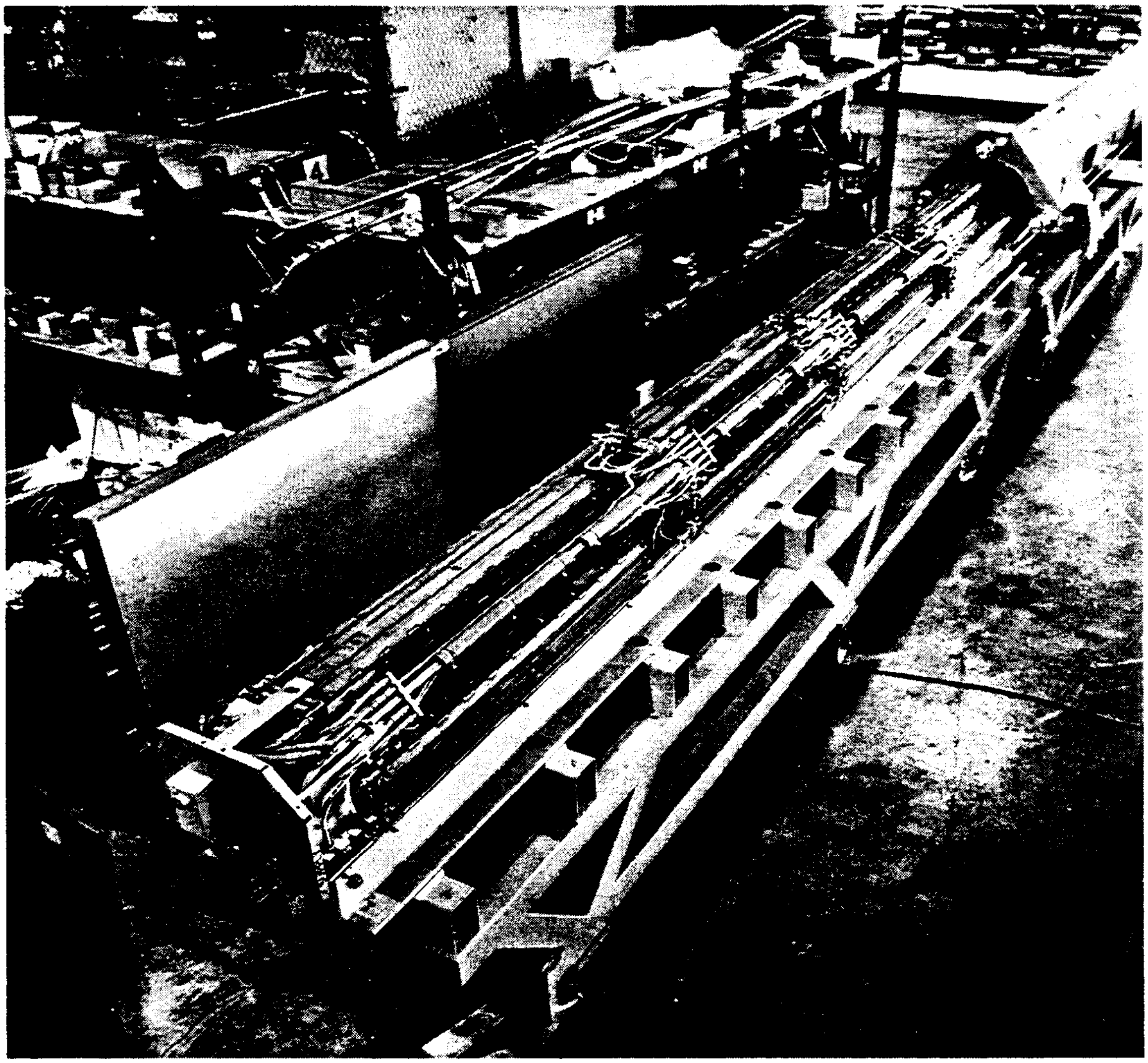

Fig. 5-18. Illustration showing the assembly technique for the SLC final focus triplet barrel.

A major reason for building all IR components into a common support barrel is to allow prealignment of beamline components prior to assembly into the detector. Once hidden inside the detector, magnets cannot easily be surveyed from the outside. The support barrel allows this alignment to be done in the laboratory under optimal conditions; Fig. 5-20 illustrates the procedure.

During alignment, the barrel will be supported in mounts identical to those to be used on the actual detector. In this way, all deflections are accurately reproduced. Access ports for either directly viewing magnet fiducials or attaching extended targets are provided on the support barrel. Magnet survey is done with computer-linked theodolites using many redundant observations to obtain a strongly over-constrained fit on the relative positions of all fiducials. A length standard is set in clear view of all theodolite locations. The raw survey data consist of precision-encoded angle measurements. All measurements are then computer processed to reconstruct the relative magnet positions. The overall resolution of

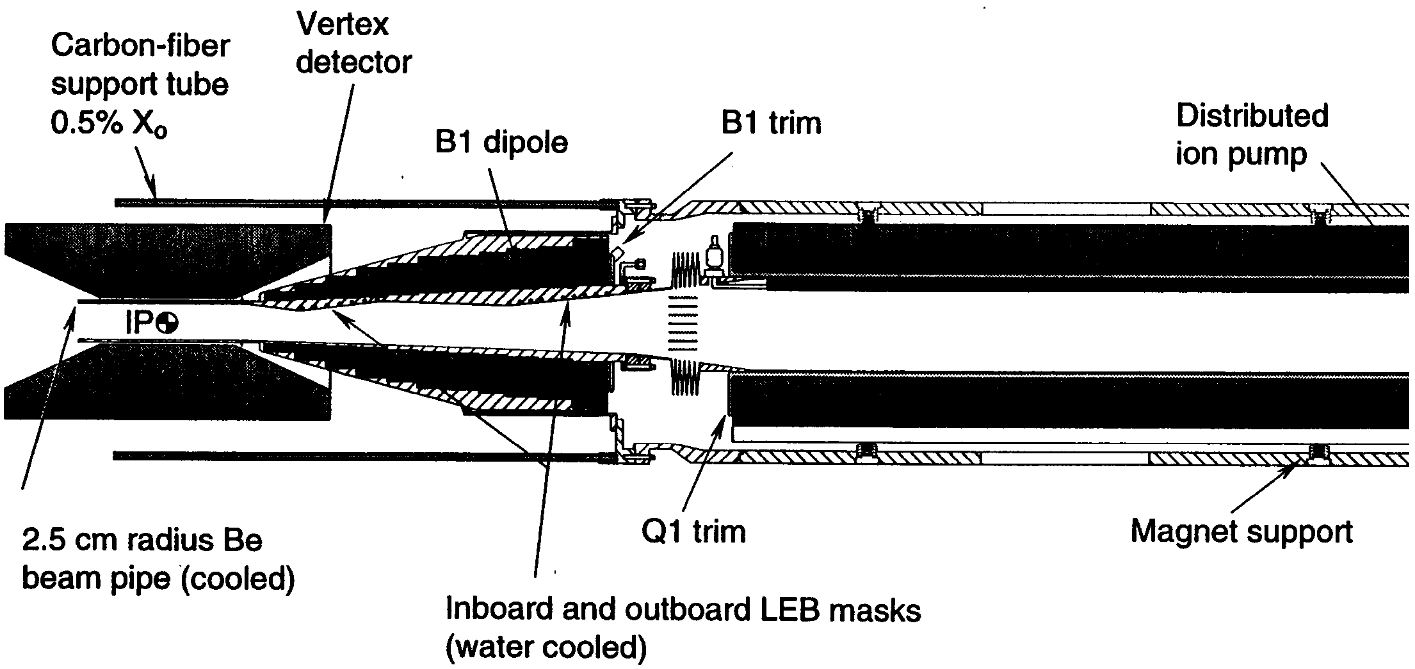

Fig. 5-19. Section through PEP-II IR barrel, showing magnet-positioning technique.

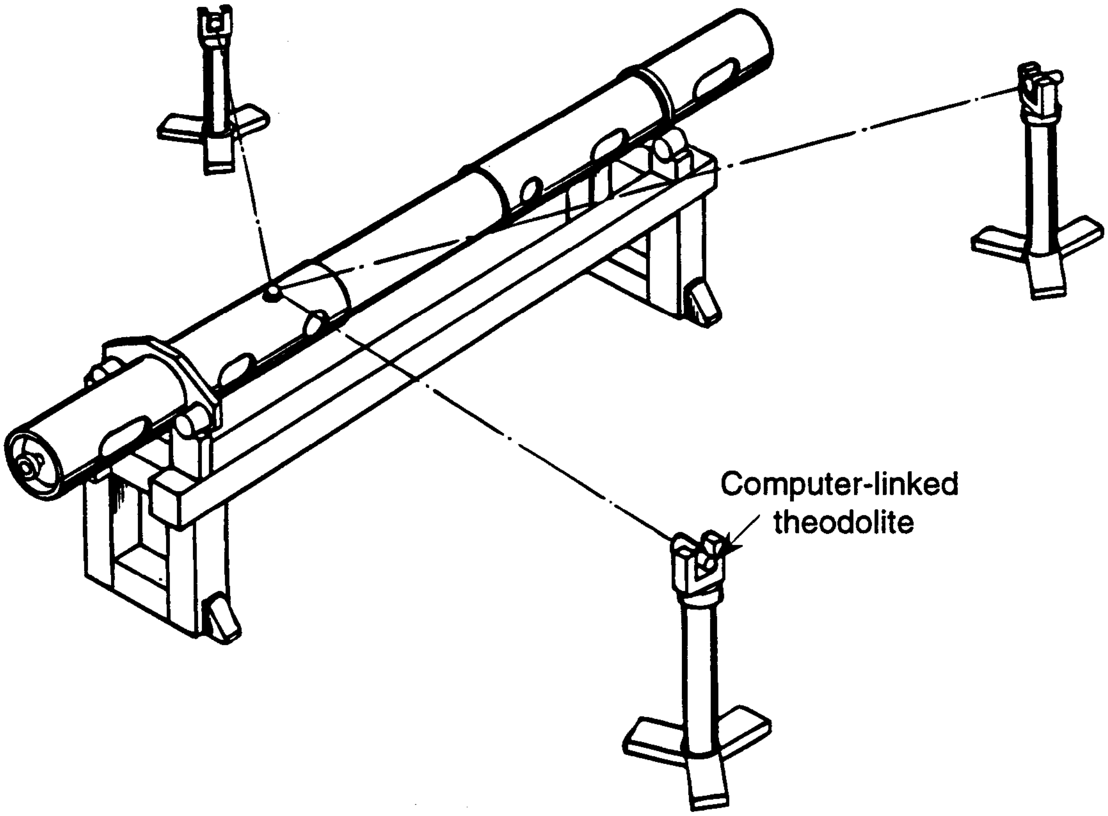

Fig. 5-20. Illustration of a method for prealigning elements inside the support barrel before installation in the detector.

such a modern system is 50 μm over 5 m. Positioning the barrel components with respect to the rest of the storage ring is straightforward. After installation into the detector, barrel-end fiducials will be clearly visible from the standard survey stations used to align other external beamline components. Furthermore, the remote positioning mounts will allow fine adjustment of the barrel position during beam operation.

5.1.3.3 Permanent-Magnet Trim Coils. To tune the collider beam optics and to permit shifting of the ring energies to reach different T resonances, Q1 and B1 will require trim coils with a 3% adjustment range. These coils, which line the bores of the permanent magnets, must be of compact design because small increases in the magnet aperture require large increases in the outer diameter of the permanent-magnet assembly to recover the lost strength.

For Q1, a set of four uniform-current-density coils are wound directly on the beam pipe. Coils are 30° wide to cancel the field of the first allowed higher multipole (octupole). The coil consists of 8 turns of 5-mm-square water-cooled copper conductor. A current of 203 A in 8 turns gives the required field of 0.0255 T at the mean trim coil radius. Figure 5-21 shows a section through the coil and a typical plan view. At 203 A, the total four-coil power is 3.8 kW at 19 V. Water cooling will be center tapped at the midpoint of

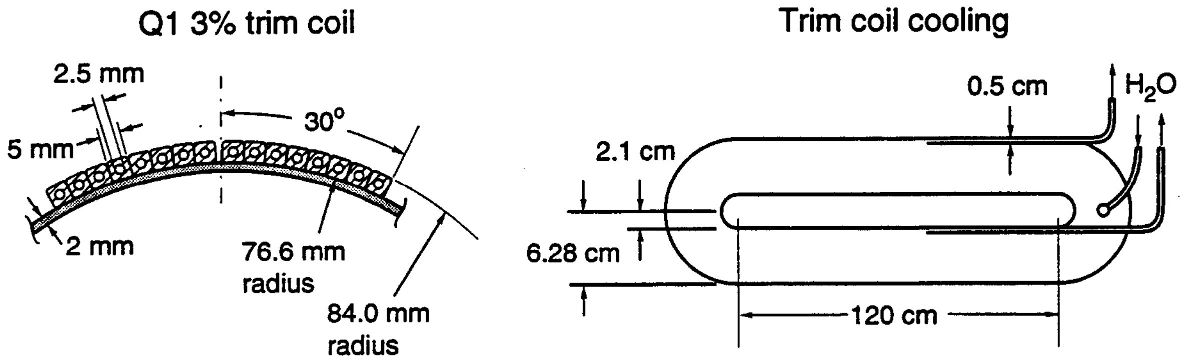

Fig. 5-21. Cross section (left) and plan view (right) of the permanent-magnet trim coils.

each coil, forming two parallel cooling flows to reduce temperatures and pressure drops. Based on a 75-psi pressure drop, water flow is about 2 L/min/coil and the water temperature rise is about 7.5°C. For turbulent flow ($R_C = 1.7 \times 10^4$), the wall-film heat transfer coefficient is about 13 W/in.$^2 \cdot$°C. This gives a modest 0.5°C temperature difference between the conductor and the water.

5.1.3.4 Septum Quadrupole (Q2). The septum quadrupoles, Q2, are the last magnets before the separate high- and low-energy beam trajectories merge into (diverge from) a common vacuum beam pipe on their way into (out of) the IP. They are located ±2.8 m from the IP and are the first storage ring magnets beyond the detector solenoid. The Q2 magnets must vertically focus the 3.1-GeV LEB while providing a low-field bypass channel for the adjacent 9-GeV HEB.

Figure 5-22 shows the 15σ beam envelopes for the two beams at the inboard face of Q2 (the face closest to the IP). Because the quadrupole aperture of Q2 is separated from the field-free bypass channel for the HEB by only 2.18 cm, a current septum must be introduced between the two regions. In addition to accommodating the two beam envelopes, a clear aperture ("fan stay-clear") must also be provided for the fan of synchrotron radiation generated in the magnets that bend the two beams onto a common collision axis at the IP. This fan (whose power is 49 kW at a beam current of 0.99 A, as discussed in Section 4.2) extends out from the collision axis by 12 mrad.

The required septum quadrupole presents two special challenges:

- An asymmetric magnet having a pure quadrupole field in the magnet aperture, and a low-field bypass channel only 2.18 cm to the side, must be designed magnetically
- A very compact, high-current-density septum having adequate cooling capacity must be designed

Solutions to both of these challenges are presented below.

Magnetic Design. Design requirements for Q2 are summarized in Table 5-10. In any magnet structure, the net flux crossing a surface of infinite extent, such as the midplane of a quadrupole, is zero. The additional field introduced by the asymmetry of the Q2 coil

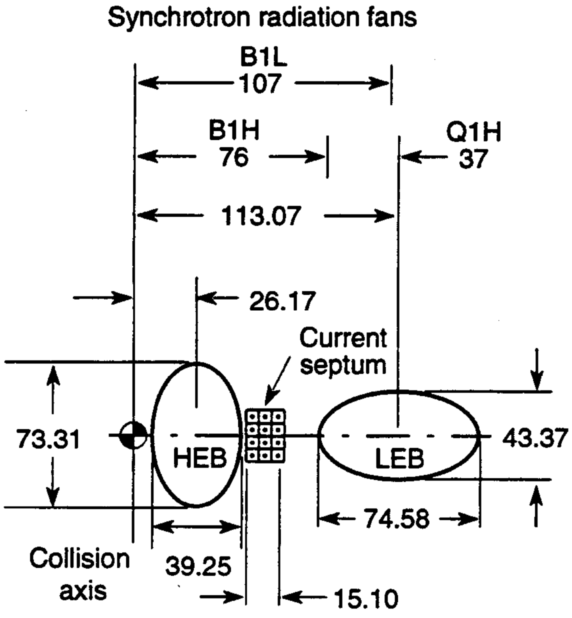

Fig. 5-22. Beam-stay-clear envelopes and locations of synchrotron radiation fans at the inboard face of Q2. All dimensions are in mm.

positions must be shunted across the midplane by iron flux returns. This preserves the high-quality quadrupole field in the magnet aperture as well as the zero field in the adjacent bypass channel. Figure 5-23 shows the flux pattern for the present septum quadrupole design with its iron return paths; the field in the yoke is below 1.1 T everywhere. A small 10-A trim coil is added to the backleg yoke opposite the septum to compensate for the small $\int H \cdot dl$ imbalance between backlegs. Except for the septum conductor on the left side, the Q2 magnet shown in Fig. 5-23 differs little from a conventional warm-iron quadrupole design. Figure 5-24 shows a mechanical layout for the Q2 magnet; its design specifications are summarized in Table 5-11.

Pole tips are shimmed, using the Poisson program MIRT, to compensate for the proximity of the current septum. Deviations from a pure hyperbola amount to 0.5 mm at most. Table 5-12 gives the relative multipole field strengths normalized to the quadrupole field ($n = 2$) at the full aperture radius, r_0. The quadrupole gradient within the ellipse corresponding to 2/3 of the beam-stay-clear aperture (roughly $10\sigma_x$ or $10\sigma_y$) remains within $\pm 2 \times 10^{-3}$ of its nominal value.

Table 5-10. Q2 design parameters.

Magnet length [cm]	50
Gradient [T/m]	11.5
Bypass channel field [T]	≤ 0.01
Multipole field contamination at 2/3 aperture	5×10^{-4}
Trim range	0–110%

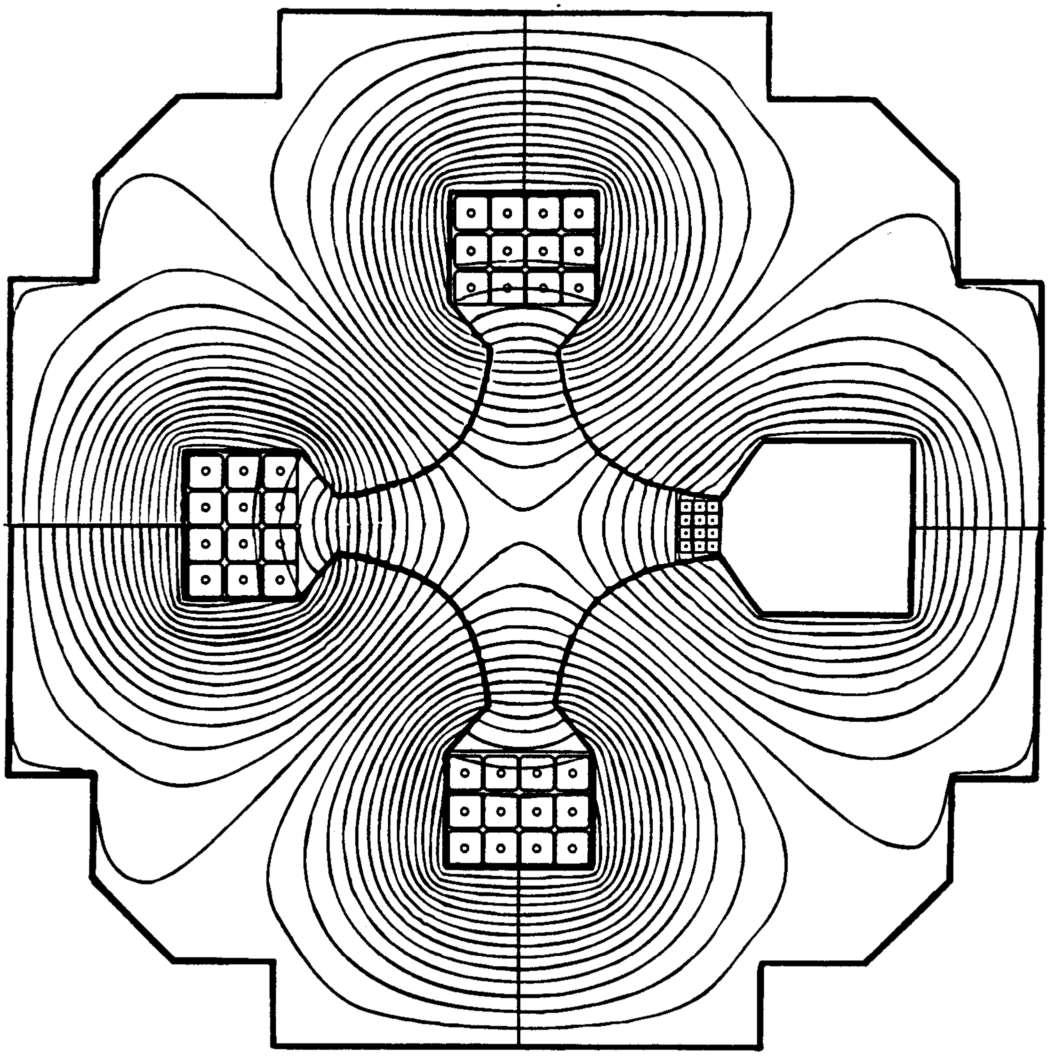

Fig. 5-23. Flux pattern for Q2.

As well as producing a high-quality quadrupole field in the LEB aperture, Q2 must also leave a low-field bypass channel for the HEB. Figure 5-25 shows the residual midplane dipole field in the HEB bypass channel. Because the separation between HEB and LEB beamlines grows as they recede from the IP, the field plotted here (at the front face of Q2) is the maximum field experienced by the HEB. The field on the HEB diminishes as the beam moves closer to the outboard end of Q2 where it is at a greater distance from the current septum.

Thermal Design. To examine the septum cooling issue, we consider the enlargement of the septum region shown in Fig. 5-26. Although the six conductors of the upper septum half are wired in series electrically, their cooling is handled with separate, parallel hydraulic circuits. Coolant streams traverse the length of the septum only once. Each conductor is separated from its neighbors by a 0.4-mm-thick insulation layer. For precise conductor

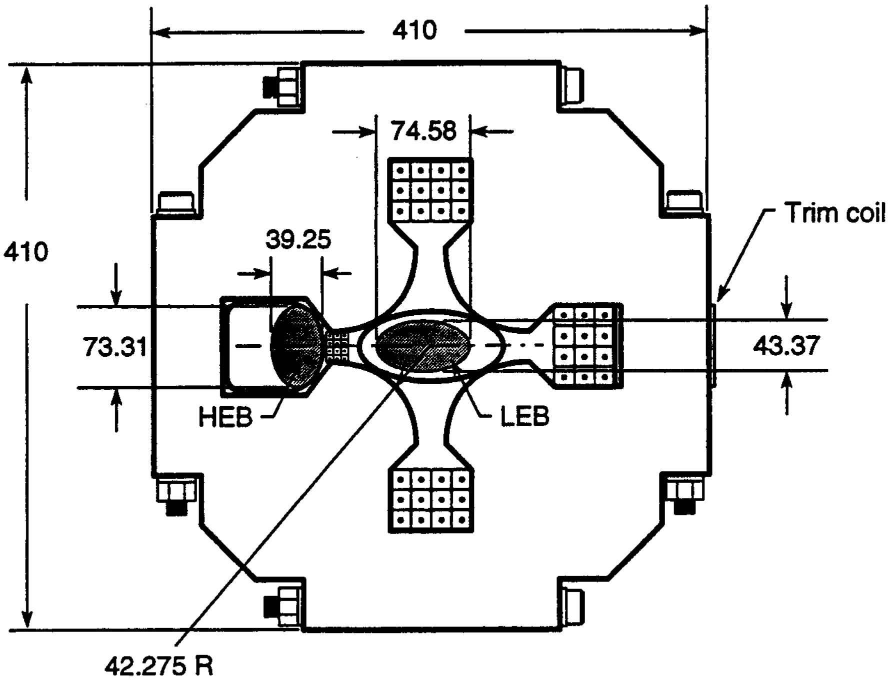

Fig. 5-24. Q2 mechanical layout.

location and mechanical integrity, the entire septum will be built as a single vacuum-impregnated assembly as outlined by Roman [1965]. The current density for the *net* copper cross section is 8.5 kA/cm^2 at the full 8200 A·turns. Starting from a water pressure drop of 75 psi and 70-cm-long conductors, Table 5-13 summarizes the septum thermal parameters.

By using parallel cooling, the total temperature rise can be held to about 15°C for the short length of these conductors. On the right side of Q2 (see Fig. 5-23) the two conventional coils are wound from six turns of 0.5-in.-square copper conductor having a

Table 5-11. Q2 specifications.

Pole-tip inscribed radius, r_0 [cm]	4.23
Gradient [T/m]	11.5
Length [cm]	50
Current [A]	1367
No. of turns	6
Peak field in iron pole [T]	0.9
Septum current density [kA/cm^2]	8.5[a]
Total power [kW]	27.0
Estimated weight [lb]	1000

[a] For net copper cross section.

Table 5-12. Q2 relative multipole field coefficients at $r_0 = 4.23$ cm.

n	b_n/b_2
1	-0.33×10^{-4}
2	1.00
3	-1.11×10^{-4}
4	1.82×10^{-4}
5	0.63×10^{-4}
6	-0.50×10^{-4}

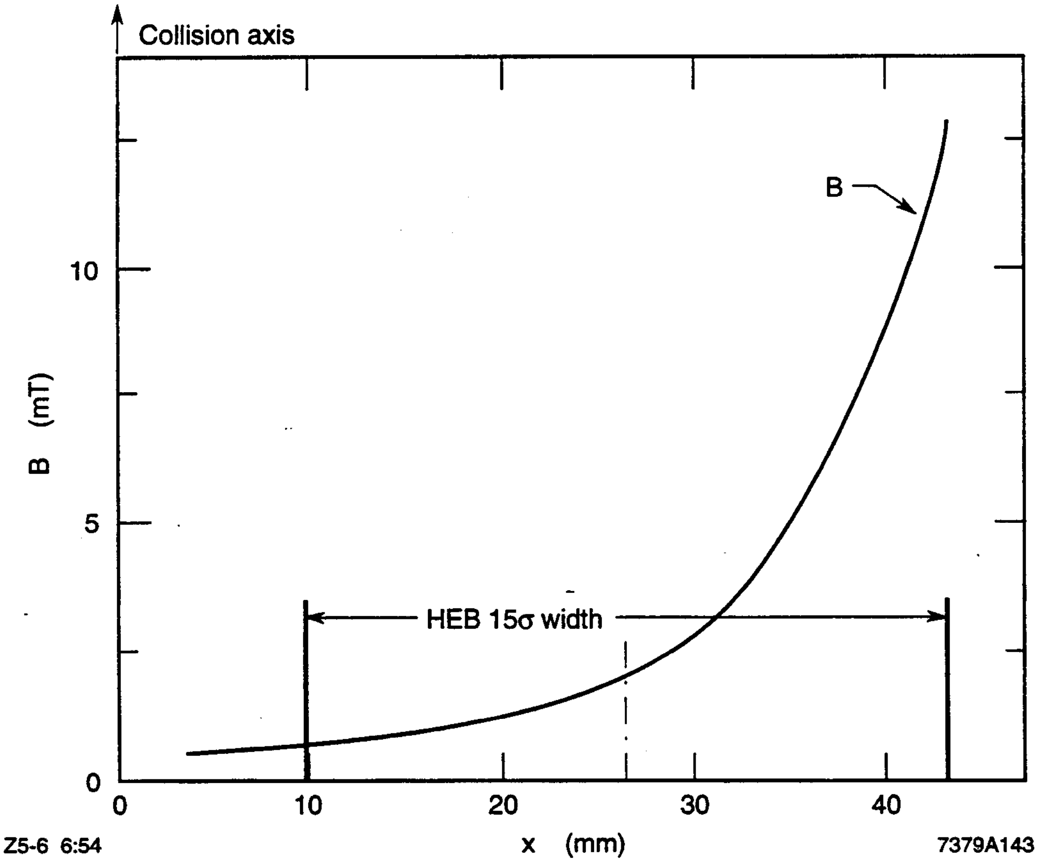

Fig. 5-25. Fringe field in the Q2 bypass channel at inboard end of magnet.

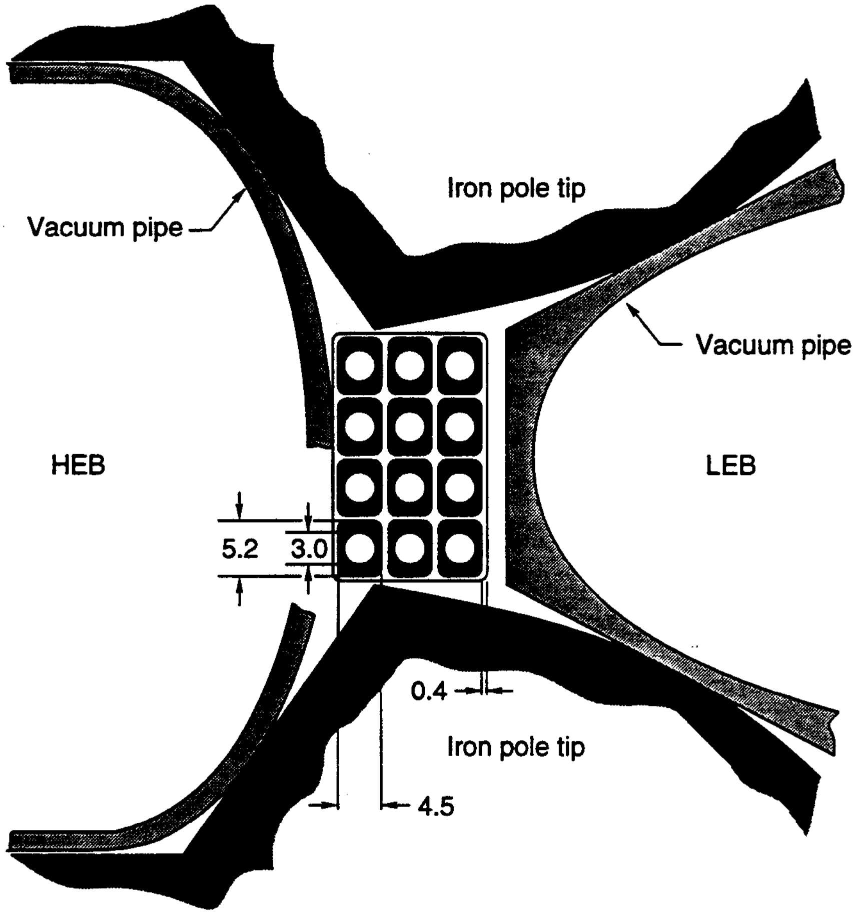

Fig. 5-26. Q2 current septum. Dimensions are in mm.

Table 5-13. Q2 septum thermal parameters.

Water pressure drop [psi]	75
Conductor length [cm]	70
Water velocity, v [m/s]	10
Water flow per conductor [cm^3/s]	70
Water temperature rise [°C]	5.54
Reynolds no., Re	65000
Prandtl no., Pr	2.8
Film coefficient, h^a [W/°C· cm^2]	5.28
Film ΔT [°C]	4.66

[a] $h = 0.023\, Re^{-0.2}\, Pr^{-2/3} v \rho c_p$.

0.25-in.-diameter cooling hole. These coils carry a current density of 1.05 kA/cm^2. This conductor size will also be used to complete the other halves of the two coils that include the septum (those coils that energize the left-hand poles in Fig. 5-23) by lap-splicing conductors at the ends of the magnet. The high-current-density septum will dissipate 19.5 kW and the other coils will add about 7.5 kW. Thus, total power dissipation amounts to 27 kW, which sets the total terminal voltage at about 20 V.

A perspective view of the Q2 magnet is shown in Fig. 5-27. The vacuum pipe is cut away to reveal the water-cooled synchrotron radiation septum mask (see Section 5.2.7.4). This specially machined vacuum pipe will be fabricated from GlidCop, as it must conduct 700 W of synchrotron radiation power from the bore of Q2 to water cooling tubes brazed to the outside. The y-shaped weldment will support the crotch mask and its associated ion pumps. By mounting the septum mask and its cooling supports with a false screen floor in the pump throat, the entire mask subassembly can be removed without disturbing the quadrupole or the y-shaped vacuum pipe. At full current, the septum bears a sideward magnetic force of 460 lb, repelling it from the quadrupole bore. By mounting the septum to a bridge rail along the HEB vacuum pipe, this load can be returned to the magnet iron.

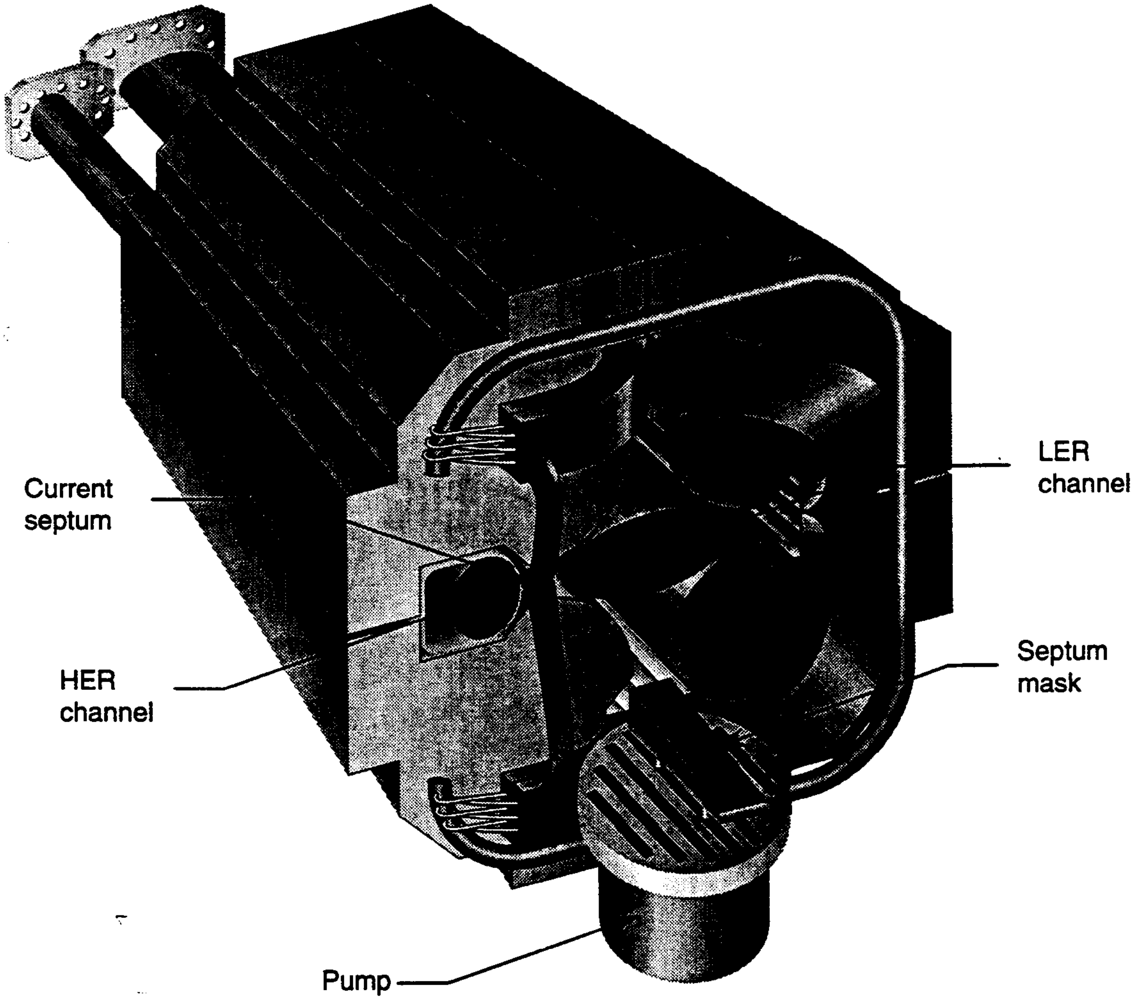

Fig. 5-27. Q2 and vacuum pipe assembly.

5.1.4 Magnetic Measurements

Five stations will be constructed for magnetic measurements, each having a computer. The computer will serve for data storage and data handling, and will also permit a comparison between the new magnetic measurements made on the refurbished PEP magnets and the original data taken at the time of their manufacture. A standardization procedure for each particular type of magnet will be stored in the computer so that it can be performed automatically prior to the commencement of measurements. The software will also prompt the operators to enter serial numbers, attach cables and water hoses, etc. Variables such as water flow, terminal voltage, and temperature rise will all become part of the database. This will ensure quality control and provide a complete pedigree for each magnet.

The choice of five stations will permit us to handle the five different types of magnets: HER dipoles, HER quadrupoles, LER dipoles, LER quadrupoles, and HER/LER sextupoles. This number of stations is perceived to be a minimum, based on the number of magnets to be tested and their different configurations. In particular, the HER dipoles present a challenge, owing to their 5.4-m length. The long coil required for these magnetic measurements will be unique. The LER bends are only 0.45 m long, so a relatively short coil can be used. Both HER and LER quadrupoles could be measured at a single station, but it is prudent to have a degree of redundancy and to avoid the possibility of bottlenecks. Because the HER and LER sextupoles are identical, the same station will be used, irrespective of the final destination of the magnet.

Magnetic measurements will be conducted using standard rotating-long-coil techniques. This method gives the integrated strength of the magnet, either $\int B \cdot dl$ or $\int G \cdot dl$, including end effects. In the case of quadrupoles, the rotating-coil measurement is a convenient way of determining the magnetic center, since a zero dipole signal occurs at this location. This measurement will provide a convenient check on the accuracy of the external fiducials built into the laminations at the time of stamping. Furthermore, the rotating-coil technique permits a determination of the higher-multipole content of the field, which is the true measure of magnet quality. Measurements will be conducted at different current settings, corresponding to the operating energies envisioned. This will provide a polynomial fit that will permit the magnets to be set accurately at any required field strength.

Magnetic tolerances for both the HER and the LER are similar to those for PEP and can be summarized as follows: The sum of all higher multipoles over the required beam-stay-clear region should be less than 0.1% of the main field component of the magnet over this same region.

5.1.5 Supports

Considerable thought has been given to the support and alignment of the two PEP-II rings. Because of the large mass of the PEP components, which are to be reused in the HER, the HER will be mounted below the LER. A side elevation of the standard HER and LER cells and a cross-sectional view of the PEP tunnel are shown in Figs 5-28 and 5-29, respectively. An artist's conception of the overall layout of the two rings is shown in Fig. 5-30.

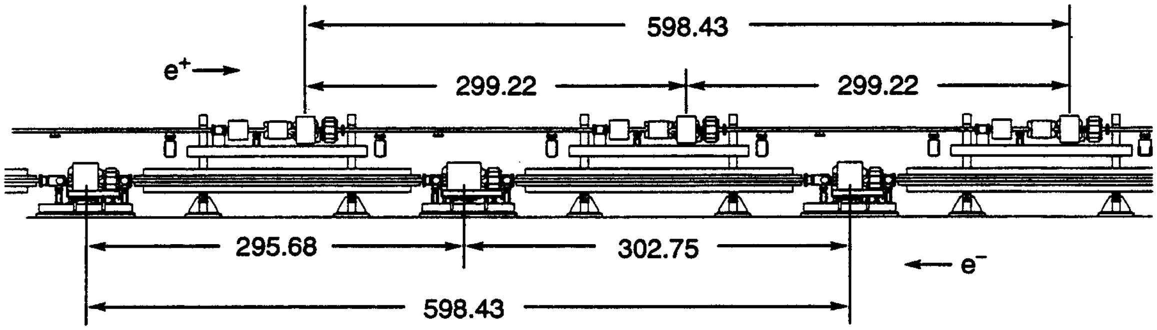

Fig. 5-28. Side elevation of standard HER and LER cells.

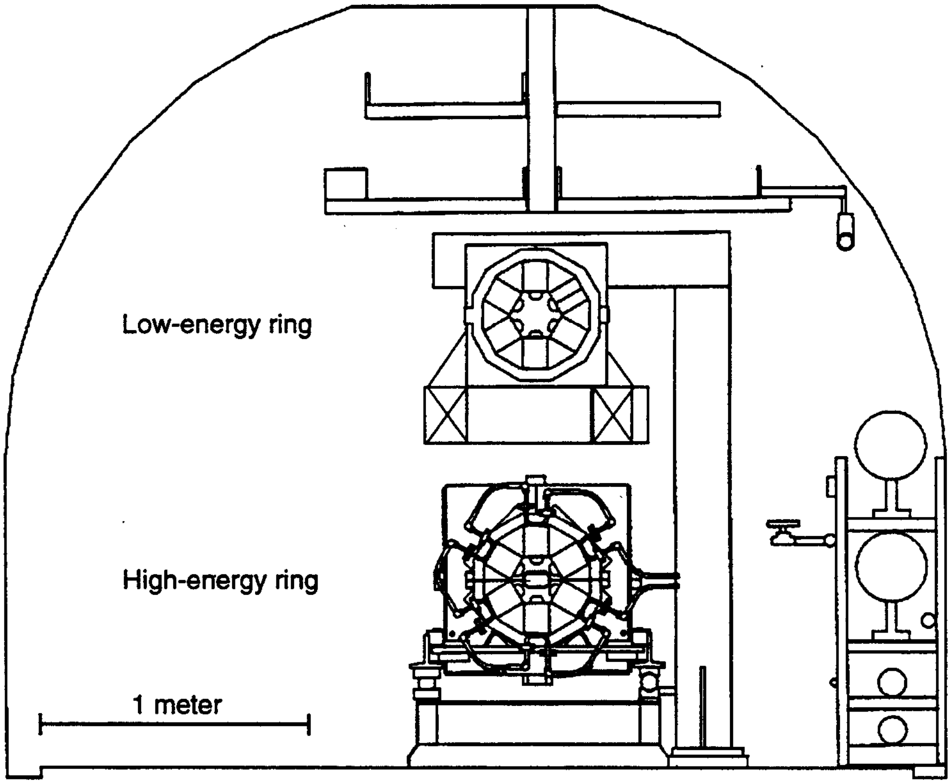

Fig. 5-29. Cross-sectional view of the PEP tunnel, showing the locations of utilities and the high- and low-energy rings.

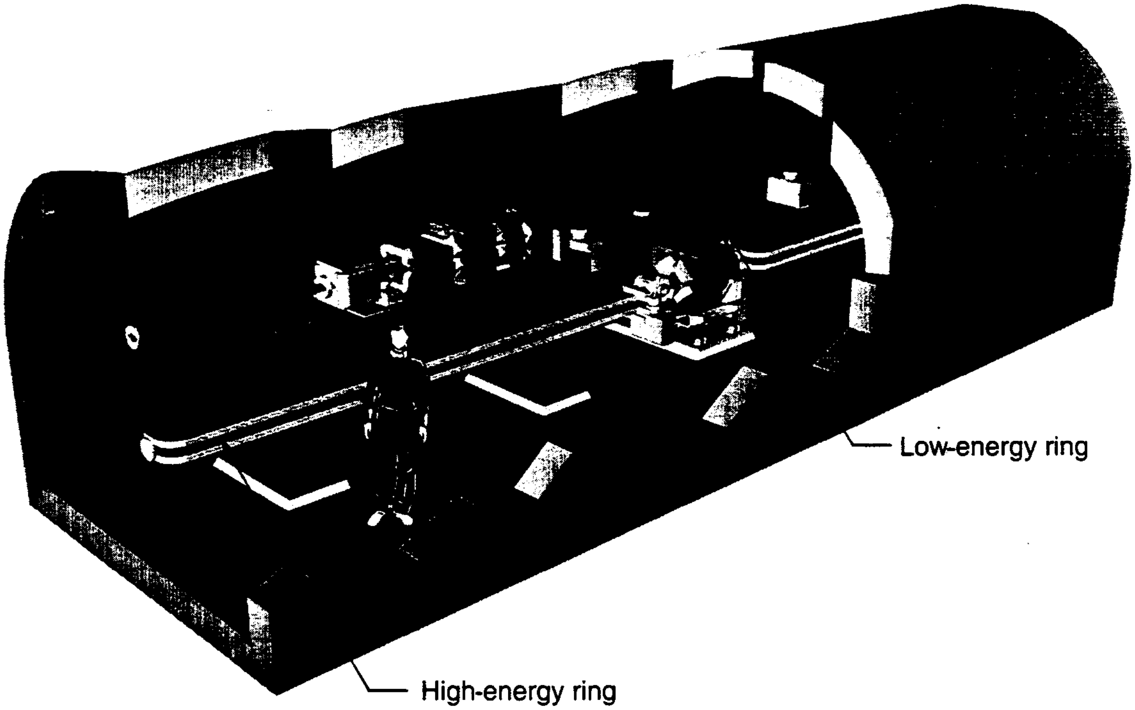

Fig. 5-30. Artist's conception of the high- and low-energy rings in the PEP tunnel

Once the PEP tunnel has been emptied, a rough alignment procedure (see Section 5.3) will locate the anchors for the lower legs of the support structures. These support structures will be placed close to the quarter-points of the HER dipole magnets, as was done in PEP, to maintain the alignment and minimize sag and twist of these long laminated magnets. The four feet necessary to adjust and maintain the alignment of the bending magnets will be mounted on these horizontal legs.

To facilitate installation, the quadrupole-sextupole pairs for the HER will be mounted on a rigid frame and aligned in a temperature-controlled facility using high-precision optical benches. In this manner, component-to-component misalignment is kept to a minimum. The vacuum spool piece for this section will be installed along with the vacuum chamber support, which must be capable of locating and fixing the associated beam position monitor with an accuracy of about 0.1 mm with respect to the magnetic center of the adjacent quadrupole. This requirement justifies our plan to prealign the individual components on a monolithic, stress-relieved frame that will avoid costly in-field alignment (which historically has proved to be more expensive and less accurate than prealignment in the laboratory)..

In the tunnel, precision alignment will locate the base support on which the frame for the quadrupole-sextupole pair rests. This base will have dowel pins identical to those at the alignment stations. Thus, when the magnetic components and base are taken to the tunnel, these pins will enable us to place the frame accurately. Although the base itself will be provided with adjustments having six degrees of freedom, we believe that it will be unnecessary to provide individual adjustment for all the quadrupole-sextupole frame components. The technique outlined here has been employed successfully at SLAC on several other projects, including PEP, the damping rings, the SLC arcs, and the final focus beamline.

After the main components of the HER ring are in place, the LER components will be installed above them. Once again, we will take the approach of using a raft or strong frame and prealigning the LER components in the laboratory. Because of their smaller size and lighter weight, we expect to be able to support and align the magnetic components of an entire half-cell (including a sextupole, a quadrupole, a bending magnet, and either a steering magnet or beam position monitor, together with the vacuum chamber and associated pumps) on one raft. As with the HER, the raft itself will be provided with six degrees of controlled freedom. We believe that it will be unnecessary to provide easy adjustments for individual raft components.

To facilitate alignment, the LER will be suspended above the HER such as to leave about an 8-in. component-free zone between the two rings for unobstructed line-of-sight. As discussed in Section 5.1.3, extensive ground-motion measurements were made at SLAC prior to building the SLC, because that accelerator was expected to be very sensitive to small, steady-state ground motions or noise. These measurements indicated which site-wide excitation frequencies are a problem. Magnet supports will be designed to avoid unwanted resonances.

Because the two rings are independently supported, at different heights in the tunnel, it is clear that changes in temperature within the tunnel can cause relative motion between them. Fortunately, time constants for such motion will be slow, of the order of hours, and steering corrections can be made in the IR to compensate for the resultant beam drifts.

5.2 VACUUM SYSTEM

The vacuum system of the PEP-II collider presents a technical challenge beyond that of any existing electron-positron collider. Each subsystem must meet demanding design criteria to satisfy the overall system requirements. These subsystems for the high-energy (electron) and low-energy (positron) rings (HER and LER, respectively) include vacuum chambers, pumps, cooling, and special components, such as bellows, beam position monitors (BPMs), and valves.

For PEP-II, the HER and LER will have circulating beam currents of 0.99 and 2.14 A, respectively, to reach the design luminosity of 3×10^{33} cm^{-2} s^{-1}. We refer to these as the *nominal* currents. The nominal beam currents are at least an order of magnitude beyond the typical values for today's colliders and, as such, present an appreciable challenge to the vacuum system designer. To provide for possible upgrades, and for luminosity "breathing room," we also specify a *maximum allowable* current in each ring of 3 A. Because the vacuum system is generally difficult to upgrade after the collider is operating, we have chosen to design for the 3-A capability from the outset.

components. The technique outlined here has been employed successfully at SLAC on several other projects, including PEP, the damping rings, the SLC arcs, and the final focus beamline.

After the main components of the HER ring are in place, the LER components will be installed above them. Once again, we will take the approach of using a raft or strong frame and prealigning the LER components in the laboratory. Because of their smaller size and lighter weight, we expect to be able to support and align the magnetic components of an entire half-cell (including a sextupole, a quadrupole, a bending magnet, and either a steering magnet or beam position monitor, together with the vacuum chamber and associated pumps) on one raft. As with the HER, the raft itself will be provided with six degrees of controlled freedom. We believe that it will be unnecessary to provide easy adjustments for individual raft components.

To facilitate alignment, the LER will be suspended above the HER such as to leave about an 8-in. component-free zone between the two rings for unobstructed line-of-sight. As discussed in Section 5.1.3, extensive ground-motion measurements were made at SLAC prior to building the SLC, because that accelerator was expected to be very sensitive to small, steady-state ground motions or noise. These measurements indicated which site-wide excitation frequencies are a problem. Magnet supports will be designed to avoid unwanted resonances.

Because the two rings are independently supported, at different heights in the tunnel, it is clear that changes in temperature within the tunnel can cause relative motion between them. Fortunately, time constants for such motion will be slow, of the order of hours, and steering corrections can be made in the IR to compensate for the resultant beam drifts.

5.2 VACUUM SYSTEM

The vacuum system of the PEP-II collider presents a technical challenge beyond that of any existing electron-positron collider. Each subsystem must meet demanding design criteria to satisfy the overall system requirements. These subsystems for the high-energy (electron) and low-energy (positron) rings (HER and LER, respectively) include vacuum chambers, pumps, cooling, and special components, such as bellows, beam position monitors (BPMs), and valves.

For PEP-II, the HER and LER will have circulating beam currents of 0.99 and 2.14 A, respectively, to reach the design luminosity of 3×10^{33} cm^{-2} s^{-1}. We refer to these as the *nominal* currents. The nominal beam currents are at least an order of magnitude beyond the typical values for today's colliders and, as such, present an appreciable challenge to the vacuum system designer. To provide for possible upgrades, and for luminosity "breathing room," we also specify a *maximum allowable* current in each ring of 3 A. Because the vacuum system is generally difficult to upgrade after the collider is operating, we have chosen to design for the 3-A capability from the outset.

5.2.1 General Issues and System Requirements

A well-designed vacuum system is the key to providing a suitable beam environment. In particular, the chamber design should have the following attributes:

- Adequate beam-stay-clear aperture for injection and for stored-beam lifetime
- Low impedance to avoid beam instabilities and to minimize higher-order-mode (HOM) power dissipation
- Sufficient pumping speed to maintain a low pressure in the face of substantial synchrotron-radiation-induced gas desorption
- Sufficient cooling to safely dissipate the heat load associated with both synchrotron radiation and HOM losses
- Capability to shield external ring components from synchrotron radiation

Most of these requirements are fairly obvious and do not differ from those of existing colliders. The main distinction in the case of PEP-II is associated with the required beam currents, which are much higher than those in present-day colliders.

Depending on the magnitude of the dynamic gas load due to photodesorption, the chamber could have a conventional elliptical or octagonal shape, or it could exploit differential pumping via an antechamber arrangement. In the PEP-II parameter regime, use of a conventional chamber shape is acceptable, provided that the material is chosen to have a low photodesorption coefficient. If the chamber material is suitably chosen, the chamber walls will also serve as the primary shield for the synchrotron radiation that would otherwise damage magnets and other beamline components. Basically, this consideration implies the use of a high-*Z* material such as copper or stainless steel, rather than the more easily fabricated aluminum. (If aluminum were chosen, the shielding would have to be provided by an additional layer of material—for example, lead—to absorb the radiation passing through the chamber walls. While this is possible, it is an undesirable complication.)

Included as integral parts of the chamber are several special sections and components, such as shape transitions, pumping ports, bellows, and BPMs. The high peak and average beam currents in PEP-II demand that the electromagnetic environment presented by the vacuum chamber and its special components satisfy a strict impedance budget for the ring. It is known that the present PEP vacuum chamber would provide a sufficiently low broadband impedance ($|Z/n| \approx 1\ \Omega$) to be acceptable for the PEP-II HER [Rivkin, 1987; Zisman, 1990b]. Thus, we are assured that standard care in the design of the vacuum chamber will permit us to reach our impedance goal.

The pumping system of the collider must maintain the specified operating pressure under conditions of a large dynamic photodesorption gas load caused by the intense synchrotron radiation bombardment of the chamber walls. (In high-energy, high-current electron rings, thermal outgassing is generally a small contribution to the gas load that mainly determines the base pressure in the absence of beam.) In addition to handling the gas load during routine operation, the pumping must also be sufficient to allow for rapid initial commissioning (cleaning) of the vacuum chamber. The *system requirements* for the vacuum system during collider operation are as follows:

- ≤10 nTorr in the arcs
- ~3 nTorr in the straight sections
- ~1 nTorr in the two half straight sections upstream of the detector
- ~0.5 nTorr base pressure due to thermal outgassing under no-beam (static load) conditions

(Note that pressure requirements are quoted here as N_2-equivalent values.) We have generally designed the vacuum systems to reach these goals even at the maximum allowable beam current of 3 A. Thus, at the nominal operating currents, we expect to do better than the requirements listed above. In this sense, the design is conservative and should operate very reliably. Clearly, the additional pumping capability will be of great benefit in reducing the conditioning time for the system.

An electron beam circulating in a storage ring subjects the vacuum chamber walls to copious synchrotron radiation. As the incident area of the radiation fan is small, the associated thermal flux is generally high enough to require considerable cooling of the chamber wall. The chamber cooling system is designed to remove the heat safely, despite high power densities. As is typical, cooling is accomplished by water flowing in channels outside the chamber. In addition to ensuring the mechanical stability of the chamber under thermal loads that could reach 10 MW in the HER, maintaining the chamber wall at a relatively low temperature serves to reduce the gas load due to thermal desorption.

5.2.2 Determination of Vacuum Chamber Aperture

The size requirements of the beam chambers are determined by the beam emittances and energy spreads and by the optical functions of the HER and LER lattices. To ensure adequate quantum lifetime, the chamber was designed to accommodate the *uncoupled* horizontal emittance and the *fully coupled* vertical emittance. It is also desirable to keep the cross section of the chamber constant throughout the arc sections to minimize the impedance contributions from shape transitions. Consequently, we considered the maximum values of the beta functions in determining the chamber sizes.

For determining the required chamber aperture, we took the uncoupled emittance value for each ring to be at least twice the value required for the nominal operating configuration. This will provide considerable flexibility to adjust the ring parameters as dictated by operational needs. Thus, the HER chamber was designed for 100 nm·rad uncoupled horizontal emittance, and the LER chamber was designed for 200 nm·rad. In the absence of wigglers, the relative energy spread of the beam in the HER should be close to its natural value of 6.1×10^{-4}. To be conservative, we took a value of 1×10^{-3} for estimating the required chamber size. For the LER, we envision that the natural energy spread from the arcs will be increased by means of wigglers to a value closer to 1×10^{-3}, which we again adopted as a design specification for evaluating aperture requirements. Since the HER optics are similar to PEP, the closed-orbit allowances were taken to be the same as those adopted for the original PEP design; these values were also assumed for the LER.

Emittance and beta function values used to evaluate the required apertures for the HER and LER are summarized in Table 5-14.

The horizontal beam-stay-clear half-aperture in the arcs is evaluated as

$$\mathrm{BSC}_x = 10\sqrt{\varepsilon_{x0}\hat{\beta}_x + \hat{D}^2\left(\frac{\sigma_E}{E}\right)^2} + \mathrm{COD}_x \tag{5-6}$$

Similarly, the vertical beam-stay-clear aperture in the arcs is

$$\mathrm{BSC}_y = 10\sqrt{\varepsilon_{y0}\hat{\beta}_y} + \mathrm{COD}_y \tag{5-7}$$

Using the values in Table 5-14, and including allowances for fabrication and mechanical positioning errors, we obtain the minimum chamber (inner) half-apertures:

HER: $\mathrm{BSC}_x \times \mathrm{BSC}_y = 45$ mm × 25 mm

LER: $\mathrm{BSC}_x \times \mathrm{BSC}_y = 45$ mm × 25 mm

The HER chamber dimensions can be accommodated by the present PEP magnets.

Table 5-14. Parameters used to evaluate vacuum chamber dimensions for the high- and low-energy ring arcs.

Beam parameter	HER	LER
Max. uncoupled horizontal emittance, ε_{x0} [nm·rad]	100	200
Max. fully coupled vertical emittance, ε_{y0} [nm·rad]	50	100
Max. horizontal beta in arcs, $\hat{\beta}_x$ [m]	26	26
Max. vertical beta in arcs, $\hat{\beta}_y$ [m]	28	26
Max. dispersion, $\hat{D}$ [m]	1.8	1.1
Max. energy spread, σ_E/E	1×10^{-3}	1×10^{-3}
Horizontal closed-orbit allowance, COD_x [mm]	10	10
Vertical closed-orbit allowance, COD_y [mm]	5	5

5.2.3 Synchrotron Radiation and Vacuum

As mentioned earlier, two design issues follow from the copious production of synchrotron radiation in a high-intensity storage ring: (i) heating of the vacuum chamber walls owing to the high thermal flux and (ii) radiation-induced gas desorption (both photodesorption and thermal desorption). In this section, we quantify these effects and evaluate their impact on collider performance. As we shall see, despite the difficulties associated with the high beam currents in the PEP-II storage rings, handling the large synchrotron radiation power is amenable to standard engineering solutions in a beam chamber of elliptical or octagonal cross section, without requiring a more exotic approach based on an antechamber design.

5.2.3.1 Wall Heating. At the design luminosity of 3×10^{33} cm^{-2} s^{-1}, each ring will contain a beam current more than an order of magnitude higher than that typical in existing high-energy storage rings; the associated heat load is, therefore, quite high. The technical difficulty lies not in removing the total synchrotron radiation power per se, but rather in handling the concentrated linear thermal flux. Thus, contrary to intuition, a small-circumference ring is more difficult to cool and pump than a large ring. (If a very small circumference were chosen for the LER, management of the high linear thermal flux would be considerably more difficult than in the HER, despite the fact that the total synchrotron radiation power would be much lower in the LER.) By adopting a design in which the LER has a circumference equal to that of the HER, such concerns are eliminated (except for the damping wiggler regions, which are discussed in Section 5.2.6, below).

To estimate the heat load, we start from the well-known expression [Sands, 1970] for the synchrotron radiation power (in kW) emitted by an electron beam in uniform circular motion:

$$P_{\mathrm{SR}} = \frac{88.5\, E^4 I}{\rho} \tag{5-8}$$

where E is the total energy (in GeV), I is the total beam current (in A), and ρ is the bend radius of the dipoles (in meters). The linear power density (in W/cm) radiated along the circumferential path length is given by

$$P_L = \frac{10 P_{\mathrm{SR}}}{2\pi\rho} = \frac{885\, E^4 I}{2\pi\rho^2} \tag{5-9}$$

For a 9-GeV beam in the HER ($\rho = 165$ m) at the maximum allowable current of 3 A, we find from Eq. 5-9 a linear power density of $P_L = 102$ W/cm. At the nominal operating current of 0.99 A (corresponding to the design luminosity of 3×10^{33} cm^{-2} s^{-1}), the linear power density is reduced to 34 W/cm. In reality, the arcs are not exactly circular in either ring—the dipoles in each cell are connected by short straight sections a few meters in length. These straight regions tend to spread out the radiation flux. Consequently, Eq. 5-9 gives the maximum value of the linear power density anywhere in the arcs.

The peak power density in the LER arcs occurs in the straight section downstream from the bending magnet, where the effect of geometry reduces the power density more than one would calculate using Eq. 5-9. For the 3.1-GeV beam in the LER ($\rho = 13.75$ m), at the maximum current of 3 A, the linear power density is 45.7 W/cm. At the nominal operating current of 2.14 A, the linear power density is reduced to 32.6 W/cm.

The vertical (half)-angular spread (in radians) of the synchrotron radiation fan containing ~85% of the radiation is given approximately by

$$\psi \approx \frac{m_0c^2}{E} = \frac{1}{\gamma} \tag{5-10}$$

For a 9-GeV beam, $\psi = 0.06$ mrad, while for the 3.1-GeV LER beam, $\psi = 0.17$ mrad. Although it is not strictly true (see Section 5.2.6), we assume the power to be uniformly distributed over this angular extent. Including the finite size and angular divergence of the electron beam, the height of the vertical band illuminated by the synchrotron radiation fan is

$$h = 2\left[\sigma_y^2 + d^2\left(\sigma_{y'}^2 + \psi^2\right)\right]^{1/2} \tag{5-11}$$

where σ_y is the rms beam height, $\sigma_{y'}$ is the rms angular spread, and d is the tangential distance from the beam orbit to the chamber wall. The value for d can be calculated from the geometry shown in Fig. 5-31, where $w/2$ is the transverse distance from the beam orbit to the outer wall of the vacuum chamber. In bend regions,

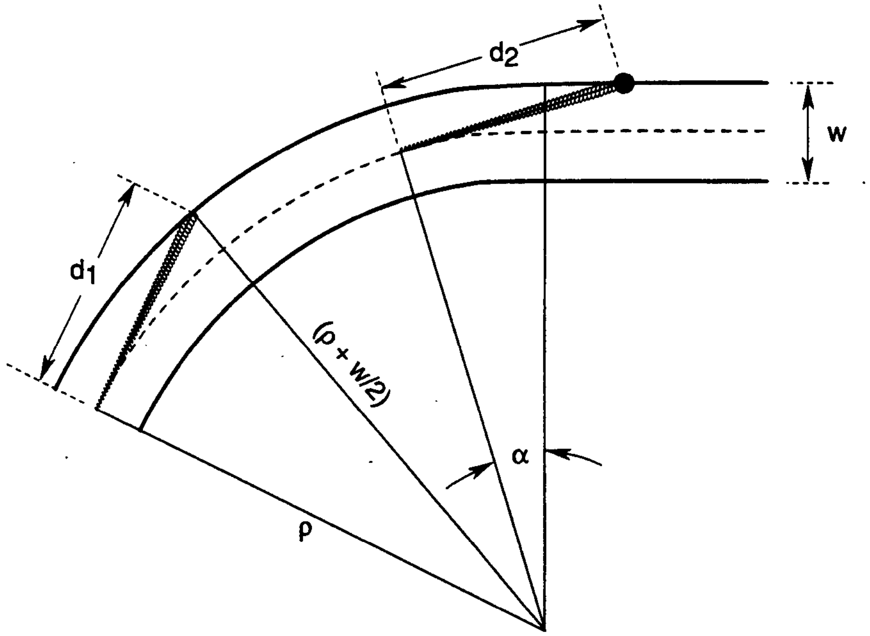

Fig. 5-31. Geometry of the synchrotron radiation fan hitting the vacuum chamber wall in curved and straight pipe sections (not to scale).

$$d_1 = \sqrt{\left(\rho + \frac{w}{2}\right)^2 - \rho^2} \qquad (5\text{-}12)$$

while in the straight regions between bend fields,

$$d_2 = \frac{\left(\frac{w}{2}\right)}{\sin\alpha} + \rho\tan\left(\frac{\alpha}{2}\right) \qquad (5\text{-}13)$$

For the HER, with a chamber half-width of 4.5 cm and a 165-m bending radius, we find that $d_{1,\max} = 3.85$ m, with a maximum angle of incidence given by $\alpha = d_1/\rho = 23$ mrad.

To be conservative in estimating the power density, we have ignored the contribution to the height of the synchrotron radiation fan from the finite beam emittance; that is, we take $\sigma_y = \sigma_{y'} = 0$ in Eq. 5-11, and we assume that all the radiation falls between $\pm\psi$. Thus, the minimum height of the illuminated strip is $h = 2\psi d = 0.44$ mm. The corresponding maximum thermal flux density in the HER, at a beam current of 3 A, is then $P_A = P_L/h = 2.3$ kW/cm^2. Tables 5-15a and 5-15b summarize both the nominal-current and maximum-current cases for the LER and HER, respectively, compared with values from PEP.

Table 5-15a. Comparison of radiation loads in PEP and the PEP-II LER. For PEP an aluminum chamber is used; the PEP-II estimates assume a copper chamber and are computed as described by Alexandrov et al. [1990].

		PEP-II	
Parameter	PEP	LER nominal current	LER maximum current
Magnetic radius [m]	165.00	13.75	13.75
Bending magnet field [T]	0.3033	0.7544	0.7544
Energy [GeV]	15.00	3.11	3.11
Current [mA]	200	2140	3000
Total synchrotron power [kW]	5,436	1,290	1,810
Peak chamber wall linear flux [W/cm]	52	33	46
Beam divergence, 2θ [mrad]	0.07	0.33	0.33
Min. tangential distance, d [m]	4.06	2.06	2.06
Max. angle of incidence, α [mrad]	24.6	32.7	32.7
Minimum beam height [mm]	0.28	0.68	0.68
Wall heat load [kW/cm^2]	1.89	0.48	0.67

Table 5-15b. Comparison of radiation loads in PEP and the PEP-II HER. For PEP an aluminum chamber is used; the PEP-II estimates assume a copper chamber.

		PEP-II	
Parameter	PEP	HER nominal current	HER maximum current
Magnetic radius [m]	165.0	165.0	165.0
Bending magnet field [T]	0.3033	0.1820	0.1820
Energy [GeV]	15.00	9.00	9.00
Current [mA]	200	1000	3000
Total synchrotron power [kW]	5,436	3,519	10,557
Chamber wall linear flux [W/cm]	52.4	33.9	101.8
Beam divergence, 2θ [mrad]	0.07	0.11	0.11
Min. tangential distance, d [m]	4.06	3.85	3.85
Max. angle of incidence, α [mrad]	24.6	23.4	23.4
Minimum beam height [mm]	0.28	0.44	0.44
Wall heat load [kW/cm^2]	1.89	0.77	2.31

In addition to the synchrotron radiation heating, we must also consider the heat loads from HOM losses. These were estimated in Section 4.3.1.6 to be 70 and 225 kW for the HER and LER, respectively. For safety, we have doubled these estimates to account for presently unidentified impedances. This power will be distributed roughly uniformly around the ring, leading to an additional 0.6-W/cm thermal load for the HER and 2 W/cm for the LER. For the LER, this value is only about 4% of the peak synchrotron radiation load in the arcs, so HOM heating represents only a small additional burden for the cooling subsystem. In the HER, the additional heat load from HOM losses is only about 1% of that from synchrotron radiation.

5.2.3.2 Gas Desorption. The gas load in electron storage rings arises from two processes: thermal outgassing and synchrotron-radiation-induced photodesorption. Thermal outgassing is common to all vacuum systems and occurs in the absence of synchrotron radiation; that is, it contributes mainly to the base pressure of a ring in the absence of circulating beam. In all high-energy electron storage rings, thermal outgassing is negligible when compared with the dynamic gas load from photodesorption. Thus, the gas load due to synchrotron radiation actually determines the operating pressure of the ring.

To estimate the desorption rate, we follow the approach of Gröbner et al. [1983]. After taking the spectrum of the synchrotron radiation photons into account, we can express the photon flux in the spectral interval $(0, x)$ in the form

$$\dot{N}(x) = \frac{\sqrt{3}\, r_e}{e\hbar c} F(x)\, E\, I \tag{5-14}$$

where

$$x = \frac{\varepsilon}{\varepsilon_{\text{crit}}} = \frac{\varepsilon}{\left(\frac{3\hbar c}{2}\right)\left(\frac{\gamma^3}{\rho}\right)} \tag{5-15}$$

with ε being the photon energy and $\varepsilon_{\text{crit}}$ being the critical energy of the radiation in the dipoles. In practical units,

$$\varepsilon_{\text{crit}} = 2.218 \frac{E^3}{\rho} \ \text{[keV]} \tag{5-16}$$

$F(x)$ is the integral over the modified Bessel function:

$$F(x) = \int_0^x \int_u^\infty K_{5/3}(y)\, dy\, du \tag{5-17}$$

For large values of x, $F(x) \to 5.23$. After rearranging terms and inserting appropriate values for the constants, we obtain a photon production rate of

$$\dot{N} = 8.08 \times 10^{20}\, E\, I \ \text{[photons/s]} \tag{5-18}$$

where E is in GeV and I is in A.

At the design current of 0.99 A, the synchrotron radiation load in the HER is 7.3×10^{21} photons per second, or a maximum of 7.1×10^{18} photons/s/m. As the minimum height of the synchrotron radiation fan in the HER is only 0.44 mm, the maximum photon flux on the walls is 1.6×10^{18} photons/cm^2/s. By contrast, the maximum photon flux on the walls of the LER chamber is 7.35×10^{17} photons/cm^2/s. For later use in computing the photon dose on the chamber walls, we note that in the HER, 1 A·hr corresponds to 2.5×10^{22} photons/m.

Gas molecules are desorbed from the walls in proportion to the photon flux; that is, the number of molecules produced per incident photon is

$$\dot{N}_{\text{Mol}} = 8.08 \times 10^{20}\, E\, I\, \eta \ \text{[molecules/s]} \tag{5-19}$$

The ideal gas law relates the number of molecules to a gas load in Torr·L by a conversion factor of 3×10^{-20} Torr·L/molecule. In these units, the effective gas load due to photodesorption is found to be

$$Q_{\text{gas}} = 24.2\ E\, I\, \eta \ \text{[Torr·L/s]} \tag{5-20}$$

The photodesorption coefficient η is a property of the chamber that depends on several factors:

- Chamber material
- Material fabrication and preparation
- Amount of prior exposure to radiation
- Photon angle of incidence
- Photon energy

In light of these complexities, it seems better to regard η as an effective engineering value that accounts for the differential illumination of the chamber walls by both direct (beam-produced) and diffusely scattered (secondary) photons, rather than considering the photodesorption coefficient to be a fundamental material property. Using a single value of η in Eq. 5-20 yields only a rough estimate of the actual dynamic gas load but one that is nonetheless useful in setting the scale of the engineering task, as well as in choosing the chamber material.

5.2.3.3 Choice of Chamber Material. Experimental measurements [Gröbner et al., 1983; Foerster et al., 1990; Ueda et al., 1990; Mathewson et al., 1990] for well-exposed samples of aluminum, stainless steel, and oxygen-free, high-conductivity (OFHC) copper indicate minimum values of η ranging from less than 2×10^{-6} for copper and stainless steel up to 2×10^{-5} for aluminum. Although the gas-scattering lifetimes in storage rings with lower critical photon energies than PEP-II suggest that aluminum chambers may eventually develop an effective $\eta \approx 10^{-6}$, we believe a more reliable design procedure is to adopt copper or stainless steel as the chamber material, despite their higher cost per kilogram. Because the data of Ueda et al. indicate that clean, machined, oxygen-free copper can attain $\eta = 2 \times 10^{-6}$, we have chosen this value as the design basis. Such a low photodesorption coefficient allows us to design the PEP-II vacuum chamber with a conventional elliptical or octagonal shape, instead of being driven to adopt an antechamber design that is more difficult and expensive to fabricate. The apparent cost disadvantage of copper or stainless steel vis-à-vis aluminum is more than offset by the relative simplicity of the chamber shape, by the reduction in the amount of pumping needed, and by the shortening of the vacuum commissioning time.

As shown below, copper and stainless steel also have the considerable advantage of being self-shielding and thus can protect the magnets and other hardware from radiation damage caused by the hard component of the synchrotron radiation. The need for lead shielding, which would be required to accompany an aluminum chamber, is completely eliminated. In that the chamber walls are subjected to very high thermal loads, copper, with its excellent thermal conductivity, appears to be the preferred material, despite the paucity of experience in building large copper vacuum chambers.

For a copper chamber with a desorption coefficient of $\eta = 2 \times 10^{-6}$, the dynamic gas load is

$$Q_{\text{gas}} = 4.84 \times 10^{-5}\, E\, I \quad [\text{Torr}\cdot\text{L/s}] \tag{5-21}$$

In Tables 5-16a and 5-16b, we use Eq. 5-21 to estimate the gas loads in the low- and high-energy rings. Maintaining a pressure of 10 nTorr in the LER requires a total pumping speed of 96,000 L/s at the maximum allowable current of 3 A. To put this requirement into perspective, we note that it is less than one-tenth of the pumping speed (per meter of ring circumference) installed on the ALS ring at LBL [LBL, 1986].

5.2.3.4 Evaluation of Gas Load Profile. To proceed beyond the estimates of the previous section to an engineering design of the vacuum system, it is necessary to specify the actual distribution of radiation along the arc, $\dot{N}(s)$, taking into account the presence of short straight sections between the dipoles. Following the prescription of Alexandrov et al. [1990], we computed the power distributions shown in Figs. 5-32a and 5-32b for the HER and LER, respectively.

Naively, one might think to compute the distributed gas load in the arcs by applying Eq. 5-20 directly to the profiles given in Fig. 5-32, with the adopted value of η. This procedure would, however, neglect the strong variation in η with material exposure. From a typical set of data, such as that reproduced in Fig. 5-33 [Foerster et al., 1990], we observe that, for large exposures, η tends to follow a power-law dependence on dose; that is,

$$\eta \propto (It + t_0)^{-p} \qquad (5\text{-}22)$$

Table 5-16a. Comparison of vacuum loads in PEP and the PEP-II LER.

		PEP-II	
Parameter	PEP	LER nominal current	LER maximum current
Gas load [Torr·L/s/mA]	5.5×10^{-6}	1.6×10^{-7}	1.6×10^{-7}
Total photon gas load [Torr·L/s]	1.1×10^{-3}	3.4×10^{-4}	4.8×10^{-4}
Assumed desorption coefficient, η	1.5×10^{-5}	2.0×10^{-6}	2.0×10^{-6}
Photon gas load [Torr·L/m/s]	1.1×10^{-6}	2.4×10^{-7}	3.3×10^{-7}
Operating pressure required [nTorr]	10	10	10
Thermal desorption coef. [Torr·L/s/cm^2]	1.0×10^{-11}	1.0×10^{-11}	1.0×10^{-11}
Total perimeter of ring [m]	2200	2200	2200
Calculated thermal load [Torr·L/m/s]	2.6×10^{-8}	2.4×10^{-8}	2.4×10^{-8}
Total calculated thermal load [Torr·L/s]	5.8×10^{-5}	5.3×10^{-5}	5.3×10^{-5}
Total gas load [Torr·L/s]	1.2×10^{-3}	3.9×10^{-4}	5.3×10^{-4}

Table 5-16b. Comparison of vacuum loads in PEP and the PEP-II HER.

Parameter	PEP	PEP-II HER nominal current	PEP-II HER maximum current
Gas load [Torr·L/s/mA]	5.5×10^{-6}	4.3×10^{-7}	4.3×10^{-7}
Total photon gas load [Torr·L/s]	1.1×10^{-3}	4.3×10^{-4}	1.3×10^{-3}
Assumed desorption coefficient, η	1.5×10^{-5}	2.0×10^{-6}	2.0×10^{-6}
Photon gas load [Torr·L/m/s]	1.1×10^{-6}	4.1×10^{-7}	1.2×10^{-6}
Operating pressure required [nTorr]	10	5	10
Thermal desorption coef. [Torr·L/s/cm^2]	1.0×10^{-11}	1.0×10^{-11}	1.0×10^{-11}
Total perimeter of ring [m]	2200	2200	2200
Calculated thermal load [Torr·L/m/s]	2.6×10^{-8}	2.5×10^{-8}	2.5×10^{-8}
Total calculated thermal load [Torr·L/s]	5.8×10^{-5}	5.5×10^{-5}	5.5×10^{-5}
Total gas load [Torr·L/s]	1.2×10^{-3}	4.9×10^{-4}	1.4×10^{-3}

where I is the beam current, t is the exposure time, and p is between 0.4 and 0.7 (depending on choice of material and preparation). The constant t_0 is chosen to yield the correct initial value of η. Assuming that $p = 0.6$ for copper, we can compute a local value of $\eta(s)$ along the beamline. Then the gas load at position s is given by a generalization of Eq. 5-20:

$$Q_{\text{gas}}(s) = \eta(s)\dot{N}(s) \tag{5-23}$$

The effect of the differential exposure of the chamber is to level the gas load along the beamline and thus to require more pumping capacity than would be needed if Q_{gas} were a constant multiple of the photon flux. By assuming that the value of η is 2×10^{-6} where $\dot{N}(s)$ assumes its *maximum* value, we compute the gas load along a half-cell of the arc as shown in Fig. 5-34. This gas profile becomes a system specification for the vacuum engineer.

Using the data of Ueda et al. [1990], we have estimated that for copper with an initial desorption rate of 10^{-3} molecules/photon, the sections of the chamber will reach $\eta \approx 2 \times 10^{-6}$ after a photon exposure of about 100 A·hr. Based on the pumping scheme described in Section 5.2.4, the vacuum-conditioning scenario can be computed as a function of the initial photodesorption rate. Such calculations are displayed in Fig. 5-35.

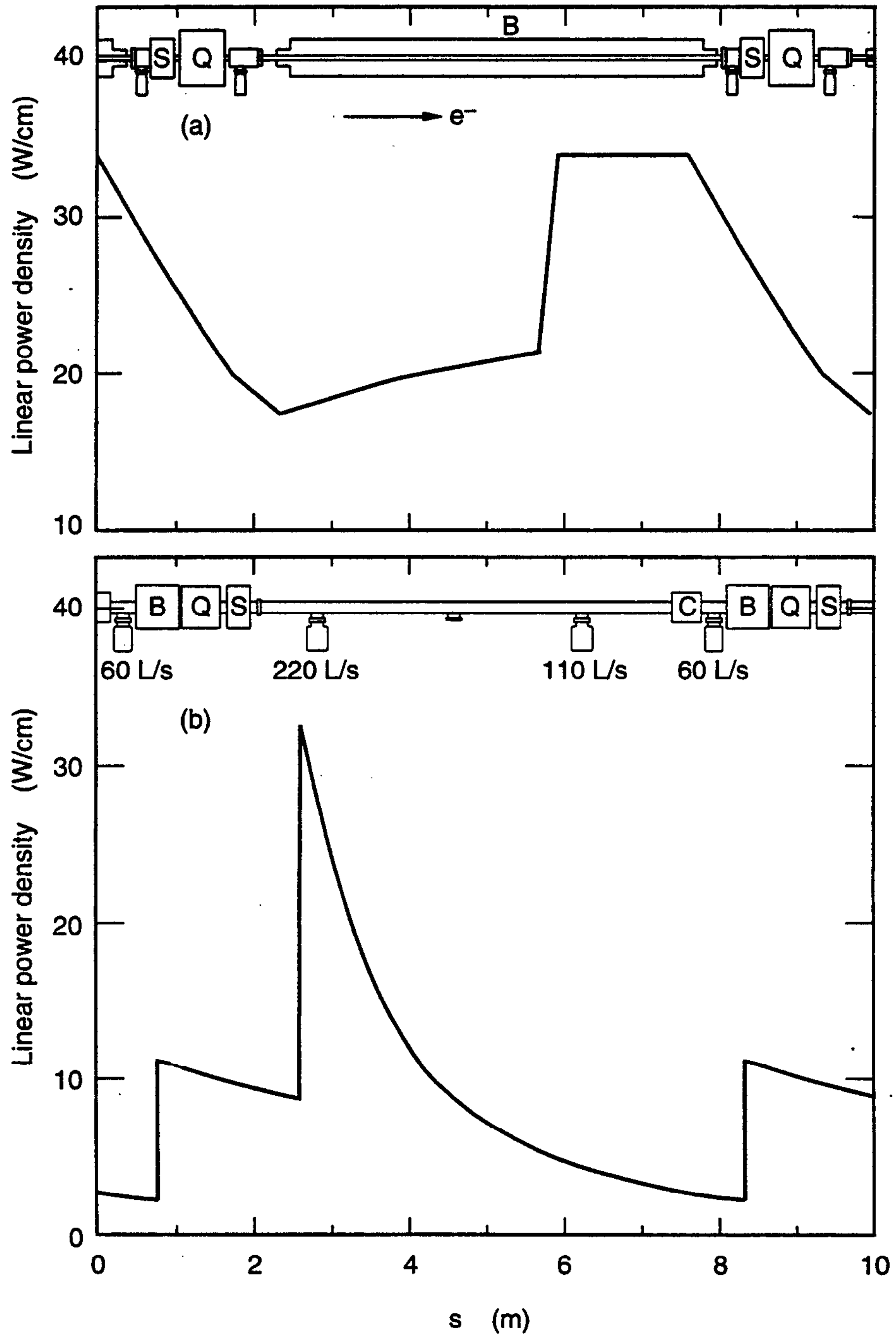

Fig. 5-32. (a) Radiation power distribution along a half-cell of the HER arc at the design current of 0.99 A. (b) Radiation power distribution along a half-cell of the LER arc at the design current of 2.14 A.

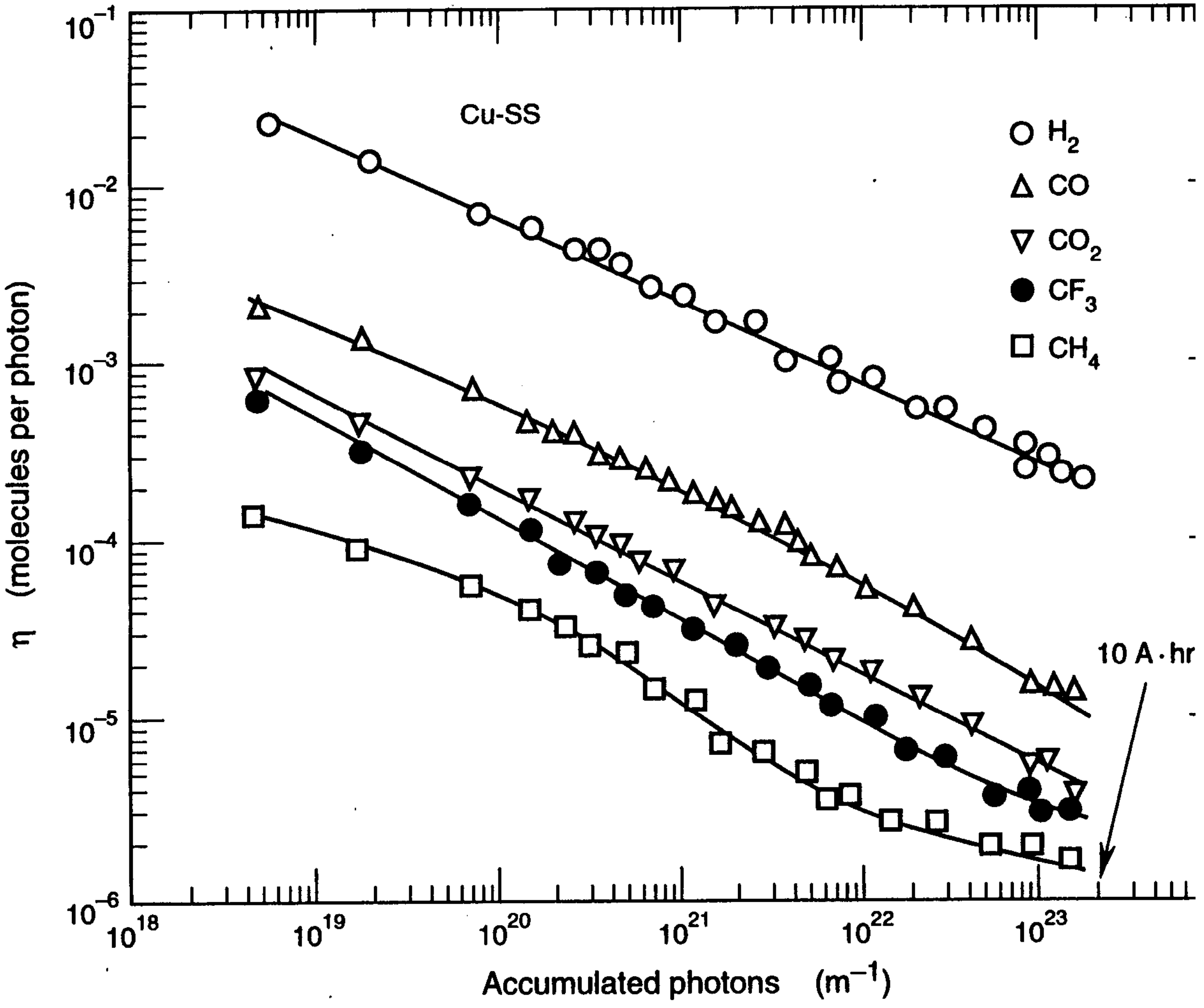

Fig. 5-33. Data from Foerster et al. [1990] showing the variation of the photodesorption coefficient η with material exposure.

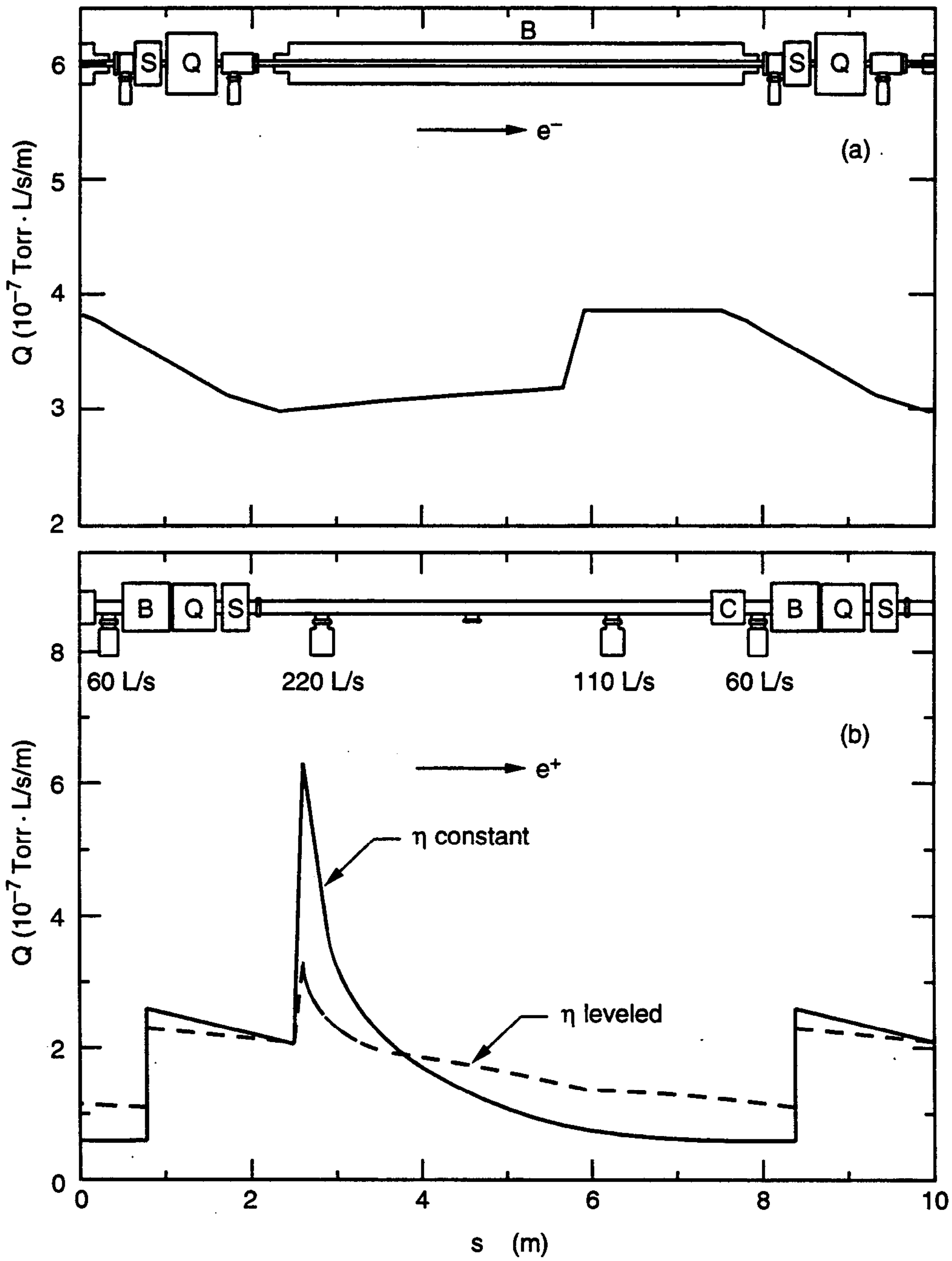

Fig. 5-34. (a) Gas load along a half cell of the arc in the HER at the design current of 0.99 A. The desorption coefficient was assumed to scale with the power profile and was normalized such that $\eta = 2 \times 10^{-6}$ molecules/photon at the location of maximum power. A contribution of 10% from reflected photons was included in the estimate of the gas load. (b) Gas load along an arc in the LER for two assumptions regarding the desorption coefficient: (i) constant value of $\eta = 2 \times 10^{-6}$ molecules/photon (solid line), and (ii) "leveled" photodesorption accounting for the variation in exposure along the arc (dashed line). In the latter case, $\eta = 1 \times 10^{-6}$ at the peak power density.

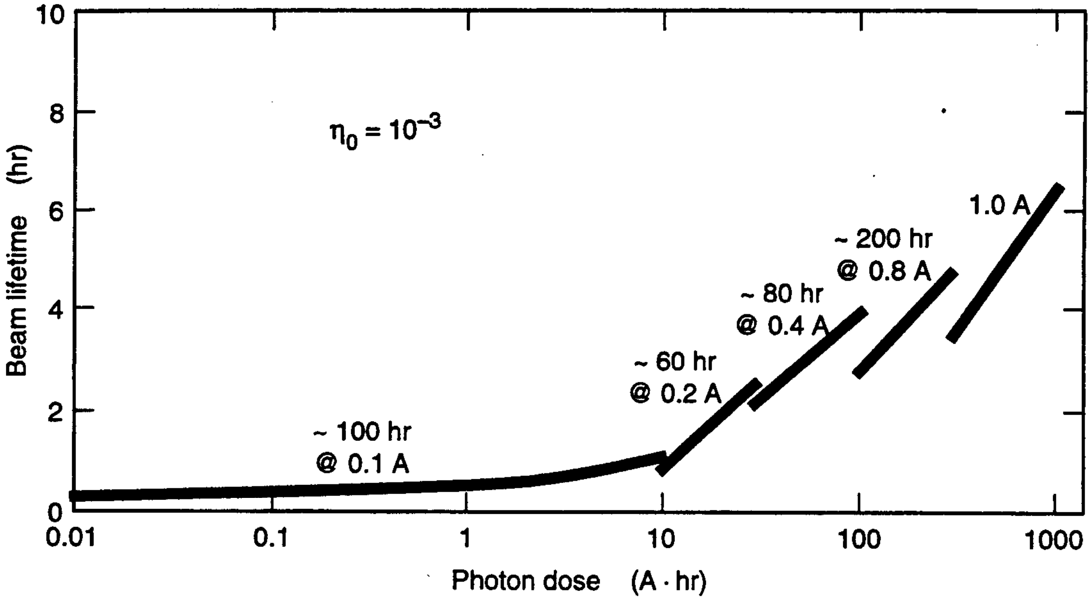

Fig. 5-35. Calculated beam lifetime in the HER as a function of exposure during initial commissioning of the collider.

5.2.3.5 Validation Test Program. The data of Ueda et al., on which the above calculations are based, were taken with a photon beam incident normal to the surface and having $\varepsilon_{crit} = 4.5$ keV. In the HER, the critical energy is nearly 10 keV and photons will strike the surface at a shallow angle. The data of Foerster et al. [1990], though taken at a shallow angle, used a photon beam of $\varepsilon_{crit} = 500$ eV and were not generally carried to such large exposures as to actually observe photodesorption coefficients as low as 10^{-6}. Therefore, our design assumption of $\eta \approx 2 \times 10^{-6}$ must be viewed as an extrapolation of existing experimental data. Although designing the pumping system to handle a photodesorption coefficient of roughly 2×10^{-6} from a copper chamber represents a reasonable extrapolation of that data, it was nonetheless considered prudent to carry out a series of validation experiments using the specific alloys, photon incidence angles, and preparation procedures that will actually be employed in the PEP-II design. Fortunately, appropriate photon sources with which to make measurements on short sections of test chamber are available at several laboratories in the U.S., Europe, and Japan.

Our photodesorption test program is being carried out at the National Synchrotron Light Source (NSLS) in collaboration with H. Halama and C. Foerster of BNL. The experimental setup is located on the U10 beamline of the VUV ring, an area that has previously been used [Foerster et al., 1990] for an extensive series of tests of the photodesorption properties of various materials. The experimental procedures we follow are closely similar to those described in the literature [Foerster et al., 1990; Ueda et al., 1990; Gröbner et al., 1983; Mathewson et al., 1990]. As the U10 beamline includes a built-in swivel point, the exposures can be conducted at the appropriate shallow angle. In our investigations, the test chamber is connected to the beamline through a rectangular duct of calibrated vacuum conductance and is pumped by a calibrated pump with a speed

S_i for the ith molecular species. Exposures are made to white light directly from the source, that is, without employing intervening monochromators or filters. The beam width and height, defined by horizontal and vertical collimators, are adjusted to restrict the area of exposure solely to the test sample. A residual-gas analyzer is used to determine the relative abundance of the principal gas species desorbed (H_2, CH_4, CO, and CO_2).

The primary quantity measured is the specific pressure rise for each molecular species, $\Delta P_i/I$ (averaged over the test chamber), as a function of photon exposure. These data are of most direct relevance to the engineering design of the PEP-II vacuum system. For photons generated over a horizontal angle θ, the average photodesorption of the ith species is

$$\eta_i = \frac{G\,S_i\,(\Delta P_i/I)}{(\dot{N}/I\theta)} \qquad (5\text{-}24)$$

We began the experimental validation program with a series of measurements of the desorption properties of 1-m copper bars mounted in a stainless-steel test chamber. Copper materials tested included samples of pure copper and of high-purity copper alloys, including one with silver and a dispersion-strengthened copper material. Except for two samples (one of C10100 copper and one of dispersion-strengthened copper material) that were machined before cleaning, all test samples were cleaned and tested with "as received" manufactured surfaces. Also, samples from several vendors having identical materials specifications were tested in order to examine manufacturing differences.

Bar samples of all materials were prepared and baked at LLNL for 48 hours at 200°C prior to shipment to BNL. At NSLS the samples were again baked for 48 hours at 200°C on the beamline prior to testing. In some cases, glow-discharge cleaning was applied when the desorption rate was assumed to be constant, resulting in about a factor of three lower rate of desorption for CO.

A test chamber, fabricated from pure copper (C10100) sheet and baked at 200°C, was also studied. This yielded a desorption coefficient for CO of 2×10^{-6} molecules per photon at 7×10^{23} accumulated photons. In a subsequent run, the vessel was oriented to a new surface and baked as before, but glow-discharge conditioned before the start of the run. As shown in Fig. 5-36, a value of $\eta = 6 \times 10^{-7}$ molecules per photon was achieved for CO at 7×10^{23} accumulated photons. Summing the results for the four measured gases, H_2, CO_2, CO, and CH_4, gave a nitrogen equivalent value of $\eta = 2 \times 10^{-6}$ molecules per photon, thus validating our design value. Additionally, and most importantly, the curves for each species were continuing to drop, indicating that lower values for the desorption coefficient can be achieved.

Initial results of our test program have been presented at vacuum workshops at Cornell (January 1992) and at The Hague [Foerster et al., 1992). Our measurements show that desorption coefficients of $\eta = 10^{-6}$ molecules per photon can be obtained, though not necessarily under exactly the same conditions as would occur at PEP-II.

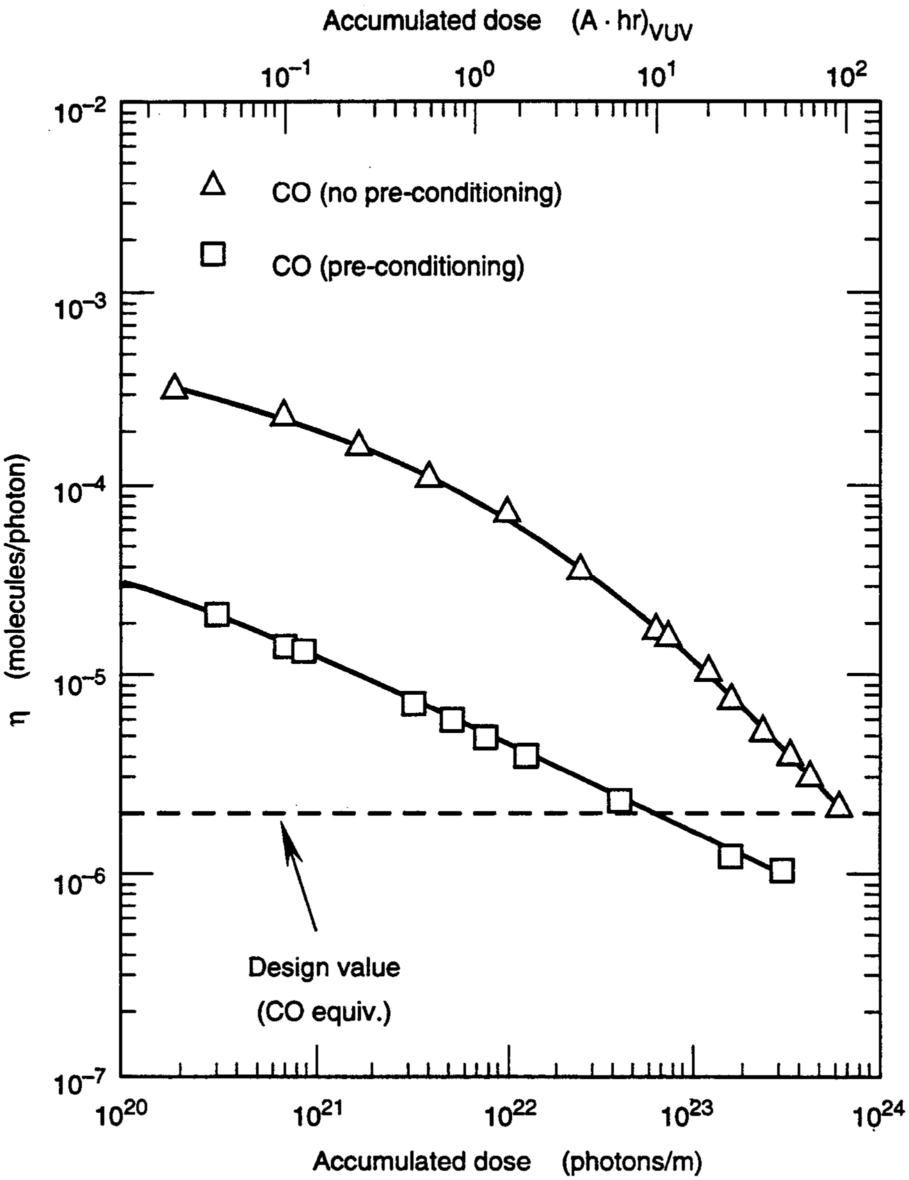

Fig. 5-36. Photodesorption yield measured at NSLS VUV ring for a fabricated copper chamber. The dose in A·hr (based on VUV ring parameters) is shown on the top scale. "Pre-conditioning" refers to performing an argon glow-discharge cleaning prior to exposing the chamber to photons.

Although the VUV ring produces large integrated photon exposures in a relatively short time, the critical energy of the radiation, as mentioned above, is only 500 eV, compared with a critical energy of about 10 keV for the PEP-II HER. For this reason, we plan to measure the dependence of the photodesorption efficiency on photon energy with subsequent exposures of two 3-m copper test chambers on the XRAY ring at NSLS (which provides radiation with a critical energy of 5 keV). One chamber will be fabricated from copper sheet having an octagonal cross section, and a second chamber will be fabricated from the actual extrusion expected to be used in the PEP-II HER.

5.2.3.6 Shielding of Synchrotron Radiation. The PEP-II HER, running at an energy of 10 GeV, generates the synchrotron radiation spectrum shown in Fig. 5-37a. (It has been contemplated that the PEP-II HER might also run at 12 GeV, though this is not part of the present design, in which case it would produce the harder spectrum shown in Fig. 5-37b.) Some of this radiation may escape and deposit energy in the surrounding material. This was originally pointed out during the design of PEP [Nelson et al., 1975] and subsequently verified by measurements both at PEP and at PETRA. Of most concern to PEP-II is magnet insulation. Other materials, such as wire insulation and cooling-water hoses, are even more sensitive to radiation, but they will be more distant from the beam.

Radiation damage to magnets depends strongly on the type of material used in the potting compound. PEP magnets, which will be used for the PEP-II HER, are insulated with an epoxy whose composition is given in Table 5-17. It is estimated that this epoxy

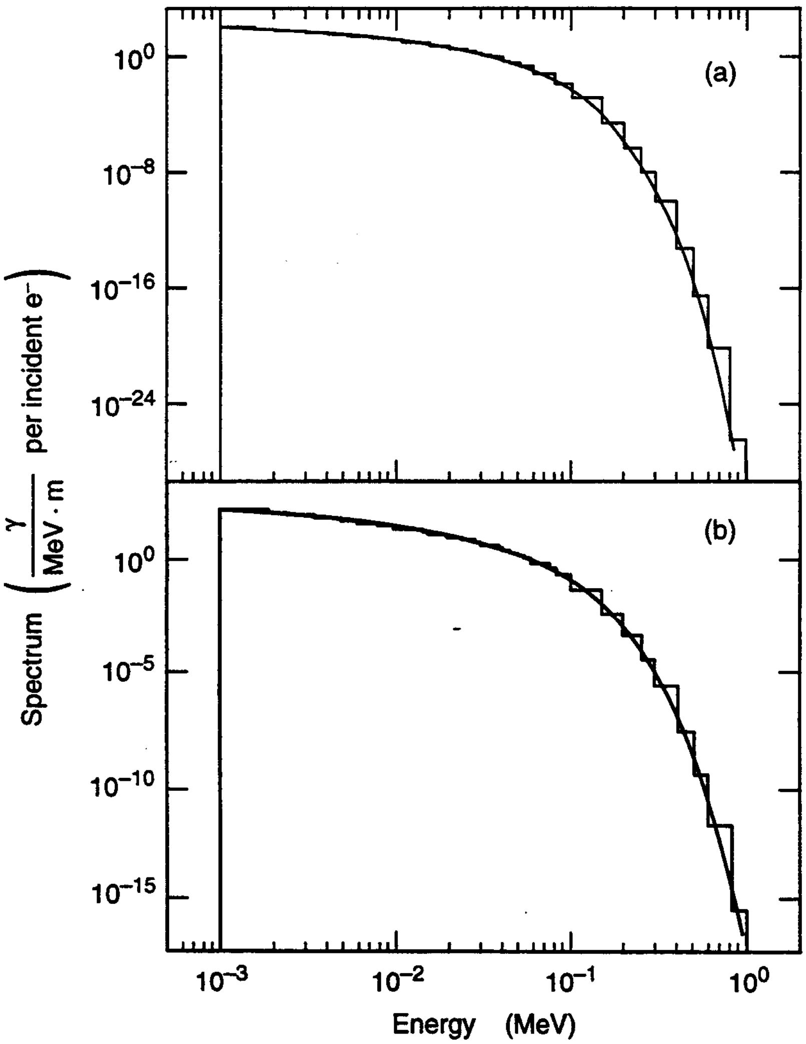

Fig. 5-37. Synchrotron radiation spectrum produced by (a) 10-GeV operation and (b) 12-GeV operation at PEP-II; solid line, analytic; histogram, EGS sampled spectrum.

Table 5-17. Chemical makeup and mass of the epoxy used in the PEP magnets.

Material	Composition	Mass[a] (g)
DER 332—epichlorohydrin + bisphenol A	$C_{21}H_{24}O_4$	851
DER 732—epichlorohydrin-polyglycol	$(C_3H_6O)_n\, C_6H_{10}O_3$	1049
NMA—nadic methyl anhydride	$C_9H_8O_3$	1832
Aluminum oxide	Al_2O_3	4252

[a] Weight fractions of the elements in the epoxy (for EGS4 purposes) are hydrogen, 2.6%; oxygen, 38.4%; carbon, 30.7%; aluminum, 28.3%.

compound should tolerate doses of the order of 10^{10} rads without degradation of its properties. However, the exact damage threshold is not known, so we rely upon other sources to set a criterion. CERN used 3×10^9 rads as the dose criterion for the LEP magnets [CERN 85-02, 1985]. They note that using fiberglass insulation tape gives a factor of ten higher tolerance to radiation damage (up to the 10^{10}-rad region). To be conservative, we have elected to use 3×10^9 rads as a criterion for the PEP-II magnet insulation. Stated another way, the criterion will be 10^8 rads/yr; this should give a magnet lifetime of 30 years or more. (Here, we ignore doses already received by the magnets from PEP running to date. These exposures are small compared with the doses expected from PEP-II operation.)

To estimate the annual radiation dose, we take 3.0 A for a 7200-hr operating year, giving roughly 22,000 A·hr/yr. The radiation strikes the wall at a 23-mrad angle of incidence. The absorbed dose D must remain below 2.0×10^{-19} rads/electron, corresponding to 10^8 rads/yr. This criterion is used when considering output from the program EGS4, which gives synchrotron radiation fluence, energy deposited, or dose (using appropriate conversion factors) per circulating electron. Various user codes built upon EGS4 have been developed specifically to study such problems. These codes all generate the synchrotron radiation spectrum both analytically and from a sampling algorithm, with scoring done in the regions outside the beam pipe. A fluence-to-dose conversion, using the surface dose numbers of Rogers [1984], modified for the SLAC epoxy compound, is performed within the code each time the epoxy region is entered. Details of the calculations can be found in Jenkins et al. [1990].

Calculations are based on the configuration of the present PEP-II HER, assuming (to be conservative) an operating energy of 10 GeV. Only the HER is considered because synchrotron radiation will not penetrate the beam pipe of the LER, which is assumed to operate at an energy of 4 GeV for our estimates.

For this study, the cutoff energies used in the EGS4 simulation were 1 keV (photons) and 1 MeV (electrons). Upper energies for both electrons and photons were 10 MeV, which is adequate because the spectra are essentially zero above a few MeV for a 10-GeV electron energy. The photon spectrum was sampled uniformly within an energy range from 0.1 $\varepsilon_{\text{crit}}$ to 10 $\varepsilon_{\text{crit}}$. A weight was carried along with each photon (and its progeny) for scoring purposes. The final results were later normalized per circulating beam electron.

The PEP-II HER vacuum chamber geometry is described in Section 5.2.4. The chamber material used for these calculations is copper, and the exact chamber geometry is used.

To summarize the results of our calculations, for typical vacuum chamber configurations, a copper chamber 0.5 cm thick (required for structural reasons) is more than adequate, as shown in Fig. 5-38.

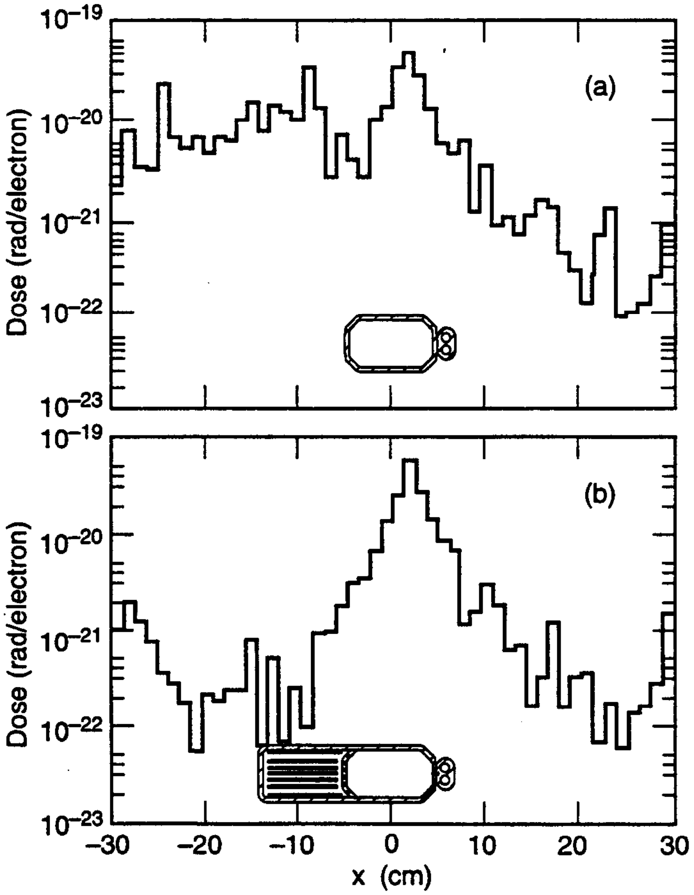

*Fig. 5-38. **Radiation dose to the magnet windings through two configurations of a 0.5-cm-thick copper vacuum chamber with no liner, computed for 10-GeV operation. The radiation dose limit corresponds to 2 × 10^{-19} rads/electron, well above the calculated values.***

5.2.4 HER Vacuum System

The configuration of the HER is shown schematically in Fig. 5-39. Figure 5-40 shows both the high- and low-energy rings in the tunnel, with the LER positioned above the HER. The circumference of each ring is 2200 m, and both ring geometries have been adjusted to fit in the existing PEP tunnel, as described in Section 4.1.

The vacuum system for the HER is designed to handle the large gas loads anticipated from photon-induced gas desorption and to carry away the large amount of power deposited on the outer chamber wall by the synchrotron radiation. The pressure requirements—quoted as N_2-equivalent values—were described in Section 5.2.1.

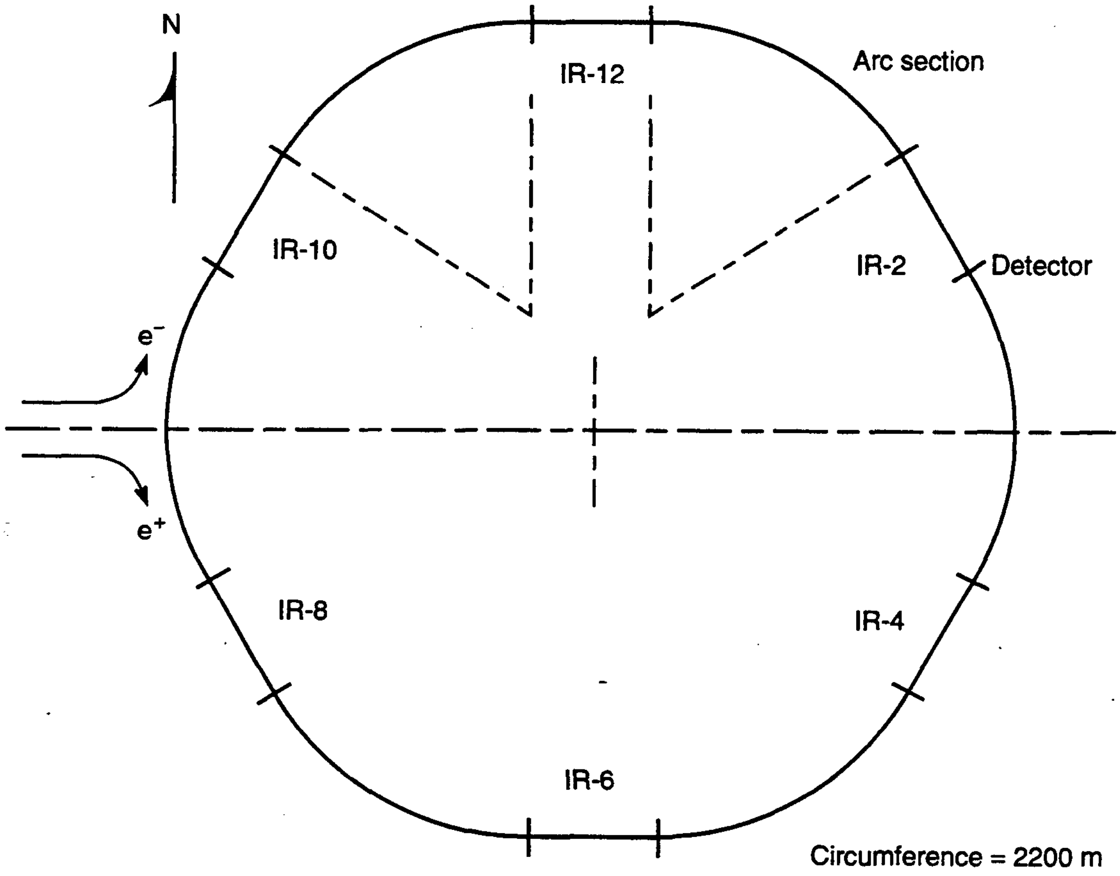

Fig. 5-39. Schematic of the PEP-II storage ring layouts.

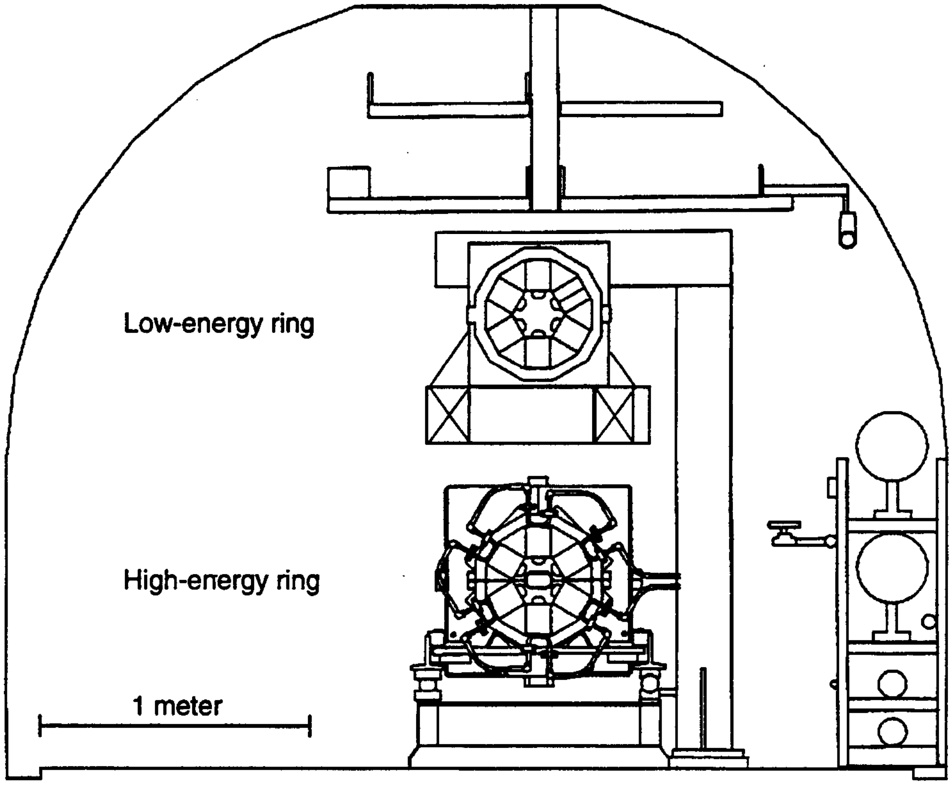

Fig. 5-40. Cross section of the PEP tunnel, showing the arrangement of the high- and low-energy rings of PEP-II.

The HER, illustrated in Fig. 5-41, contains 40 empty FODO cells grouped in five straight sections (the remaining straight section houses the interaction region) and 96 regular FODO cells in the arcs. As discussed above, copper was chosen for the vacuum chamber in the arcs because of its low photon-induced gas desorption coefficient, its high thermal conductivity, and its large absorption coefficient (which obviates the need for adding lead shielding). Vacuum chambers in the straight sections will be fabricated from stainless steel.

5.2.4.1 System Overview.

Arc Sections. Each arc section consists of four dispersion suppressor cells and 12 regular cells, each 15.2 m long, giving an overall arc length of 243.2 m. The magnet arrangement in each of the regular cells consists of a defocusing quadrupole (QD) with sextupole, a dipole, a focusing quadrupole (QF) with sextupole, and finally a second dipole. A beam position monitor (BPM) is located at each QD. The cell vacuum chamber is constructed of four sections of extruded copper in order to facilitate fabrication and assembly in the PEP tunnel. Chamber sections are joined at the ends with 10-in.-diameter, stainless-steel Conflat flanges. A bellows is located near each quadrupole to accommodate thermal expansion during operation and to facilitate installation and servicing.

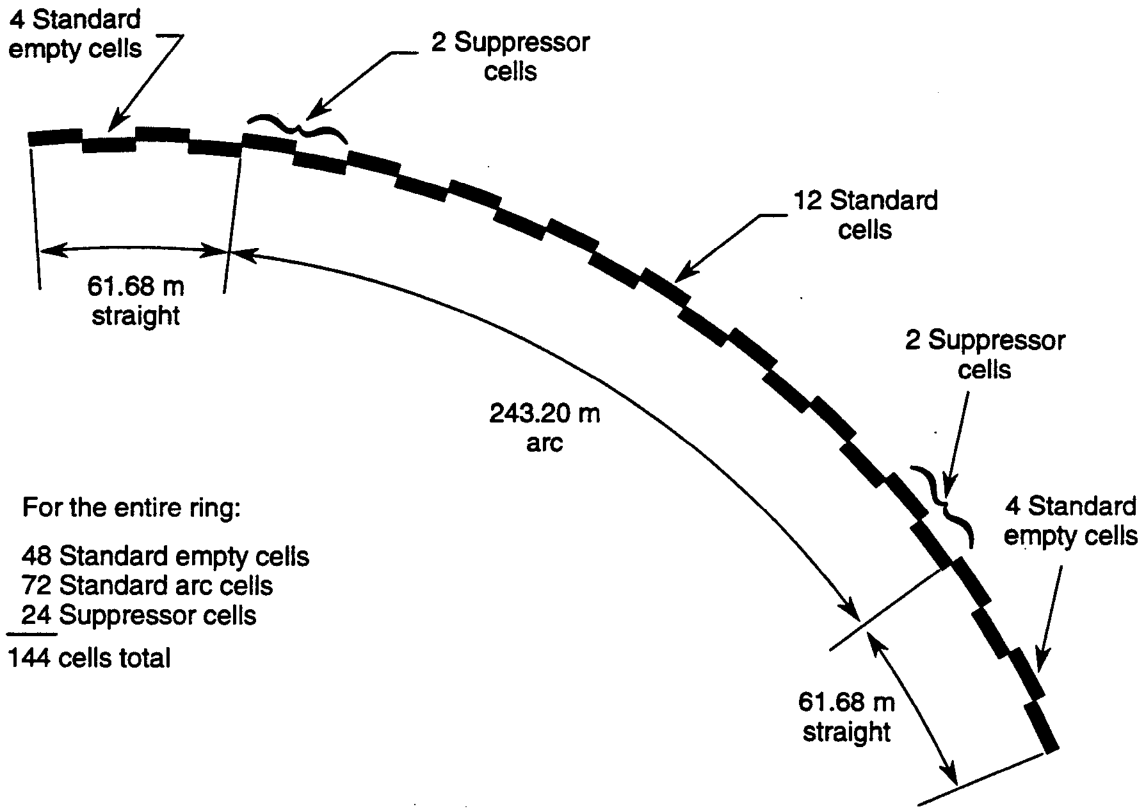

Fig. 5-41. Schematic of one sextant of the PEP-II HER.

Different vacuum chamber cross sections will be used through the dipoles and quadrupoles, as shown in Figs. 5-42 and 5-43. The chamber running through the quadrupoles is octagonal, to maximize conductance. Its outside dimensions are 100 mm wide by 60 mm high, with a uniform wall thickness of 5 mm. The chamber through the dipole magnet includes a passage for distributed ion pumps (DIPs), which is separated from the main beam chamber by a slotted screen. The pumping passage for the DIPs has an inner size of 84 mm wide by 50 mm high. Slots in the screen between pump and beam passages are designed to provide an overall conductance of about 1400 L/s/m. Both the beam tube and the pumping channel will be fabricated from UNS C10100, high-purity, oxygen-free, high-conductivity copper. A double-holed cooling bar attached to the outer wall of the beam tube carries away the heat produced by synchrotron radiation hitting the chamber wall. The bar will be fabricated from UNS C10300, an oxygen-free copper alloy having a thermal conductivity of 93% International Annealed Copper Standard. Discrete ("lumped") ion pumps are provided at each of the pumping plenums adjacent to the quadrupoles, as shown in Fig. 5-44; pressure gauges and pumpdown connections are also located there.

Should the need arise, 180°C water can be circulated through the cooling bar, to provide in situ baking to 150°C without opening the chambers. The additional thermal expansion will be accommodated by the bellows. Bakeout will reduce the initial outgassing rate and thus allow for base pressures in the 0.5-nTorr range, if needed.

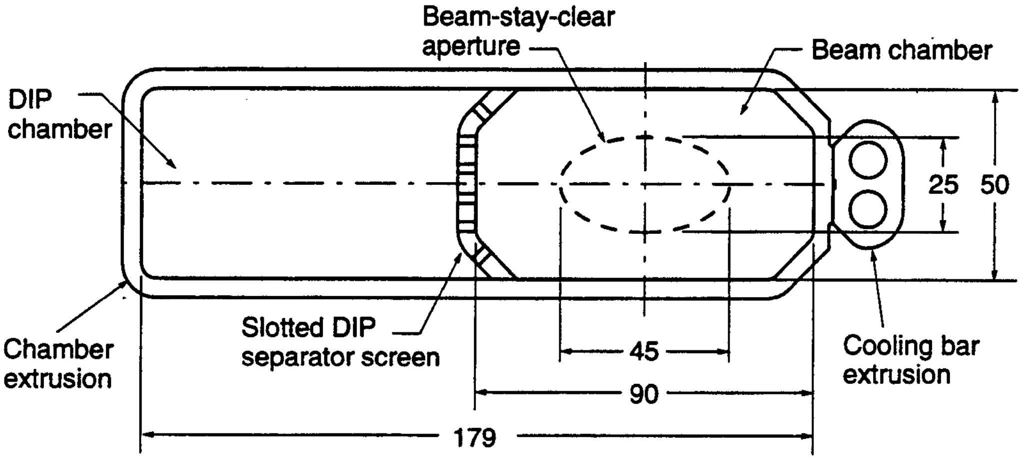

Fig. 5-42. HER vacuum chamber cross section at a dipole; dimensions are in millimeters.

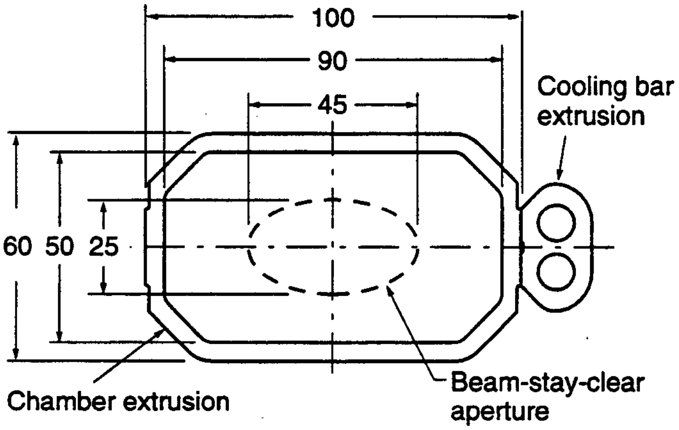

Fig. 5-43. HER vacuum chamber cross section at a quadrupole ; dimensions are in millimeters.

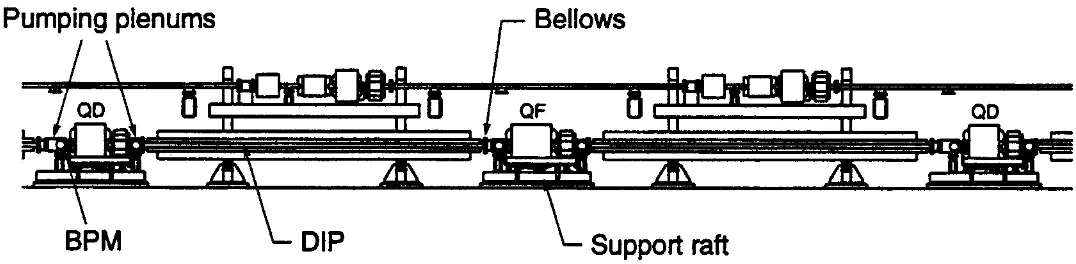

Fig. 5-44. Typical HER arc cell, with DIPs in the dipole magnet and lumped ion pumps in the pumping plenums on either side of the quadrupoles.

Straight Sections. A standard cell in the straight sections is 15.419 m in length, and contains no dipoles. The vacuum pipe is a made from 3.75-in. OD 316L stainless-steel tubing, sized to clear the 100-mm bore of the quadrupole magnets. Because there are no dipole magnets and hence no distributed ion pumps, larger lumped ion pumps are used to produce the 3-nTorr average pressure required. A diagram of a straight-section cell is shown in Fig. 5-45.

Various straight sections contain the injection septum, RF cavities, beam collimators, and optical monitors. Each special component will have its own individual requirements for the vacuum system, and each will require a custom interface.

In situ baking, if needed, will be accomplished using resistive heaters and insulation wrapped around the stainless-steel beam pipe. This can be done without disturbing the vacuum chamber integrity.

5.2.4.2 Analysis.

Thermal Analysis. As discussed in Section 5.2.3.1, one of the main challenges in designing the vacuum system is to adequately handle the high thermal flux densities incident on the vacuum chamber outer wall due to the synchrotron radiation. The peak linear flux in the HER reaches 102 W/cm, which corresponds to a flux density of 2.3 kW/cm^2. Finite-element analysis of a dipole chamber subjected to this high flux shows that the peak local temperature reaches 68°C above the cooling-water temperature. Furthermore, the average temperature of the entire chamber reaches about 25°C above the cooling-water temperature, as shown in Fig 5-46a. This 43°C difference between peak and average chamber temperature produces a 12,000-psi compressive stress in the region near the incident radiation. (The stress arises because the local hot spot is trying to expand but is forced to follow the bulk expansion of the cooler chamber.) Figure 5-46b shows this high axial compressive stress. Note that this stress arises every time the HER is filled with a 3-A beam. We assume a worst-case scenario for thermal analysis of 10,000 maximum-current fills over the life of the machine. The chamber is subjected to cyclic fatigue loading from the stress. The effect of this cyclic loading on the chamber depends largely on the temper of the copper and the residual stresses in the chamber.

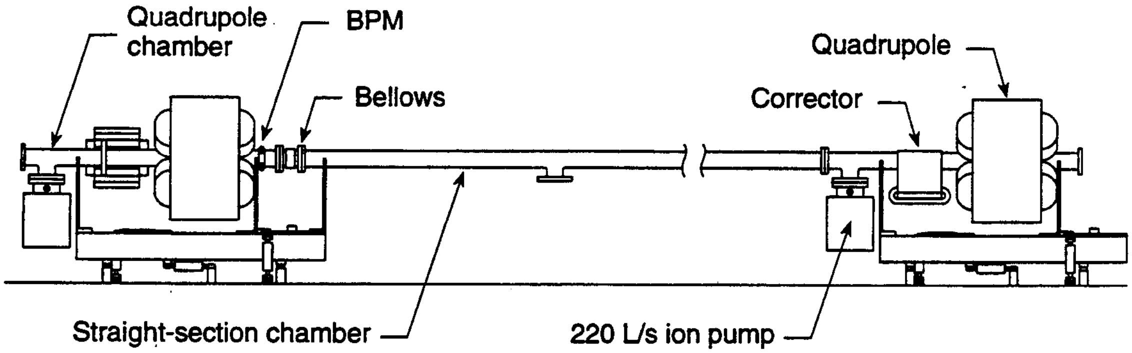

Fig. 5-45. Side view of HER straight-section vacuum chamber.

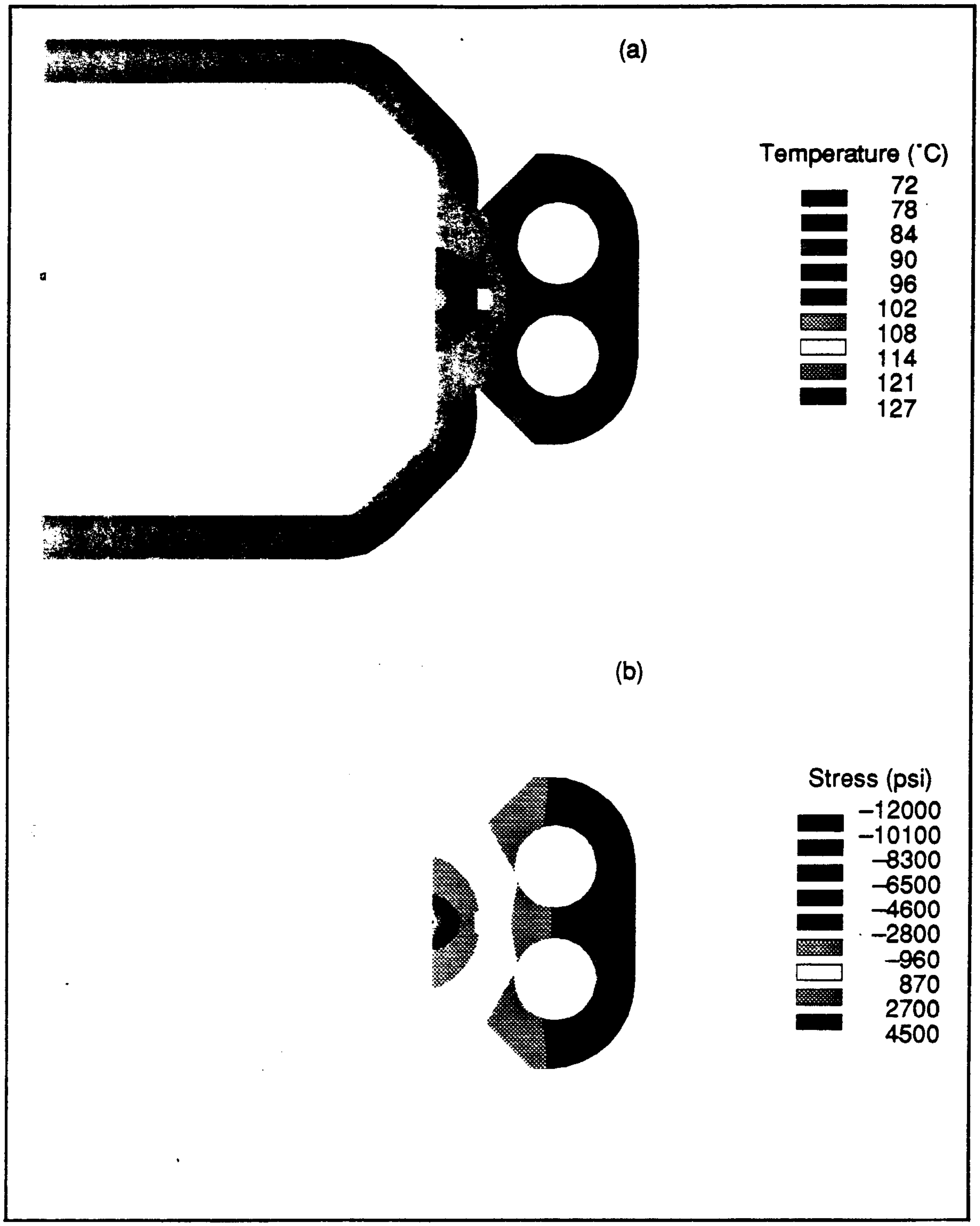

Fig 5-46. (a) Temperature distribution and (b) axial stress distribution in heated region of PEP-II HER bending magnet vacuum chamber with cooling bar, for an incident linear power density of P_L = 102 W/cm. The bulk temperature of the cooling water was 59°C, which corresponds to the maximum expected outlet temperature.

As detailed in Section 5.2.4.3, the chambers will be extruded and drawn to a half-hard temper, the cooling bar will be electron-beam welded in place, then the chamber will be bent to the correct radius. Manufacturing data for the drawn, half-hard-temper C10100 copper shows that, under a cyclic compressive loading of 12,000 psi, the material will not yield and will not develop fatigue-related cracking for at least 10^8 cycles. Furthermore, as long as the stresses remain compressive, any cracks will not propagate through the material. Therefore, to avoid potential fatigue cracking, further assembly processes must neither remove the half-hard temper of the original drawn material, nor produce additional stresses in the region of high thermal stress. Electron-beam welding tests have shown that, indeed, temper is not affected in the high-stress zone, and thus that the cyclic thermal loading can be absorbed by the copper chamber.

The above analysis assumes a high rate of heat convection to the cooling water. To produce the convection, water will flow through each passage at 3.5 gpm, or 10 ft/s. Water inlet temperature is 30°C, and the total temperature rise through a half-cell water circuit is 29°C. By routing the cooling water in the chambers to take advantage of the variable heating from the synchrotron radiation, we maintain the peak chamber temperature below 118°C, which minimizes any loss of strength associated with elevated temperatures.

Bakeout Heat Transfer. If the HER chambers must be baked in situ to reduce the operating vacuum pressure, 180°C water will be run through the cooling channels. Finite-difference analysis of the natural convection from the heated chamber shows that, with no insulation at all, the chamber loses only 5 kW per half-cell, and the minimum wall temperature is 165°C. Water flow rate and velocity for the bakeout are the same as for normal operation.

Thermal Expansion. During operation and bakeout, the arc chambers expand due to the increased temperature. Because the dipole chambers are bent in an arc, this expansion is not exactly in a line, but has some lateral component. Furthermore, during an operation the asymmetric temperature distribution across the dipole chamber, shown above (Fig. 5-46a) increases the radius of curvature by 4%, producing an additional lateral offset of the chamber. Table 5-18 details these values.

Two features are included in the vacuum system to accommodate these dimensional changes. First, a bellows is added every half-cell to allow the neighboring chambers to expand. The bellows is designed to compress as the chambers expand, even during an in

Table 5-18. Thermal expansion of HER arc half-cell.

	Operation	Bakeout
Expansion along beamline [mm]	3.6	16.9
Lateral offset [mm]	0.1	0.32
Rotation at bellows [mrad]	0.01	0.06

situ bakeout, so no special procedures are needed to prepare for bakeout expansion. They also allow for the (very small) rotation of the chambers because the expansion occurs around a large radius. Second, the chamber supports are designed to flex as the chambers expand. The supports carry the weight and seismic loads of the chambers, while still allowing adequate flexure along the beamline.

Vacuum Analysis. The main issue in designing a pumping scheme for the HER arcs is the high, variable gas load produced by the synchrotron radiation. The pumps must adequately pump this gas load through relatively low-conductance beam pipes. We have adopted a design based entirely on sputter-ion pumps. These provide sufficient pumping speed to attain the required pressures and are very reliable, causing minimal operational interference. Unlike non-evaporable getters (NEGs) or titanium sublimation pumps (TSPs), there is no need for regeneration or filament replacement.

Distributed ion pumps (DIPs) are installed in the dipole vacuum chambers to provide the bulk of the pumping needed. Detailed calculations have been completed to optimize the DIP design to provide maximum pumping speed in the 0.18-T field of the dipole magnets. Furthermore, lumped differential ion (DI) pumps are installed on either side of the quadrupole to pump the quadrupole chamber and to serve as holding pumps when the beam and DIPs are off. To improve conductance to these pumps, a plenum surrounds the beam pipe in this region. The plenum is slotted to provide conductance while minimizing changes in the beam pipe cross section.

Analysis of the vacuum system was carried out using a finite-volume analysis program developed for this application. Variable gas loads, chamber conductances, and pump sizes were all included in the model to ensure that the results adequately simulated the system. The calculation assumes a minimum photodesorption coefficient, scaled with incident power, of 2×10^{-6} molecules per photon. As expected, the results show that the average pressure is strongly dependent on the pumping speed of the DIPs. Furthermore, the quadrupole chamber pressure profile is limited by the conductance of the chamber cross section. Figure 5-47 shows the calculated pressure profile for a half-cell with an optimized DIP pumping speed of 165 L/s/m and two 60-L/s differential ion pumps, one at each end of the quadrupole chamber.

Using the above-mentioned pumping configuration, the average pressure for a half-cell is 8.8 nTorr at 3 A, which is slightly below the design value of 10 nTorr for the arcs. This value provides some margin if the DIP speed turns out to be somewhat lower in practice or if the chambers produce more gas than expected. Also, each pump plenum has sufficient conductance to accommodate two additional differential ion pumps, which could make up for reduced DIP pumping or increased gas load. Table 5-19 shows the pumping configurations we are considering, along with the average pressure while running at the nominal 0.99-A beam current and the average holding pressure. We can implement either of these, depending on actual running conditions.

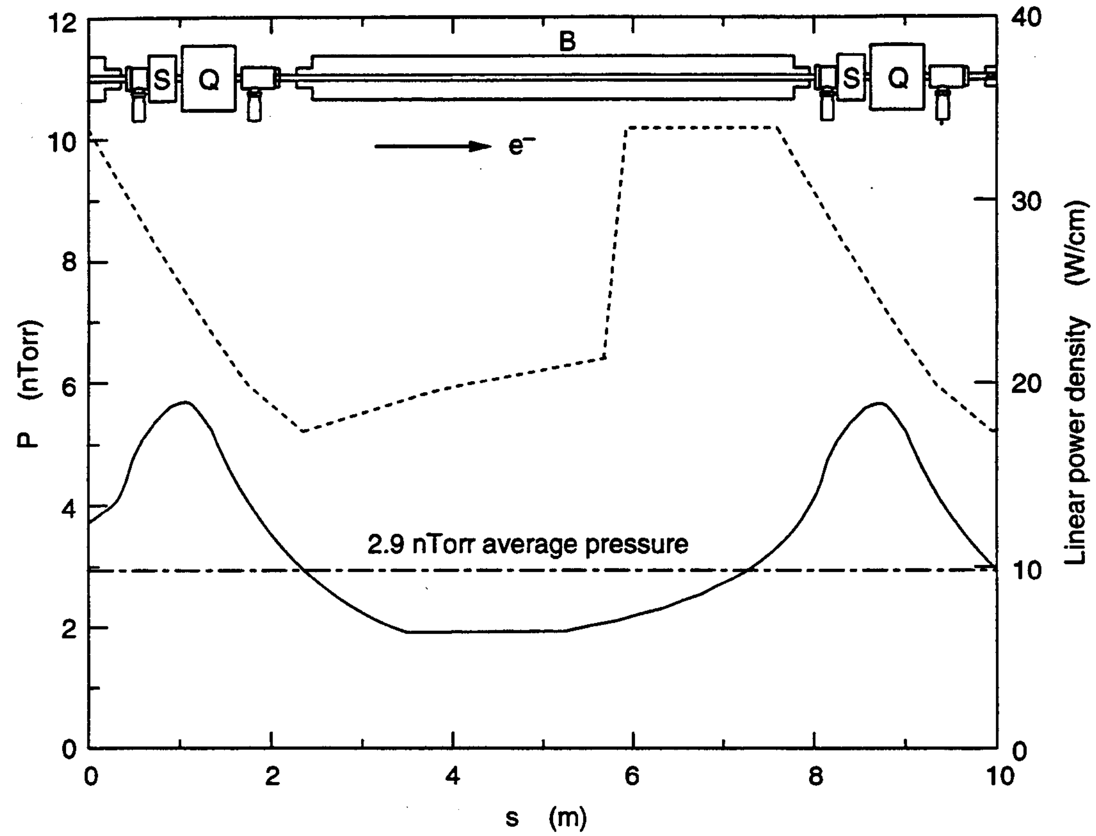

Fig 5-47. Pressure profile for an HER arc half-cell (solid line), shown with power distribution (dashed line).

Table 5-19. Vacuum pumping scenarios for HER arcs at nominal 0.99-A beam current.

	Design configuration	Alternative configuration[a]
Beam current [A]	1.0	1.0
DIP speed [L/s/m]	165	120
Upstream pump speed [L/s]	60	110
Downstream pump speed [L/s]	60	60
Running pressure [nTorr]	2.9	3.4
Holding pressure[b] [nTorr]	1.3	1.1

[a] Alternative is based on a more pessimistic estimate of DIP speed.

[b] With DIPs off.

5.2.4.3 Arc Chamber Design.

Dipole Chamber. The dipole chamber (Fig. 5-48) consists of an extruded copper chamber and cooling bar, the DIPs, a screen that separates the beam and DIP channels, and two Conflat-type end flanges. The chamber will be extruded in full lengths, with no press stops, from UNS C10100 copper, while the cooling bar will be extruded from UNS C10300 copper. These are both drawn to achieve their final shape and to produce a minimum half-hard temper. The pieces are then cleaned and electron-beam welded together. After welding, the subassembly is stretch-formed to its correct radius, then the ends are machined and the part recleaned. The slots in the separator screen are machined, then the screen is bent to its correct cross section and cleaned. The screen is then pulled into the chamber and electron-beam welded into place. Meanwhile, the DIP modules have been fabricated, cleaned, and assembled. They are pulled into the dipole chamber and connected. Finally, the end flanges are TIG-brazed onto the ends of the chamber.

This optimized fabrication sequence is the result of significant design, analysis, and testing of each of the components and fabrication processes. This is summarized in the descriptions below.

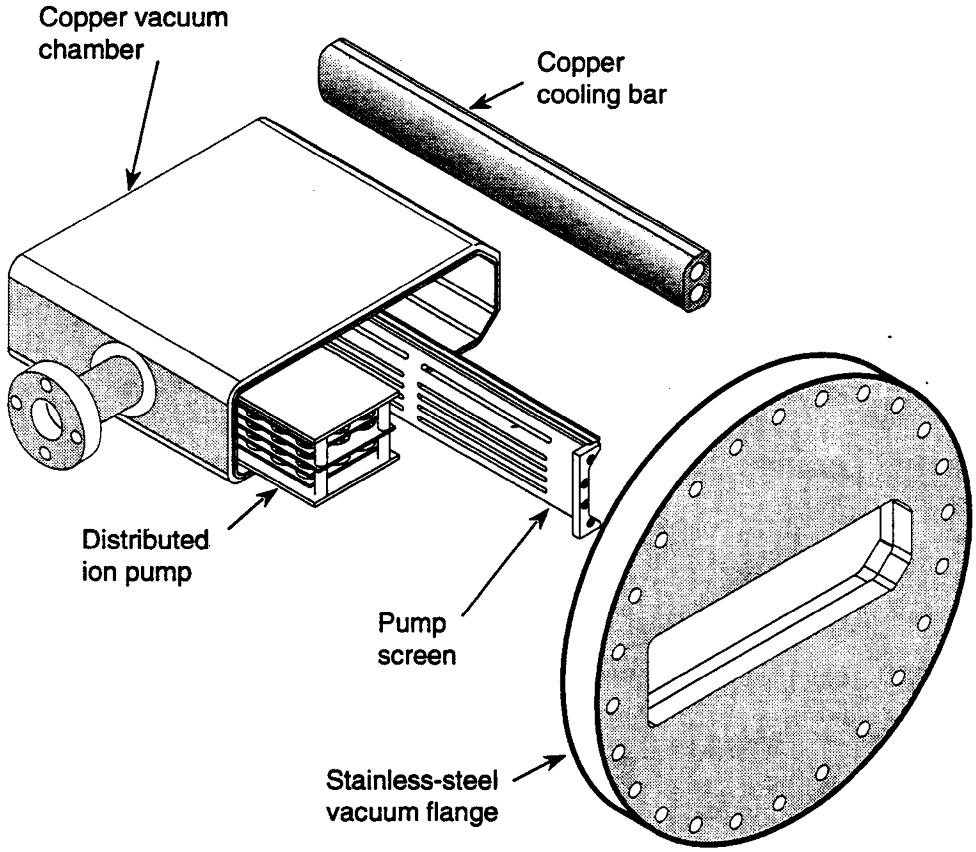

Fig. 5-48. Isometric view of the end of a typical HER arc dipole chamber.

Chamber Extruding. Although various bent sheet-metal fabrication designs were investigated, extrusion is the preferred fabrication method. A one-piece chamber extrusion eliminates all longitudinal vacuum welds, which affords a more accurate and dependable chamber. Three extrusion cross sections will be used (see Fig. 5-49), one each for the dipole and quadrupole chambers and a third for the cooling bar that runs along the outside radius of both chambers. A curved screen will be pulled into the dipole chamber to separate the beam and DIP passages. (If aluminum were used instead of copper, the cooling passages and separator screen could all be extruded into one complex, multiport extrusion. However, copper is needed for the arc chambers to provide the required shielding and low photodesorption coefficient. Because of machine capacity limitations and the flow characteristics of copper during the extrusion process, such a multihole extrusion cannot be fabricated.) We have worked closely with copper extruders to optimize the extrusion shapes and tolerances to ensure the best possible results. Furthermore, prototype chambers have been extruded and delivered to SLAC for

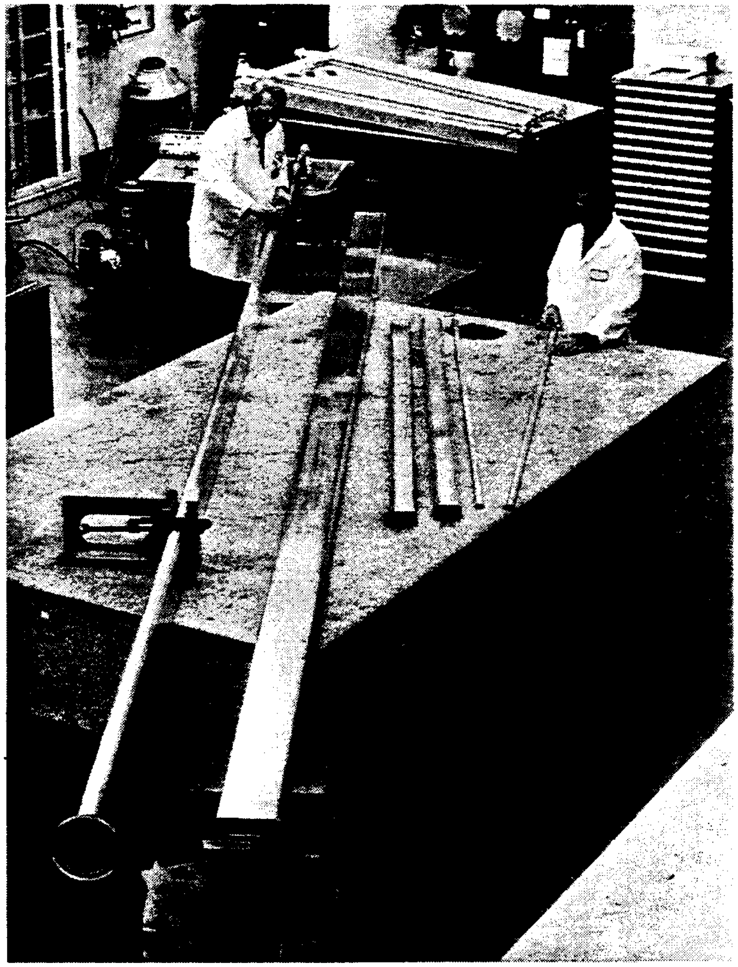

Fig 5-49. Photograph of prototype dipole chamber (long) and quadrupole chamber (short) extrusions being dimensionally inspected at SLAC.

analysis and testing. Recent dimensional, chemical, and material testing has shown that these extrusions exceed our requirements for dimensional stability, material quality, and physical properties. We are currently setting up a photodesorption test at BNL to confirm the manufacturer's data, as well as our earlier test data on similar material.

Electron-Beam Welding. As noted above, the selection of C10100 copper as the material for the arc vacuum chamber makes it necessary to join the cooling bar and DIP separator screen to the beam chamber. The joining process must minimize the heat input to the chamber, be compatible with ultrahigh-vacuum (UHV) standards, and be economically feasible. Several methods were considered to accomplish this task, including bolting, gluing, soldering, brazing, and welding. Low-temperature soldering, brazing, and electron-beam welding were further evaluated as viable options. However, low-temperature solders cannot withstand the thermal stresses, are brittle at room temperature, and outgas unacceptably in UHV systems. Although brazing produces joint geometries that are attractive for UHV applications, the elevated temperature that must be employed destroys the temper and strength of the material being brazed. As detailed in Section 5.2.4.2 above, stress analysis shows that the surface where synchrotron radiation is incident (and some distance into the wall) must be kept half-hard so as to be able to withstand the compressive stress caused by the synchrotron radiation.

Electron-beam joining satisfies all application criteria of cleanliness, strength, and low heat input. Therefore, we will use two electron-beam welds (in each case) to join the cooling bar and the DIP screen to the chamber—one weld from above and one from below. The cooling-bar welds are kept as shallow and narrow as possible, with a void at the cooling-bar midplane that is not welded. Analysis shows that the small void does not affect the temperature distribution significantly, yet provides a needed weld-spike gas vent at the root of the weld, which reduces weld porosity. The cooling bars are chamfered to reduce the required weld depth. The reduction in contact area actually spreads out and reduces the peak stresses by averaging the high temperature over a larger area. This weld joint design and the electron-beam welding procedure were further optimized by test-welding short beam chambers. The chambers were then sectioned and examined to obtain hardness, structural, and quality data. Figure 5-50 shows a micrograph of a typical weld joint. Test results show minimal annealing near the heat-affected zone next to the weld recast, retention of the half-hard temper in the areas of synchrotron radiation incidence, low levels of porosity, and a good weld-depth-to-width ratio. The remaining two-thirds (3.3 mm) of the wall thickness is unaffected by the weld, retaining its half-hard temper and strength.

For the DIP screen welds, the electron beam will be defocused to produce a weld that fuses 75% of the screen width and that is just deep enough to provide good attachment. Testing has shown that this method eliminates the possibility of missing the screen with the welder beam, and thus causing vacuum leaks.

These tests have shown that the selection of the electron-beam welding process will reliably join the chamber, cooling bar, and separator screen together, and maintain the material properties needed.

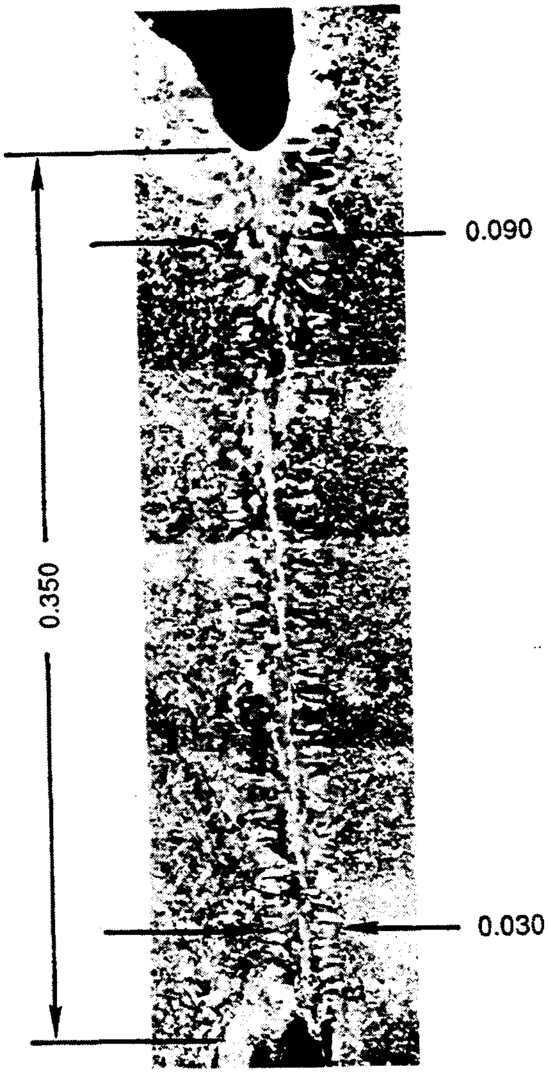

Fig. 5-50. Micrograph of electron-beam weld of the cooling bar to the dipole chamber.

Stretch Forming. The dipole chambers must be bent to conform to the nominal 165-m radius of the beam orbit. At this radius, the angle of incidence for synchrotron radiation on the bend chamber wall is 23 mrad. The thermal analysis discussed above (Section 5.2.4.2) indicates that, in order to stay below PEP-II limits for power density at maximum current, the chambers must be bent sufficiently uniformly that the angle of incidence does not exceed 26 mrad; this determines the tolerance on the bending radius.

We have successfully tested two bending techniques, use of a pin press and use of a stretch-forming apparatus, with 2.4-m test chambers. One chamber was bent to a 36.6-m radius using the pin press with long shoes. The technique gives a satisfactory bend but is tedious and time consuming, and results in a series of small "kinks" that could potentially exceed the maximum allowable incidence-angle criterion. This chamber was subsequently baked at 200°C and exhibited no noticeable relaxation of curvature or other dimensional changes.

Two additional chambers were bent by stretch forming. In this technique, the chambers are stretched axially to their yield point and then, while in the yield condition, are bent over a form of the appropriate radius. Stretch forming has several advantages. It is fast, it produces a smooth continuous bend, and (because the stretching raises the stress in the entire chamber to its yield point) it results in the lowest possible residual stresses after fabrication is completed. Furthermore, it actually releases the residual stresses left in the chamber from the welding. This, in turn, ensures the lowest operating thermal stresses. Clearly, this method is superior for our application. We have designed and built a stretch-forming apparatus (see Fig. 5-51) and have used it to bend the first 6-m-long prototype extruded chamber to well within the required tolerance.

Cusil TIG Brazing. The dipole and quadrupole chambers will be connected by Conflat-type vacuum flanges. The flanges will be fabricated from 316LN stainless steel and will be joined to the C10100 copper chambers. Typically, the dissimilar joint would be made using an intermediate copper piece that is brazed to the stainless-steel flange and then gas-tungsten arc-welded (GTAW) to the copper chamber. However, this involves a separate piece, an expensive braze joint, and an additional vacuum joint. An alternative

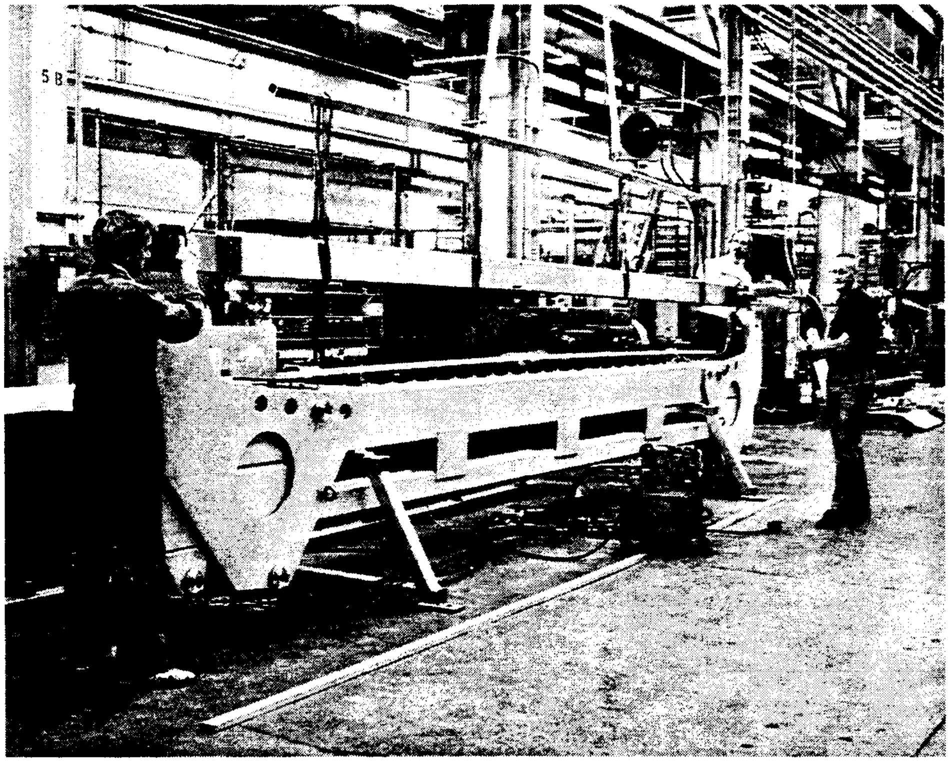

Fig. 5-51. Photograph of HER dipole chamber during stretch-forming at SLAC.

joining method is a single dissimilar-metal weld. Two welding configurations are being investigated.

The first configuration is a two-pass GTAW weld. The first pass deposits a nickel weld bead onto the copper chamber wall, then the second pass overlays this with Inconel wire. This process produces extremely strong, ductile welds, but requires significant heating of both pieces, with the associated thermal distortion. Also, the weld quality is sensitive to variations in the relative dilution of the various base metals.

The second weld configuration is technically a braze joint, which uses a tungsten inert-gas (TIG) torch as a heat source. The TIG torch heats, but does not melt, the two base metals, then Cusil braze wire is deposited into the joint. Preliminary weld tests show that this TIG-braze is stronger than the copper base metal, yet as ductile as the stainless steel. UHV vacuum-tight welds have been made on prototype flange joints and have survived high-temperature cycling under vacuum (see Fig 5-52). Ongoing tests are now quantifying weld-joint strength at room temperature and at 200°C.

In parallel with the welding research, finite-element stress analysis is being used to optimize the weld-joint geometry and location. The weld joint brings together not only dissimilar materials, but dissimilar shapes as well. This produces stress concentrations near the corners of the rectangular beam chamber. Initial finite-element analysis results show that the local stress is high, but manageable. Further analysis and joint design optimization is now under way.

Cleaning. To achieve the desired vacuum environment for the beam, cleanliness during all phases of the fabrication process is of paramount concern. Care must be taken to ensure that no fabrication process contaminates vacuum components after cleaning. Weld joints and machining processes must all be designed to produce cleanable parts that reflect good vacuum design practices.

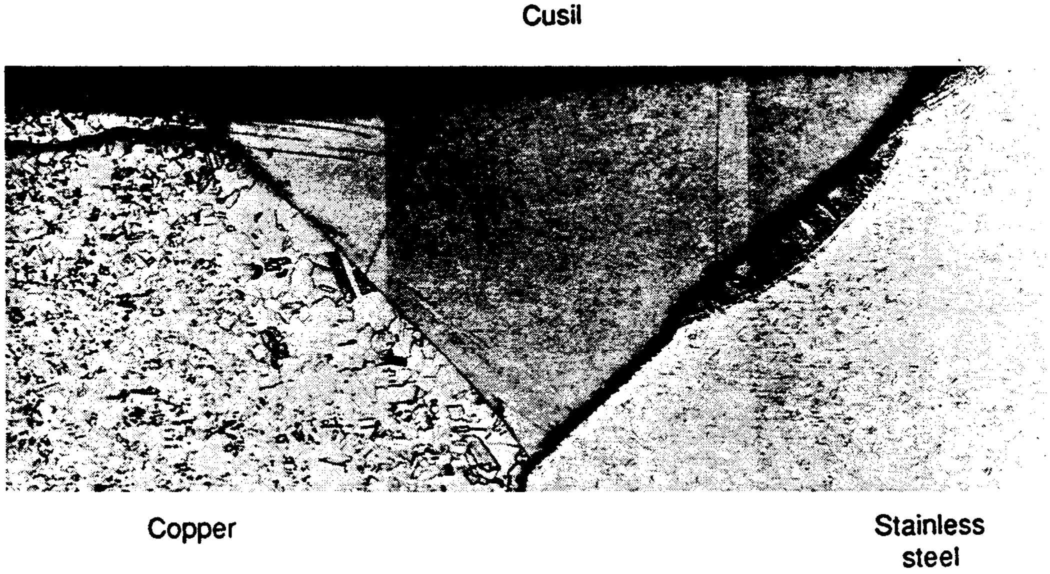

Fig. 5-52. Micrograph of a Cusil TIG braze.

To ensure this, all parts will be cleaned before assembly using existing SLAC cleaning processes and procedures. The process for cleaning stainless-steel parts is summarized in Table 5-20. The copper chambers and other copper parts will be cleaned in a separate process, outlined in Table 5-21.

Finally, following chemical cleaning, all parts will be assembled in a clean-room setting. Nylon gloves will be used when handling parts, and further fabrication, such as welding, brazing, and assembling, will be done using UHV-clean techniques.

DIP Design and Testing. As discussed in Section 5.2.4.2 above, the UHV environment in the HER arcs is attained using a combination of DIPs and discrete differential-ion pumps. The DIPs have been designed to maximize the available pumping using the 0.18-T HER dipole field, which is just over half of the 0.3-T field used in PEP. Our design is expected to provide an average pumping speed of 165 L/s/m, which is more than sufficient to provide the required 10-nTorr pressure at the maximum beam current of 3 A.

To achieve this pumping speed, a plate-type DIP has been chosen. The five-plate stainless-steel anode, shown in Fig. 5-53, contains four rows of pump cells, 1.8 cm in diameter, that intercept the dipole magnetic flux. The flux varies from 0.18 T at the magnet pole center to about 0.10 T at the edges. Theoretically, the cell diameter should increase as the field diminishes to maintain the same pumping speed per cell. We have elected to maintain a uniform cell diameter, however, in order to maximize the total number of cells in the pump. This approach maximizes the overall pumping speed, even though not all cells are pumping at maximum efficiency. Furthermore, the cells are arranged in staggered lines to produce a hexagonal close-packed pattern, which improves the cell-area density to 68%.

Table 5-20. Process for chemical cleaning of austenitic stainless steel.

Vapor degrease in hot 1,1,1 trichloroethane vapor for 5 minutes
Rinse in cold running tap water for 1 minute
Alkaline soak clean for 5 minutes at 180°F
Rinse in cold running tap water for 2 minutes
Pickle in Prepalloy and nitric acid (25 vol-%) at 100°F
Rinse in cold running tap water for 2 minutes
Alkaline soak clean for 5 minutes
Rinse in cold running tap water for 2 minutes
Immerse in room-temperature nitric acid (25–30 vol-%) for 2 minutes
Rinse in cold running tap water for 2 minutes
Rinse in cold de-ionized water for 2 minutes
Rinse in 150°F de-ionized water for 2 minutes
Rinse in isopropyl alcohol at 115°F
Dry in oven at 150°F
Wrap in lint-free paper and food-grade aluminum foil

Table 5-21. Process for chemical cleaning of OFE copper.

Vapor degrease in 1,1,1 trichloroethane for 5 minutes
Alkaline soak clean in Enbond Q527 cleaner at 180°F for 5 minutes
Rinse in cold tap water for 2 minutes
Immerse in room-temperature hydrochloric acid (50%) for 1 minute
Bright dip to produce desired surface finish
Rinse in cold tap water for 2 minutes
Immerse in room-temperature potassium cyanide for 15–20 seconds
Rinse in cold tap water for 1 minute
Rinse in cold de-ionized water for 30 seconds
Rinse in 150°F de-ionized water for 30 seconds
Immerse in isopropyl alcohol at 115°F for 30 seconds
Blow dry with dry nitrogen gas
Dry in oven at 150°F
Wrap openings in lint-free tissue and food-grade aluminum foil

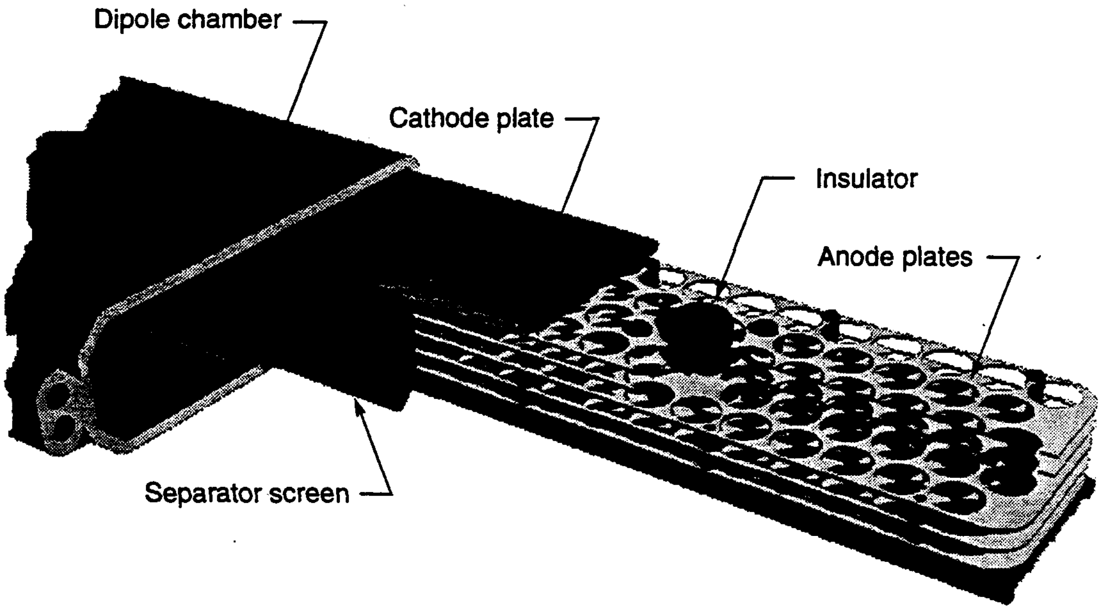

Fig. 5-53. CAD model of HER DIP module.

Beryllium-copper contact fingers between the titanium cathode and chamber wall provide conduction cooling for the cathode plates. These spring contacts, spaced along the length of the cathode, are designed to remove the heat flux of 0.01 W/cm^2 generated by the cathodes. The cathode plates have been shaped to provide the necessary stiffness to carry the contact spring force.

A formed, slotted screen, which separates the beam passage from the pump passage, provides RF continuity for the beam yet allows high conductance between the two passages. The screen contains six rows of slots on a pitch of 10 cm; each slot is 0.25 cm high by 9 cm wide, providing a calculated conductance of 1400 L/s/m. Where possible, slots in the screen have been aligned with the spaces between the anode plates to improve the overall conductance of the pump-screen combination. The height of the slot was selected to keep the contribution to beam impedance to a negligible level, and the height-to-depth ratio of 0.52 for the slot was chosen to minimize the effects of RF interference during operation.

We plan to validate the distributed ion pumping calculations by testing a series of DIP modules in a test stand using a PEP-II dipole magnet to simulate actual ring conditions. The test stand, now nearing completion at LLNL, will test various pump parameters, including cell diameter, cell arrangement, spacing between plates, magnetic field strength and uniformity, and anode voltage.

Test anodes will have five or seven plates, and the separator screen will contain either six or eight lines of slots to match the anode geometry. Initial testing will begin with N_2 gas. However, the final design will be tested with CO, CO_2, H_2, CH_4, and H_2/CO gas mixtures. We also intend to test a DIP module design from NSLS to provide a comparison and calibration with the production PEP-II design.

Tests by Laurent [1992] have shown that, in practice, DIP pumping speed can match theoretical calculations. However, this agreement with theoretical performance is contingent on maintaining extreme cleanliness during fabrication and assembly. Therefore, we will fabricate and clean all parts using the cleaning procedures described above. Then, all stainless-steel parts will be baked at 900°C for four hours; the titanium cathodes will be baked at 800°C for four hours, and the copper parts will be baked at 200°C for 24 hours. Following baking, all parts will be stored and assembled in a clean environment.

Quadrupole Chamber. The quadrupole chamber is actually a combination of elements. Pumping plenums for the two lumped differential ion pumps are included as part of this chamber, as are the BPMs, located at every QD magnet (one per cell). Each quadrupole chamber also includes a bellows to accommodate the thermal expansion of the dipole chambers. Finally, inside the pumping plenums, low-angle masks shield the downstream bellows and flanges from synchrotron radiation. This entire unit is supported by the same raft that supports the quadrupole and sextupole magnets, as shown in Fig. 5-54.

Although the pieces of the quadrupole chamber perform various functions, they are all integrated into a single assembly. Indeed, a single extrusion spans the entire quadrupole chamber, and the various components, such as the masks, BPM, and pumping plenums, register into, and weld onto, this extrusion. This approach ensures maximum

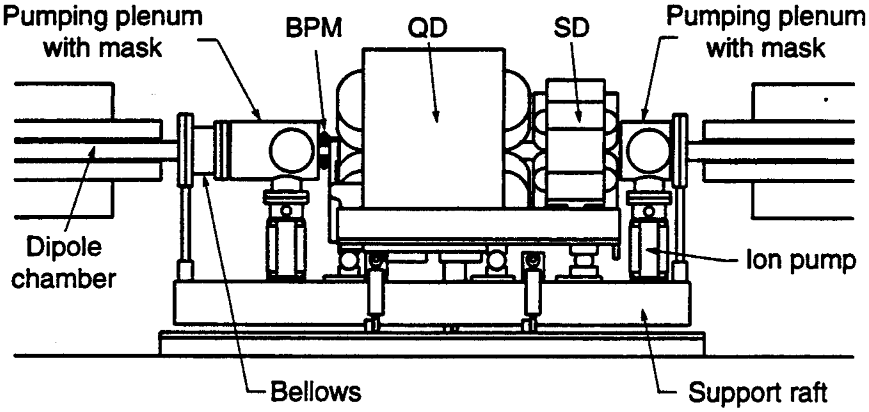

Fig. 5-54. Layout of HER arc quadrupole chamber.

accuracy for the positions of the BPM and masks, both of which must be precisely located.

The quadrupole chamber will be fabricated using the same techniques as the dipole chamber: An extruded chamber and a cooling bar are electron-beam welded together, and the stainless-steel flanges are TIG-brazed with Cusil. The pumping plenums, masks, and bellows will be assembled using conventional techniques, such as GTAW and hydrogen-furnace brazing. Below is a description of the various parts of the quadrupole chamber, their design criteria, and the present state of the development work.

BPM Design and Testing. Approximately 150 BPMs will be installed in each PEP-II storage ring. They will be located adjacent to the QD quadrupole in each cell, 96 in the arc sections, 40 in the straight sections, with some special BPMs in the IR. The design we have chosen (see Fig. 5-55) is based on a BPM feedthrough used in Sincrotrone Trieste, ESRF, APS, and other machines. Small ports will be welded into the quadrupole chamber pump cell, and the feedthroughs will be connected to the chamber by mini-Conflat flanges. The miniflange-mounted feedthrough assembly integrates a ceramic insulator, a 1-cm-diameter metallic button, and a type-N connector in an electrically smooth 50-Ω unit. This design is simple, reliable, and easily replaceable in the field. As noted, the synchrotron radiation masks in the pumping cell absorb radiation that would otherwise strike the BPM. The masks are water cooled and thermally isolated so that movement of the BPM unit is minimal.

The BPM will be fabricated such that the location of its electrical centerline is within ±0.004 in. (±0.1 mm) of its mechanical centerline. The unit will be calibrated using a technique used in the SLC and the ALS whereby each button is pulsed and the response of the other buttons is measured. This technique eliminates the need for expensive calibration fixtures and may be repeated in the tunnel should a problem be suspected. The BPM will be located within ±0.010 in. (±0.25 mm) of the quadrupole axis. The BPM position will be surveyed to within 0.002 in. (0.05 mm) and the measured offset entered into the project database. The BPM support will be designed to maintain long-term positional stability with respect to the quadrupole within ±0.001 in. (±0.025 mm).

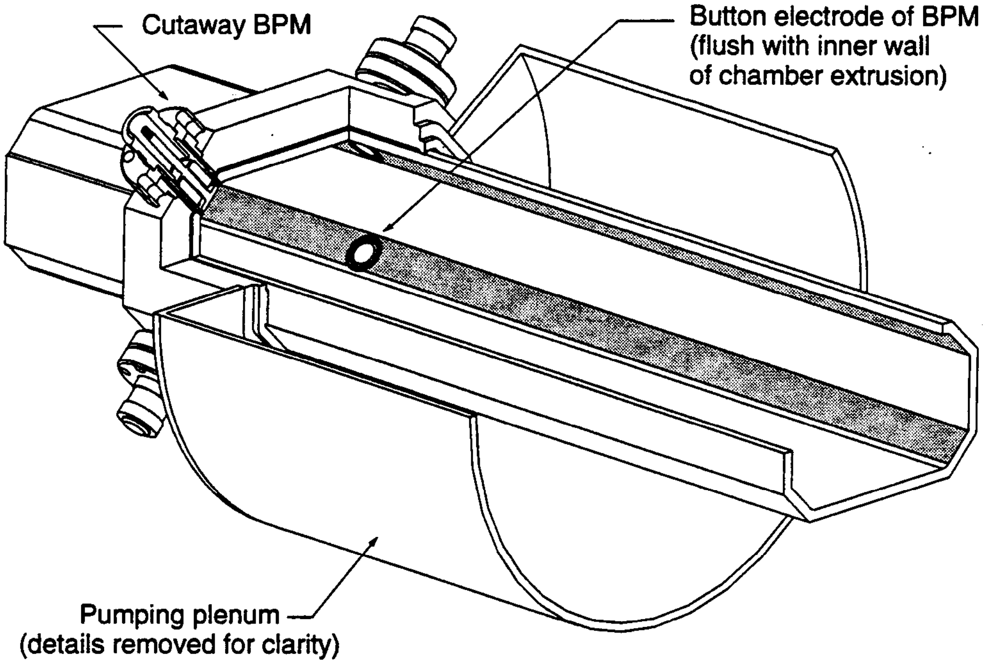

Fig. 5-55. CAD model of an HER arc BPM, integrated with the pumping plenum and quadrupole chamber extrusion.

Prototype feedthroughs are on order from two manufacturers for electrical bench tests and mechanical lifetime testing. A prototype BPM has been fabricated and is being prepared for installation in the SLAC linac for testing with electron and positron beams.

Bellows Design and Testing. The bellows (see Fig. 5-56) allows for the expansion of the vacuum chambers, while still providing a uniform chamber cross section to reduce the impedance seen by the beam to less than 0.05 Ω. Furthermore, it serves as the capstone for the cell—it is the last piece installed and the first removed should servicing be needed. The bellows provides sufficient room to maneuver the large and heavy vacuum chambers into place.

As discussed in Section 5.2.4.2, the chamber expands by different amounts depending on the operational mode of the machine. Table 5-22 summarizes these different operational modes, the corresponding compression requirements for the bellows, and the number of cycles for each of the compressions for which the bellows is designed.

Part of the bellows assembly is a bellows shield, which isolates the welded bellows shape from the beam chamber and ensures that the beam sees a beam pipe of uniform cross section. This shielding is done with prestressed cantilevered beryllium-copper spring fingers that slide along the inside of the beam passage as the bellows is being compressed. RF testing of this finger design is now being performed at LBL. Preliminary results show that the impedance of the bellows shield is as low as that of the chamber itself and that the finger shape will not lead to HOM power losses from the beam. The fingers are designed to maintain a relatively high contact pressure of 0.20

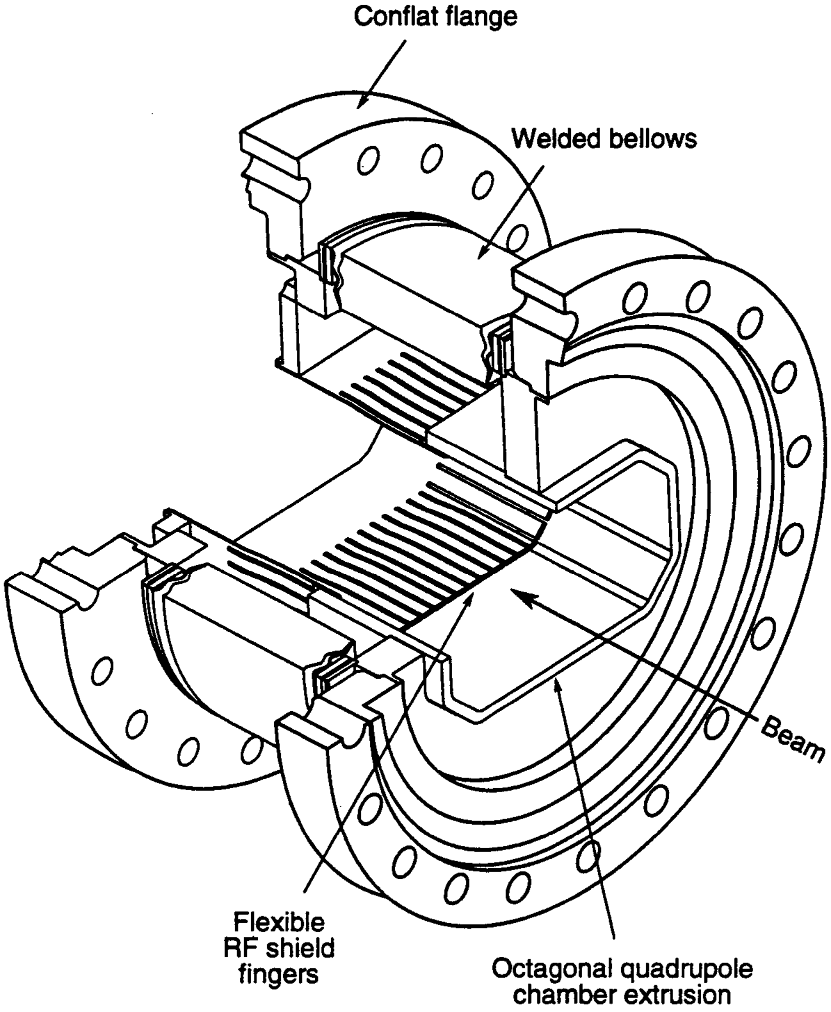

Fig 5-56. CAD illustration of the HER arc bellows, showing inner RF shield.

Table 5-22. Compression requirements for HER arc bellows.

Operational mode	Bellows compression (in.)	Number of cycles
Installation	1.0	100
Nominal (0.99-A beam)	0.09	100,000
Max. design (3.0-A beam)	0.2	100,000
150°C in situ bakeout	0.65	10

pounds per finger, despite any lateral offset introduced into the bellows assembly. Fatigue testing of the sliding contact joint will determine the optimal surface finish and plating material to eliminate both galling and the potential for cold-welding in the UHV environment.

Mask Design. Each quadrupole chamber pumping plenum contains one mask, which shields the neighboring flanges and bellows from the synchrotron radiation (see Fig. 5-57). (The thin bellows fingers and RF gaskets at the flange joints cannot be sufficiently cooled to preclude overheating, so the masks must protect them from damage.) The masks are independently cooled, and thermally and mechanically isolated from the rest of the chamber. The slope of the upstream face of the mask is only 3°, so the maximum linear thermal flux on it is 225 W/cm, compared with a maximum of 102 W/cm on the chamber wall (at 3-A beam current). Finite-element analysis shows that, although the maximum temperature of the mask reaches 90°C, and the local temperature at the point of incidence of the radiation exceeds 180°C, the peak stresses are low. This is because the mask is free to expand as it heats and is not constrained by cooler parts of the chamber. Thermally isolating the mask from the neighboring chamber ensures that it is not a heat source that could locally distort the chamber. This is especially important for the mask shielding the BPM, a component that requires high thermal and mechanical stability.

The masks protrude into the beam chamber by as much as 4.5 mm. Although they stay well outside the beam-stay-clear aperture, they would give an asymmetry to the

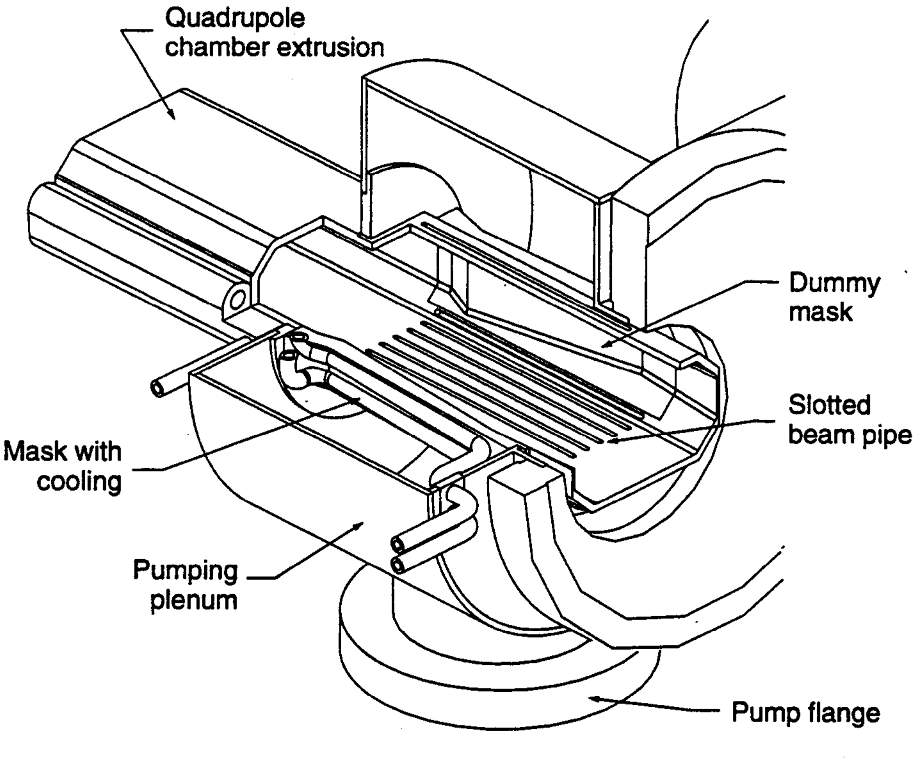

Fig 5-57. Mask and symmetrical dummy mask inside a typical pumping plenum chamber. Note slotted beam pipe for improved vacuum conductance to pump.

chamber. To restore transverse symmetry, dummy masks will be added to the opposite side of the chamber.

Supports. The quadrupole and dipole vacuum chambers sit on supports that mount to the quadrupole magnet support raft. Thus, the vacuum chambers maintain close alignment with respect to the quadrupole magnets of each cell. As discussed above, the BPM position must be tightly maintained, thus the support for the BPM provides rigidity to hold position, despite the weight of the vacuum pumps, transient loads, and thermal expansion of the chamber at operating temperature. (These loads exert up to 500 pounds of force on the support.)

The two remaining supports, one supporting the opposite end of the quadrupole chamber and the second supporting the dipole chamber across the bellows from the BPM, must also provide vertical and lateral rigidity, but must flex axially to accommodate the thermal expansion of the chamber. These supports will be modeled after the original SLAC flex plates, which have been supporting the disk-loaded linac waveguides for 30 years. This support consists of two stainless-steel sheets that are pretensioned by a copper-alloy plate that is cooled in liquid nitrogen, inserted between the sheets, then allowed to warm to room temperature. The resulting prestress produces a support that is extremely rigid laterally and rotationally, yet free to flex along the beamline.

5.2.4.4 Straight Section Design.

Standard Chambers. Although the six straight sections of the HER contain all of the nonstandard equipment for the machine, there is still a "standard" cell, consisting of a focusing and defocusing quadrupole, whose centers are spaced 7.709 m apart. The beam pipe consists of 3.75-in.-diameter 316L stainless-steel tubing, sized to clear the 100-mm bore of the quadrupole magnets. As in the arc cells, each QD has an associated BPM. A bellows at each quadrupole takes up the thermal expansion of the chambers, and two pump cells complete the layout of the straight section half-cell.

The other components used in the straight sections are generally adaptations of the corresponding items used in the arcs. The BPM uses identical electrodes, but will be installed in round tubing instead of the octagonal arc chamber. The bellows will be designed using the same sliding-finger RF shield, and incorporating the same criterion for maximum compression at bakeout as in the arcs. However, for the straight sections, they will be modified to fit the 3.75-in. tubing. The pump chambers will be modified slightly to accommodate the round tubing and will also be fitted with different pumps to better handle the particular pumping requirements of the straights (see below). Because there is no synchrotron radiation produced in the straight sections, local masking is not needed at every pump cell. Instead, discrete masks will be placed at three places along the straight section to intercept the low-angle radiation coming from the last bend magnet of the arcs. For the same reason, cooling of the chamber is not needed.

Vacuum Analysis. There are two significant differences between the arcs and the straight sections—in the straights there is little or no synchrotron radiation and there are no dipole bending magnets. Thus, the vacuum design of the arcs, based on the use of distributed ion pumps in the dipoles to provide the bulk of the pumping, cannot easily be transferred to the straights. A different approach is required, which considers only the thermal gas desorption from the stainless-steel chamber walls and which counts only on discrete ion pumps to maintain the required pressure.

Because of the symmetry of the vacuum system in the straight sections, the pressure curve can be modeled analytically, using the following formula:

$$P_x = q_D B\left[\left(\frac{L}{S_p}\right) + \left(\frac{x}{C}\right) - \frac{x^2}{(2CL)}\right] \qquad (5\text{-}25)$$

This quadratic equation models the pressure curve as an inverted parabola, which reaches its peak value midway between pumps. Parameters used to evaluate the straight section pressure profile are summarized in Table 5-23.

The values in Table 5-23 correspond to the use of two 220-L/s ion pumps in each cell, one at each quadrupole magnet. With this configuration, the average pressure is

$$\begin{aligned} P_{\text{av}} &= \left(q_D \frac{BL}{C}\right)\left(\frac{C}{S_p} + \frac{1}{3}\right) \\ &= 2.4 \text{ nTorr} \end{aligned} \qquad (5\text{-}26)$$

This is below the 3-nTorr design pressure for the straight sections. A plot of the pressure profile for a half-cell is shown in Fig. 5-58.

Table 5-23. Parameters used in evaluation of straight section pressure profile.

Thermal outgassing rate, q_D [Torr·L/s/cm^2]	1.0×10^{-11}
Perimeter of beam chamber, B [cm]	28.9
Half-length of a half-cell, L [cm]	385
Pumping speed[a], S_p [L/s]	100
Chamber conductance, C [L/s]	24.8

[a] For half-length of half-cell.

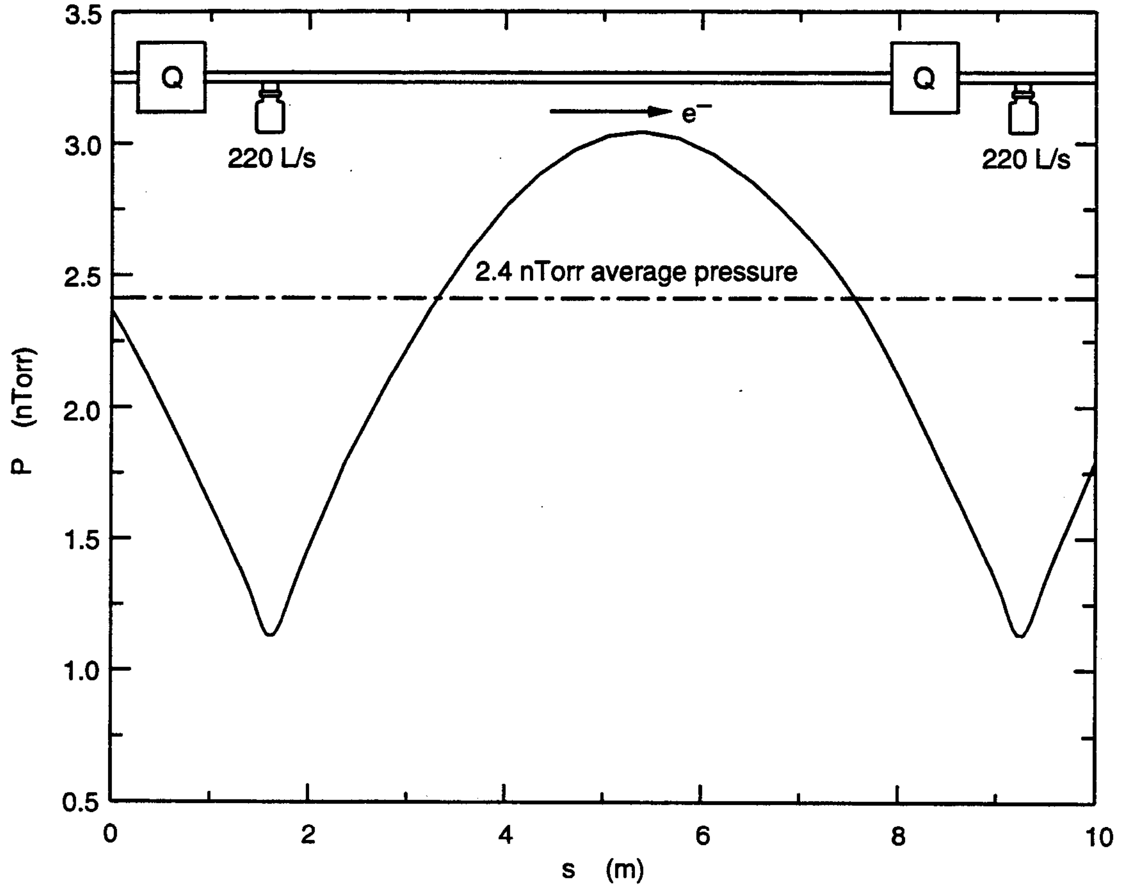

Fig. 5-58. Pressure profile of HER straight section half-cell.

5.2.5 LER Vacuum System

5.2.5.1 System Overview. The LER vacuum system concept is considerably different from that of the HER. Optimization of the LER magnetic lattice, and differences in the bending magnet design have resulted in extensive differences in the arc vacuum system. Nonetheless, the design has been optimized to take advantage of the fabrication techniques developed for the HER vacuum chambers. Operating pressure requirements for the LER are the same as those for the HER. However, due to the lower beam energy, the LER heat loads are lower, making the thermal design less demanding than that of the HER.

All pumping in the LER is by means of lumped sputter-ion pumps. To provide stable argon pumping speed (in case of small air leaks), one pump in each cell will have "differential cathodes" (of titanium and tantalum). An evaluation was done on the use of TSPs and NEG pumps, which potentially provide high pumping speed at low pressures and at somewhat lower cost. Calculations showed that the gas loads in the PEP-II LER arcs would require frequent regeneration of either type of pump. For PEP-II, the loss of operational time during regeneration was considered an undesirable feature and the risk of lost beam time due to accidents during the frequent regenerations was judged unacceptable. Ion pumps, in contrast, are very reliable and many of them are available from PEP for reuse. It is expected that some combination of TSPs and NEG pumps will be used in special sections of the machine where gas loads are not so high and where very low pressure must be maintained.

The periodic layout of the magnet lattice in the LER is similar to that of the HER—the cells of the two rings are the same length and stacked one atop the other, as shown in Fig. 5-59. Major differences between the two rings, however, are the length and placement of the dipoles. A standard FODO cell in the LER contains the following magnetic elements: (1) focusing quadrupole, (2) focusing sextupole, (3) drift, (4) corrector, (5) dipole, (6) defocusing quadrupole, (7) defocusing sextupole, (8) drift, (9) corrector, and (10) dipole. Alternate arcs are mirror-symmetric both for the magnet lattice and vacuum chambers, reflected about an axis from the interaction point at IR-2 to the injection point in IR-8; that is, the pattern on one side is sextupole-quadrupole-dipole and on the other is dipole-quadrupole-sextupole.

As in the HER, copper was chosen as the most suitable material for fabrication of the arc vacuum chambers. In the straight sections, where the synchrotron radiation is minimal, the vacuum chambers will be fabricated from 316L stainless-steel tubing. Experience from SPEAR and PEP has demonstrated the wisdom of installing a large vacuum system with flanged rather than welded interconnections. Standard stainless-steel Conflat flanges with copper gaskets will be used, as these have proved very reliable in the past. The inner dimensions of the vacuum chamber accommodate the beam-stay-clear region required by beam dynamics and allow for the unavoidable errors in fabrication and mechanical positioning. The cross section (Fig. 5-60) was made as large as would fit in a composite magnet pole profile in order to minimize the synchrotron radiation linear power density and to maximize vacuum conductance.

As in the HER, HOM losses will be kept to a minimum by keeping a uniform chamber cross section where possible. Gently tapered transitions smoothly blend the unavoidable shape changes. Pumping ports on the beam chamber are shielded by screens. Copper contact rings between the flanges provide a smooth electrical path and eliminate RF losses. In the interest of reducing the number of different components, the LER and HER vacuum systems will be standardized wherever possible. For example, the isolation valves, pump-out valves, vacuum gauges, and ion pumps with their associated controllers will be the same type in both rings.

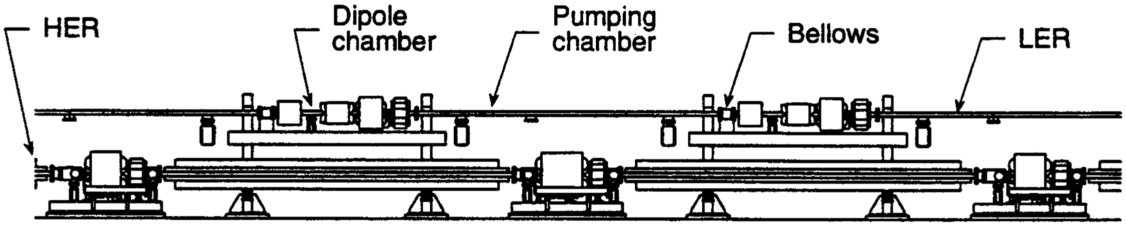

Fig. 5-59. Illustration of standard arc cells, showing the LER above the HER.

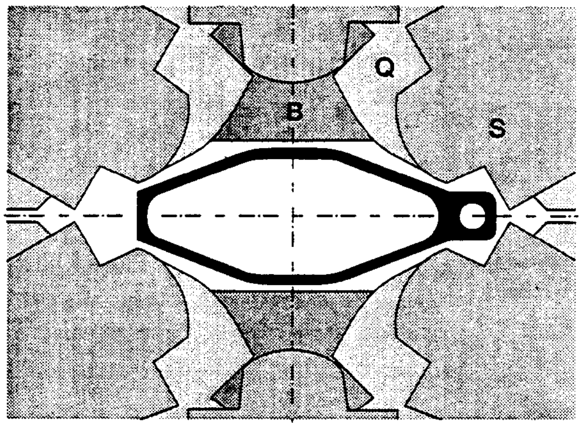

Fig. 5-60. Cross section of the LER vacuum chamber in the arcs; dimensions are in millimeters.

5.2.5.2 Analysis. At a beam energy of 3.1 GeV, the critical energy of the synchrotron radiation is 4.9 keV. In this photon-energy regime, almost all the power is absorbed on the inside wall of the vacuum chamber. With a nominal stored-beam current of 2.14 A, the total power radiated in the arcs is 1288 kW, or 13.4 kW per cell. The power distribution in Fig. 5-61 shows that the peak linear power flux, 33 W/cm, is deposited approximately 1.6 m beyond the exit of the dipole magnet; thereafter, the power decreases rapidly along the cell. A maximum design energy of 3.5 GeV with a 3-A stored-beam current was assumed for the thermal design. With these parameters, the peak linear power density is 73 W/cm, which results in a calculated thermal stress of 1,000 psi and a wall temperature at the point of peak-power incidence of about 80°C.

A series of finite-element calculations has been completed using the maximum design values for synchrotron radiation power. The temperature differential across the water-cooled metal wall of the chamber was calculated to be 26°C, with a 21°C rise across the surface film in the water. At the required flow rate of 10 gpm, the bulk temperature rise per cell is 11°C.

Within each cell, low-conductivity water (LCW) from the supply header will flow out, in both directions, from the center of the cell through an LER dipole and quadrupole chamber in series and then to the return header. A flow switch will be installed to monitor for low flow.

A second consequence of synchrotron radiation is photodesorption. The gas load produced by this mechanism is plotted in Fig. 5-34b, assuming a value for the photodesorption coefficient of $\eta = 1 \times 10^{-6}$ molecules per photon at the maximum value of P_{SR}. As a result of leveling (see Section 5.2.3.4), the photodesorption coefficient used in the pressure profile calculations varied from 1×10^{-6} molecules per photon at the peak to 4.3×10^{-6} molecules per photon at the point of minimum P_{SR}. These leveled values are in good agreement with values measured in the NSLS desorption tests [Foerster et al., 1992]. The arrangement of sputter-ion pumps in the arc cells is shown in the layout of Fig. 5-59. The total installed pumping speed per cell for machine startup is 780 L/s (two 220-L/s pumps, two 110-L/s pumps, and two 60-L/s pumps). (The pumping chamber

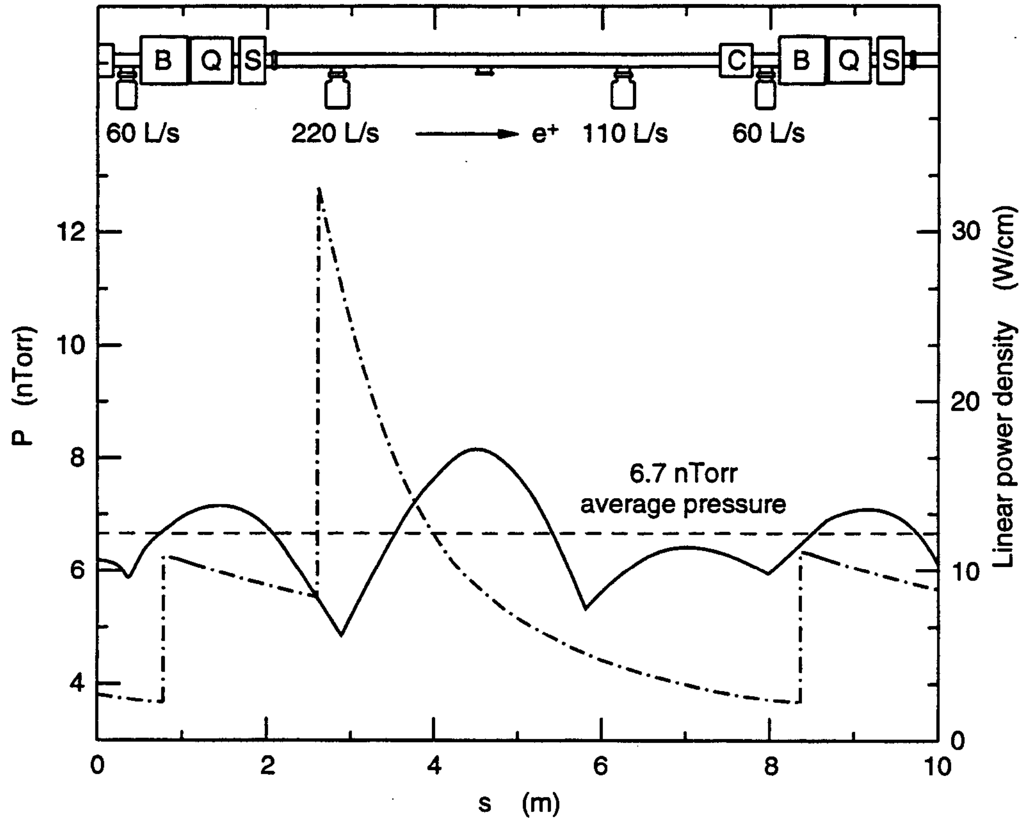

Fig. 5-61. Plot of synchrotron radiation linear power density and vacuum pressure along LER arc cell for the nominal beam energy and current.

will have an extra port to permit additional pumping if required to reach 3-A operation.) The pressure distribution calculated with this configuration is included in Fig. 5-61. Based on the above estimate of the desorption coefficient, the average pressure in the arcs during nominal operation at 3.1 GeV and 2.14 A stored beam current will be 6.7 nTorr, which is below the design requirement.

In the straight sections, the design pressure of 3 nTorr will be maintained by installing 220-L/s sputter-ion pumps at intervals of 7.7 m (that is, two per cell). Based on SLAC experience, we have assumed a thermal outgassing rate of 1×10^{-11} Torr·L/s/cm^2. For the region immediately upstream of the interaction region, 220-L/s pumps will be installed at intervals of 3.85 m to obtain an operating pressure of 1 nTorr. With this pump arrangement, the average pressure around the LER circumference is 6 nTorr. This pressure was used in the lifetime estimate discussed in Section 4.3.

5.2.5.3 Arc Chamber Design. Each arc region vacuum system consists of sixteen standard cells of dipole vacuum chambers with a 4-m-long straight pumping chamber between magnet groups. The layout of one standard cell is shown in Fig. 5-59. There are six beam chamber components per cell: dipole chamber, pumping chamber, bellows, dipole chamber with BPM, pumping chamber, and bellows. The length of the dipole was chosen such that all of the synchrotron radiation it produces strikes the vacuum chamber wall downstream from the magnet (see Fig. 5-61), where lumped vacuum pumps can be easily located to remove the desorbed gas. Distributed ion pumps inside the dipole are thus unnecessary. (Indeed, for a ring which such a low dipole packing factor, distributed pumping in the dipoles would be ineffective.) As is typical of storage rings, the beam chamber, which is of continuous cross section throughout the arc, is vacuum-conductance limited.

The arc chambers are made from a single-wall copper extrusion such as that illustrated in Fig. 5-60, with an extruded copper cooling bar electron-beam welded to the outer wall of the beam passage. The adopted cross section gives a small incident angle between the synchrotron radiation and the vacuum chamber wall, thereby lowering the linear power density to very modest values. The 2.36-m-long dipole chamber, shown in Fig. 5-62, passes through the sextupole, quadrupole, dipole, and corrector magnets. It is rigidly attached to the support girder between the sextupole and quadrupole, at the location of the BPM. (Only alternate dipole chambers in the cell will contain a BPM, those near the QD magnets.) Flex plates at the ends of the chamber will hold the lateral position while allowing thermal expansion. A screened pumping port is provided between the quadrupole and dipole. At the flange joints, RF seal rings will provide continuity along the inner surface of the vacuum chamber. The outer wall of the vacuum chamber will be tapered away from the beam so that synchrotron radiation does not strike the vacuum flanges or RF seals.

Nearly all of the synchrotron radiation power is absorbed in the 5.01-m pumping chamber, which is located immediately downstream of the dipole. The design, shown in Fig. 5-63, uses a water-cooled, extruded copper beam chamber identical to that used in the dipole chamber, with end flanges for interconnection. A bellows module at the downstream end of the pumping chamber provides the necessary space for installation

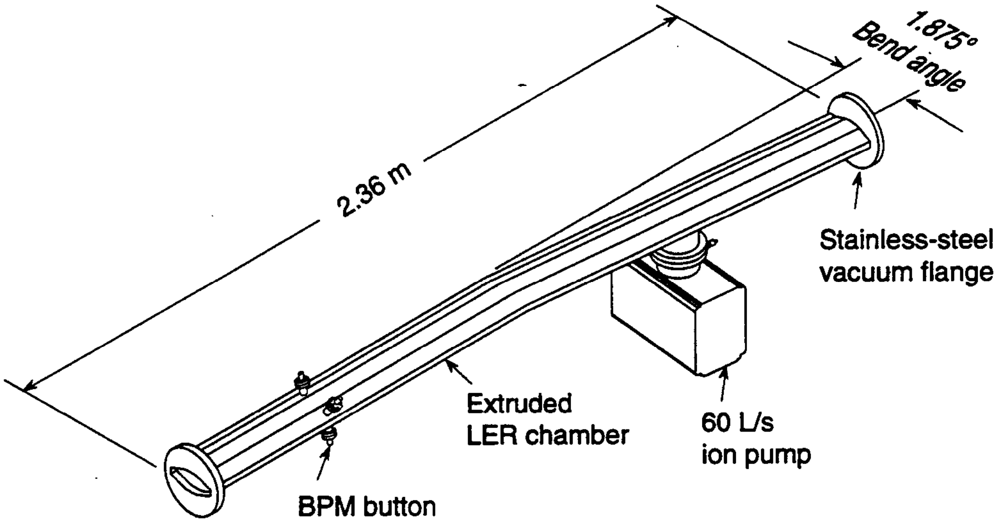

Fig. 5-62. Illustration of LER dipole vacuum chamber.

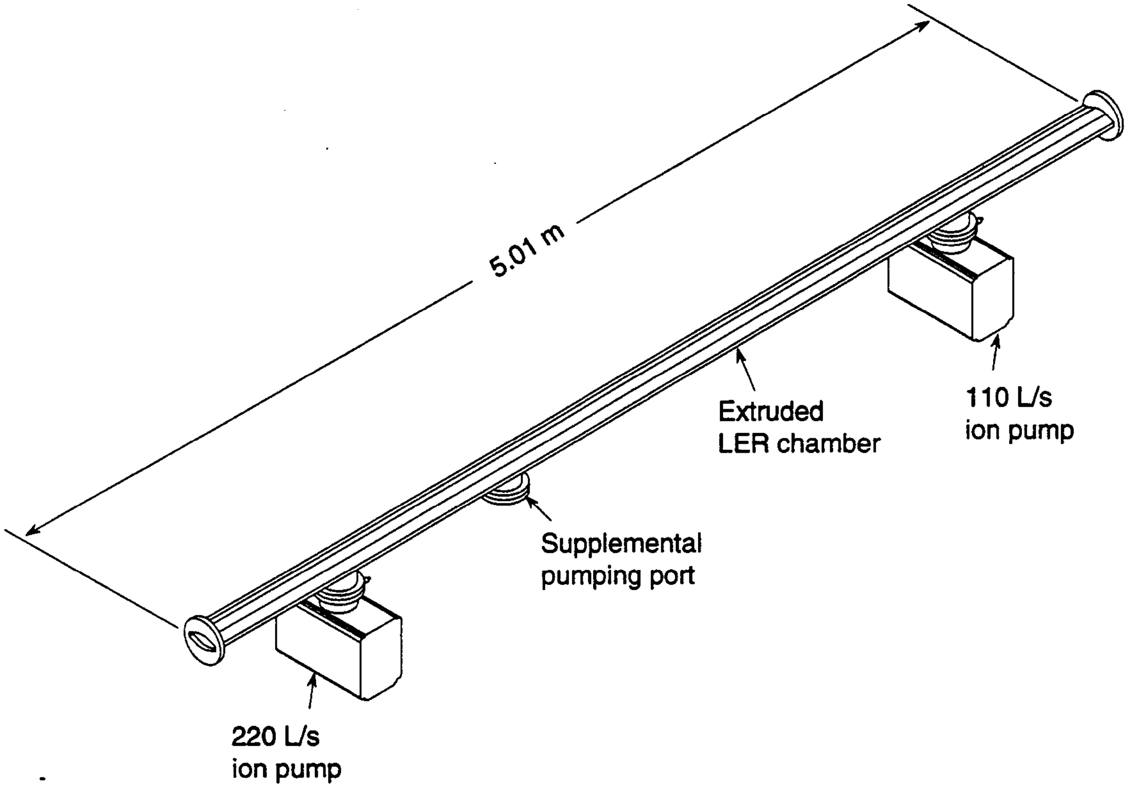

Fig. 5-63. Illustration of LER pumping chamber.

and accommodates thermal expansion. To facilitate connection to the dipole chamber, a flex-joint at the upstream end of the pumping chamber allows angular compliance in the flange joint. A strong-back support structure is envisioned for the pumping chamber to support the weight of the ion pumps and to protect the long slender extrusion from damage. Connections to the LCW system are external to the vacuum system, thus eliminating water-to-vacuum welds that might develop leaks.

The arc vacuum system will be equipped to accommodate an in situ bakeout to 150°C. Hot water at 180°C, circulated through the LCW system, will supply the heat. Testing done for PEP [Winch, 1977; Jurow, 1976] showed that spacing the vacuum chamber away from the magnet poles to create an air gap provides sufficient insulation. Finite-element analysis of the PEP-II vacuum chambers shows that, for a copper chamber (which conducts even better than an aluminum PEP chamber), the desired bakeout temperature is reached without requiring thermal insulation of the vacuum chambers. The existing PEP hot-water bakeout system will be upgraded for PEP-II operation.

The LER BPM assembly will be similar to that of the HER. The BPM feedthrough assemblies are identical to those of the HER but are mounted directly on the dipole chamber extrusion via individual flanged ports, as shown in Fig. 5-64. BPMs will be calibrated using the same noninvasive technique as in the HER, and will be rigidly mounted to the quadrupole magnet to the same level of accuracy as in the HER.

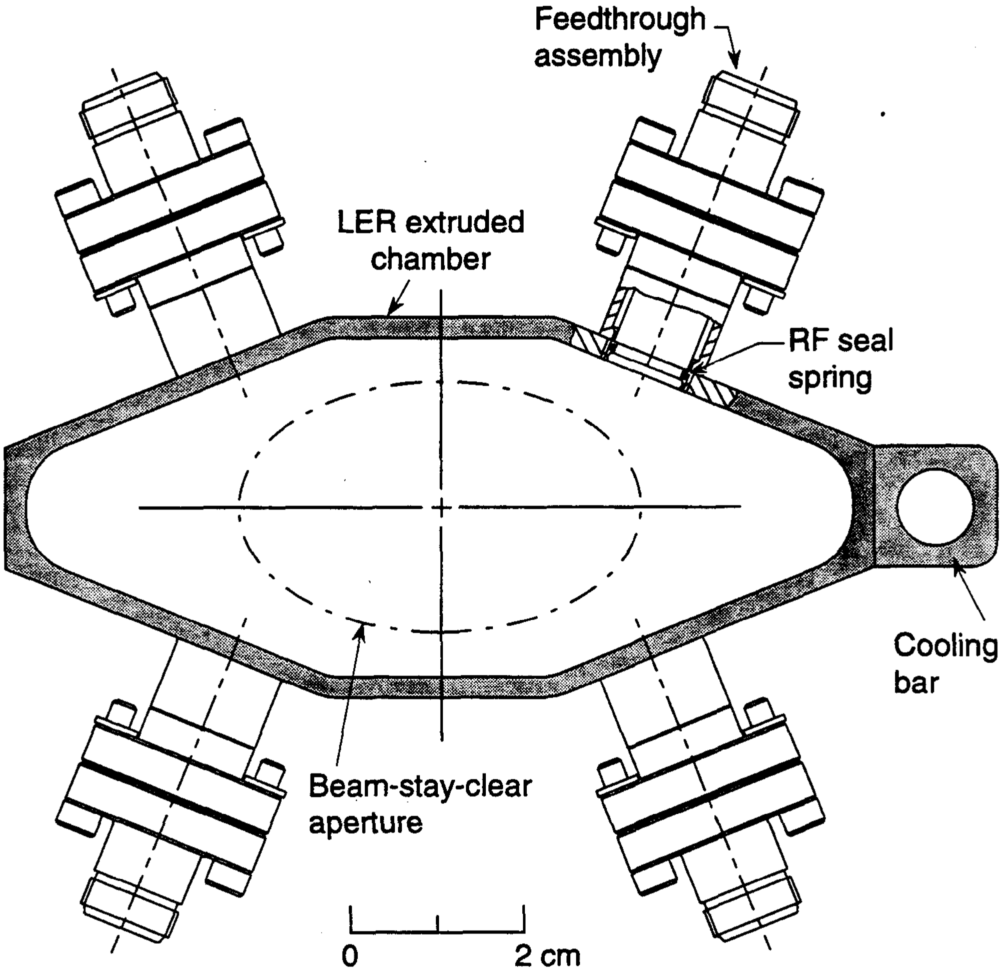

Fig. 5-64. Cross section of LER arc dipole chamber showing BPM configuration.

The basic bellows concept shown in Fig. 5-65 is identical to that for the HER, except for a mask located upstream from the bellows to mask it (and associated vacuum flanges) from synchrotron radiation. The bellows is located in the region with lowest power density, so the linear flux on the mask is very small.

5.2.5.4 Straight Sections. Each of the six straight sections has a length corresponding almost exactly to eight standard cells. Included in these sections are the RF cavities, the injection septa, beam pickups and kickers, horizontal and vertical beam collimators, and BPMs. One of the straight sections houses the common interaction region for PEP-II and thus has a unique layout. There are also 28 empty FODO cells in the ring. The beam pipe in the LER straight sections, made from standard 3.75-in.-OD stainless-steel tubing,

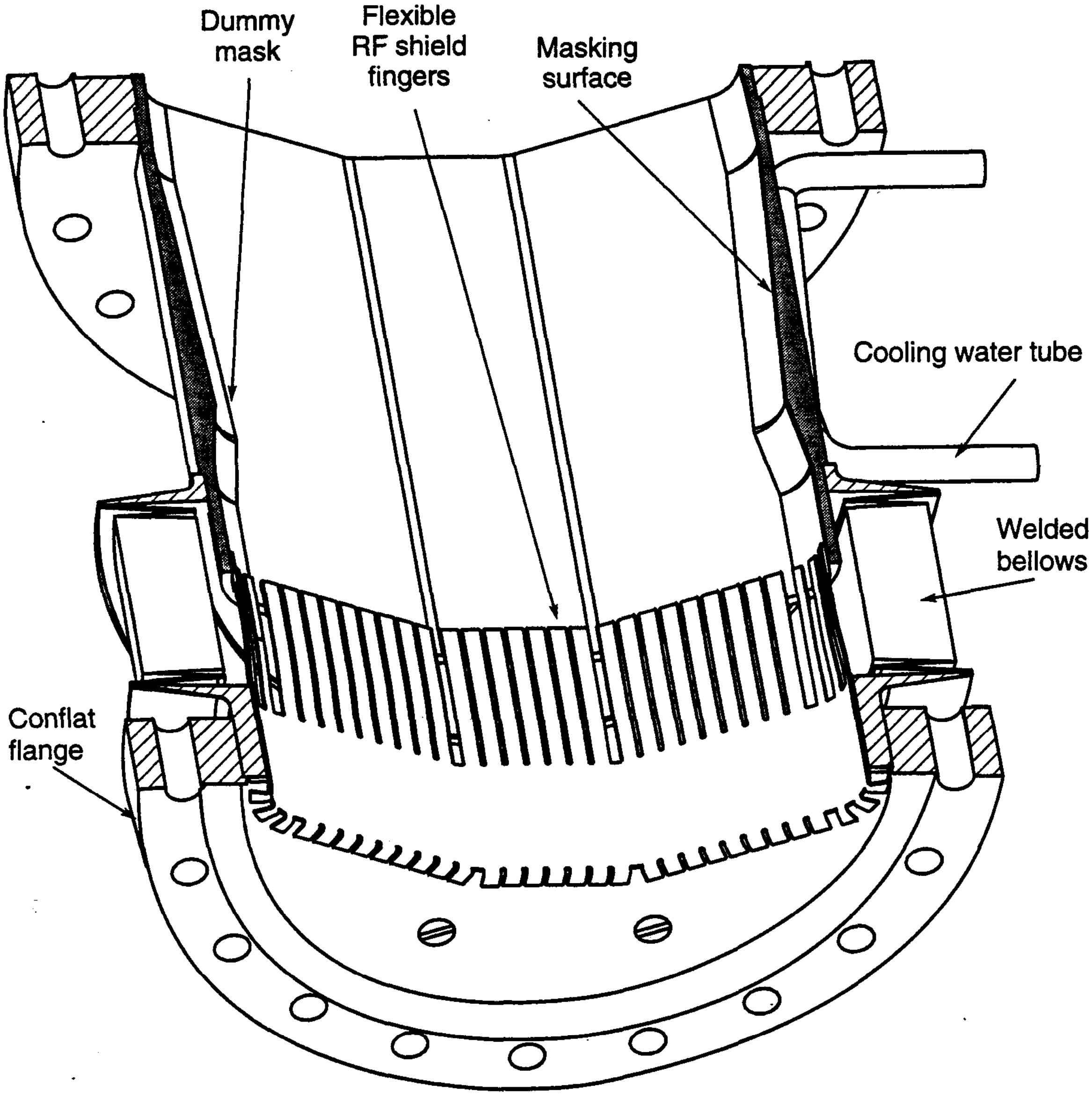

Fig. 5-65. Perspective of LER arc bellows.

along with the bellows, BPMs, and supports, will be essentially identical to components in the HER straight sections. The pumping configuration will be consistent with that designed for the HER. All-metal, RF-sealed, 100-mm-bore isolation valves are located in the straight sections at the end of each arc. To protect the RF cells in the event of an accidental vent to air, and to facilitate their conditioning, additional valves are also provided to isolate them. Isolation valves will also be installed on either side of the interaction region at ±5.2 m from the IP.

5.2.6 Radiation from Wigglers

To provide acceptable beam-beam tune shifts, the natural emittance of the LER must be increased considerably beyond that resulting from the arc dipoles alone. In addition, we have discussed in earlier reports [LBL, 1989; LBL, 1990] the potential advantages of having equal damping decrements in the high- and low-energy rings to minimize the effects of the energy asymmetry on the beam-beam interaction. For these reasons, wigglers will be used to create additional energy loss and control the beam emittance in the LER.

The damping decrement for a storage ring can be written as

$$\lambda = \frac{T_0}{\tau_x} = \frac{U_0}{2E} \qquad (5\text{-}27)$$

from which it is clear that, for equal damping decrements, the required synchrotron radiation energy loss per turn for the high- and low-energy rings must simply scale proportionately to the beam energy in the ring.

In the high-energy lattice (ρ = 165 m; E = 9 GeV), the total energy loss, which is dominated by the normal bends, is $U_0 = 3.58$ MeV/turn. For equal damping decrements, then, we need an energy loss in the LER of

$$U_{0,+} = U_{0,-}\frac{E_+}{E_-} = 3.58\left(\frac{3.1}{9.0}\right) = 1.24 \quad \text{[MeV/turn]} \qquad (5\text{-}28)$$

In the LER, we have a bend radius of ρ = 13.75 m. The energy loss from the horizontal bends can be estimated as

$$U_0 = 0.0885\frac{E^4}{\rho} \quad \text{[MeV/turn]} \qquad (5\text{-}29)$$

giving $U_0 = 0.59$ MeV/turn, that is, only about half of the requisite amount. (To create the matched damping decrement from the bending magnets alone would require a bend radius of 6.75 m, which would be, at best, inconvenient in terms of thermal power density.) In addition to the contribution from the horizontal bends, we must take account of the synchrotron radiation emission in the horizontal and vertical bends used to steer the low-energy beam from the IP into the arc sections (which lie above the plane of the HER). The energy loss from all of the magnets in the IR can be calculated from

$$U_{0,V} = 1.266\times 10^{-3}E^2\sum_i B_i^2 L_i \quad \text{[MeV/turn]} \qquad (5\text{-}30)$$

where E is in GeV, B_i is the dipole field in T, and L_i is the bend length in meters of the ith magnet. This gives a total contribution of 0.12 MeV/turn. Thus, the lattice itself contributes a total energy loss of 0.71 MeV/turn from the bending and separation magnets.

To reach equal damping decrements, then, we must produce an additional energy loss of 0.53 MeV/turn. This will be accomplished by including wiggler magnets in two of the

LER straight sections. As already mentioned, these wigglers also serve as a means of emittance adjustment for the LER; this adjustment works by creating a dispersion "bump" at the wiggler locations. By locating the wigglers in shallow chicanes off the principal axis of the straight section, the rms dispersion in the wiggler can be controlled externally to the wiggler. This additional degree of freedom extends the range of allowable wiggler characteristics. It also allows us to project the radiation into a distant photon dump and to spread the wiggler radiation along the side walls of the dump beamline.

Four wiggler sections, with six periods of $l_W = 0.67$ m, are included in each of two utility straight sections, as discussed in Section 4.1. The total length of wigglers is thus 32 m and the magnetic length is 19.2 m. A schematic drawing of the layout is shown in Fig. 5-66. For a wiggler composed of alternating-field dipoles, the total radiated power in MeV/turn is again given by Eq. 5-30. A wiggler field of $B = 1.51$ T is therefore needed to provide the additional 0.53 MeV/turn to fully equalize the damping decrements.

At the nominal current of 2.14 A, each wiggler will produce about 0.6 MW of synchrotron radiation power, with a critical energy of 9.6 keV. Most of this power will be dealt with externally to the ring vacuum chamber in specially designed photon beam dumps. However, some of the power will be deposited on the side walls of the vacuum chamber in the vicinity of the wiggler. To compute the power density at the dump and on the walls, we must estimate the angular distribution of the radiation. A precise description of radiation from a nonsinusoidally varying wiggler in the near field is not given in the literature, but we can modify the far-field description for standard wigglers given by Kim [1986] and apply it to segments of the wiggler to evaluate the resultant vacuum system requirements [Barletta and Garren, 1990].

Denoting the horizontal angle by θ and the vertical angle by ψ, we can write the power density in W/mrad^2 as

$$\frac{dP}{d\Omega}(\theta,\psi) = \frac{21\gamma^2}{16\pi K} U_{0,w}\, I\, N_W\, G(K)\, f_K(\gamma\theta,\gamma\psi) \tag{5-31}$$

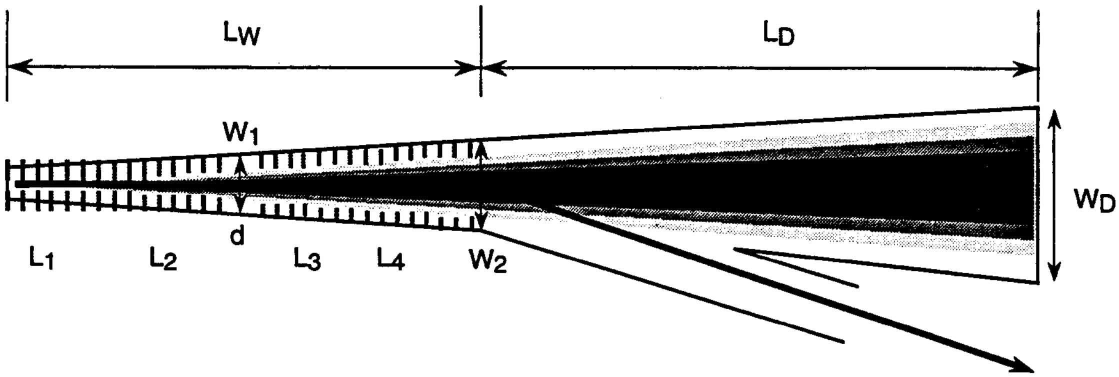

Fig. 5-66. Schematic representation of the vacuum chamber in the region of the LER damping wigglers.

where $U_{0,w}$ is the synchrotron radiation loss in one wiggler period, I is the beam current in A, N_W is the number of wiggler periods, and G and f_K are universal functions. For the bend-drift configuration, $U_{0,w}$ is given by Eq. 5-30, where the wiggler magnetic length is substituted for L_i. For a standard wiggler, K is the usual wiggler parameter defined (for B in T and λ in cm) by

$$K = 0.934 \; B_w \lambda_w \tag{5-32}$$

The normalization factor $G(K)$ is

$$G(K) = K \frac{\left(K^6 + \frac{24}{7} K^4 + \frac{16}{7}\right)}{\left(1 + K^2\right)^{7/2}} \tag{5-33}$$

For $K \gg 1$, $G(K) \rightarrow 1$; moreover, the angular distribution is sharply cut off in the wiggler bend plane. In the limit $K \rightarrow \infty$, the normalized angular distribution function $f_K(\gamma\theta, \gamma\psi)$ is given by

$$f_K(\gamma\theta, \gamma\psi) = \sqrt{1 - (\gamma\theta/K)^2} \left\{ \frac{1}{\left[1 + (\gamma\psi)^2\right]^{5/2}} + \frac{5\,(\gamma\psi)^2}{7\left[1 + (\gamma\psi)^2\right]^{7/2}} \right\} \tag{5-34}$$

From Eq. 5-34 one sees that the radiation is spread over a horizontal angle $2\theta_w$, where

$$\theta_w = \frac{K}{\gamma} \tag{5-35}$$

For the bend-drift configuration, θ_w is the bend angle in a single dipole. In that case Eq. 5-35 becomes the defining relation for an effective K value, K_{eff}. Given this K_{eff}, we apply the formalism for the standard wiggler. In the nonbend (vertical) plane, the rms angle of the radiation is

$$\psi_w = \left(\frac{\varepsilon_y}{\beta_y} + \frac{0.63}{\gamma^2} \right)^{1/2} \tag{5-36}$$

At 3.1 GeV, the second term in Eq. 5-36 is dominant, and $\psi_w \approx 1/\gamma = 0.13$ mrad to a good approximation. At the nominal operating current of 2.14 A, each wiggler generates 35 kW/m. The opening half-angle of the radiation is 15 mrad. Therefore, if the vacuum chamber is to intercept less than 20% of the radiation generated (to avoid an impractically high power loading on the crotch and on the side walls), the enclosure needs to be quite wide. By integrating Eq. 5-31 over ψ for K_{eff}, one can determine the power density on the side walls of the enclosure.

With regard to pumping requirements, there is a weak trade-off between increasing the static load from widening the chamber and minimizing the dynamic load by avoiding the photon fan. In the wiggler region, which occupies only 1.5% of the circumference of the ring, we have relaxed the required operating pressure to 10 nTorr.

The broad radiation fan suggests the use of a tapered stainless-steel chamber, as illustrated in Fig. 5-66. The photodesorption coefficient of the chamber is assumed to be 2×10^{-6}. The width W_1 should be as narrow as possible to maintain a practical quadrupole design. With this constraint in mind, the required pumping, which ranges from less than 5 L/s/m in L_2 to about 30 L/s/m in L_4, is obtained for $W_1 = 24$ cm and $W_2 = 40$ cm. The corresponding thermal loads range from less than 0.1 to 1.3 kW/m, respectively, on each side wall of the wiggler enclosure.

From Eq. 5-31, we can estimate that, at 2.14 A, the power density in the forward direction will be 1.0×10^5 W/mrad^2. We also find that 80% of the radiation is emitted into 7.7 mrad^2. Hence, we can compute the distance from the end of the wiggler to the photon dump, such that the power density is limited to a maximum value of 1 kW/cm^2. The distance from the wiggler to the dump, L_D, can be foreshortened by tilting the dump at an angle of about 15° with respect to the vertical. For a tilted dump, L_D should be about 27 m. Although roughly 10% of the power will actually be deposited on the walls of the wiggler chamber, we estimate the gas load at the dump assuming that all the power is incident there. We find that, for a copper dump with a photodesorption coefficient of 2×10^{-6}, the gas load at the dump is $Q_{\text{dump}} = 7.4 \times 10^{-5}$ Torr·L/s.

By considering the flared vacuum chamber from the wiggler to the dump to be a long, differentially pumped manifold, we can allow the pressure at the dump to rise to a much higher value than that required in the beam pipe. At the dump, the maximum horizontal extent of the radiation fan is 1.3 m, whereas the vertical extent of the radiation is only 1.3 cm. To lower the conductance of the photon channel, we take the chamber height to be 8 cm; baffles will also be added as needed to reduce the vacuum conductance into the wiggler straight section to 250 L/s.

The minimum total pumping of the dump plus photon channel is obtained by choosing the pressure at the dump to be 30 nTorr. This pressure requires 2000 L/s of pumping at, or near, the dump. This could be provided, for example, by installing large titanium sublimation pumps. Distributed pumping of 50 L/s/m along the photon channel reduces the pressure to 10 nTorr at the exit of the wiggler. More novel approaches, such as having the radiation fan strike NEG panels, are under study [Halama and Guo, 1990].

A C-frame bending magnet 5 m downstream from the wiggler exit bends the positron beam out of the radiation fan and into the straight beamline. The crotch can thereby be located away from the radiation fan of the wiggler. The straight beam pipe leaving the crotch is a special section of stainless-steel pipe, with a restricted aperture of less than 3 cm. Lumped ion pumps, providing 80 L/s of pumping speed in the region starting 10 m beyond the crotch and extending 5 m downstream of it, will reduce the pressure to 3 nTorr. At this point, a transition section will match the beam pipe dimensions to the standard straight-section vacuum chamber cross section.

5.2.7 Interaction Region Considerations

The interaction region is the heart of the entire PEP-II facility. Because the detector is located in the IR, and because the separation of the two beams takes place here, there are a number of special requirements and special constraints that must be accommodated by the hardware. The design issues that must be considered are mainly those associated with the need to protect the detector from backgrounds. As discussed in Section 4.2, various masks are used in this region to protect the detector components and other sensitive equipment from the synchrotron radiation emitted as the beams are being magnetically separated, and these masks perforce intercept some of the synchrotron radiation power. The issues that we consider here include:

- Local pumping to deal with the photodesorption from those mask and beam pipe surfaces hit by the synchrotron radiation fans
- Cooling of the detector beam pipe masks to remove the synchrotron radiation power
- Cooling of the septum masks that shield the septum quadrupole (Q2) from the high-power synchrotron radiation fans
- Cooling of the very thin beam pipe in the center of the detector to remove the power due to wall-current and HOM heating

5.2.7.1 Local Pumping. The pressure requirements inside the detector in the region upstream of the permanent-magnet quadrupoles are set by beam-gas bremsstrahlung events leading to lost beam particles. Within about ±20 cm of the IP, the limitation arises from electron-nucleus events leading to spurious triggers. For beam-gas interactions, we would like a pressure of 0.2 nTorr or lower outboard of the upstream Q1 magnet (for each beam). Very near the IP, estimates based on calculations [Lightbody and O'Connel, 1988] indicate that some tens of nanotorr should suffice, although measurements with Mark II at PEP suggest a more stringent limit. For PEP-II, a precise calculation requires more knowledge of the detector and trigger design than is now available, so the simple estimates must suffice.

Pumping inside the detector is provided by DIPs inside the permanent-magnet Q1 quadrupoles. It seems feasible to provide pumps with 150-L/s effective speed, including the conductance of the RF screen required to isolate the pump structure from the beam [Hartwig and Kouptsidis, 1974]. The principal gas load comes from photodesorption by the synchrotron radiation hitting the HEB and LEB masks inside the B1 magnets. To estimate the magnitude of the gas load, we use a desorption coefficient of 2×10^{-6} molecules/photon and a thermal outgassing coefficient of 1×10^{-11} Torr·L/s/cm^2. With these parameters, it will be possible to achieve the desired pressures.

As mentioned, maintaining a low pressure in the HER and LER straight sections that contain the interaction region is critical in order to reduce detector backgrounds. Guided by the background estimates discussed in Section 4.2, we have taken a design goal of 0.2 nTorr (N_2-equivalent) for estimating the amount of pumping needed in the "source" regions upstream of the IP (about 35 m for the HER and 15 m for the LER).

The incoming straight section of the HER has a photodesorption gas load associated mainly with the high-power upstream dump (HPUD, see Section 5.2.7.9). About 6 kW of synchrotron radiation from the low-energy beam impacts the wall in the upstream HER straight section at this dump, which begins 17 m from the IP. Assuming a photodesorption coefficient of 2×10^{-6} molecules per photon, the gas load will be 4.5×10^{-7} Torr·L/s/m in the vicinity of the dump. If this gas load were produced within the beam chamber, it would be necessary to provide about 2300 L/s/m of pumping along the dump to reduce the pressure to 0.2 nTorr. For this reason, we have considered an alternative approach—using a differentially pumped antechamber.

The arrangement we envision is shown schematically in Fig. 5-67. The duct connecting the antechamber to the beam chamber has a height of 1.1 cm and a length of 30 cm. Cooling along the duct entrance and exit provides fault protection in case of beam orbit shifts. In this arrangement, most of the gas load is removed in the antechamber by TSPs that provide a pumping speed of 1200 L/s/m (just after pump regeneration). Gas that leaks into the beam chamber through the long, low-conductance duct is pumped by two rows of NEG modules. Although rows of virgin NEG modules will pump CO and CO_2 at 700 L/s/m just after regeneration, we assume a maximum pumping speed of 350 L/s/m to account for degradation due to exposures to air early in the commissioning history of the collider. As both the NEGs and TSPs have speeds that vary with time, the upstream HER straight section pressure will not remain constant but will be bounded by the values indicated in Fig. 5-68. These curves determine the required regeneration time for the NEGs to be about 2 months and that for the TSPs to be about 1 week.

The LER gas load is due mainly to photodesorption associated with the horizontal and vertical separation magnets that guide the low-energy beam into the IP. To handle the thermal load and provide sufficient pumping to achieve the desired operating pressure, a differentially pumped antechamber design similar to the chambers for the HER dumps will be used. The IR straight section bending magnets are relatively short, 0.5 to 1.2 m in length, so the radiation produced in them first strikes the vacuum chamber wall downstream of the magnet. At these locations, the synchrotron radiation fans will pass through slots in the beam chamber wall to be absorbed on a water-cooled outer wall. The absorber surfaces will be sloped so as to limit the maximum linear power density to 10 W/mm. A combination of TSPs and 400-L/s sputter-ion pumps (obtained from PEP) will be used to achieve the desired operating pressures in the LER upstream straight section.

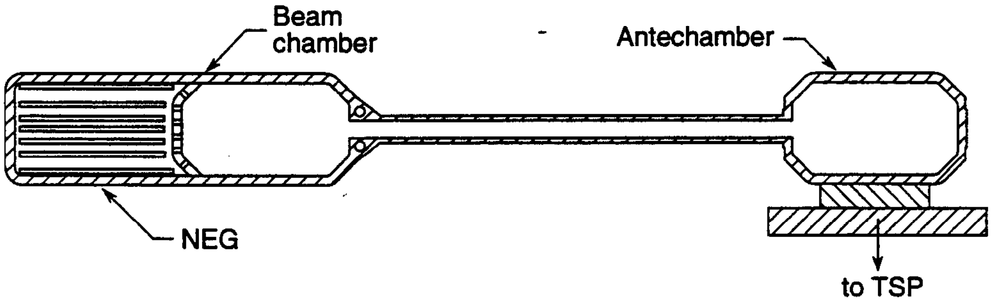

Fig. 5-67. Schematic of differentially-pumped beam chamber in HER beamline upstream of the IP.

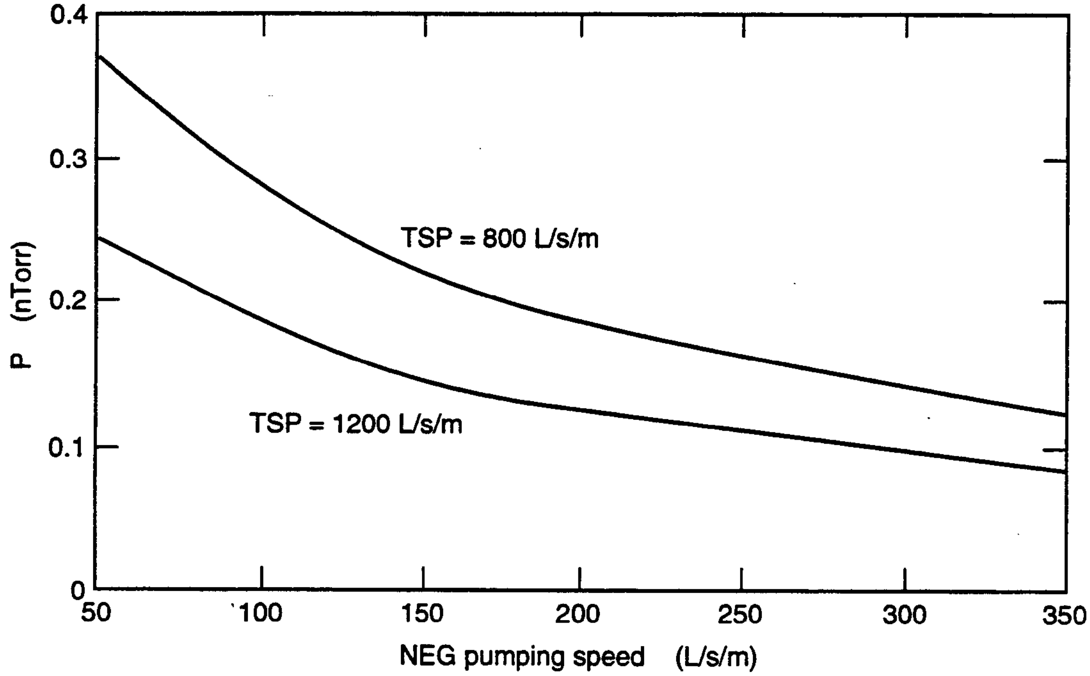

Figure 5-68. Pressure in beam chamber as a function of NEG pumping speed for two TSP pumping speeds. The TSP curves shown bound the expected range of pumping speed that will be covered between regenerations.

5.2.7.2 Synchrotron-Radiation-Absorbing Surfaces Near the IP. Areas in and around the IP where synchrotron radiation energy is deposited are indicated schematically in Fig. 5-69. These areas include the masks to protect the two septa, and the masks to stop radiation from impinging on the walls of the vertex chamber and portions of the walls of the vacuum chambers leading to and from the IP. All of these are considered in the following sections; a more detailed description of the masks can be found in the note by Lisin [1993]. Because reliability is crucial to the operation of PEP-II, it is important that the masks in the interaction region be designed conservatively. Below we estimate the power from the high-energy beam based on a beam current of 1.48 A, rather than the nominal 0.99 A. This will accommodate β_y^* in the HER up to 3 cm. The HEB septum mask will be discussed first as it sees the most severe conditions and therefore poses the greatest design challenge.

HEB Septum Mask. It is important that the vacuum walls of the septa in the two Q2 magnets be protected from incident synchrotron radiation. The septum on the incoming HEB side (left side in Fig. 4-46) sees synchrotron radiation generated by the low-energy beam as it passes through both of the B1 magnets. The HEB septum mask, located just inboard of the septum, intercepts some of the synchrotron radiation from the B1 magnets. Characteristics of those portions of the B1 synchrotron radiation fans that hit the mask are summarized in Table 5-24.

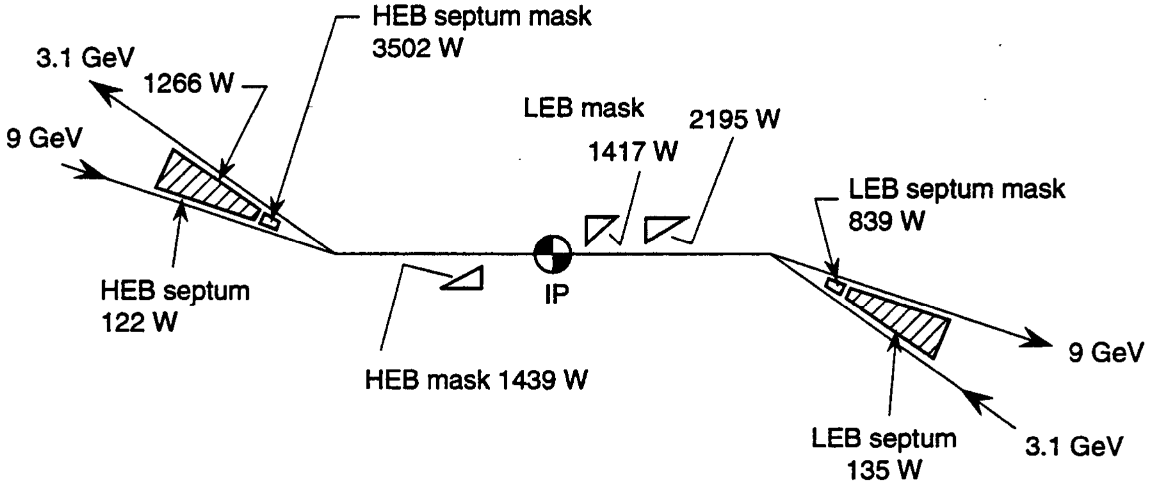

Fig. 5-69. Synchrotron radiation absorption in the vicinity of the interaction region. Power values correspond to a nominal beam current of 2.14 A in the LER and a 1.48-A beam current (compatible with a 3-cm vertical beta function at the IP) in the HER.

As shown in Fig. 4-47, the fans from the two B1 magnets overlap, so their heat inputs are additive. This results in a total power deposition in the HEB septum mask of 3502 W and a linear power density (normal to the radiation fan) of 168 W/mm. Table 5-24 shows the contribution from each source. The table also lists the synchrotron radiation fan height for a zero-emittance beam, which we take for design purposes.

A linear heat flux of 168 W/mm in a narrow stripe would result in excessive temperature and stresses, so the surface on which the synchrotron radiation is incident must be sloped relative to the radiation fan. In this case, we must create the slope by rotating the surface of the mask about an axis that lies in the plane of the radiation fan and is normal to the direction of the fan. Such a rotation avoids having the photons hit the leading edge of the mask, which cannot be adequately cooled. The central portion of the mask must have a very shallow slope in order to be able to absorb the very intense linear heat deposition rate of a narrow fan, while the mask must be sufficiently tall to intercept the fan from a more diffuse beam. The slopes at the ends of the mask can be much

Table 5-24. Synchrotron radiation power on the HEB septum mask.

Source	Power (W)	Normal linear flux (W/mm)	Fan height (mm)
HEB side B1	2078	102	0.67
LEB side B1	1424	66	1.02
Total	3502	168	—

steeper than that of the central portion, because the synchrotron radiation power density is lower with a broad fan. A slope of 1:50 in the central portion is sufficiently flat to give a reasonable heat flux through the body of the mask and across the metal-to-water interface with a 0.67-mm-high fan. With such a slope, the fan is absorbed over a length of 34 mm. The steeper ends are designed to give the same heat flux through the body of the mask and across the metal-to-water interface as for a zero-emittance beam striking the 1:50 slope. The central 1:50 sloping portion is extended to a total length of 137 mm to cover a 1 mm vertical steering error. The total length of the mask is approximately 390 mm.

Figure 5-70 shows the HEB septum mask geometry. The lightly shaded area represents the synchrotron radiation fans streaming from right to left. The tip of the mask lies below the plane of the fans and sees no radiation. As the absorbing plane rises, it intersects the bottom surfaces of the fans at about 180 mm from its leading edge. The next 34-mm section (more heavily shaded area) absorbs the synchrotron radiation. The last 180-mm section lies above the plane of the fans and sees no synchrotron radiation. To coincide with the beam-stay-clear boundaries, the sides of the mask are angled such that the mask is 14.5 mm wide at its tip and 22 mm wide at the septum end. The corner of the septum is located 46 mm from the collision axis.

Figure 5-71 shows the mask configuration used for the thermal analysis. The cooled surface is scalloped so that cooling tubes can be brazed to it. The use of scallops gives the maximum possible contact surface between the mask body and the cooling tubes. Three 6.3-mm (1/4-in.) OD cooling tubes, slightly flattened at the 14.5-mm-wide end, fit into the scallops. (Three tubes are used, rather than a single large passage, to give a greater convective heat transfer area.) Cooling water flows through the three tubes in parallel.

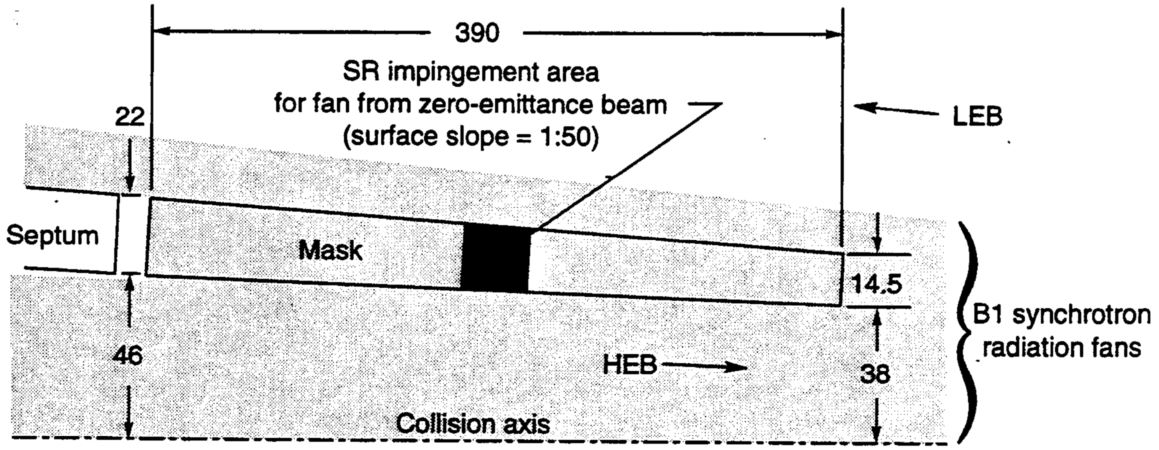

Fig. 5-70. HEB septum mask geometry (plan view). The incident synchrotron radiation fans from the B1 magnets originate approximately 2.2 and 3.1 m away from the mask surface.

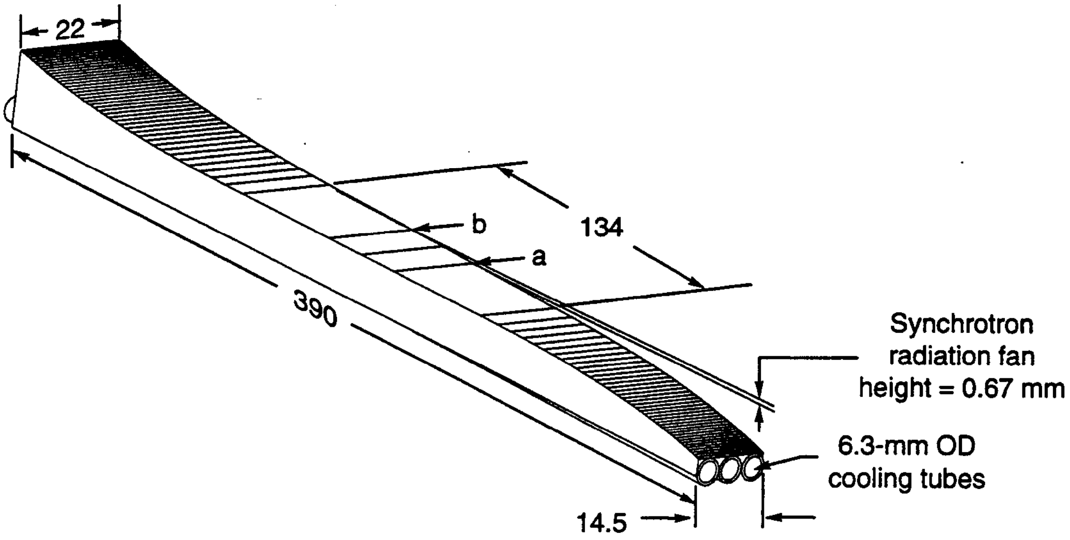

Fig. 5-71. Heat transfer model of HEB septum mask. The total power deposited is 3502 W. Synchrotron radiation from a centered, zero-emittance beam strikes the mask between points a and b.

The HEB septum mask design is summarized below:

- Geometry as shown in Fig. 5-71
- Three cooling tubes, 6.3-mm OD × 1-mm wall thickness
- Cooling water flows through the tubes in parallel, at a velocity of 4.6 m/s; total flow required is 15 L/min (4 gpm)
- Cooling water bulk temperature rise of 3.3°C
- Heated-surface-to-cooling-tube distance of 8 mm
- Mask body made of a dispersion-strengthened copper such as GlidCop AL-15
- Maximum metal temperature of 310°C for 20°C inlet water
- Maximum thermal stress of less than 40,000 psi

The above parameters are based on two-dimensional spread-sheet calculations of temperatures and hand calculations of stresses. Comparisons with earlier analyses of similar designs indicate that hand-calculated stress values are higher than those found from a full three-dimensional thermal and stress analysis using ANSYS. To avoid operational problems, thermocouples will be mounted at several locations along the mask to protect against excessive temperatures; the thermocouples may also prove useful to sense vertical beam position.

LEB Septum Mask. As on the incoming HEB side, the septum on the incoming LEB side (the right side of Fig. 4-46) must be protected from synchrotron radiation. The radiation fans that hit the front of the LEB septum mask are generated by the high-energy beam as it passes through B2, Q4, and BH1 (see Fig. 4-48). Characteristics of the fans that hit the LEB septum mask face are listed in Table 5-25.

The B2 fan extends over the entire width of the septum. The Q4 fan extends across approximately half of the septum and the BH1 fan across the other half (that is, the Q4 and BH1 fans do not overlap). Therefore, half the septum sees a linear power density normal to the fan of 60 W/mm and the other half sees 113 W/mm. The total power deposited is 839 W. (An additional 62 W coming from B6 on the LEB side strikes the edge of the mask.)

Compared with the HEB septum mask, the LEB septum mask must handle about one-fourth of the total power and has a maximum linear heat flux only two-thirds as much on half its surface (and one-third as much on the other half). The fan heights are essentially the same. The LEB septum mask surface on which the synchrotron radiation is incident will again have to be sloped. Although the heat flux is appreciably lower on half the mask, it is still too high in this region to be absorbed by a sharp corner. Therefore, the mask face will be sloped about an axis lying in the plane of the fan, as is the case for the HEB septum mask. The lower power absorbed by the LEB septum mask means that it could be sloped slightly more steeply than the HEB septum mask, making it shorter.

LEB Mask. The LEB mask (see Fig. 4-47) has two surfaces on which synchrotron radiation is incident. We refer to these as the "inboard" surface (nearer the IP) and the "outboard" surface (farther from the IP). Both the inboard and outboard mask surfaces prevent synchrotron radiation generated by the low-energy beam as it passes through Q1 from striking the vertex detector vacuum chamber wall; the outboard surface of the mask additionally intercepts the synchrotron radiation fans generated in Q2, B5, and B6. Figure 5-72 shows the LEB mask geometry. Table 5-26 lists the characteristics of the synchrotron radiation fans that strike the mask.

The outboard surface is struck by 1358 W of synchrotron radiation power in a fan of 0.5-mm height, 72 W in a fan of 0.8-mm height, plus 765 W in a fan of 4.5-mm height. The total power deposited on the outboard surface is thus 2195 W. The Q1 and Q2 fans do not overlap, but the B5 and B6 fans overlap both the Q1 and Q2 fans. The inboard surface is struck by 1417 W of radiation in a fan that is 0.49 mm high. The small portion of the Q1 fan that is not intercepted by the LEB mask (see Fig. 4-61) flies harmlessly past

Table 5-25. Synchrotron radiation power on the LEB septum mask.

Source	Power (W)	Normal linear flux (W/mm)	Fan height (mm)
HEB side B2	110	7	1.58
HEB side Q4	379	53	0.76
HEB side BH1	350	106	0.73
Total	839	60 or 113	—

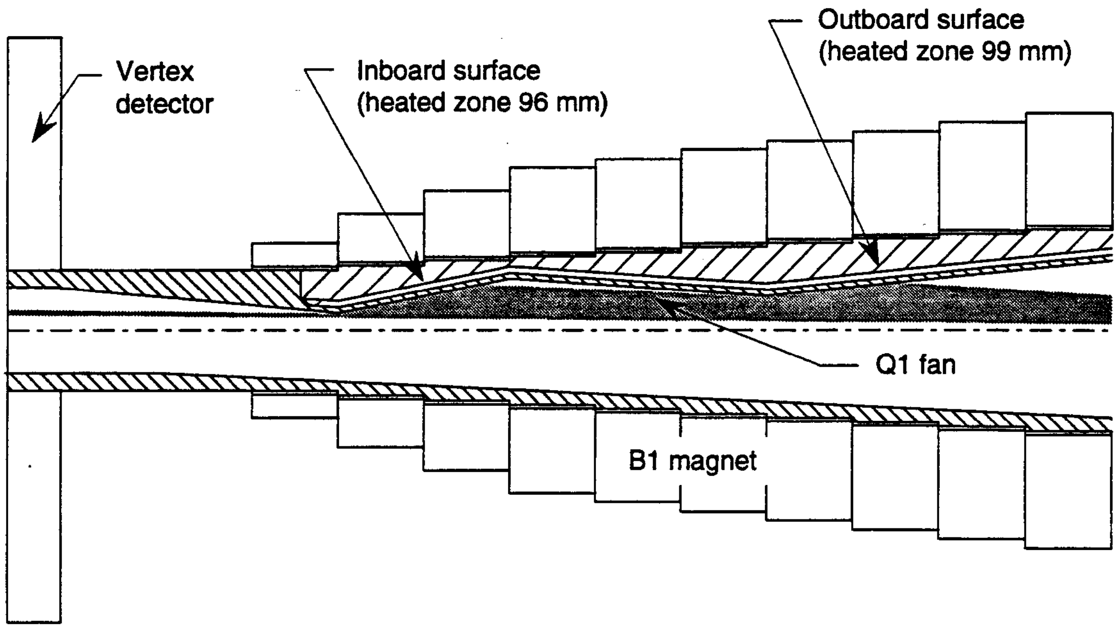

*Fig. 5-72. **LEB mask geometry, top view, showing zones heated by Q1 synchrotron radiation fan.***

*Table 5-26. **Synchrotron radiation power on the LEB mask.***

Incident on	Power (W)	Normal linear flux (W/mm)	Fan height (mm)
Outboard surface			
B5 and B6	765	9.4	4.5
Q2	72	10	0.8
Q1	1358	91.7 (max)	0.5
Total	2195	—	
Maximum	—	101.1	—
Inboard surface			
Q1	1417	71.0 (max)	0.5

the IR and is deposited on the wall of the outgoing LEB vacuum chamber beyond Q2; its intensity is sufficiently low that its energy deposition can be ignored.

The linear power density normal to the fans striking the mask is sufficiently high that the walls on which the synchrotron radiation is incident must be sloped. The outboard surface has a slope of 1:6.7, and the inboard surface has a slope of 1:5; these slopes result in surface linear fluxes of 15 and 14 W/mm, respectively. The slopes are created by rotating about an axis perpendicular to the plane of the fan to gain full advantage of the heat spreading normal to the plane of the fan. The slopes were chosen to be as flat as possible while still precluding the possibility of scattered radiation entering the vertex chamber after only one bounce. Fortunately, the slopes constrained in this way are still sufficiently flat to reduce the surface linear flux to levels that can be readily handled.

Both surfaces of the mask will be cooled by the same water passages. Two parallel water passages are milled into the body of the LEB mask/vacuum chamber straddling the horizontal centerline, as shown in Fig. 5-73. Water is supplied at the outboard end of the mask. The incoming water flowing through the passages removes the heat deposited by the synchrotron radiation fan. Two similar passages, located approximately ±90° away, are used to return the water to the outboard end of the mask. Transverse flow passages to connect the incoming and outgoing passages are milled into the mask body at its inboard end. The outflowing water removes most of the heat generated by scattered radiation, HOM losses, and resistive losses. A total water flow rate of 7.3 L/min (2 gpm) gives a velocity of 4.6 m/s (15 fps) and results in a bulk water temperature rise of 6.8°C. The water temperature rise due to the other heat sources is small and has been ignored.

Heat transfer and stress analyses of the model described above indicate that stresses are sufficiently high to require the use of a dispersion-strengthened copper. Results of a two-dimensional spread-sheet calculation of temperatures and hand calculations of stresses (assuming a zero-emittance beam) are summarized below:

• Cooling water flow rate	7.3 L/min (2 gpm)
• Inlet water temperature	20°C
• Outlet water temperature	26.8°C
• Metal temperature drop (max.)	70°C
• Film temperature drop (max.)	37°C
• Maximum metal temperature	134°C
• Maximum thermal stress	<40,000 psi

The above stresses appear to be reasonably conservative for a material like GlidCop AL 15, which has a fatigue strength of 48,000 psi at 10,000 cycles even after brazing at 800°C.

A more detailed analysis, using a three-dimensional thermal and stress code, will be performed to verify the design.

HEB Mask. The HEB mask prevents synchrotron radiation generated by the incoming high-energy beam as it passes through B2 and Q4 from striking the vertex detector vacuum chamber wall. Table 5-27 lists the characteristics of the fans that strike the mask.

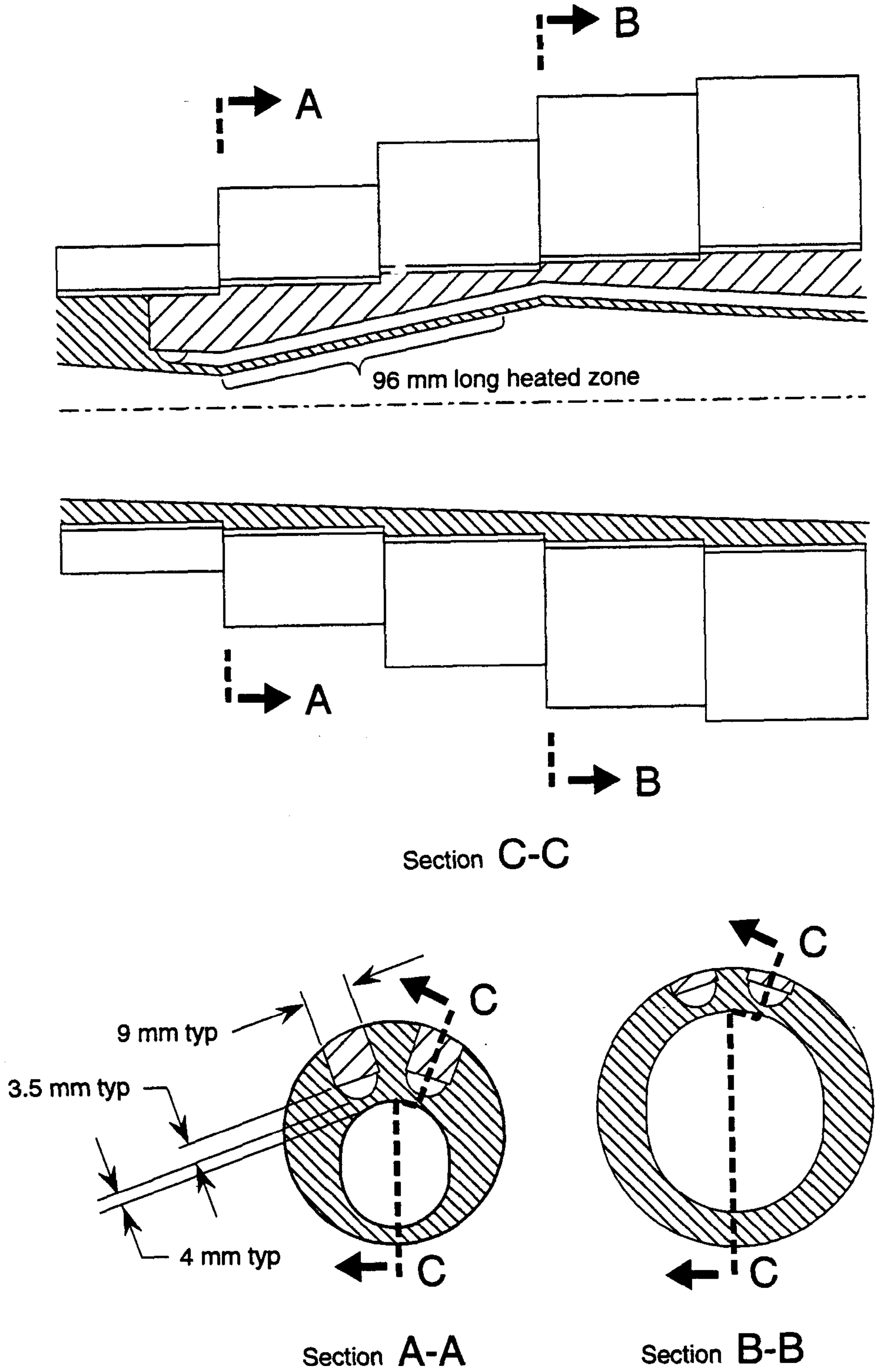

Fig. 5-73. Heat transfer model of LEB mask. Only inboard surface (see Fig. 5-83) and incoming cooling channels shown.

Table 5-27. Synchrotron radiation power on the HEB mask.

Source	Power (W)	Normal linear flux (W/mm)	Fan height (mm)
HEB side B2	158	13	0.94
HEB side Q4	1281	96	0.43
Total	1439	109	—

The effects of the two fans are additive—the total power deposited in the mask is 1439 W, and the linear power density normal to the fan is 109 W/mm. As for the LEB mask, the normal linear flux is undesirably high, so the mask surface must be sloped. A slope of 1:8.5 was chosen so that no scattered radiation can enter the vertex chamber after only one bounce. Such a slope reduces the surface flux to a level that can be readily handled. The total combined surface linear flux is 13 W/mm.

Because the surface linear power density on the HEB mask is comparable to that on the surface of the LEB mask, a cooling arrangement like that used for the LEB mask is adequate and will be employed.

Vacuum Chamber Thermal Issues. The septum side of the incoming HEB vacuum chamber absorbs radiation generated by the high-energy beam as it passes through B2. The total power incident on this wall is only 122 W, and the surface linear power density is 0.3 W/mm. The septum side of the incoming LEB vacuum chamber also sees a small amount of synchrotron radiation (135 W) generated by the LEB passing through B6. These low-intensity heat sources do not require special cooling arrangements.

Portions of the same synchrotron radiation fans that hit the HEB septum mask (see above) continue through the LEB exit chamber (see Fig. 4-62). The surface linear power densities are 1.2 and 1.3 W/mm for a total of 2.5 W/mm. A water-cooling line will be attached to the wall of the vacuum chamber to remove this heat. Heat removal in this area will not be a problem, of course, as the surface linear heat flux is considerably lower than that being handled in the arc vacuum chambers.

Vertex Detector Vacuum Chamber. The vertex detector vacuum chamber must be designed to be compatible with the detector requirements. This means that it must have the following features:

- It must be as transparent as possible to outgoing particles and photons from the collisions over a length of 170 mm
- It must have as small an outside diameter as possible
- It must have an inside diameter of 50 mm or less

Because heat deposited in the chamber by HOM heating and resistive heating will be about 200 W, the vertex detector vacuum chamber must also be cooled.

Beryllium was chosen for the chamber wall material because of its low Z and relatively high strength. The possibility of a beryllium tube cooled only at its ends was considered, but a double-walled tube with a cooling fluid in the annular space was found to be a more transparent and more efficiently cooled design. An illustration of the chamber concept is shown in Fig. 5-74. The ends of the beryllium tubes are brazed to stainless-steel ends. A spacer ring between the inner and outer tubes at each end maintains concentricity between the tubes to form an annular cooling passage 2 mm wide. The stainless-steel ends are welded to the spacer ring to seal the ends of the passage. Stainless-steel-to-beryllium joining technology that was used in the construction of the SLD beryllium vertex chamber will be used. Figure 5-75 is a photograph of the SLD chamber using such joining technology.

The outer wall thickness of the vertex detector chamber pipe is 0.4 mm, and its inner wall has a thickness of 0.8 mm. Both will withstand a pressure of about 50 atm. Coolant pressure will be considerably lower than this, so the safety margin is substantial. Indeed, the thickness was chosen primarily to make the chamber more rugged and to minimize chances of damage in handling.

Helium, hydrogen, and water were all considered as possible coolants. Although helium is not quite as good a coolant as either water or hydrogen, the fact that it is inert led to its being the coolant of choice. Beryllium and water appear to be compatible, but some beryllium would certainly enter the water and be carried by it. Concern about leaks and spills, and the resulting possibility of contamination, thus ruled out water. Hydrogen should be compatible with beryllium, but was ruled out because of its flammability.

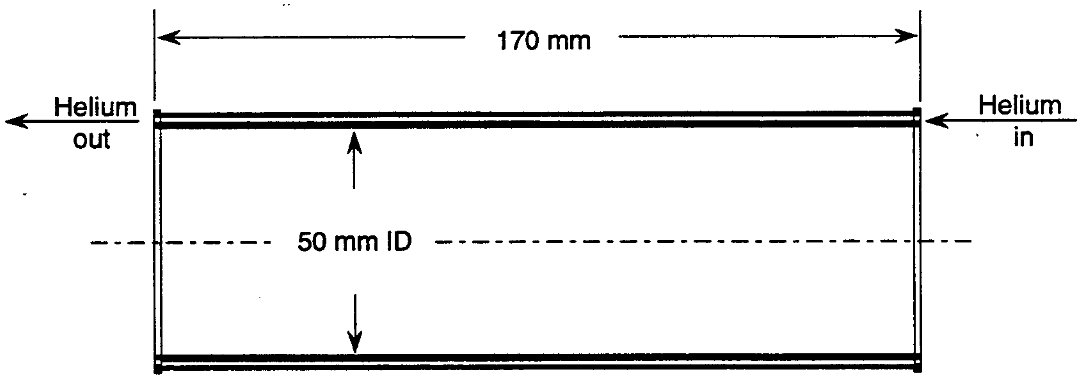

Overall length, 170 mm
Inner tube thickness, 0.8 mm
Outer tube thickness, 0.4 mm
Gap between tubes, 2 mm

Fig. 5-74. Design for the double-walled beryllium vacuum chamber for the vertex detector. Helium at 2 atm is used as the coolant.

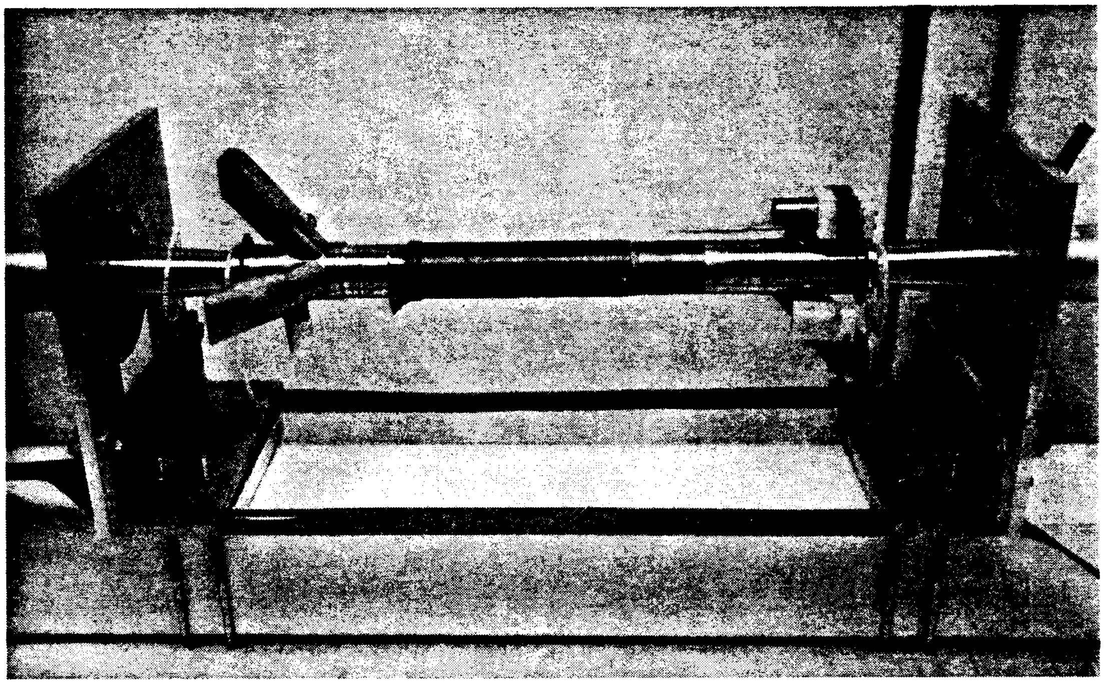

Fig. 5-75. Photograph of SLD vertex chamber.

Helium pressurized to 2 atm is quite adequate as a coolant. A flow of 22 g/s (Mach number = 0.2) gives a helium temperature rise of 1.1°C and a film temperature drop of 2°C for a 200-W heat input. Thermal stresses are quite low at these temperature differences. At least twice as much heat could be removed by the above flow should it prove necessary. Furthermore, the wall thicknesses adopted would allow the use of higher-pressure helium in the event that still more heat needed to be removed. Thus, the vertex chamber beam pipe is very reliably and conservatively designed for use in PEP-II.

5.2.7.3 High-Power Beam Dumps. There are several radiation sources close to the IP where the majority of the synchrotron radiation power is generated—the B1 dipoles and offset Q1 quadrupoles. Although both the HEB and LEB liberate considerable power in this region, the proximity of the sources to the IP means that most of the upstream synchrotron radiation fans (and nearly all of the downstream fans) pass through the detector area without hitting anything. To absorb the power, special dump areas are installed on both the upstream and downstream sides of the IP. The high-power downstream dump (HPDD), located in the HER outgoing beam pipe, absorbs the power generated by the HEB going through the IR (about 75 kW). The high-power upstream dump (HPUD) is the repository of about 6 kW of power generated by the LEB. Because those portions of the B1 fans from the LEB that do not strike the septum mask actually exit the IP area in the HER pipe, this dump too is located in the HER, but in the "upstream" portion (as seen by the HEB). Clearly heat removal per se will not be a problem for either the HPDD or HPUD, as the total power values are moderate. Nonetheless, the power densities are high enough to require special attention.

High-Power Downstream Dump. The synchrotron radiation fans generated by the high-energy beam (dominated by the contributions from the two B1 magnets) carry about 75 kW of power. To keep detector backgrounds low, and to allow the synchrotron radiation fans to spread, the bulk of the HEB radiation fan is dumped at a location 17–24 m away from the IP, just beyond the downstream string of B2 magnets in the HER (see Fig. 4-49). We refer to this area as the high-power downstream dump. Locating the HPDD at 17 m avoids congestion in the B2 area and allows flexibility in the design of the B2 magnets. Furthermore, at a distance of 17 m from the IP, the fans have spread out vertically to $\sigma_y = 2$ mm (assuming a zero-emittance beam), a size sufficient to ease the challenges of thermal management.

The HPDD vacuum chamber has an antechamber design, with sufficient differential vacuum pumping to maintain the required low pressure in the beam chamber. The synchrotron radiation fan passes through a slot in the beam chamber wall and is absorbed on a water-cooled outer wall in the antechamber. At 17 m, the linear power density normal to the synchrotron radiation fans is 375 W/mm, which is unmanageably high. However, if the absorbing surface has an initial slope of 1:40 relative to the fan, and the slope gradually steepens as the fan power density decreases, the radiation can be absorbed over a length of about 7 m, and the maximum linear power density can be held to an easily manageable value of about 10 W/mm.

High-Power Upstream Dump. We must also deal with the power carried by synchrotron radiation fans created by the low-energy beam passing through the IR. In this case, the total power that escapes the IP area is only 5.8 kW—much reduced compared with that from the high-energy beam. Furthermore, because of the lower beam energy, the vertical spreading (which goes as $1/\gamma$) will be even greater than for the HEB. Here too, the synchrotron radiation fans will be absorbed by a water-cooled dump (the HPUD) starting at about 17 m upstream of the IP in the HER.

5.3 SURVEY AND ALIGNMENT

The primary goal of the survey and alignment activity for PEP-II is to align the lattice components along a "smooth" curve. This should be done in such a way that the rms deviations of components from this curve do not exceed 150 μm and that the resulting circumference is within 5 mm of its design value. Overall tolerances for the alignment of the various ring components are summarized in Table 5-28. As can be seen from this table, the most important alignment criterion is the *relative* accuracy requirement. Consequently, long-period systematic effects on the measurements and computations are unimportant. This means that we need not be concerned about effects like geoid undulations, deflections of the vertical, earth tides, site-wide water table changes, etc.

Modern computer-aided methods and procedures, which have been tested and proved at SLC, HERA, and LEP, will be applied to perform the alignment. While great care and attention to procedural detail will be required to achieve relative alignment tolerances of 150 μm, much more demanding alignment projects are either ongoing at SLAC or have been successfully completed in the recent past. Magnet-to-magnet deviations obtained for the SLC arcs were 100 μm, despite the fact that, unlike the PEP-II rings (each of which